1987

NMR line shape studies of static and dynamic systems

Po-Jen Chu
Iowa State University

INFORMATION TO USERS

While the most advanced technology has been used to photograph and reproduce this manuscript, the quality of the reproduction is heavily dependent upon the quality of the material submitted. For example:

- Manuscript pages may have indistinct print. In such cases, the best available copy has been filmed.

- Manuscripts may not always be complete. In such cases, a note will indicate that it is not possible to obtain missing pages.

- Copyrighted material may have been removed from the manuscript. In such cases, a note will indicate the deletion.

Oversize materials (e.g., maps, drawings, and charts) are photographed by sectioning the original, beginning at the upper left-hand corner and continuing from left to right in equal sections with small overlaps. Each oversize page is also filmed as one exposure and is available, for an additional charge, as a standard 35mm slide or as a 17"x 23" black and white photographic print.

Most photographs reproduce acceptably on positive microfilm or microfiche but lack the clarity on xerographic copies made from the microfilm. For an additional charge, 35mm slides of 6"x 9" black and white photographic prints are available for any photographs or illustrations that cannot be reproduced satisfactorily by xerography.

Chu, Po-Jen

N. M. R. LINE SHAPE STUDIES OF STATIC AND DYNAMIC SYSTEMS

Iowa State University PH.D. 1987

PLEASE NOTE:

In all cases this material has been filmed in the best possible way from the available copy. Problems encountered with this document have been identified here with a check mark __✓__.

1. Glossy photographs or pages _____
2. Colored illustrations, paper or print _____
3. Photographs with dark background _____
4. Illustrations are poor copy _____
5. Pages with black marks, not original copy __✓__
6. Print shows through as there is text on both sides of page _____
7. Indistinct, broken or small print on several pages __✓__
8. Print exceeds margin requirements _____
9. Tightly bound copy with print lost in spine _____
10. Computer printout pages with indistinct print _____
11. Page(s) _____ lacking when material received, and not available from school or author.
12. Page(s) _____ seem to be missing in numbering only as text follows.
13. Two pages numbered _____. Text follows.
14. Curling and wrinkled pages _____
15. Dissertation contains pages with print at a slant, filmed as received _____
16. Other _____

_____

_____

N.M.R. line shape studies of static and dynamic systems

by

Po-Jen Chu

A Dissertation Submitted to the

Graduate Faculty in Partial Fulfillment of the

Requirements for the Degree of

DOCTOR OF PHILOSOPHY

Department: **Chemistry**

Major: **Physical Chemistry**

Approved:

Signature was redacted for privacy.

In Charge of Major Work

Signature was redacted for privacy.

For the Major Department

Signature was redacted for privacy.

For the Graduate College

Iowa State University
Ames, Iowa

1987

TABLE OF CONTENTS

PURPOSES AND GENERAL INTRODUCTION

The purpose of the current work is to extended the investigation of the line shape studies of quadrupole nuclei under (a) a combination of internal Hamiltonians, (b) rapid variable-angle sample spinning and (c) coherent or random nuclear dynamic motion. These studies exhibit some novel results which either provide a systematic approach to the analysis of the quadrupole NMR line shape or to the recognition of new qualitative NMR line shape features.

Strong quadrupole nuclei, which can not be studied by conventional transient techniques in conventional NMR, are now studied through: (a) indirectly observing the heteronuclear dipolar interaction reflected in the nearby spin 1/2 nucleus NMR spectra and (b) directly observing the singularities in the quadrupole (weak Zeeman) regime. These results will provide some valuable approaches to the studies of strong quadrupole nuclei.

The structure of the thesis is briefly described as follows:

Part I: The studies of the NMR spectra line shape under the influence of the internal Hamiltonians are based upon the knowledge of the spatial dependent transition frequencies of the combined Hamiltonians. Hence these spatial relations should be first derived before the NMR powder line shape can be calculated. In deriving these relations, the concept of the "Effective Hamiltonians" are introduced in the first part of the thesis. To demonstrate the accuracy of this line shape theory, a static system is examined by the field dependence of the characteristic frequency. The mutual orientation of the interaction tensor determined are compared with that obtained from single crystal.

Part II: The theory obtained from PART I is applied to the spinning system of Cs exchanged mordenite. The electric field gradient and the local electronic environment of the ^{133}Cs nucleus is determined by monitoring the line shape of the second order quadrupole central transition.

Part III: The theory is further extended from a static system to a dynamic system such as ^{23}Na in $NaMo_4O_6$ where the quadrupole nucleus of interest exhibits a multisite discrete jumping motion. Through the studies of the dynamic line shape of the second order central transition, the incommensurate structural transition, and the molecular dynamics can be distinguished. The position of sodium nuclei can also be determined from the dynamic line shape studies.

Part IV demonstrates that NMR spectra of spinning samples for spin-half nuclei in the presence of dipolar coupling to quadrupolar interaction can be used as an indirect probe for the nearby quadrupolar nucleus. This study is applied to ^{1}H in $ZrClO_xH_y$ system where the internuclear distance between the spin-half hydrogen nucleus and the quadrupole nuclei, Cl can be determined. The presence of the phase $Zr_6Cl_{12}H$ is detected by an unpaired electron density as inferred from the proton shift following Curie-Weiss law. From these line shape studies, the proton position can be determined.

PART I. FIELD DEPENDENCE OF NMR STATIC POWDER LINE SHAPE: STUDIES OF THE MUTUAL ORIENTATION OF INTERACTION TENSORS FROM THE FIELD DEPENDENCE OF THE CRITICAL FREQUENCIES

Field dependence of NMR static powder line shape: studies of the mutual orientation of interaction tensors from the field dependence of the critical frequencies

P.J. Chu , B.C. Gerstein,

Department of Chemistry, Iowa State University

Energy and Mineral Resources research Institute*

Ames, Iowa 50011

*Operated for the US Department of Energy by Iowa State University under contract # W-7405-Eng. 82. This research was supported by the Assistant Secretary for Energy Research, Office of Energy Sciences, WPAS-KC-03-02-01.

ABSTRACT

A procedure for determining the interaction tensor orientations and the interaction parameters for mutually oriented electric field gradient (e.f.g.) or dipolar and shielding tensors has been developed based upon the magnetic field dependence of the critical frequencies from the polycrystalline NMR spectrum. Analytical expressions for the field dependent critical frequencies have been determined for special orientations when the shift principal Z axis lies on the XZ, YZ or XY plane of the e.f.g. (or dipolar) tensor. The analytical expressions provide a convenient pattern recognition for determining the approximate tensorial orientation and the interaction parameters. For general orientations, a numerical procedure has been developed to determine these parameters by iteratively minimizing the squares of the differences of the calculated and the experimental critical frequencies. Higher order perturbation terms can be incorporated in the present treatment.

The method is demonstrated by variable field static proton spectra of tri-chloroacetic acid at three different fields (1.3T, 2.3T, 5.2T). The near-orthogonal orientation between the dipolar and shielding tensors and the interaction parameters obtained from this approach are consistent with those obtained previously from single crystal studies.

INTRODUCTION

NMR powder spectra associated with a single inhomogeneous interaction under static conditions, sample spinning, or under the influence of molecular motion have been studied.[1] In general, however, there will exist two or more internal interactions affecting the energy levels of a nucleus in a solid. The spectra are therefore different from those predicted by a single interaction. A standard approach in studying the interactions under the circumstances is to selectively average, or suppress one or more interactions by transient techniques in NMR[2,3] which allow the study of the interaction unaffected. These techniques include Magic angle sample spinning (MAS)[4,5,6] applied to suppress the interactions possessing spatial dependence ($3\cos^2\theta-1$); multi-pulse homonuclear decoupling experiments (MP)[2,3,7] are employed to suppress the $3I_zI_z-I^2$ spin dependent interactions. Numerous applications have been reported applying these approaches.[8] However there are some limitations and drawbacks of these applications:

(1). The relative orientations of the principal axis of the component interaction tensors is completely lost upon applying the MP or MAS techniques. The orientation relation of interactions in solids are closely related to the molecular or crystal structure and reflect indirectly the electronic and bonding structure about the nucleus.[1,3]

(2). When a system experiences a nonnegligible dipolar interaction, under MAS the intensities of the rotational side bands are modulated not only by the shift anisotropy and shift asymmetry, but also by the dipolar coupling constant. Extracting the interaction parameters under these conditions, requires extensive modification of the formulae

proposed by Hertzfield and Berger[9] where only a single shift interaction is considered.

(3). Due to finit rf power, the condition $H_{rf} >> H_i$ limits the application of the MP techniques to systems of relatively narrow inhomogeneous line widths. For strongly dipolar coupled systems or those experiencing a Knight shift, the spectrum is subject to distortions upon the application of M.P. techniques. When the nuclear motion frequency is of the order of the sampling rate ($\simeq$ 50kHz), this technique becomes useless.

(4). Interactions that do not satisfy the special spatial dependence required by MAS can only be suppressed but not eliminated. The resulting spectra are not independent of the eliminated or suppressed interaction. For example the central transition of the second order quadrupolar interaction exhibits a residual line shape also dependent upon the size and the orientation of the shift interaction,[10] although the shift interaction has nominally been eliminated under magic angle spinning.

To avoid the artifacts and to regain the lost information associated with the above factors, the most direct and simplest approach from the experimental point of view is to study the static spectrum of a single crystal.[11] For systems where growing sufficiently large single crystals for NMR studies is not possible, the information can in principle be extracted from the one-dimensional (1-D) NMR powder spectra. The caveat is that the resulting spectrum can be calculated from the interaction parameters and the three relative orientation angles.

Taylor et al. have studied the static powder line shape of both the central transitions of half integer quadrupolar nuclei and the satellite transition of nuclei with spin greater then 1/2 in the presence of a nonnegligible shift interaction.[12,13] To obtain the interaction parameters, the powder spectrum governed by the internal interactions is iteratively fitted using a least squares routine. A large number of calculations and a spectrum of good signal-to-noise ratio are required. This method has also been applied to the analysis of ESR spectra to determine the orientation between the g tensor and the internal Hamiltonians,[13] since the spatial orientation of the g tensor can be described in the same manner as the shift (chemical of Knight) tensor. Considering the many parameters involved and the insensitivity of the NMR spectra to the tensor orientation, this analysis may not be fruitful even when spectra of high signal-to-noise ratios are available.

To provide more experimental data so as to yield unambiguous results, two approaches can be taken. The first is to use two dimensional (2-D) resolved experiments, and the second is a variable field experiment.

The correlation of tensorial interactions between heteronuclear dipolar coupling and chemical shifts has been studied by Linder et al.[14] The unique pattern of the ridges shown in the 2-D spectra served as an identification of the mutual orientation between the dipolar and the shift interactions. From the simulation of the chemical shift resolved dipolar powder spectra in the 2-D NMR, the parameters of the individual interactions as well as the orientations can be determined.

Torgeson et al.[15] and Jones et al.[16] have studied the field dependence of the singularities for both the central transition vs. Knight shift and the satellite transition vs. Knight shift for half integer quadrupole nuclei. These studies show that determination of the interaction parameters can be accurately determined by fitting of the field dependence of the critical frequencies, instead of using a large number of iterative calculations of the powder spectrum.

The approaches by Creel et al.[17] and by Bauger et al.[18] however, have assumed that the principal axes of the electric field gradient (e.f.g.) tensor and the shielding tensor are coincident. This assumption, although reducing three of the eight parameters required to describe the spectrum which are essential in both calculating the static powder spectrum and the analysis of the critical frequencies, is in general not correct. The absence of appropriate pulse techniques to resolve the shift from the quadrupolar interaction in the two dimensional spectrum makes it impossible to perform the 2-D analysis proposed by Linder et al. for quadrupole nuclei. In this report, the idea proposed by Barnes of mapping the critical frequencies with the magnetic fields is amplified. The general case where the interaction tensors are not coincident is considered. The influence of tensor orientations upon the static powder spectrum and the most prominent features of the spectrum for combined quadrupolar and shift interactions are discussed. Finally it is shown that the results are consistent with previous studies by Creel and Bauger in which the Euler angles (α, β, γ) between the interactions considered are zero.

EFFECTIVE HAMILTONIANS AND THE TRANSIENT DECAY

Two purposes are served in this section. The first is to derive the effective Hamiltonian corresponding to first and second order perturbations. Secondly the results are applied to demonstrate that the powder averaged transient decay can be derived directly from the Liouville-Von Newman equation.

Using superoperator notation[1] the Liouville-Von Newman equation is:

$$|\dot{\rho}(t)) = -i(\hat{H}_Z+\hat{H}_\lambda)\,|\rho(t)) \qquad \text{L-N equation}$$

here the superoperator is defined as $\hat{H} = [H, \ ]$

The general solution of the density matrix governed by a time independent Hamiltonian is

$$|\rho(t)) = \exp^{-i\int^t(\hat{H}_Z+\hat{H}_\lambda)d\tau}\,|\rho(0)) \qquad [1]$$

Using irreducible spherical tensor operator formalism, H_λ is given by[3]

$$H_\lambda^{ij} = \sum_k \sum_{m=-k}^{k} C^\lambda\,(-1)^m R_{k,-m}^{ij;\lambda}\ T_{k,m}^{ij;\lambda} \qquad [2]$$

The subscript λ represents the different interactions with λ=Z for Zeeman, λ=D for dipolar interaction, λ=C for chemical shift interaction, λ=Q for quadrupolar interaction and λ=J for scalar j coupling. The indices i, j represent a single spin interaction if i=j and spin-spin interactions if i≠j.

The scalar coefficient C^λ depends only on the fundamental interaction constants and the properties of the nuclear ground state.

T_{km}^{λ} are the irreducible tensor spin operator for interaction λ. Details of these tensors can be found in Mehring[1] and Haeberlen.[3]

R_{km}^{λ} are the irreducible tensor spatial operators. Transformation of these operators under rotations in both physical (spatial) or spin space have been given by Haeberlen,[3] and Maricq and Waugh.[19]

For simplicity in the following discussion, H_{λ} is treated as a single internal Hamiltonian. With the appearance of two or more interactions, as discussed later, H_{λ} represents the sum of all the Hamiltonians of the nuclear spin interactions in solids.

When the Zeeman Hamiltonian is much larger than the internal Hamiltonian(s), it is legitimate to retain only the first few terms of the series implied by [1] due to the fast convergence of the series. Using the factoring theorem for two time independent Hamiltonians, the density matrix becomes:

$$|\rho(t)) = T\exp^{-i\int^{t}\tilde{H}_{\lambda}(t')dt'} \exp^{-i\hat{H}_{Z}t} |\rho(0)) \qquad [3]$$

$$\text{Where } \tilde{H}_{\lambda}(\tau) = \exp^{i\hat{H}_{Z}\tau} |H_{\lambda}) \qquad [4]$$

and T represents the well known Dyson time ordering operator.[7] The first term in [3] is conveniently evaluated by the Magnus expansion which becomes:

$$T\exp^{-i\int_{0}^{t}\tilde{H}_{\lambda}(\tau)d\tau} = \exp^{-i\bar{H}_{e}t} \qquad [5]$$

$$\text{and } \bar{H}_{e} = V_{\lambda}^{(0)} + V_{\lambda}^{(1)} + V_{\lambda}^{(2)} + \ldots$$

The averaged Hamiltonian $V_\lambda^{(0)}$ and the next two terms are well known

$$V_\lambda^{(0)} = \frac{\omega_0}{2\pi} \int_0^{t_c} \tilde{H}_\lambda(t)dt \qquad [6]$$

$$V_\lambda^{(1)} = \frac{-i\omega_0}{4\pi} \int_0^{t_c} dt' \int_0^{t'} [\tilde{H}_\lambda(t'), \tilde{H}_\lambda(t")]\, dt" \qquad [7]$$

$$V_\lambda^{(2)} = \frac{-\omega_0}{12\pi} \int_0^{t_c} dt' \int_0^{t'} dt" \int_0^{t"} \{[\tilde{H}_\lambda(t'),[\tilde{H}_\lambda(t"),\tilde{H}_\lambda(t"')]] + [\tilde{H}_\lambda(t"'),[\tilde{H}_\lambda(t"),\tilde{H}_\lambda(t')]]\} dt"' \qquad [8]$$

where t_c, the cycle time, equals one Larmor period $2\pi/\omega_0$. For shift and dipolar interactions which are much smaller then the Zeeman term, the averaged term $V_\lambda^{(0)}$ already gives accurate results. The second term $V_\lambda^{(1)}$ corresponds to a second order perturbation and is required only for the central transition of the half integer quadrupolar spin.

Before evaluating the truncated Hamiltonian, it is necessary to evaluate the internal Hamiltonian, $\tilde{H}_\lambda(t)$ expressed in the Zeeman rotating frame.

$$\begin{aligned}\tilde{H}_\lambda(t) &= \exp^{-i\omega_0 t\cdot I_0} \{ \sum_{m=-k}^{k} C^\lambda (-1)^m R^k_{-m} T^k_m \} \exp^{i\omega_0 t\cdot I_0} \\ &= \sum_{m=-k}^{k} C^\lambda (-1)^m R^k_{-m} \exp^{-i\omega_0 t I_0} |T^k_m) \\ &= \sum_{m=-k}^{k} C^\lambda (-1)^m R^k_{-m} \exp^{-im\omega_0 t} |T^k_m) \end{aligned} \qquad [9]$$

In the current case, we consider the nucleus to be in the rigid lattice of a static sample. Therefore, R^k_m is considered to be time-

independent. The average Hamiltonian $V_\lambda^{(0)}$ after integration over one Larmor period as from [6] and [9] becomes:

$$V_\lambda^{(0)} = C^\lambda R_0^k T_0^k \qquad k=0,1,2 \text{ only} \qquad [10]$$

Similar to the averaged Hamiltonian, the next term in the Magnus expansion for a second rank (k=2) tensor which appears in the dipolar and quadrupolar interactions can be calculated. The result is

$$V_\lambda^{(1)} = \frac{-i\omega_0}{4\pi} (C^\lambda)^2 \int_0^{t_c} dt' \int_0^{t'} \sum_{mm'} (-1)^m (-1)^{m'} R^2_{-m'} R^2_{-m} \cdot [\, T^2_{m'}, T^2_m \,] e^{-im'\omega_0(t''+t')} dt'' \qquad [11]$$

After evaluating the commutators and the double integral according to [7], this term is written specifically for the quadrupolar interaction:

$$V_Q^{(1)} = \frac{2}{9\omega_0} \left(\frac{3eQ}{4I(2I-1)}\right)^2 \cdot \{ |R_1^2|^2 (4I^2-8I_0^2-1)I_0 - |R_2^2|^2 (2I^2-2I_0^2-1)I_0 + \frac{\sqrt{6}}{2} R_0^2 [R^2_{-1}(4I_0^2-4I_0+1)I_+ - R_1^2 (4I_0^2+4I_0+1)I_-] + \sqrt{6}\, R_0^2 [R_2^2 (I_0+1)I_-^2 + R^2_{-2}(I_0-1)I_+^2] \} \qquad [12]$$

The first two terms yield identical results to that given by Volkof[20] and later by Cohen and Reif[21] derived using the second order perturbation theory for the quadrupolar interaction. The rest of the terms although nonsecular have not been averaged to zero according to

the averaged Hamiltonian treatment. To evaluate the density matrix incorporating the nonsecular Hamiltonian terms requires diagonalization of [12]. The influences of the nonsecular terms upon the powder spectra are however minor[5,19] and are neglected in order to simplify the calculations.

Higher order terms in the Magnus expansion are harder to evaluate. In the high field or in the weak quadrupole limit, the first two terms are sufficiently accurate. Under this condition the density matrix, [3] can be rewritten according to [5] as

$$|\rho(t)) = \exp^{-i\bar{\hat{H}}_e t}|\tilde{\rho}(0)) \qquad [13]$$

or can be expressed similar to the L-N equation as follows:

$$|\dot{\rho}(t)) = \bar{\hat{H}}_e|\rho(t)) \quad \text{with condition} \quad |\rho(0)) = |\tilde{\rho}(0)) \qquad [14]$$

$$\text{and} \quad \bar{\hat{H}}_e = V_i^{(0)} + V_i^{(1)} \qquad [15]$$

At this point we want to emphasize that the spatial dependence implied in R_m^k, is directly related to the above quantities; the density matrix, the effective Hamiltonian, and the averaged Hamiltonian. The parameter, $\Omega=(\theta, \phi)$ denotes this spatial dependence, representing the orientation of the principal axes frame of the internal interactions with respect to the external field.

To calculate the spectrum, the expectation value of a transverse component of the angular momentum in the time domain is first calculated from the stationary state energy levels of an ensemble of nuclei exposed

to one or more internal interactions leading to inhomogeneous broadening. The powder spectrum is then obtained from the Fourier transform of the appropriately apodized time decay.

The time decay of the magnetization associated with the single crystal orientation Ω, with phase detection along y can be determined once the density matrix is calculated from [13].

$$\langle I_y(t,\Omega)\rangle = (I_y|\rho(t,\Omega)) \qquad [16]$$

Recall that all terms in [16] are matrixes evaluated in the basis, $|m\rangle$, which makes the effective internal Hamiltonian $\bar{H}_e$ diagonal. These are basically the Zeeman states if the off diagonal terms appearing in the $V^{(1)}$ is neglected. By the definition of the trace and noting that the propagator $U=\exp\{-i\bar{H}_e t\}$ is also diagonal, the terms in [16] are evaluated as

$$\begin{aligned}\langle I_y(t,\ \Omega)\rangle &= \sum_{j,k} U_{jj} I_{y,jk} U_{kk}^{-1} I_{y,kj} \\ &= \sum_{j,k} U_{jj} U_{kk}^{-1} I_{y,jk} I_{y,kj} \\ &= \sum_{j,k} |\langle j|I_y|k\rangle|^2 \exp\{-i[\omega_j(\Omega)-\omega_k(\Omega)]t\} \qquad [17]\end{aligned}$$

The U_{nn}'s are the diagonal matrix elements of the propagator $\exp\{-i\bar{H}_e t\}$, evaluated within the Zeeman basis set $|m\rangle$. Note that the stationary state eigen frequency is given by

$$\omega_k(\Omega) = \langle k|\bar{H}_e(\Omega)|k\rangle = \langle k|V_\lambda^{(0)}(\Omega)|k\rangle + \langle k|V_\lambda^{(1)}(\Omega)|k\rangle \qquad [18]$$

Since the transition probability $|\langle j|I_y|k\rangle|^2$ is nonzero only when $|j-k|=1$, the double summation over j and k in [17] is reduced to a single summation over each transition k. Equation [17] then becomes:

$$\langle I_y(t,\Omega)\rangle = \sum_k P_k \exp\{-i\Delta\omega_k(\Omega)\} \qquad [19]$$

Where the k-th single quantum transition frequency for $(k \rightarrow j)$ equals $\Delta\omega_k = \omega_j - \omega_k$ with the index subject to the constraint that $j=k-1$. The corresponding transition probability is $p_k = |\langle j|I_y|k\rangle|^2$, which may be evaluated directly from the eigen functions of the problem at hand. For example, if the internal Hamiltonians are acting on a spin 1/2 system, all transition probabilities are unity. If the internal Hamiltonian is acting on a quadrupolar nucleus of spin I, the transition probabilities will depend upon the final state of the z component k-1, and calculated using the result that $|\langle k-1|I_y|k\rangle|^2$ is proportional to $I(I+1)-k(k-1)$. We introduce a relaxation function, $g(t) = \exp\{-t/T_{2k}\}$ which accounts for the incoherent transient processes originating from the nonsecular terms that has been neglected previously. Then

$$\langle I_y(t,\Omega)\rangle = \sum_k P_k \exp\{-i\Delta\omega_k(\Omega)\}\exp\left(\frac{-t}{T_{2k}}\right) \qquad [20]$$

To obtain the FID of the inhomogeneously broadened lines, a superposition of all of the above oscillations for all possible values of Ω, with individual decays given by the same relaxation function $\exp-\{t/T_2^{eff}\}$, is made. This superposition is made by integrating $\langle I_y(t,\Omega)\rangle$ over all space Ω, leading to the powder averaged transient

signal;

$$\langle\overline{I_y(t,\Omega)}\rangle = \sum_k \int_\Omega \int \sin\theta d\theta\, d\phi \cdot P_k \exp\{-i\Delta\omega_k(\Omega)\}\exp(\frac{-t}{T_{2k}}) \qquad [21]$$

Thus the only information necessary in calculation of the spectrum from the averaged transient decay are the stationary state eigen-energies $\omega_k(\Omega)$, or the transition frequencies $\Delta\omega_k(\Omega)$ as a function of orientation parameter $\Omega = (\theta, \phi)$. As previously stated in [18] these can be directly evaluated from the related first two terms in the Magnus expansion, [10] and [12].

The NMR spectra can be immediately calculated by the inverse Fourier transform of [21]. This procedure of line shape calculation is different from that generally used by summing a Lorentzian or Gaussian broadened stick spectrum or by other direct methods. In Appendix A, the identity between all these methods are demonstrated and the advantages of the current scheme are discussed.

Of particularly interest in the current study is that when more than a single interaction is present, transition energies $\Delta\omega_k(\Omega)$ are the differences in energy states of the system associated with any sum of the internal interactions leading to inhomogeneous broadening. Examples are: (a) shielding plus second order quadrupole; (b) shielding plus two body dipole; or (c) a sum of shielding, second order quadrupole and two body dipole. The parameter Ω in the multi-interaction case is subject to an important constraint that the individual interaction tensors orients independently and maintain constant mutual orientations within molecular frame or within unit lattice of a solid. As a result, the eigen-energies or the transition frequencies for a micro-crystallite

orientation; Ω is not a simple sum of the individual spatially dependent energies or transition frequencies written as

$$\omega_k(\Omega) = \sum_\lambda \omega_k^\lambda(\Omega)$$

but rather this should be

$$\omega_k(\Omega) = \sum_\lambda \omega_k^\lambda(\Omega^\lambda) \qquad [22]$$

with angles Ω^λ subject to a fixed mutual orientations between all internal interactions. This can be achieved by expressing the spatially dependent transition frequencies according to a "referenced" frame (vide infra).

ORIENTATION DEPENDENT TRANSITION FREQUENCIES

As mentioned in [21], the spatially dependent transition frequencies are the only information required to calculate the NMR line shape. In this section we wish to obtain these spatially dependent relations for those fundamental interactions involved in the later discussions. The procedure to obtain these expressions is briefly discussed.

First the effective Hamiltonian in [15] is determined for the individual interactions. In the current study, only the averaged term $V_\lambda^{(0)}$ is retained for the dipolar and shift interactions. This truncation gives identical results to a first order perturbation. For integer spin nuclei, and the satellite transitions ($k \neq 1/2$) of half integer quadrupole nuclei, the effect of higher order terms other then the averaged Hamiltonian are also neglected. We consider the $V_\lambda^{(1)}$ term only for the central transition of the quadrupole nuclei, which is the major nonzero term. This truncation is equivalent to a second order perturbation treatment when all off diagonal terms in [12] are neglected.

Second the irreducible tensor components $R_m^2(\Theta,\phi)$ which yield the spatial dependence of the Hamiltonians is determined. A single interaction frame transformation that relates the principal axis (PAS) frame to the laboratory frame is performed according to the Wigner rotation[3,22] as follows:

$$R_m^2 = \sum_{m'} D^{(2)}_{m',m}(0,\Theta,\phi)\ \rho^\lambda_{2m'} = \sum_{m'} e^{im'\phi}\, d^{(2)}_{m',m}(\Theta)\ \rho^\lambda_{2m'} \qquad [23]$$

The Wigner rotation matrices and the definition of the Euler angles

have been described.[1,3,9] Edmonds'[22] definition, where the reduced rotation matrices $d_{m',m}(\beta)$ are related to the Jacobian polynomials[1,22] is used. The irreducible spherical components of the shielding interaction in its principal axis system are:[23]

$$\begin{aligned}
\rho^{\lambda}_{2\pm2} &= \rho^{\lambda}_{22} = \frac{1}{2}\,(\sigma^{\lambda}_{xx}-\sigma^{\lambda}_{yy}) \pm i\sigma^{\lambda}_{xy} = \frac{1}{2}\,\eta^{\lambda}\delta^{\lambda} \\
\rho^{\lambda}_{2\pm1} &= (\sigma^{\lambda}_{xz} \pm i\ \sigma^{\lambda}_{yz}) = 0 \\
\rho^{\lambda}_{20} &= \sqrt{3}/2\ (\sigma^{\lambda}_{zz}-\sigma^{\lambda}_{0}) = \sqrt{3}/2\ \delta^{\lambda}
\end{aligned} \qquad [24]$$

The anisotropy $\delta=\sigma_{zz}-\sigma_0$, asymmetry $\eta=(\sigma_{yy}-\sigma_{xx})/\sigma_{zz}-\sigma_0$, and isotropic value $\sigma_0=(\sigma_{xx}+\sigma_{yy}+\sigma_{zz})/3$, are obtained from σ_{xx}, σ_{yy}, σ_{zz}; the three principal values of the interaction tensor. Notice that the antisymmetric elements of the interaction tensor are completely neglected. This approximation is not necessarily valid for heavy nuclei.[24,25] Written specifically for the case of m=0, [23] yields

$$R^{2}_{0}(\theta,\phi) = d^{(2)}_{0,0}(0,\theta,\phi)\,\rho^{\lambda}_{20} + \rho^{\lambda}_{22}[e^{2i\phi}d^{(2)}_{20}(\theta) + e^{-2i\phi}d^{(2)}_{-20}(\theta)] \qquad [25]$$

Finally, the spatially dependent eigen-energies and the transition frequencies according to [18] are determined for the effective Hamiltonians determined previously.

In the presence of more than one interactions, the procedure described previously is repeated for individual interactions. However, it is necessary to take into account the fixed mutual orientations between these tensors as mentioned in [22]. The most direct method in

correlating the orientations is by performing an interaction frame transformation of the irreducible tensor components R^2_m for each interactions with respect to a reference frame which is conveniently chosen to be the PAS of one of the interaction tensors and is characterized by Euler angles $(\alpha, \beta, \gamma)^{\lambda}$. The relation of the Euler angle $(0, \Theta, \phi)$ and the orientations are depicted in Fig. 1.

The spatial components are now generated by using:

$$R^2_m(\Theta,\phi) = \sum_{m'} D^{(2)}_{m',m}(0,\Theta,\phi) \sum_{m''} D^{(2)}_{m'',m'}(\alpha,\beta,\gamma)\, \rho^{\lambda}_{2m''} \qquad [26]$$

which is written particularly for the case m=0 ;

$$R^2_0 = \sum_m e^{im\phi} d^{(2)}_{m0}(\Theta) \sum_{m'} e^{im'\gamma} d^{(2)}_{m'm}(\beta)\, e^{im\alpha}\, \rho^{\lambda}_{2m'} \qquad [27]$$

In the cases studied, λ=C, Q or D.

This double frame transformation performed for an electric field gradient (e.f.g) tensor, i.e., λ=Q, gives a complicated spatial dependence of the second order quadrupolar interaction (involving evaluation of R^2_1 and R^2_2) and makes it difficult when one proceeds to evaluate the critical frequencies (vide infra). To simplify the derivation and the calculation we express the transition frequencies of the shift interaction in the principal axes frame of the e.f.g. or the dipolar PAS frame, knowing that the mutual orientations, (α, β, γ) between these two tensors are characteristic of the nuclear electronic environment and are independent of crystal orientation.

The spatially dependent relations of the shift, dipole, and quadrupole interactions governed by first order perturbation theory will

now be derived. For a first order perturbation, it is found that

$$V_\lambda^{(0)} = C^\lambda R_0^2 T_0^2 + C^c R_0^0 T_0^0 \qquad [28]$$

The second term is the isotropic shift term, only appearing in the shift interaction since other interaction tensors have zero trace. The first order Hamiltonians after a single frame transformation become:

$$H_\lambda(\theta,\phi) = C^\lambda \delta^\lambda [P_2(\cos\theta) + \frac{1}{2}\eta^\lambda \sin\theta\cdot\cos 2\phi] T_0^2 \qquad [29]$$

The single quantum spatially dependent transition frequency for the individual interaction is then

$$\omega_\lambda(\theta,\phi) = \frac{2\pi}{h}\{\langle k|H_e^\lambda|k\rangle - \langle k-1|H_e^\lambda|k-1\rangle\} \qquad [30]$$

For the shift interaction, the single quantum transition frequencies are equal for all all $|k\rangle \rightarrow |k-1\rangle$ transitions.

$$\omega_c(\theta,\phi) = \omega_0\sigma_0 - \omega_0\delta[P_2(\cos\theta) + \frac{\eta}{2}\sin^2\theta\cdot\cos 2\phi] \qquad [31]$$

For the first order quadrupolar interaction, the spatial dependence of the transition frequencies is identical to that of the shift interaction.

$$\omega_{qd}^{(1)} = \delta_q[P_2(\cos\theta) + \frac{\eta_q}{2}\sin^2\theta\cos 2\phi] \qquad [32]$$

where $\delta_q = \omega_q(2k-1)$

The constant ω_q is defined individually for interactions due to

e.f.g. and two body dipolar coupling.

$$\omega_q = \frac{3e^2qQ}{4\cdot I(2I-1)h} \qquad \omega_d = \frac{3}{2}\frac{\gamma_i\,\gamma_s}{r^3}\bar{n}^{\,2} \qquad [33]$$

The factor 2k-1 originates from the fundamental quadrature on the second rank zero order tensor, $3I_z^2-I^2$ of the spin part, with k being the final state quantum number of the single quantum transitions. Equation [32] implies: (a) the central transition (k=1/2) is not influenced by the first order perturbation; and (b) for each of the 2I transitions of spin I nuclei, there corresponds another transition that gives the same resonance frequency but with inverse sign. This predicts that under the first order perturbation, the quadrupolar or dipolar spectrum should be symmetric about the center of mass for either powder or single crystal.

For the first order dipolar (homonuclear or heteronuclear) interaction, the effective Hamiltonians differ only in the interaction constants. The spatial dependence of the transition frequency is identical to [32]. However due to the axial symmetry of the dipole interaction, only the $P_2(\cos\Theta)$ term remains.

In the above equations, the sign of the term $\cos 2\phi$ can be inverted depending upon the definition of the Euler angles without affecting the results. The positive sign which corresponds to the right hand convention in the Wigner rotation will be used.

Second order corrections are only necessary for the (1/2→ -1/2) central transition of half integer quadrupolar nuclei since the averaged Hamiltonian, $V^{(0)}$ is zero for the quadrupole interaction. The second

Magnus term, $V^{(1)}$ must be evaluated. The effective Hamiltonian for the quadrupolar interaction when neglecting the nonsecular term in [12] can be written as:

$$V_{qd}^{(1)} = \frac{(\omega_q)^2}{2\omega} \cdot \{|R_2^2|^2(2I^2-2I_0^2-1)I_0 + |R_1^2|^2(4I^2-8I_0^2-1)I_0\}$$

We need to calculate both R_2^2 and R_1^2 after a single transformation according to [23]. After inserting these expressions with final state k=1/2 for the central transition, the spatial dependence of the second order quadrupole interaction, $\omega_{qd}^{(2)}$ are evaluated as follows:

$$\omega_{qd}^{(2)} = \frac{-R}{6\cdot\omega_0}\{ A(\phi)\cos^4\Theta + B(\phi)\cos^2\Theta + C(\phi)] \qquad [34]$$

where

$$R = \omega_q^2[4\cdot I(I+1)-3]$$

$$A(\phi)= -\frac{27}{8} - \frac{9}{4}\eta\cos2\phi - \frac{3}{8}\eta^2\cos^2 2\phi$$

$$B(\phi)= \frac{30}{8} - \frac{\eta^2}{2} + 2\eta\cos2\phi + \frac{3}{4}\eta^2\cos^2 2\phi$$

$$C(\phi)= -\frac{3}{8} + \frac{\eta^2}{3} + \frac{\eta}{4}\cos2\phi - \frac{3}{8}\eta^2\cos^2 2\phi \qquad [35]$$

This result is consistent with that given by Bauger et al.[18] and with those proposed previously.[26,27]

As mentioned previously, the constant spatial relation correlation between shielding and e.f.g. or dipole tensors is described by a double frame transformation of the shift tensor into the e.f.g. principal axis frame. Since only the first order effect is considered, the spatial dependence is conveniently obtained by evaluating only the $R_0^2(\Theta,\phi)$ term.

According to [27] we obtain:

$$R_0^2 = \rho_{20}^c \{P_2(\cos\theta)\cdot P_2(\cos\beta) + \frac{3}{4}[\sin^2\theta\cdot\sin^2\beta\cdot\cos 2\chi - \sin 2\theta\cdot\sin 2\beta\cdot\cos\chi]\} + \rho_{22}^c\sqrt{\frac{3}{2}}\{\sin^2\theta\cdot[\frac{1+\cos^2\beta}{2}\cos 2\alpha\cdot\cos 2\chi - \cos\beta\cdot\sin 2\alpha\cdot\sin 2\chi] - 2\cos\theta\cdot\sin\theta\cdot\sin\beta\cdot[\cos\beta\cdot\cos 2\alpha\cdot\cos\chi - \sin 2\alpha\cdot\sin\chi] + p_2(\cos\theta)\cdot\sin^2\beta\cdot\cos 2\alpha\} \quad [36]$$

where $\chi=\gamma+\phi$. The single quantum transition frequency is evaluated from [28] and [30] for the shift interaction. This gives,

$$\omega_{cs}(\theta,\phi) = \frac{2\pi}{h}\{\langle m|V_C^{(0)}(\theta,\phi)|m\rangle - \langle m-1|V_C^{(0)}(\theta,\phi)|m-1\rangle\}$$
$$= Cs_0 + Cs_1\cos\chi + Ss_1\sin\chi + Cs_2\cos 2\chi + Ss_2\sin 2\chi \quad [37]$$

with

$$Cs_0 = \delta\cdot P_2(\cos\theta)[P_2(\cos\beta) + \frac{\eta}{2}\sin^2\beta\cos 2\alpha]$$

$$Cs_1 = \delta\cdot\sin 2\theta[\frac{-3}{4}\sin 2\beta + \frac{\eta}{2}\sin\beta\cdot\cos\beta\cdot\cos 2\alpha]$$

$$Ss_1 = \delta\cdot\sin 2\theta[-\frac{\eta}{2}\sin\beta\cdot\sin 2\alpha]$$

$$Cs_2 = \delta\cdot\sin^2\theta[\frac{3}{4}\sin^2\beta - \frac{\eta}{2}(\frac{1+\cos^2\beta}{2}\cos 2\alpha)]$$

$$Ss_2 = \delta\cdot\sin^2\theta[-\frac{\eta}{2}\cos\beta\sin 2\alpha]$$

This expression resembles to the spatial dependent transition frequencies of a shift interaction under variable-angle sample spinning,[9,19,28] except that the definition of the Euler angles are

different. This expression can be written in more concise form when combining the cosine and the sine terms of the same χ angle;

$$\omega_{cs} = C_0 P_2(\cos\Theta) + C_1 \sin 2\Theta \cos(\chi+\Psi_1) + C_2 \sin\Theta \cos 2(2\chi+\Psi_2) \qquad [38]$$

The new coefficients are

$$\begin{aligned} C_0 &= \delta[P_2(\cos\beta) + \frac{\eta}{2}\sin^2\beta\cos 2\alpha] \\ C_1 &= \frac{\delta}{2}\sin\beta\{[(\eta\cos 2\alpha - 3)\cos\beta]^2 + (\eta\sin 2\alpha)^2\}^{1/2} \\ C_2 &= \frac{\delta}{2}\{[\frac{3}{2}\sin^2\beta + \frac{\eta}{2}\cos 2\alpha(1+\cos^2\beta)]^2 + (\eta\cos\beta\sin 2\alpha)^2\}^{1/2} \end{aligned} \qquad [39]$$

The effective angles Ψ_1 and Ψ_2 are defined as:

$$\begin{aligned} \mathrm{Tan}\Psi_1 &= \frac{\eta\sin 2\alpha}{(\eta\cos 2\alpha - 3)\cos\beta} \\ \mathrm{Tan}\Psi_2 &= \frac{2\eta\sin 2\alpha\cos\beta}{3\sin^2\beta + \eta\cos 2\alpha(1+\cos^2\beta)} \end{aligned} \qquad [40]$$

Combining Ψ_1, Ψ_2 with χ and 2χ and denoting these two angles by Ω_1 and Ω_2, expression [38] is further simplified;

$$\omega_{cs} = C_0 P_2(\cos\Theta) + C_1 \sin 2\Theta \cos(\Omega_1) + C_2 \sin^2\Theta \cos(\Omega_2) \qquad [41]$$

with

$$\Omega_1 = \Psi_1 + \chi = \Psi_1 + \gamma + \phi \qquad \Omega_2 = \Psi_2 + 2\chi = \Psi_2 + 2(\gamma+\phi)$$

Expression [41] has been checked in three ways: (a) when inserting zero for the value of Euler angles α, β, γ in the spatial orientation expression, [41] automatically reduces to [31]; (b) This expression

yields the same static powder spectrum after averaging over Θ , ϕ; as that calculated from [31] for arbitrary α, β, γ values; and (c) the center of mass obtained from [41] equals that obtained from [31], which is σ_0. These results are physically meaningful since when the system is composed of only the shift interaction, the powder average over the random distribution of the sample should be independent of any principal axis frame transformation.

The separation of the Θ, ϕ term from the constant angle α, β, and γ facilitates the calculation of the critical frequencies and the evaluation of the analytical expression of the singularities and shoulders. One should also be careful in assigning the angles Ψ_1 and Ψ_2 during the calculation. These angles depend on the sign of the tangent values in [40]. In the case when the denominator of [40] equals zero the angle will not necessarily be $\pi/2$. When the shift term is axially symmetric, i.e., $\eta=0$, both angles Ψ_1 and Ψ_2 must be zero. Finally Ψ_1 equals to zero implies that Ψ_2 must be zero.

FIELD DEPENDENT CRITICAL FREQUENCIES

The transition frequency governed by the shift interaction plus either the first order or the second order quadrupolar interaction is a simple sum of the spatially dependent transition frequencies of the two individual interactions. We write:

$$\omega^{(1)} = \omega_{cs} + \omega_{qd}^{(1)} \qquad \text{for satellite transitions} \qquad [42a]$$

$$\omega^{(2)} = \omega_{cs} + \omega_{qd}^{(2)} \qquad \text{for central transitions} \qquad [42b]$$

The shift anisotropy δ_c in frequency units is linearly dependent upon the magnetic field according to first order, and therefore so is ω_{cs}. The second order quadrupole transition frequency $\omega_{qd}^{(2)}$, on the other hand is inversely proportional to the static magnetic field while the first order perturbation for quadrupolar or dipolar interactions are independent of the magnetic field. Due to the different field dependence of the interactions, the spectrum as well as the critical frequencies governed by either $\omega^{(1)}$ or $\omega^{(2)}$ will show systematic changes with varying magnetic fields. The critical frequencies corresponding to critical points in the $\omega(\theta, \phi)$ surfaces, and the characters of these critical frequencies (shoulder, step, or singularity), locate the prominent features of the powder spectrum. It is the purpose of the current studies to utilize the field dependent critical frequencies to infer the relative tensorial orientations and the individual interaction parameters. This approach in obtaining the parameters is shown to be more efficient than a complete powder NMR line shape simulation of the variable field spectra.

The equation applied to evaluate the critical frequencies is derived in a manner similar to the algorithm provided by Jellison et al.[29] as shown in [A-9], or [A-10] in Appendix A. Equations [A-9] instead of [A-10] is used in the following. Although $\sin\theta = 0$ is a natural singularity when using [A-9], the boundary condition that $\cos\theta = \pm 1$ will be required to account for the step of the spectrum if [A-10] is employed. [A-9] written in its discrete (θ, ϕ) analogue as

$$I(\omega) = N' \int d\theta \sin\theta \int d\phi \left|\text{grad}\{\omega_k(\theta,\phi)\}\right|^{-1}_{\omega=\omega_k}$$
$$= N \sum_i \left|\text{grad}\{\omega(\theta_i, \phi_i)\}\right|^{-1} \qquad [43]$$

Where N is the normalization constants which is a function of the transition probability and the density of the nucleus present. The index i represents the individual crystalline orientations. Subscript k, denoting the k-th transition is dropped from [43]. This equation states that the contribution to the intensity of the spectrum at $\omega=\omega(\theta_i, \phi_i)$ is the inverse of the amplitude of the gradient at that frequencies. Hence the locations of the critical points in the $\omega=\omega(\theta,\phi)$ surface can be determined by evaluating the zeros of the gradient where the contribution of intensity to the spectrum from this orientation (θ_0, ϕ_0) is infinity at the frequency $\omega=\omega(\theta_0, \phi_0)$. The corresponding critical frequencies in the spectrum are determined by inserting the solution (θ_0, ϕ_0) to the spatially dependent resonance frequency [42a], [42b].

The character of these critical points are determined by the sign of the Wronskian determinant D, where

$$D= [(\partial^2\omega/\partial\theta\partial\phi)^2 - (\partial^2\omega/\partial\phi^2)(\partial^2\omega/\partial\theta^2)] \qquad [44]$$

If D>0 then solution (θ_0, ϕ_0) will be a saddle point. If D>0 then (θ_0, ϕ_0) will be a local extremum in the $\omega(\theta, \phi)$ surfaces.

In order to calculate the critical frequencies it is necessary to solve the two nonlinearly coupled equations corresponding to the two components of the gradient of [43]. The solution is obtained by applying Brown's method where an iterative algorithm starting from a randomly grided (θ, ϕ) pair is used. Numerical techniques are employed to avoid missing or overlapping the critical points. Although an analytical expression of these critical frequencies facilitates the determination of the parameters from the experimental data, this expression can only be found for several limited orientations. In the next two sections, these expressions will be evaluated.

FIRST ORDER QUADRUPOLE VS. SHIFT INTERACTION

In this section is derived the expression for the critical frequencies as a function of interaction parameters for the system governed by the first order quadrupole and the shift interactions. The result is also applicable to the dipolar (homonuclear or heteronuclear) vs. the shift interaction due to the identity of the spatial dependence of the dipolar interaction and the first order quadrupolar interaction. Some simple cases have previously been studied.[30] For a general condition, more accurate field dependent relations will be derived in the follows and will later be demonstrated by an example.

The two first order interactions should be of comparable magnitude to exhibit the combined effect of the interactions and the tensorial orientation. Hence the case for first order dipole vs. chemical and the quadrupole satellite transition vs. Knight shift are two frequently encountered cases. We shall consider the general case for the satellite transition governed by the first order quadrupolar and relatively large shift interactions, and simply replace the coupling constant by Δ, and η_q by 0 when the dipole vs shift case is encountered.

The transition frequency for oriented first order quadrupolar and shift interactions associated with the spatial orientations (θ, ϕ) and the mutual orientation (α, β, γ) is found from [32] and [41]

$$\begin{aligned}\omega^{(1)} &= \omega_{cs} + \omega_{qd}^{(1)} \\ &= C_0 P_2(\cos\theta) + C_1 \sin 2\theta \cos(\Omega_1) + C_2 \sin^2\theta \cos(\Omega_2) \\ &\quad + \delta_q \left[P_2(\cos\theta) + \frac{1}{2}\eta_q \sin^2\theta \cos 2\phi\right] \qquad [45]\end{aligned}$$

Note that δ_q contains two frequencies with inverse sign. Evaluating the location of the critical points in the $\omega=\omega(\theta, \phi)$ surfaces as described above, and determining the critical frequencies is achieved by finding the zeros of the component of the gradient. The two gradient components of [45] are:

$$\frac{d\omega^{(1)}}{d\theta} = \frac{-1}{2}\sin 2\theta[\delta_q(3-\eta_q\cos 2\phi)+(3C_0-2C_2\cos(\Omega_2)]+2C_1\cos 2\theta\cos(\Omega_1) \quad [46a]$$

$$\frac{d\omega^{(1)}}{d\phi} = \sin^2\theta[\delta_q\eta_q\sin 2\phi+ 2C_2\sin(\Omega_2)] +C_1\sin 2\theta\sin(\Omega_1) \quad [46b]$$

(1). Obvious solutions for [46b] are $\cos\theta=\pm 1$ ($\theta = 0, \pi$). Because of the C_1 term, this condition may not give zero for [46a] if $C_1 \neq 0$; however by choosing ϕ appropriately, the solution $\cos\theta=\pm 1$ may still exist. Hence two conditions that give simultaneous zeros for both equations are:

1a: $\cos\theta=\pm 1$, $C_1=0$, in this case, ϕ is not determined, and is immaterial.

1b: $\cos\theta=\pm 1$, $C_1\neq 0$, in this case, ϕ is determined by $\cos(\phi+\Psi_1)=0$, e.g., $\phi=\Psi_1\pm\pi/2$.

It can be readily seen that for both cases the critical frequencies will be independent of the angle ϕ since only the $P_2(\cos\theta)$ term in the first order quadrupole part and the C_0 term in the shift part will remain after inserting $\cos\theta=\pm 1$ into [45]. This is the fundamental critical frequency that will appear as a step in all the spectra. For ω_{1a}, and ω_{1b} the fundamental frequencies are identical and are

independent of angle ϕ as well as C_1. The critical frequency is :

$$\omega^{(1)}_{1a,1b} = \delta_q - \omega_0 \delta[P_2(\cos\beta) + \frac{\eta}{2} \sin^2\beta\cos 2\alpha] \qquad [47]$$

If evaluating the critical points by employing [A-10], [47] is obtained from the boundary on the $\omega(\theta, \phi)$ surfaces where $\mu=\cos\theta=\pm 1$. This frequency is also referred to as the distributing edge since all orientations that are perpendicular to the external magnetic field will resonate at this frequency.

(2). If $C_1=0$, it is observed that $\cos\theta=0$ will be a solution of [46a]. This is then inserted to [46b] to yield the two possible values of $\cos 2\phi$. The corresponding critical frequencies are:

2a: $\cos 2\phi=1$, $\Psi_2=0$, $C_1=0$

$$\omega^{(1)}_{2a} = \frac{1}{2} \delta_q(\eta_q-1) - \frac{1}{2} \delta[\cos^2\beta(1-\eta\cos 2a) - 2\sin^2\beta] \qquad [48]$$

2b: $\cos 2\phi=-1$, $\Psi_2=0$, $C_1=0$

$$\omega^{(1)}_{2b} = \frac{-1}{2} \delta_q(\eta_q+1) - \frac{1}{2} \delta(1+\eta\cos 2a) \qquad [49]$$

Both solutions exist simultaneously under the condition $C_1=0$. When $C_1\neq 0$, one of the above critical frequencies still appears, providing that the solutions of $\cos 2\phi(=\pm 1)$ also satisfies condition $\cos(\phi+\Psi_1)=0$. This implies Ψ_1 should be equal to multiples of $\pi/2$. In this case, the critical frequency will be described by either **2a** or **2b**, but not by both.

There are other solutions to the two coupled equations [46a], [46b] under the condition $C_1=0$. However, they yield identical results to those discussed above, as will now be seen. One solution is $\sin\theta=0$. This is identical to the case in **1b** for varying ϕ. Another possible solution to [46a] is:

$$\cos 2\phi = \pm 3(C_0+\delta_q)/(\delta_q \eta_q + 2C_2) \qquad [50]$$

which after insertion into [46b] yields

$$\sin^2\theta[(\delta_q \eta_q + 2C_2)^2 - 9(C_0+\delta_q)^2]^{1/2} = 0 \qquad [51]$$

The solutions yield either $\sin\theta=0$ or $\sin 2\phi=0$, which are found to be identical to case **1b**, or **2a, 2b** discussed before.

For the functions, $\cos\theta$ and $\sin\theta$ not equal to the special values, 0 or ± 1, the solution is slightly complicated but solvable as shown in the following:

$$\text{Let} \quad K = 4C_1\cos(\Omega_1)/[\delta_q(3-\eta_q\cos 2\phi)+3C_0-2C_2\cos(\Omega_2)] \qquad [52]$$

then [46a] can be written as:

$$\sin 2\theta = K\cos 2\theta \qquad [53]$$

hence $\cos 2\theta$ expressed in terms of K becomes

$$\cos 2\theta = \pm(1+K^2)^{-1/2} \qquad [54]$$

This relation is when substituted into [46b], gives

$$\frac{\partial\omega}{\partial\phi} = 0 = (1-\cos 2\theta)[\delta_q \eta_q \sin 2\phi + C_2\sin(\Omega_2)] + 2C_2 K\cos 2\theta \sin(\Omega_1) \qquad [55]$$

Let $Z = \cos\phi + i\sin\phi$. Multiplying Z^2 on both sides yields:

$$Z^3(pZ+q) + sZ+r = 0 \qquad [56]$$

with coefficients p, q, r, and s equal to

$$\begin{aligned} p &= (1-\cos 2\theta)(\delta_q \eta_q + C_2 e^{i\Psi_2}) & q &= 2C_1 K \cos 2\theta\, e^{i\Psi_1} \\ r &= -(1-\cos 2\theta)(\delta_q \eta_q + C_2 e^{-i\Psi_2}) & s &= -2C_1 K \cos 2\theta\, e^{-i\Psi_1} \end{aligned} \qquad [57]$$

These equations together with [53] form an iterative set. Problems of missing the singularities using Brown's algorithm in solving the two coupled nonlinear equations can thus be avoided by solving the two iterative relations [53] and [56] for general orientation (α, β, γ) where C_1 or Ψ_2 will not necessarily be zero.

Based upon the above derivation, explicit relations can be derived for some special orientations. Similar to the cases discussed previously, the special orientations satisfy $\sin\Psi_2=0$, and(or) Ψ_1 being a multiple of $\pi/2$ (include 0). These conditions are satisfied when the shift principal Z axis lies in the XZ, YZ, or XY plane of the e.f.g. tensor.

Because the constraint, $\sin\Psi_2=0$ is imposed for the special orientations, value p equals -r and are both real. Depending on Ψ_1, two cases may occur.

(a) When p=-r, and q=-s, i.e., $\Psi_1 = 0, \pm\pi$, polynomial [56] becomes:

$$[p(Z^2+1)+q](Z^2-1)=0 \qquad [58]$$

which gives an obvious solution, $\cos\phi=\pm 1$. Consequently $\cos 2\phi=\cos 2\Psi_1=1$.

(b) When P=-r, and q=s, e.g., $\Psi_1=\pm\pi/2$, [56] becomes:

$$[p(Z^2-1)+q](Z^2+1)=0 \qquad [59]$$

where another solution, $\cos\phi=\pm i$ is obtained. This corresponds to $\cos 2\phi=\cos 2\Psi_1=-1$.

For these special angles Ψ_1 and Ψ_2, the critical frequency $\omega^{(1)}$ can be expressed as follows:

$$\omega^{(1)}= \frac{1}{4}\cos 2\theta[3(C_0+\delta_q)+ 4C_1K\cos(\phi+\Psi_1) \qquad [60]$$
$$-\cos 2\phi(2C_2\cos\Psi_2+\delta_q\eta_q)]+ \frac{1}{4}[\delta_q+C_0+\cos 2\phi(2C_2\cos\Psi_2+\delta_q\eta_q)]$$

with $\cos 2\theta$ defined in [54], and

$$K= \frac{4}{Q}C_1\cos(\phi+\Psi_1) \qquad [61]$$

The denominator Q in [61] is given by

$$Q= \delta_q(3-\eta_q\cos 2\phi)+(3C_0-2C_2\cos\Psi_2\cos 2\phi) \qquad [62]$$

Because the solutions of [58], [59] insure that $\cos 2\phi=\cos 2\Psi_1=\pm 1$, the term $\cos(\phi+\Psi_1)^2$, will always be equal to unity. This conclusion implies:

(a) combining [54],[61],[62], $\cos 2\theta$ becomes

$$\cos 2\theta = \pm \frac{Q}{\{Q^2+ (4C_1)^2\}^{1/2}} \qquad [63]$$

(b) the critical frequency will not be dependent upon the sign of

$\cos(\phi+\Psi_1)$, because when [61] is replaced in the second term of [60] it is found that the critical frequencies depend only on $\cos^2(\phi+\Psi_1)$. In other words, the $\sin 2\theta$ dependent term; $C_1 \sin 2\theta \cos(\phi+\Psi_1)$ in [45] is completely independent of the sign of $\cos(\phi+\Psi_1)$. Therefore the sign of K which determines the value of $\cos 2\theta$ and the quadrant of the θ angle, will be immaterial in determining the critical frequencies. This implies that both positive and negative values of $\cos 2\theta$ will be the solution of the critical points that are independent of the quadrant of the θ angles.

The angle Ψ_2 is maintained in the equation because $\cos\Psi_2$ may take two values, ± 1. To simplify the notation, we shall denote $\varepsilon = \cos\Psi_2 = \pm 1$. Hence we have the following (3) and (4) cases.

(3). From [58] we have $\cos 2\phi = \cos 2\Psi_1 = 1$. Inserting the solution for $\cos 2\theta$ and the related conditions into [60], four singularities can be found.

3a: $\cos 2\theta > 0$, $\sin\Psi_2 = 0$

3b: $\cos 2\theta < 0$, $\sin\Psi_2 = 0$

The corresponding critical frequencies from [60] are:

$$\omega^{(1)}_{3a,3b} = \pm\frac{1}{4}\left[Q^2+(4C_1)^2\right]^{1/2} + \frac{1}{4}\left[\delta_q(1+\eta_q)+(C_0+2C_2\varepsilon)\right] \qquad [64]$$

where the positive sign in [64] corresponds to positive values of $\cos 2\theta$ and the constant, Q is given by

$$Q = \delta_q(3-\eta_q)+(3C_0-2C_2\varepsilon) \qquad [65]$$

(4). From [59] we have $\cos 2\phi = \cos 2\Psi_1 = -1$. Inserting the solution for $\cos 2\theta$ we have

4a: $\cos 2\theta > 0$, $\sin\Psi_2 = 0$

4b: $\cos 2\theta < 0$, $\sin\Psi_2 = 0$

The corresponding frequencies are:

$$\omega^{(1)}_{4a,4b} = \pm\frac{1}{4}\left[\, Q^2+(4C_1)^2\right]^{1/2} + \frac{1}{4}\left[\delta_q(1-\eta_q)+(C_0-2C_2\varepsilon)\right] \qquad [66]$$

where the definition of Q is slightly different then [65]:

$$Q = \delta_q(3+\eta_q)+(3C_0+2C_2\varepsilon) \qquad [67]$$

This concludes the evaluation of the critical frequencies for the first order quadrupolar and the shift interactions.

Some features of the solutions are discussed and compared. Cases (3) and (4) are mutually exclusive, again because of the equality, $\cos 2\phi = \cos 2\Psi_1$ cannot take both positive and negative values. Also **3a** and **3b** exist simultaneously as do **4a** and **4b**. Notice that when ε $(=\cos\Psi_2)$ changes sign, which can be a result of rotating γ by π, the result does not equal to interchange of cases (3) and (4). The conclusion that a completely different critical frequency and hence different spectra occur when γ is incremented by π is contradictory to the coincident assumption that spectra are independent of orientation α, β, γ. If $C_1=0$, all cases in (1) and (2) but neither cases of (3) or (4) characterize the critical frequency. However if $C_1 \neq 0$ one need consider only (3) or (4) and the fundamental frequencies (1) and possibly either **2a** or **2b**.

The shift anisotropy δ_c (in frequency units), linearly dependent upon the magnetic field to first order, is the only term that will be affected when the field strength has been changed. The critical frequency can be mapped as a function of the magnetic field. This mapping allows the extraction of the interaction parameters and the mutual orientation of the two interactions.

Calculations have been performed for several special orientations. The calculation uses $|\delta_q| = \Delta$ as the reduced unit for both the x and y axis, the asymmetry parameters are η_q=0., η_c=0.3. The calculated critical frequencies as referenced to σ_0=0 are plotted as a function of the Larmor frequency (magnetic field) as shown in Fig. 1. One interesting feature of these plot is that the mapping is not all linear, as might be expected, since the shift is linearly dependent upon the field and the quadrupolar interaction is completely independent of the field according to first order. The nonlinear behavior as a combined effect of shift and the first order quadrupolar interaction, found in the curves represented by case (3) and (4) is due to the coefficient C_1, and C_2 appearing quadratically in [64] and [66]. Also notice that the intercepts at zero field, which determine the critical frequencies of the first order quadrupolar interaction are dependent upon the asymmetry parameter η_q, while the patterns are totally dependent upon the choice of both η_c and η_q and the orientation.

As a comparison to the calculated critical frequency curves, the complete powder line shape at three fields corresponding to δ/Δ = 0.2, 0.5 and 1.8 are also shown for each orientation in Fig. 2. Notice the two calculations are consistent.

SECOND ORDER QUADRUPOLE VS. SHIFT INTERACTION

In this section are derived expressions for the critical points as a function of the field for spectra that are inhomogeneously broadened by shift and second order quadrupole interactions. The central transitions of half-integer quadrupolar nuclei in the presence of nonnegligible shift anisotropy are thus described. The resonance energy as a function of the spatial orientation is found from [34] and [41]:

$$\omega^{(2)} = \omega_{cs} + \omega_{qd}^{(2)}$$

$$= C_0 P_2(\cos\theta) + C_1 \sin 2\theta \cos(\Omega_1) + C_2 \sin^2\theta \cos(\Omega_2)$$

$$\frac{-R}{6\omega_0}\left[A(\phi)\cos^4\theta + B(\phi)\cos^2\theta + C(\phi)\right] \qquad [68]$$

The location of the critical points in the $\omega=\omega(\theta, \phi)$ surfaces as described above are obtained by the zeros of the components of the gradient. From [68] the two components of the gradient are:

$$\frac{d\omega^{(2)}}{d\theta} = \frac{-R\sin 2\theta}{4\omega_0}\{(3+\eta_q\cos 2\phi)^2\cos^2\theta - (5-\frac{2}{3}\eta^2 + \frac{8}{3}\cos 2\phi + \eta^2\cos^2 2\phi)$$

$$+ \frac{4\omega_0}{R}[3C_0 - 2C_2\cos(\Omega_2)]\} + 2C_1\cos 2\theta\cos(\Omega_1) \qquad [69a]$$

$$\frac{d\omega^{(2)}}{d\phi} = \frac{-R}{12\omega_0}\sin 2\phi \sin^2\theta\,[\eta_q(9\cos^2\theta + 1) - 3\eta_q^2\cos 2\phi\sin^2\theta]$$

$$- 2C_2\sin^2\theta\sin(\Omega_2) - C_1\sin 2\theta\sin(\Omega_1) \qquad [69b]$$

(1). One obvious solution for [69b]=0 is $\cos\theta=\pm 1$ ($\theta = 0, \pi$). If $C_1 \neq 0$, [69a] may not be zero unless ϕ has been chosen such that $\cos\Omega_1=0$.

Hence the following two conditions yield simultaneous zeros for [69a] and [69b]:

1a: $\cos\theta=\pm1$, $C_1=0$, in this case, ϕ is undetermined.

1b: $\cos\theta=\pm1$, $C_1\neq0$, in this case, ϕ is determined by $\cos(\phi+\Psi_1)=0$, e.g., $\phi=\Psi_1\pm\pi/2$.

For both cases, the critical frequencies are independent of ϕ. Since after inserting the condition $\cos\theta=\pm1$ into [68], only the C_0 term in the shift part remain and the sum, $A(\phi)+B(\phi)+C(\phi)= \eta^2/6$ as evaluated from [35], is independent of angle ϕ. Hence the two fundamental frequencies ω_{1a}, and ω_{1b} are:

$$\omega^{(2)}_{1a,1b} = \frac{R\eta^2}{36\omega_0} - \omega_0\delta[\, P_2(\cos\beta)+ \frac{\eta}{2}\sin^2\beta\cos2\alpha] \qquad [70]$$

These critical frequencies appear as a step in all the spectra. These critical frequencies will not appear when evaluating the critical points using [A-10], but can be retrieved by applying the boundary condition $\cos\theta = \pm1$ to the $\omega(\theta, \phi)$ surfaces. This is referred to as the distribution edge. All orientations parallel to the magnetic field will resonate at this frequency.

(2). If $C_1= 0$, $\cos\theta=0$ is found to yield a solution to [69a]. This is inserted to [69b] to obtain the condition on ϕ, which gives

$$\frac{\partial\omega}{\partial\phi} = \frac{R}{12\omega_0}(\eta-3\eta^2\cos\phi-\frac{1}{R}\,24\omega_0C_2\cos\Psi_2)\sin2\phi +2C_2\sin\Psi_2\cos2\phi \qquad [71]$$

$\cos\phi$ in this equation can be solved as a polynomial of fourth order and hence gives a maximum of four solutions within the range $|\cos\phi|<1$.

These can be obtained numerically using Newton's method. Identical critical frequencies may be obtained for different solution of $\cos\phi$ after insertion into $\omega^{(2)}$.

The critical frequency evaluated at $C_1=0$, $\cos\Theta=0$ and ϕ obtained from the condition [71]=0 will be:

$$\omega_2^{(2)} = \frac{-R}{6\omega_0} C(\phi) - \frac{1}{2} C_0 + C_2 \cos(\Omega_2) \qquad [72]$$

Special cases are discussed when the shift principal Z axis lies in the meridian or the equators of the e.f.g. principal axis, (i.e., either XY, YZ, or XZ plane). Ψ_2 in this condition must equal zero or $\pm\pi$. Hence [72] can be further simplified after inserting $\sin\Psi_2=0$. This gives the following solutions of angles and critical frequencies which are independent of value C_1:

2a: $\cos\Theta=0$, $\cos 2\phi=1$, $\Psi_2 = 0, \pm\pi$

$$\omega_{2a}^{(2)} = \frac{-R}{144\omega_0}(3-\eta_q)^2 - \frac{\delta}{2}[\cos^2\beta(1-\eta\cos 2\alpha) - 2\sin^2\beta] \qquad [73]$$

2b: $\cos\Theta=0$, $\cos 2\phi=-1$, $\Psi_2 = 0, \pm\pi$

$$\omega_{2b}^{(2)} = \frac{-R}{144\omega_0}(3+\eta_q)^2 - \frac{\delta}{2}[1+\eta\cos 2\alpha] \qquad [74]$$

A third solution is obtained where the conditions on ϕ are solved from the zeros of the bracket in [71] instead of from $\sin 2\phi=0$. This frequency is denoted as curve 2c.

2c: $\cos\theta=0$, $\Psi_2=0,\pm\pi$ with

$$\cos 2\phi = (\eta_q - \frac{24}{R}\omega_0 C_2 \cos\Psi_2)/3\eta_q^2 \qquad [75]$$

The corresponding frequency for 2c is:

$$\omega_{2c}^{(2)} = \frac{R}{18}(1-\eta_q^2) - \frac{1}{2}C_0 + \frac{1}{3\eta_q}C_2 - \frac{4}{R\eta_q^2}C_2^2\,\omega_0 \qquad [76]$$

Although the condition $C_1=0$ has been assumed in the above results, which leads to the solution of $\cos\theta=0$ from [69a] and alternatively yields the solution for $\cos 2\phi$, this requirement is not required if the condition on ϕ also satisfies $\cos(\phi+\Psi_1)= 0$. In the case, the above solutions and the corresponding critical frequencies will also appear.

For a general orientation, $\sin\Psi_2$ is not zero. In this case, the solution can be obtained by solving [69] as mentioned previously. We will refer to this solution as frequency **2d**. The expression of the critical frequency is that of [72].

There are other solutions when $\cos\theta$ or $\sin\theta \neq 0$ or ± 1 which are considered below in the case (3), (4), (5) and (6). Again the analytical solutions are available only for the case, $\sin\Psi_2 =0$, i.e., when the principal Z axis of the shift lies in the meridian or the equator of the e.f.g. principal axis.

If $C_1 =0$, and $\sin\Psi_2=0$, [69b] yields a solution for $\sin 2\phi=0$, e.g., $\cos 2\phi=\pm 1$. This leads to the following two cases:

(3). $\cos 2\phi=1$, $C_1=0$, $\sin\Psi_2=0$. Inserting these condition to [69a] $\cos\theta$ can be determined as follows.

$$\cos^2\theta = -4\omega_0(3C_0-2C_2)/R(\eta_q+3)^2 + (\eta_q+5)/3(\eta_q+3) \qquad [77]$$

From [68] the corresponding critical frequency is

$$\omega_3^{(2)} = -R(\eta_q+1)/9\omega_0 - [3C_0+2C_2(\eta_q+2)]/3(\eta_q+3) - \omega_0(2C_0-3C_2)^2/(\eta_q+3)^2R \qquad [78]$$

(4). $\cos 2\phi=-1$, $C_1=0$, $\sin\Psi_2=0$. In this case, $\cos\theta$ is determined from [69a] as follows:

$$\cos^2\theta = -4\omega_0(3C_0+2C_2)/R(\eta_q-3)^2 + (\eta_q-5)/3(\eta_q-3) \qquad [79]$$

The corresponding critical frequency from [68] is

$$\omega_4^{(2)} = R(\eta_q-1)/9\omega_0 - [3C_0+2C_2(\eta_q-2)]/3(\eta_q-3) - \omega_0(3C_0+2C_2)^2/(\eta_q-3)^2R \qquad [80]$$

The signs of $\cos\theta$ in [77] and [79] is immaterial since all remaining terms in [68] depend only on $\cos^2\theta$.

Unlike the cases discussed in 2a, 2b, 2c, or 2d, the requirement that $C_1=0$ is essential for these two singularities since if $C_1 \neq 0$, those solutions that satisfy $\cos(\phi+\Psi_1)= 0$ in [69a] gives nonzero terms such as $C_1\sin 2\theta$ in [69b]. Although $\cos\theta$ or $\sin\theta$ equals 0 or ± 1 yield zero for value $C_1\sin 2\theta$, this case is identical to 2a — 2d and will not be considered.

For the general case, $C_1 \neq 0$ and nonspecial values of θ, the following (5), (6) cases appear. The condition $\sin\Psi_2=0$ is required as in case (3), (4). This orientation corresponds to the principal Z axis of teh shift tensor lies on the XY, YZ, or XZ plane of the e.f.g. tensor. The accompanying condition $\sin(\phi+\Psi_1)=0$ may frequently occur in this orientation. Hence the solution $\sin 2\phi=0$ inferred from [69b] will also exist as cases (3), (4) above. This implies $\phi = \pm\pi, 0$ and consequently Ψ_1 should equal $\pm\pi$ or 0. Furthermore, for arbitrary orientations (α, β, γ), solution $\cos 2\phi = 1$ and $\cos 2\phi = -1$ appear separately. Therefore the following two case (5), (6), are exclusive of each other. To obtain the critical frequencies we insert the above conditions in [69a]:

$$\frac{\partial\omega}{\partial\theta} = 0 = \frac{R\sin 2\theta}{8\omega_0}\left[(3\pm\eta_q)^2\cos^2\theta - \frac{1}{3}(\eta_q\pm 3)(\eta_q\pm 5)\right.$$
$$\left. + \frac{4}{R}\omega_0(3C_0 \mp 2C_2) - 2\cos 2\theta C_1\cos(\phi+\Psi_1)\right] \qquad [81]$$

The $\pm$ sign corresponds to the two solutions when $\cos 2\phi = \pm 1$. This is again a polynomial of fourth order where the solutions of $\cos 2\theta$ can be obtained numerically. The critical frequency can be evaluated after inserting solution $\cos 2\theta = \xi$ obtained from [81] to [68]. This yields the next two critical frequencies,

(5). $\cos 2\phi = 1$, $C_1 \neq 0$, $\sin\Psi_2 = 0$ and $\cos(\phi+\Psi_1) = \pm 1$

$$\omega_5^{(2)} = \frac{R}{144\omega_0}\left[9(\eta_q+3)^2\xi^2 - 6(\eta_q+3)(\eta_q+5)\xi + (\eta_q-3)^2\right]$$
$$+ \frac{1}{2}(3C_0-2C_2)\xi - \frac{1}{2}(C_0-2C_2) + C_1(1-\xi^2)^{1/2} \qquad [82]$$

(6). $\cos 2\phi=-1$, $C_1\neq 0$, $\sin\Psi_2=0$ and $\cos(\phi+\Psi_1)=\pm 1$

$$\omega_6^{(2)} = \frac{R}{144\omega_0}[9(\eta_q-3)^2\xi^2-6(\eta_q-3)(\eta_q-5)\xi+(\eta_q+3)^2] + \frac{1}{2}(3C_0+2C_2)\xi-\frac{1}{2}(C_0+2C_2)+C_1(1-\xi^2)^{1/2} \qquad [83]$$

For each of the cases (5) or (6), there are four independent solutions for ξ and hence the critical frequencies. The notation **5a**, **5b**, **5c**, and **5d** or **6a**, **6b**, **6c**, and **6d** are used to denote these solutions. The sign of C_1 term is always positive because positive $\cos\Omega_1$ gives negative $\sin 2\Theta$ and vise verse.

Calculations have been performed for some orientations. In Fig. 3, the critical frequencies vs. the magnetic field as represented by the Larmor frequency ν_0 have been shown. The parameters used in these calculation are: δ_c = -40 ppm, η_c =1.0, e^2qQ= 2.0 MHz, η_q=1.0. Since the effect of an e.f.g. is inversely proportional to the magnetic field to second order, while the shift interaction is linearly proportional to the magnetic field, the critical frequency curves governed by these two interactions are found to be nonlinear with the magnetic field. At high fields the critical frequencies gradually converge to that observed for a nonaxially symmetric shielding spectrum, while in the low field limit the second order character gradually dominates. In the limit of zero field, the perturbation treatment breaks down. Hence the second order perturbation treatment becomes less accurate and may be invalid at the low field limit.

Similar to the previous case, a complete powder line shape calculation using equation [21], has been performed to compare with the calculations of the critical frequencies as shown on the right of Fig. 3. The ratio used in Fig. 3 are defined as follows:

$$\text{Ratio}= \frac{6\ \delta_c}{R} (\nu_0)^2 \cdot 10^6$$

δ_c is the shift anisotropy in unit of ppm, ν_0 is the larmor frequency of the quadrupolar nuclei in units of Mhz, and R is defined in [33], [34] and [35] in $(MHz)^2$. The values used in the calculation gives R= 3 Mhz^2 for spin I=3/2 and the three ratios shown in Fig. 3 corresponds to the magnetic field of 50 MHz, 79.0 Mhz and 150 MHz respectively. It can be seen from Fig. 3 that the critical frequencies observed in the powder line shape are predicted correctly at these three frequencies.

As a comparison of the effect of mutual orientation upon the powder spectra, the critical frequencies for coincident orientation, (α, β, γ)= (0.0, 0.0, 0.0) and noncoincident orientation (α, β, γ) = (60.0, 90.0, 0.0) are shown together in Fig. 4 for three different e.f.g. and shielding asymmetry.

EXPERIMENTAL

Here the applicability of the above treatment is demonstrated by determining the interaction parameters for a system composed of two major interactions with one being the shift interaction.

The simplest approach in determining the interaction parameters would seem to perform an iterative powder line shape fitting for spectra taken at a single magnetic field. The iterative calculation should include the six interaction parameters and the mutual orientations between the two interactions. As a result of the larger number of unknowns involved, the iteration converges relatively slowly. Although unambiguous results can be attained in principle by iteratively fitting the spectra taken at several different magnetic fields with good signal-to-noise ratios; the calculation involves a large number of iterative calculations is in some case, a formidable task and impossible or impractical to perform.

The current approach reduces the scale from fitting of the powder line shape to fitting of the field dependent critical frequencies in determining the interaction parameters and the mutual orientations. This approach is simpler and more accurate than an iterative fitting at a single field.

The system trichloro-acetic acid (TCAA) has been chosen to illustrate the applicability of the theory since the internal interactions of the protons in this sample are governed by both chemical shift and homonuclear dipolar interactions from an isolated dipolar pair, and neither interaction dominates the spectrum in the magnetic fields measured. Two features of the spectrum are expected: (a) the

spectrum can not be approximated by either the shift powder pattern or the dipolar Pake doublet; and (b) the resulting spectrum will be strongly dependent upon the mutual orientation of the two interactions as previously shown. The field dependent critical frequencies of mutually oriented shift and first order quadruple interaction tensor discussed previously can be readily applied after replacing δ_q with Δ, and a zero asymmetry η_q of the dipolar interactions. The dipolar coupling constant Δ is the peak-to-peak splitting of the Pake doublets.

The sample was dried under He gas and pyrophosphate (P_2O_5) before sealing under vacuum in a Pyrex NMR tube. A simple $\pi/2$ pulse was applied to obtain the transient signal. The spectra were taken at three different fields and are referenced externally to water. These are shown in Fig. 5.

The critical frequencies are located from the derivatives of the absorption spectrum which are listed in the first half of Table I. These critical frequencies correspond to the shoulders of the spectrum and are harder to locate than those corresponding to steps or singularities and therefore are only roughly estimated.

A fitting of these values is performed by matching the frequencies calculated from the zeros of the gradient according to equation [46] for the three different fields while iteratively varying the six parameters σ_0, δ, η, Δ, α, and β until the minimum value of the difference squares is reached. The curves correspond to the shoulder are not incorporated in the fitting due to the larger errors related to these points. The angle γ is undetermined (and not important) since one of the interactions (dipolar) is axially symmetric. This iterative fitting

takes ~30 seconds cpu time in the VAX/VMS system. The results are listed in the first row in Table III.

A even faster and less rigorous approach based upon the above procedure can be found. This approach involves comparing the calculated and experimental patterns of the critical curves. First the critical frequencies are referenced to the isotropic shift, σ_0, before correlating with the magnetic field. Second, the approximate orientation (α, β) is found by comparing the characteristic pattern of the frequency vs. field curves with that calculated for the seven special orientations. Finally, using the analytical expression corresponding to the critical curves for that orientations, the other three interaction parameters δ, η_c, Δ are determined.

For spectrum governed by the first order perturbation, the center of mass of each spectrum corresponds to the isotropic shift value σ_0. This condition is satisfied in the current system. Hence σ_0 is calculated by zeroing the first moment of each spectrum. The critical frequencies are further referenced to the center of mass of the spectrum as listed in the second half of Table I. In Fig. 6 is shown the correlation of the corrected critical frequencies vs. magnetic field. The correlation curves for TCAA resemble most those calculated for the orientation α=0, β=90 in the low field region (Fig. 1). This orientation is a reasonable approximation of the true orientation. The solid and the broken curves drawn through the related points are the linear least square fits of the points of these curves with the series number denoting the analytical critical frequency expression for orientation (α, β)= (0.0, 90.0). The analytical expressions of these curves from [47], [48] and [49] are

rewritten below:

$$\omega_{\pm 1b} : \quad \pm\Delta + \omega_0\delta[P_2(\cos\beta) + \frac{\eta}{2}\sin^2\beta\cos 2\alpha) \qquad [85]$$

$$\omega_{\pm 2a} : \quad \pm\frac{\Delta}{2} - \omega_0\frac{\delta}{2}[1+\eta\cos 2\alpha] \qquad [86]$$

$$\omega_{\pm 2b} : \quad \pm\frac{\Delta}{2} - \omega_0\frac{\delta}{2}[\cos^2\beta(1-\eta\cos 2\alpha) - 2\sin^2\beta] \qquad [87]$$

the parameter Δ can be determined from either the spacing or the intercepts of the parallel pairs, which is Δ for the inner two pairs and 2Δ between 1b and -1b. Therefore, δ and η can also be found after inserting the value α, β and Δ into the analytical expressions [85], [86] or [87] and solving the coupled linear equations. This results are listed in the second column of Table III.

Features of these critical frequencies are noted: (a) although six critical curves appear, only three distinctive slopes exist, i.e., curves 1b, 2a and 2b. The corresponding parallel curves -1b, -2a, -2b yield the intercepts of opposite sign, and (b) the intercept at zero field represents the critical frequencies in the absence of the shift interaction. Therefore, the intercept of 2a, 2b coincide at $\Delta/2$ and -2a, -2b at $-\Delta/2$ while 1b and -1b yield intercept at $\pm\Delta$ respectively, which clearly shows the features of a Pake-doublet. The critical ferquencies shown in Fig. 1, further illustrates these relations.

The above approach limits the mutual orientation to the closest special orientation where the analytical expressions of all critical curves are available. Although this simplification introduces errors in the orientation α, β and the asymmetry parameter η, the dipolar coupling

constant, Δ and the shift anisotropy δ determined are quite accurately determined. The results are to be compared with those obtained from the iterative approach by matching the zeros of the gradient at the three fields as shown in the first row of Table III. Note that the second approach is not intended to replace the iterative fitting of the critical frequencies but simply to serve as a convenient estimation of the interaction parameters. The near orthogonal orientation between shielding tensor and the internuclear vector, and the interaction parameters are consistent with those obtained from a single crystal studies by Dybowski et al.[31]

A static powder line shape calculated is finally performed using the best fitted values from the critical frequencies of mutually oriented dipolar and chemical shift tensors. This calculation is performed according to [21], where the transient decay signal governed by the orientation dependent eigen-energies is first calculated followed by Fourier transform of this averaged decay to yield the spectra. The calculated results are shown in Fig. 7 which is to be compared with Fig. 5; the experimental spectra.

DISCUSSION

The orientation of individual spin interaction tensors in solids is dependent upon the local electronic environment of the nucleus studied. For example, the orientation of the shielding tensor depends upon the local electron density, the quadrupole interaction depends upon the orientation of the electric field gradient tensor and the tensor orientation of dipolar interaction is coaxial with the internuclear vector. These orientations are in general independent of each other. From the analytical expressions given for the special orientations, it can be inferred that imposing the assumption that the two interaction tensors have the same orientation will lead to large errors in determining interaction parameters. The asymmetry, in particular, is sensitive to the choice of the orientation angles. As a result, it will be hard if not impossible to obtain consistent results when the fitting is performed for spectra taken at different magnetic fields. This error becomes more severe when the magnitudes of the two interactions are comparable.

On the other hand the effect of the mutual orientation of the interaction tensors will be less dramatic if one of the interactions is larger compared to the other. Such a situation may occur when experiments are performed at extremes of magnetic fields. This conclusion can be inferred from the calculation shown in Figs. 1 and 3. At low magnetic fields when the magnitude of the shift is much smaller than the dipolar or the quadrupolar interactions, the effects of different orientations upon the spectra and the critical frequency curves are much harder to differentiate.

From the above discussion we concluded that: (a) the method of finding the interaction parameters by monitoring the field dependent critical frequencies is most useful in the regime where the two interactions are of comparable size; and (b) to be able to yield the most accurate results when applying this method, particularly in the mutual orientation and the asymmetry parameters, data should be obtained at a sufficiently large range of magnetic fields.

In the following is discussed the limitations of the method according to the assumptions made in inferring the mutual orientations and the analytical expressions.

(1). The major interactions governing the spectrum are assumed to be inhomogeneous. In other words the broadening of the spectrum originates from a superposition of inherently sharp lines associated with the random distribution of powder sample, or possibly a distribution of the interaction parameters (the electron density, the electric field gradient) throughout the micro-crystallite. Homogeneous effects originating from nonsecular terms in the internal Hamiltonians are assumed to be weak compared to the effects of inhomogeneties causing only a "smoothing" of the inhomogeneous spectra. In calculating the powder spectra as shown in Figs. 2 and 3, the "smoothing" or "broadening" effect has been accounted for by multiplying a decay function to the calculated transient signal before Fourier transformation.

When homogeneous broadening becomes sufficiently large, the spectrum gradually loses its prominent inhomogeneous features and assumes a form approaching that of a Gaussian or a Lorentzian line. This approach

becomes useless in this condition as is also true for other methods of isolating the individual interactions such as multiple pulse techniques or MAS of iterative line shape simulations.

(2). In the presence of sufficiently large shifts, such as Knight shifts in a metal or the shift for heavy nuclei, where the anisotropy and the shifts may be few percent, the calculation must be carried to second or higher order. Therefore care should be taken in applying the current method to systems where higher order perturbations may be necessary to account for the observed spectra.

(3). The antisymmetric component in both the shielding and the e.f.g. principal axes tensors have been completely neglected in the calculations. The presence of these components depend upon the nuclear site symmetry[24] and are found to contribute to the second order. While this may not be important for the shift interaction it may produce extra features for the central transition spectra where the second order perturbation dominates. Quantitative effects of the antisymmetric component of the e.f.g. tensors upon the quadrupolar central transition line shape have not previously been reported.

(4). The calculation is performed in the Zeeman region (as opposed to the quadrupole region) where the effect of the electric field gradient can be treated as a perturbation on the Zeeman interaction. In this limit, it is legitimate to consider only first order perturbations for quadrupole satellite transitions or the dipole interaction and second order perturbation for the half-half central transition of half-integer quadrupolar nuclei. As the quadrupolar coupling increases, the perturbation approach may yield incorrect results even when higher order

contributions are incorporated. A scheme in solving for the eigen-energies and the spatial dependent expressions is required. Studies of this type when the quadrupole interaction is comparable to or much larger than the Zeeman interaction have been discussed by Nicol[32] and Abragam.[23] Unlike the case of the Zeeman limit, the coincident orientation assumed for the e.f.g. and shielding tensor in these studies is a reasonable one,[33] since in the low field limit where the shift is much smaller than the quadrupolar interaction, the mutual orientation is less influential to the spectrum.

(5). There are cases when the three major inhomogeneous interactions, i.e., quadrupole, dipole, and shift interactions are simultaneously present. Analysis of the spectrum may be tedious in some cases, but can be carried out in the same manner as demonstrated in the previous section as long as the spatially dependent transition frequencies are determined. Evaluating the analytical expression for those special orientations is more difficult. Nevertheless the numerical procedure in determining the field dependent critical frequencies according to [46] or [69], and using the spatially dependent transition frequencies and equation [21] to calculate the powder line shape are still the same. The fundamental frequency 1a, 1b still holds in this case. Torgeson at al.[34] have performed this type of analysis involving three interactions. The assumption that all three principal axis tensors are coincident, make the treatment possible. However, this may produce a large error in the derived parameters.

(6). Finally we shall mention that the spatial dependent expression of the transition frequency are only valid for single quantum coherence.

The transition probability P_k for the m-th single quantum transition is assumed to be independent of the orientation and proportional to $|\langle k|I_y|k-1\rangle|^2$ for both the first order and the second order perturbation. During the period of the rf irradiation, the evolution effect of internal Hamiltonians large compared with the rf field may produce higher quantum coherence and an orientational dependent transition probability for the micro-crystallite sample. Although the powder spectra line shape is distorted by the effect, the position of the critical frequencies where an infinity in the intensity occurs is less affected.

CONCLUSION

In a nuclear system governed by two interactions where neither interaction dominates, the combined effects are an inhomogeneously broadened spectrum which depends not only upon the individual interaction parameters but also strongly upon the mutual orientations between these tensors. The studies shows that: (a) the effects of the mutual orientation between interaction tensors are reflected in both the static powder line shape and the distinctive features of the field dependent critical frequencies as shown in Figs. 1 to 4, and (b) the tensorial orientation between interactions and the individual interaction parameters can be determined by analyzing the critical frequencies (singularities, shoulders, and steps) of a powder spectrum vs. the magnetic field strength.

Field dependent critical frequencies and the powder spectra are calculated for oriented e.f.g. tensor and shielding tensor to both the first order and the second order perturbations. Although the method developed is valid for both satellite transitions and the central transition of spectra of quadrupolar nuclei under the influence of a shift interaction, modification can be made easily to incorporate three interactions, e.g., quadrupolar, dipole and shift interactions, or to involve higher order perturbations.

Table I

The critical frequencies of TCAA spectrum at three fields

B_0 (MHz)	56.05	100.09	220.16
C.M.(kHz)[a]	-0.6±0.2	-1.0±0.2	-2.2±0.2
A(kHz)	10.5	10.0	8.0
B	5.4[b]	5.1	4.8
C	4.4	3.7	1.7
D	-5.2	-5.3	-5.4
E	-6.4[b]	-7.0	-8.6
F	-11.9	-12.5	-14.1
Below: corrected frequencies w.r.t to the center of mass			
A(kHz)	11.1	11.0	10.2
B	6.0[b]	6.1	7.0
C	5.0	4.7	3.9
D	-4.6	-4.3	-3.2
E	-5.8[b]	-6.0	-6.4
F	-11.3	-11.5	-11.9

[a] Center of mass is calculated by zeroing the first moment. This value is taken as the isotropic shift.

[b] This critical frequency is only estimated roughly due to the broadness of the peaks and the ambiguity of the position of the shoulders.

Table II

Properties of the six critical frequency curves

	A	B	C	D	E	F
Series[a]	-1b	2a	2b	-2a	-2b	1b
Intcps.(KHz)	11.5	5.6	5.4	-5.3	-5.6	-11.2
Slope(PPm)	-5.2	9.4	-7.7	10.9	-6.6	-4.6
Character[b]	Stp	Sdr	Sng	Sng	Sdr	Stp

[a] The series number of the critical frequencies vs. Field curves for orientation α=0, β=90.0.

[b] The characters of the critical frequencies, where Stp= Step, Sdr= Shoulder, Sng= Singularity.

Table III

Parameters of the two interaction tensors in TCAA

methods	σ_0(ppm)	δ(ppm)	η	Δ(KHz)	α	β
Iterative	-10.5	13.5±1.	0.2±.1	11.1±.2	20.±30	80±10
Linear	-10.0	10.5±1.	0.4±.2	11.3±.4	0.0	90.0
Single X'tal[a]	-10.0	13.7±.5	0.15±.1	11.25	0.	80.

[a] From Dybowski et al.[31]

REFERENCES

1. M. Mehring, Principles of High Resolution NMR in Solids, second Ed. (Springer-Verlag, Berlin, 1983).

2. U. Haeberlen, and J. S. Waugh, Phys. Rev. 175, 453 (1968).

3. U. Haeberlen, Chapter 2 in High Resolution NMR in Solids, Selective Averaging, J. S. Waugh eds. (Academic Press, New York, 1976).

4. E. R. Andrew, M. Firth, A. Janinski, and P. J. Randall, Phys. Lett. A, 31, 446 (1970); M. G. Munowitz, and R. G. Griffin, J. Chem. Phys. 76, 2848 (1982).

5. E. Kundla, A. Samoson, and E. Lippmaa, Chem. Phys. Lett. 15, 229 (1981).

6. S. Ganapathy, S. Schramm, and E. Oldfield, J. Chem. Phys. 77, 4360 (1982).

7. B. C. Gerstein, and C. R. Dybowski, Chapter 4 in Transient Techniques in NMR of Solids; an Introduction to the Theory and Practice (Academic Press, New York, 1985).

8. B. C. Gerstein, Phil. Trans. Roy. Soc. London, A299, 521 (1981)

9. J. Hertzfield, and A. E. Berger, J. Chem. Phys. 73, 6021 (1980).

10. A. Samoson, E. Kundla, and E. Lippmaa, J. Magn. Reson. 49, 350 (1982).

11. R. G. Griffin, J. D. Ellett, Jr., M. Mehring, J. G. Bullitt, and J. S. Waugh, J. Chem. Phys. 57, 2147 (1972).

12. P. C. Taylor, and P. J. Bray, J. Magn. Reson. 2, 305 (1970).

13. P. C. Taylor, J. F. Bauger, and H. M. Kriz, Chem. Reviews, 75, 238 (1975) and the references therein.

14. M. Linder, A. Hohener, and R. R. Eenst, J. Chem. Phys. 73, 4959 (1980).

15. D. R. Torgeson, and R. G. Barnes, J. Chem. Phys. 62, 3968 (1975).

16. W. H. Jones, T. P. Graham, and R. G. Barnes, J. Chem. Phys. 132, 1898 (1963).

17. R. B. Creel, S. L. Segel, R. J. Schoenberger, R. G. Barnes, and D. R. Torgeson, J. Chem. Phys. 60, 2310 (1974).

18. J. F. Bauger, P. C. Taylor, T. Oja, and P. J. Bray, J. Chem. Phys. 10, 4914 (1969).

19. M. M. Maricq, and J. S. Waugh, J. Chem. Phys. 70, 3300 (1978).

20. G. M. Volkof, Can. J. Phys. 31, 820 (1953).

21. M. H. Cohen, and F. Reif, in Solid State Physics, Vol. 5, F. Seitz and D. Turnbull eds. (Academic Press, New York, 1957).

22. A. R. Edmonds, Angular Momentum in Quantum Mechanics (Princeton University Press, Princeton, 1974).

23. A. Abragam, Chapter 4 in The Principles of Nuclear Magnetism (Oxford University Press, London, 1961).

24. A. D. Buckingham, and S. Malm, Mol. Phys. 22, 1127 (1971).

25. R. F. Schneider, J. Chem. Phys. 48, 4905 (1968).

26. F. Wolf, D. Kline, and H. S. Story, J. Chem. Phys. 53, 3538 (1970).

27. K. Narita, J. Umeda, and H. Kusumoto, J. Chem. Phys. 44, 2719 (1965).

28. M. G. Munowitz, and R. G. Griffin, J. Chem. Phys. 76, 2848 (1982).

29. G. E. Jellison, Jr., S. A. Feller, and P. J. Bray, J. Magn. Reson. 27, 121 (1977).

30. D. L. VanderHart, H. S. Gutowsky, and T. C. Farrar, J. Chem. Phys. 50, 1058 (1969).

31. C. R. Dybowski, B. C. Gerstein, and R. W. Vaughn, J. Chem. Phys. 67, 3412, (1977).

32. A. T. Nicol, Ph.D. thesis, California Institute of Technology, Pasadina, CA (1977).

33. S. L. Segel, and R. G. Barnes, Phys. Rev. Lett. 15, 886 (1965); E. D. von Meerall, R. B. Creel, C. F. Griffin, and S. L. Segel, J. Chem. Phys. 59, 5350 (1973).

34. D. R. Torgeson, R. G. Barnes, and R. B. Creel, J. Chem. Phys. 56, 4178 (1972).

Figure 1. Field dependent critical frequencies of the dipolar vs the shift interaction are calculated from [45] and the zeros of the gradient from [46] for eight selected orientations. The shift anisotropy is expressed in the reduced units of the dipolar coupling constant. The asymmetry value of the shift interaction is chosen to be η=0.3. If the first order quadrupolar instead of dipolar interactions presents, $\eta_q \neq 0$, the calculated pattern will be different.

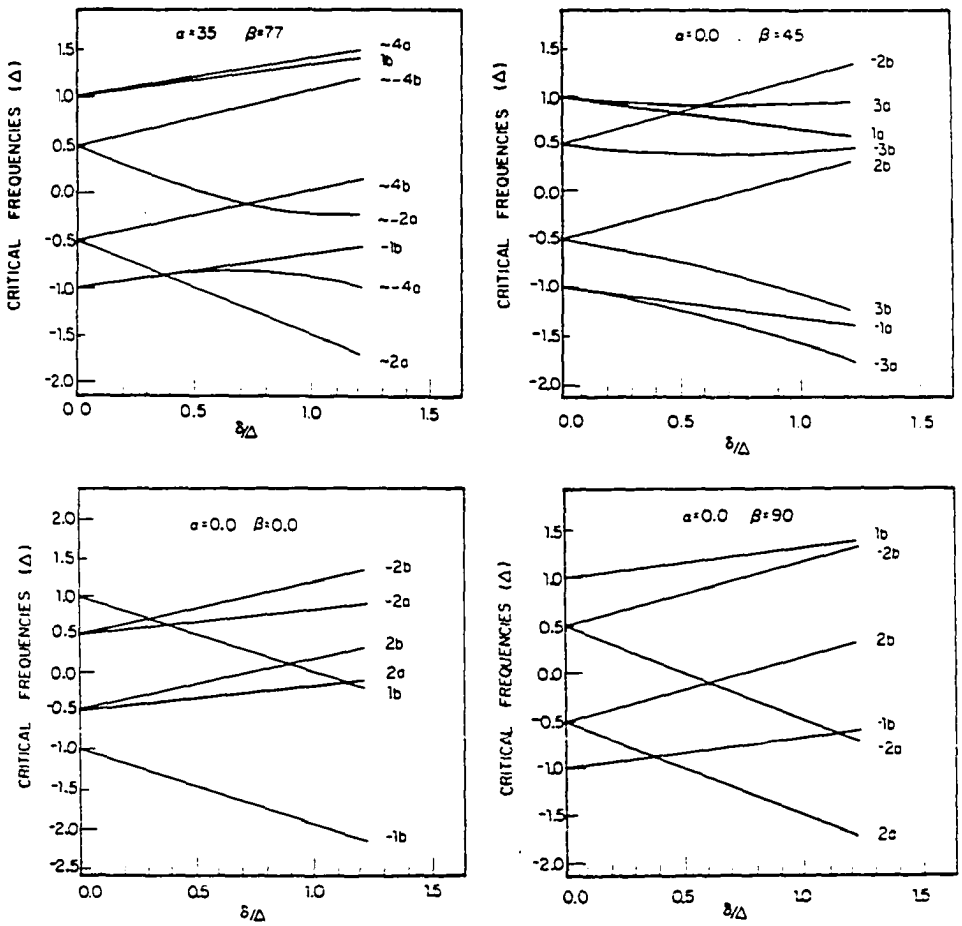
α=35 β=77
-4a
b
-4b
-4b
-2a
-1b
-4a
-2a
α=0.0 β=45
-2b
3a
1a
-3a
2a
3b
-1a
-3a
α=0.0 β=0.0
-2b
-2a
2b
2a
1b
-1b
α=0.0 β=90
1b
-2b
2b
-1b
-2a
2a
CRITICAL FREQUENCIES (Δ)
δ/Δ
0.0
0.5
1.0
1.5

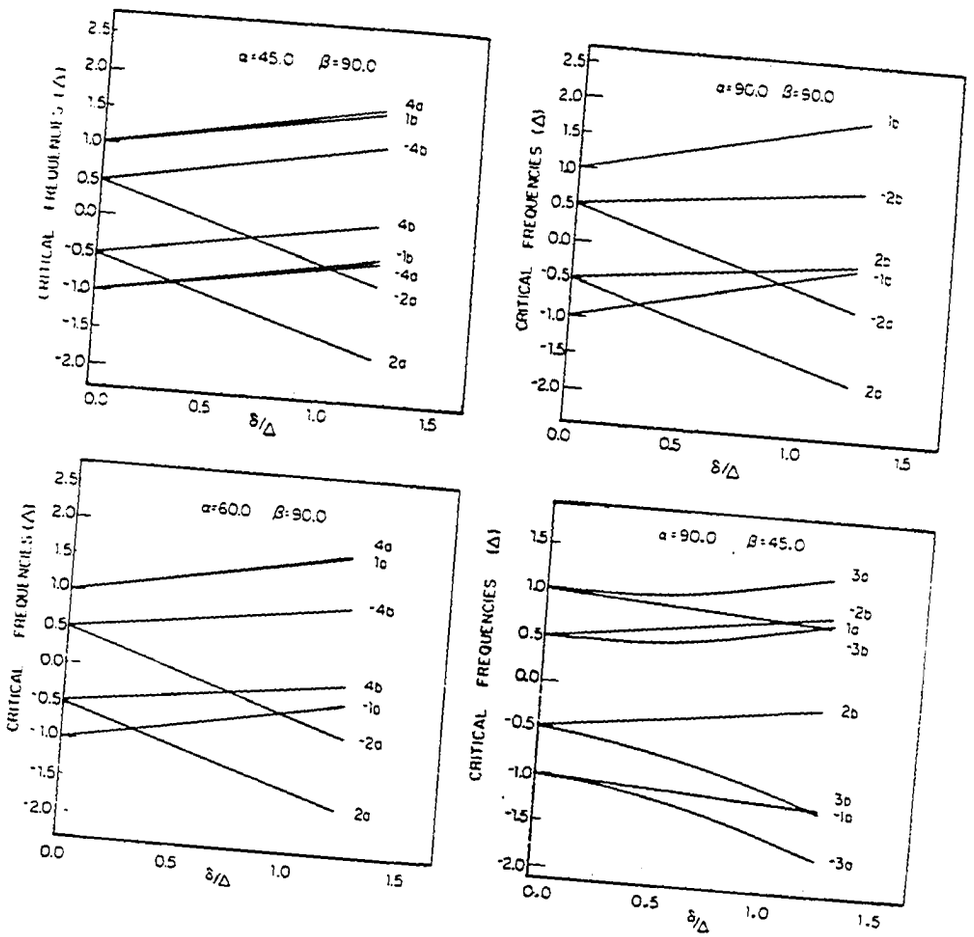

Figure 1 (continued)

Figure 2. The complete powder line shape at two field strengths for the eight orientations calculated in Fig. 1. (a) α=35.0, β=77.0 (b) α=0.0, β=0.0 (c) α=0.0, β=45.0 (d) α=0.0, β=90.0 (e) α=45.0 , β=90.0 (f) α=60.0 , β=90.0 (g) α=90.0 , β=90.0 (h) α=90.0 , β=45.0.

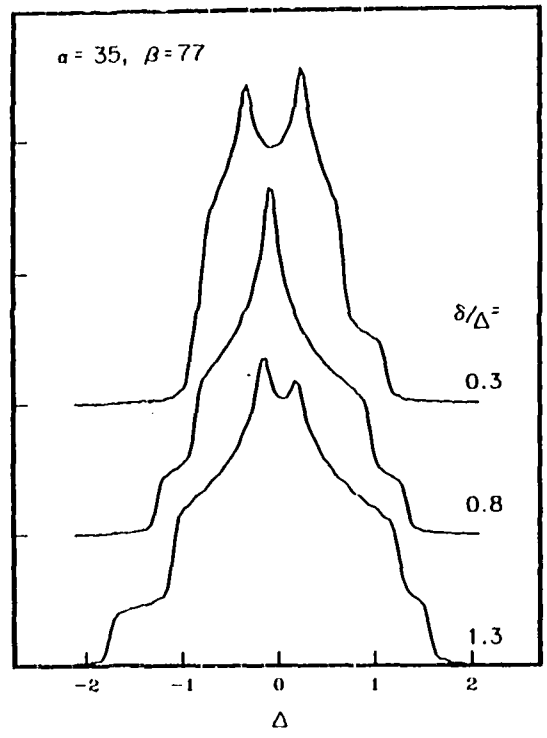
α = 35, β = 77
δ/Δ =
0.3
0.8
1.3
−2
−1
0
1
2
Δ

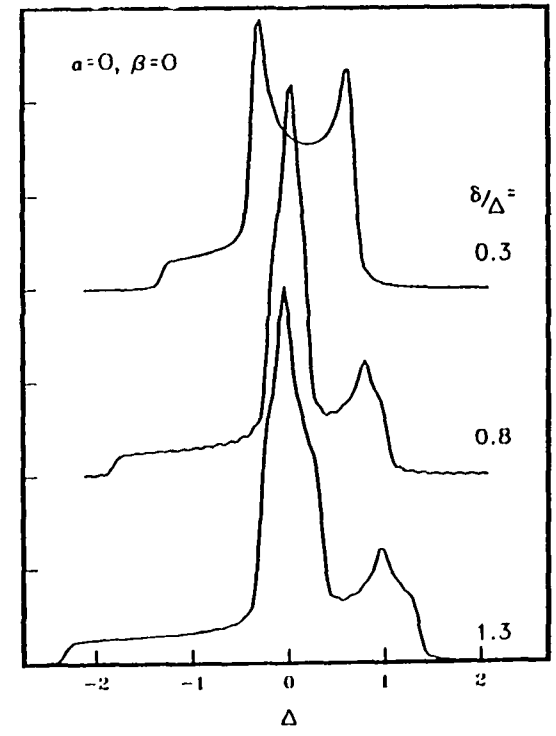
α = 0, β = 0
δ/Δ =
0.3
0.8
1.3
−2
−1
0
1
2
Δ

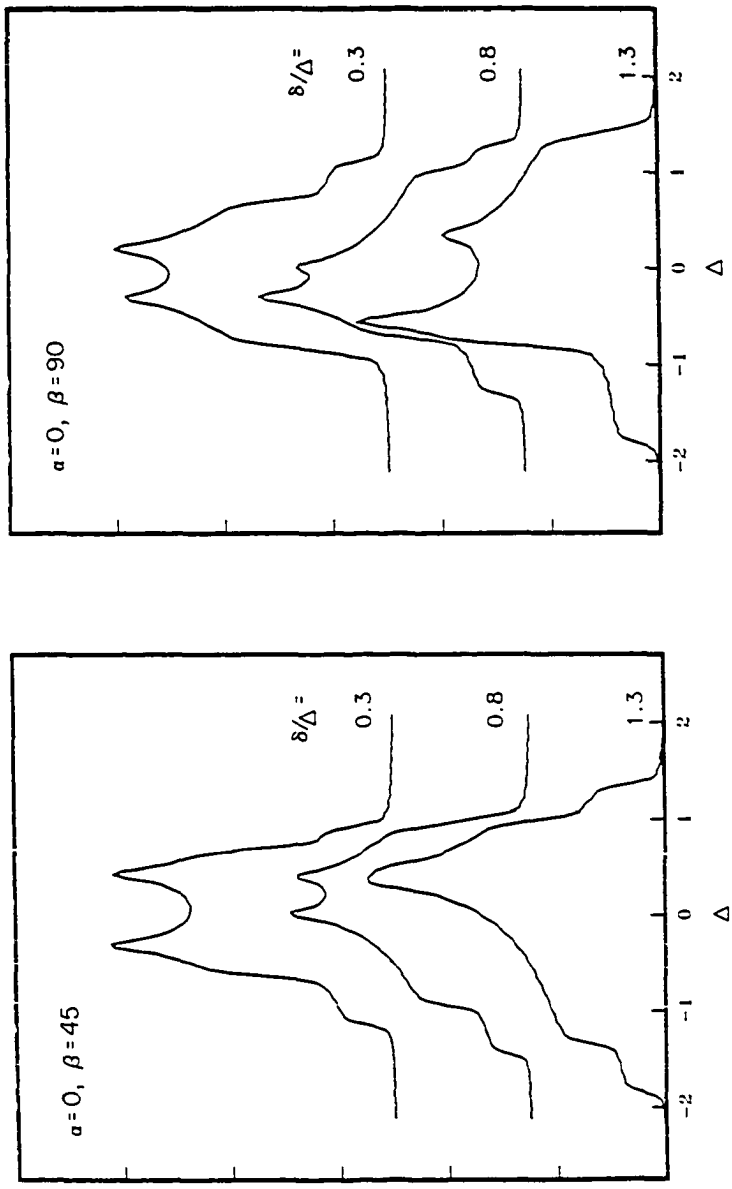

Figure 2 (continued)

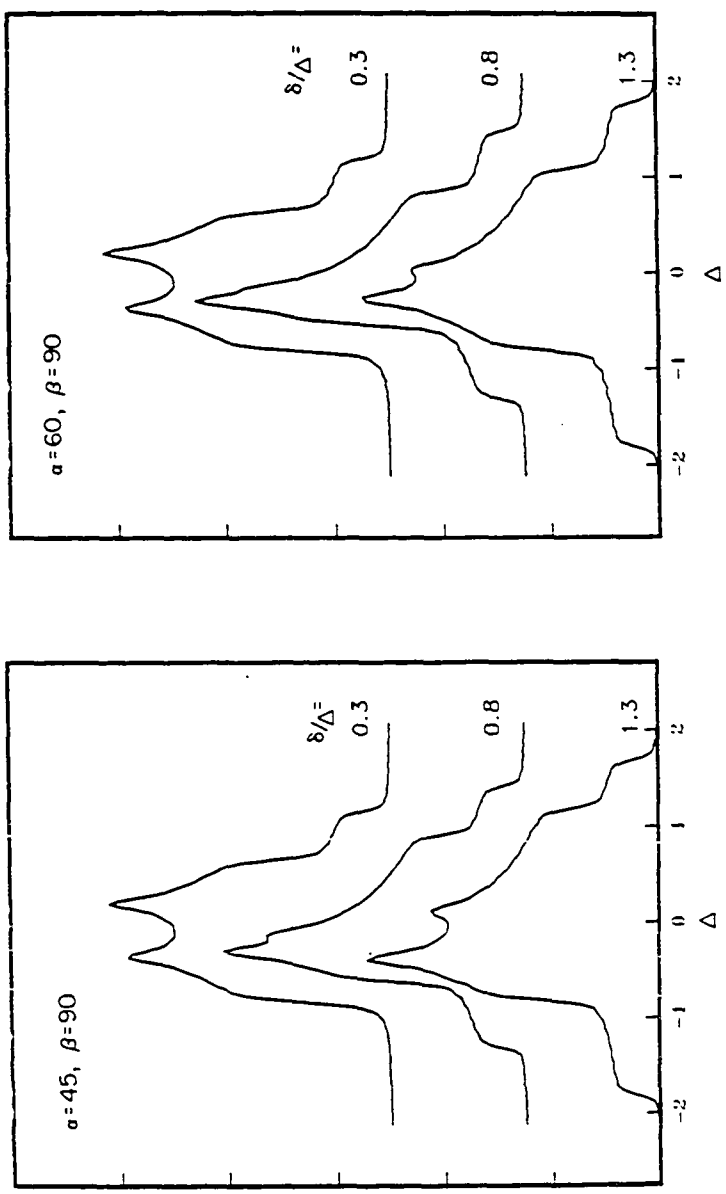

Figure 2 (continued)

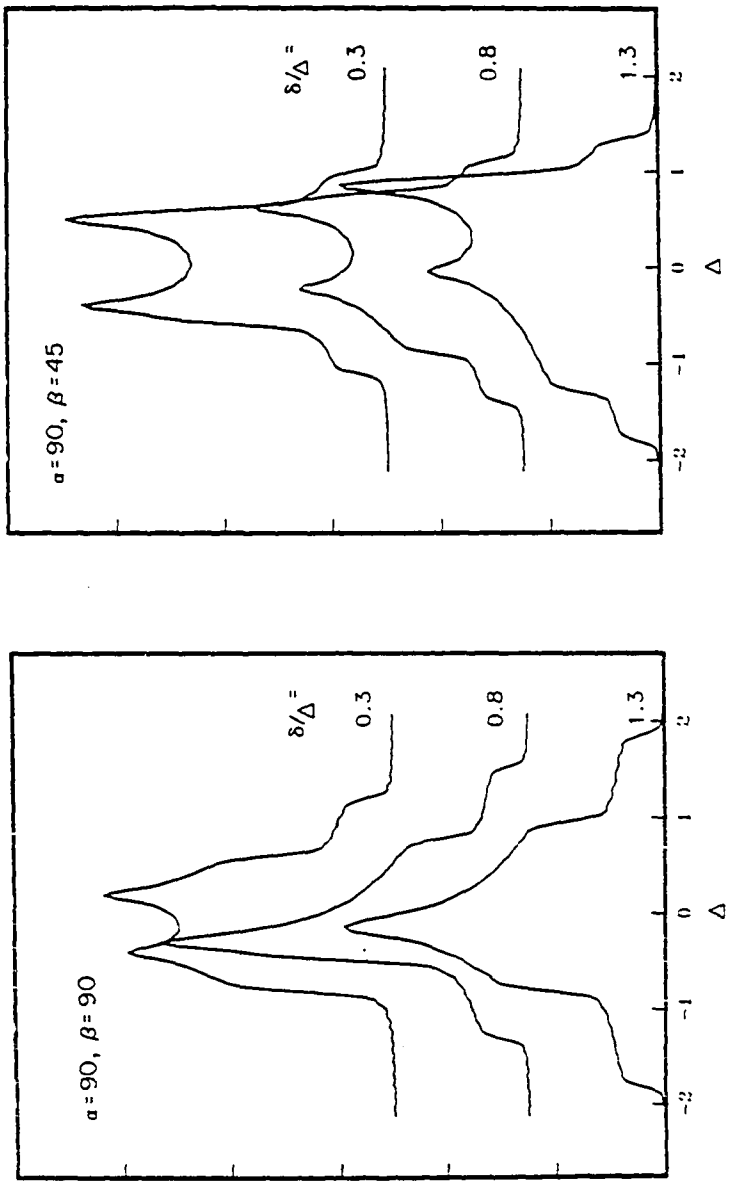

Figure 2 (continued)

Figure 3. Field dependent critical frequencies for the second order quadrupolar vs the shift interaction are calculated from [68] and the zeros of the gradient from [69]. This case is only applicable to the central transition of half integer quadrupolar nuclei. The shift anisotropy and the quadrupole constant ν_q are expressed in units of KHz. The complete powder line shape calculation using [21] at three field strengths are shown at the left side of each critical frequencies curve as a comparison (see text for detail). The seven orientations calculated are: (a) α=0.0 ,β=0.0 (b) α=0.0 ,β=45.0 (c) α=0.0 ,β=90.0 (d) α=45.0 ,β=90.0 (e) α=60.0 ,β=90.0 (f) α=90.0 ,β=90.0 (g) α=90.0 ,β=45.0.

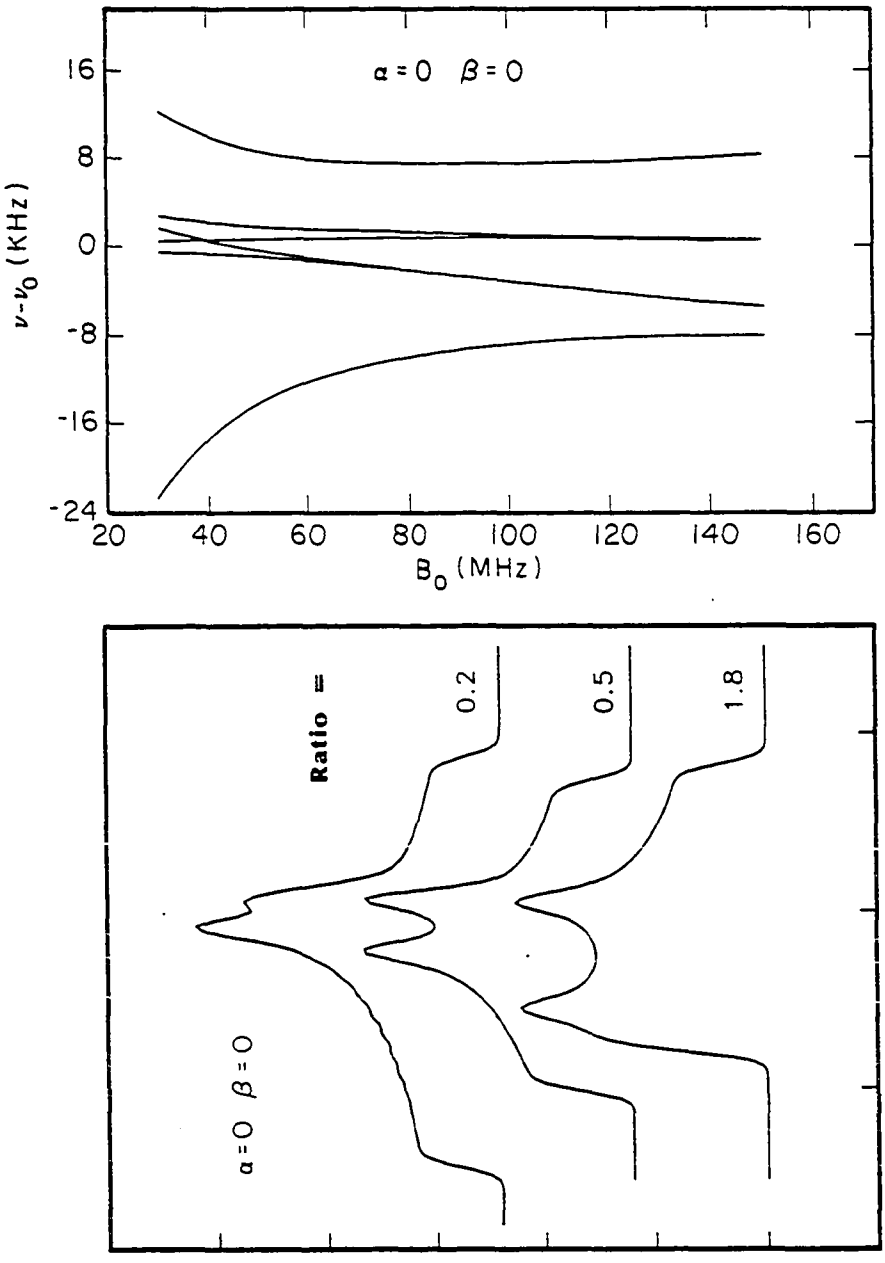
α = 0 β = 0
16
8
0
-8
-16
-24
ν-ν0 (KHz)
20
40
60
80
100
120
140
160
B0 (MHz)
α = 0 β = 0
Ratio =
0.2
0.5
1.8
10
0
−10
Frequency (KHz)

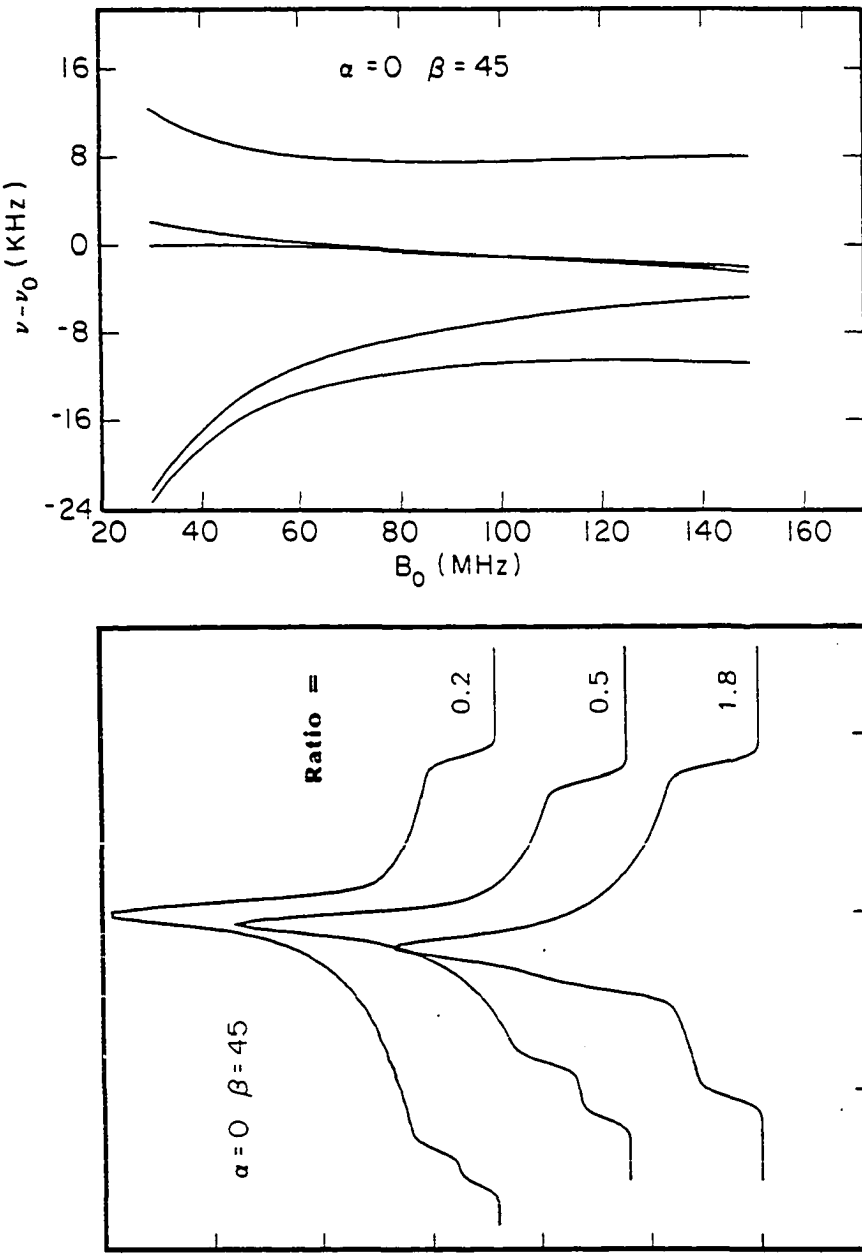

Figure 3 (continued)

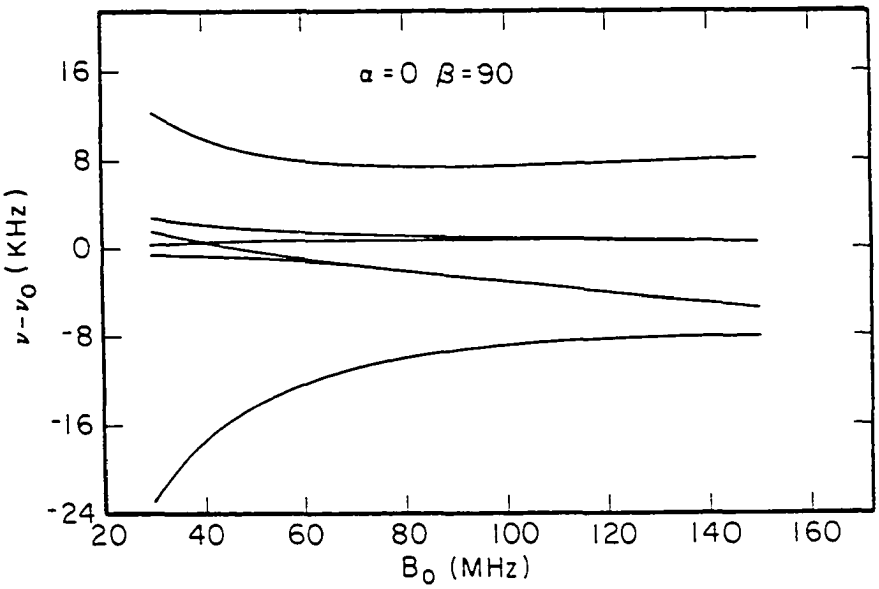

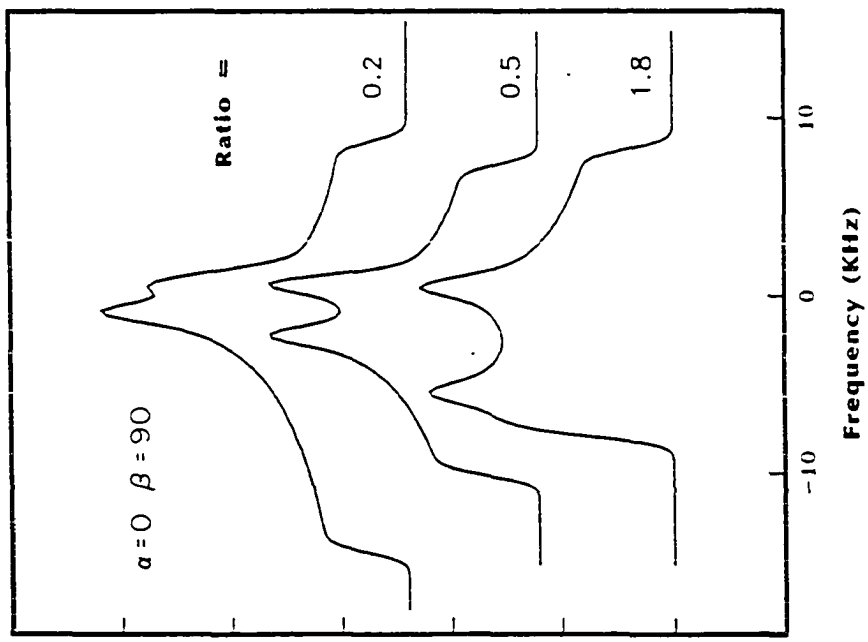

Figure 3 (continued)

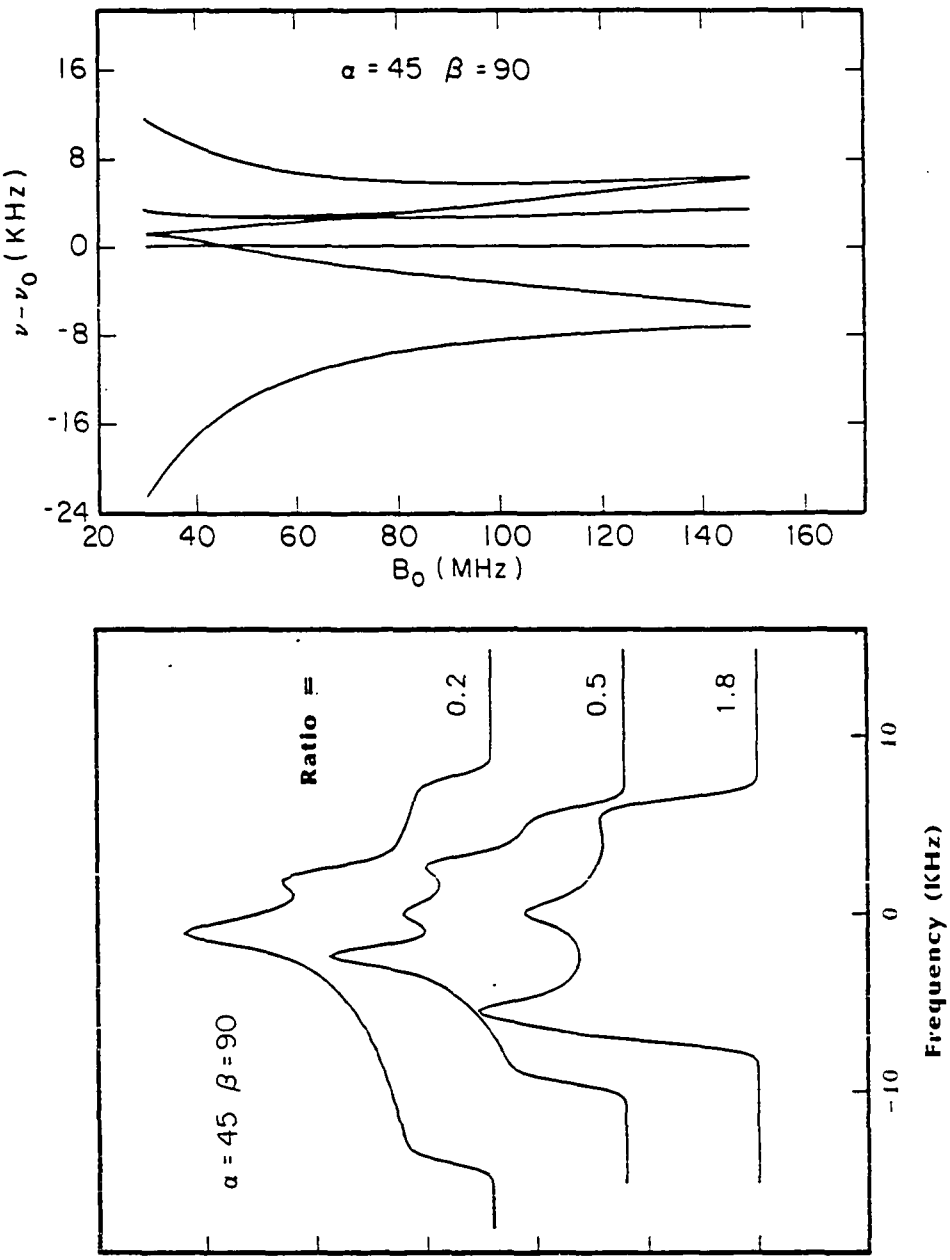

Figure 3 (continued)

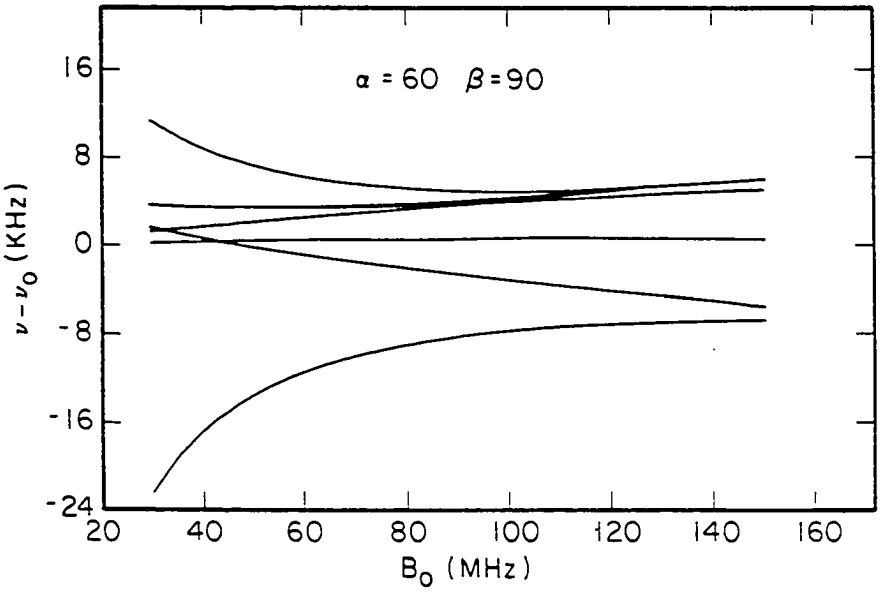

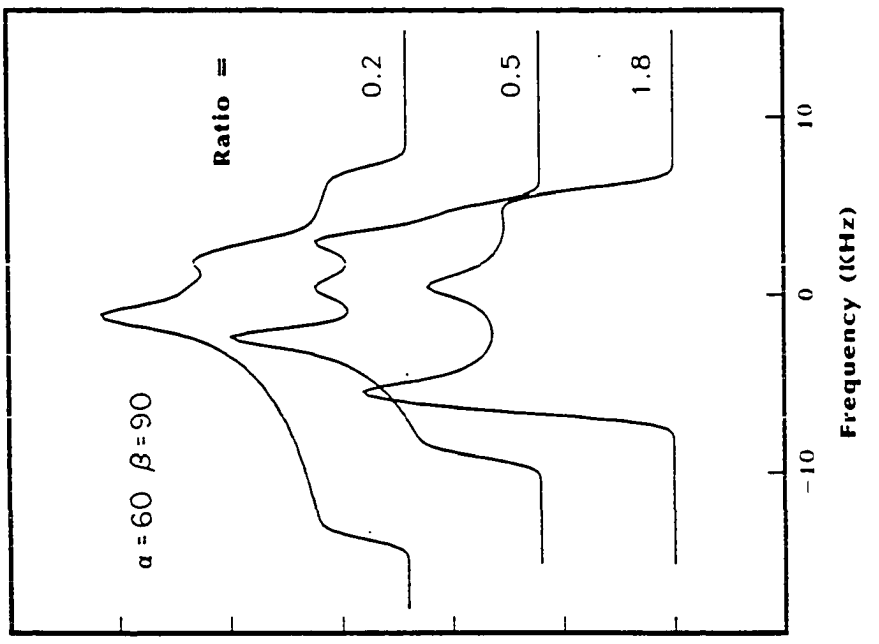

Figure 3 (continued)

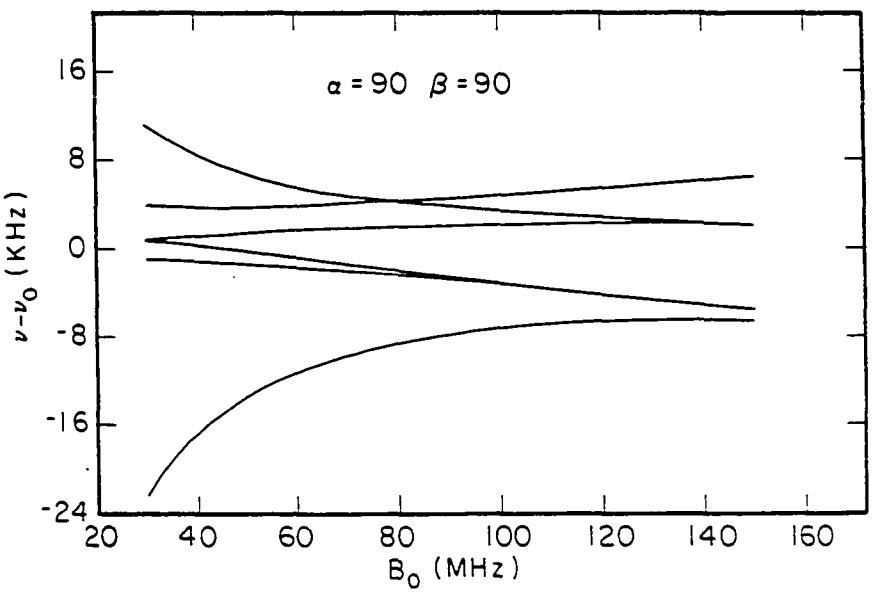

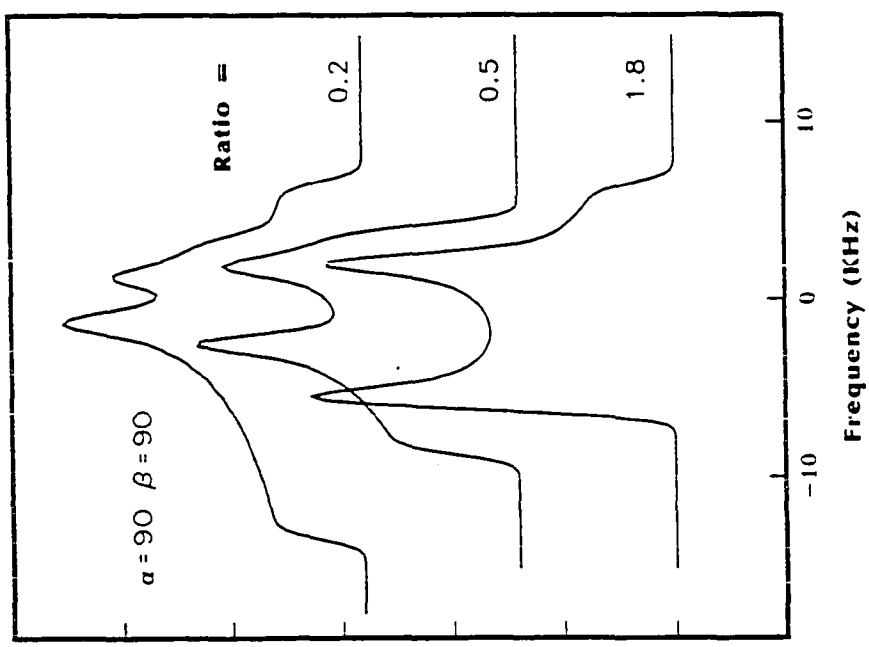

Figure 3 (continued)

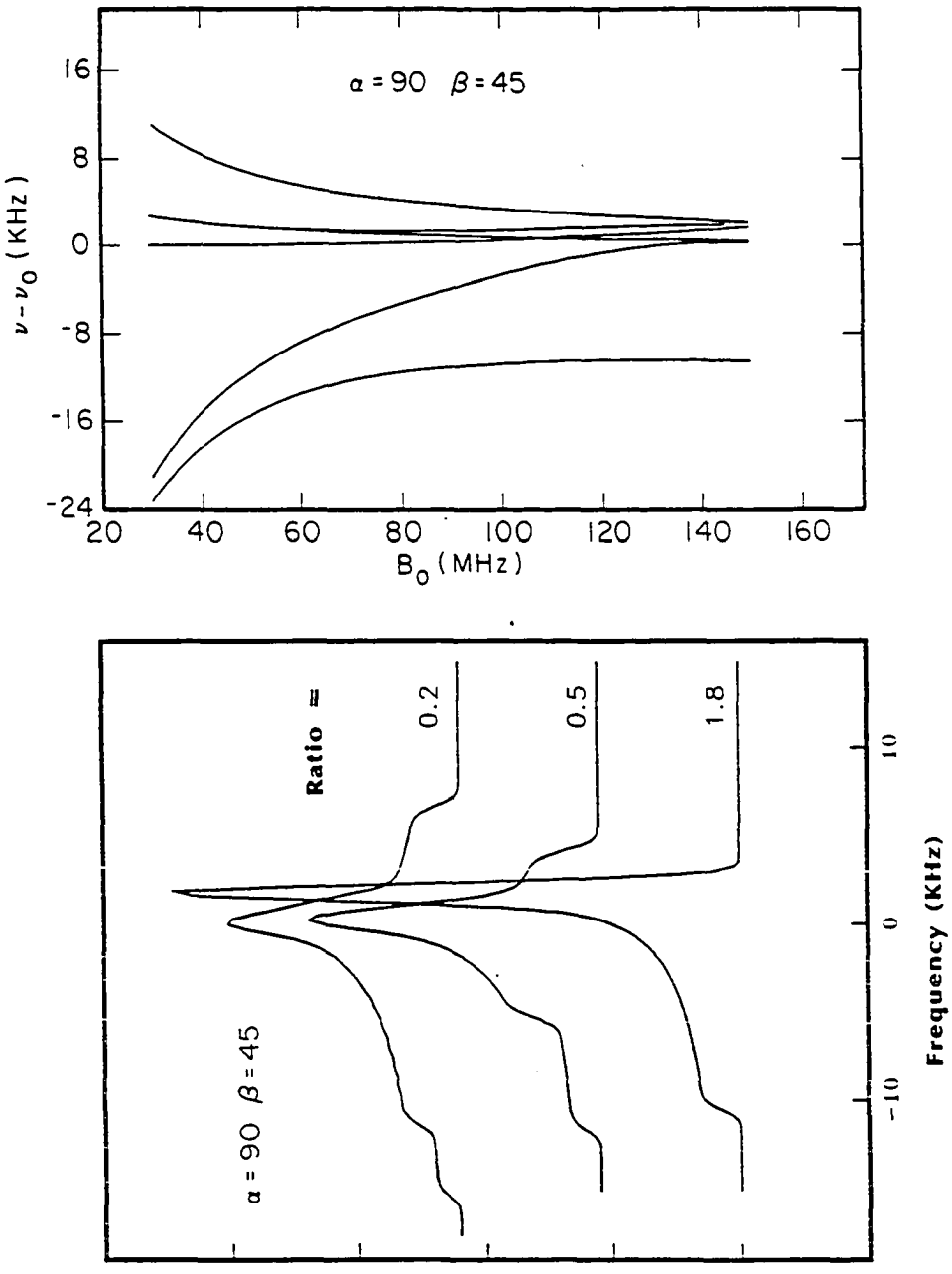

Figure 3 (continued)

Figure 4. Comparison of the critical frequencies for (α, β)=(0.0, 0.0), and (α, β)=(60.0, 90.0) case for various asymmetry parameters. (a) η=0.5, η_q=0.0, (b) η=1.0, η_q=0.0, (c) η=0.0, η_q=1.0. The rest of interaction parameters are the same as used in the previous calculation.

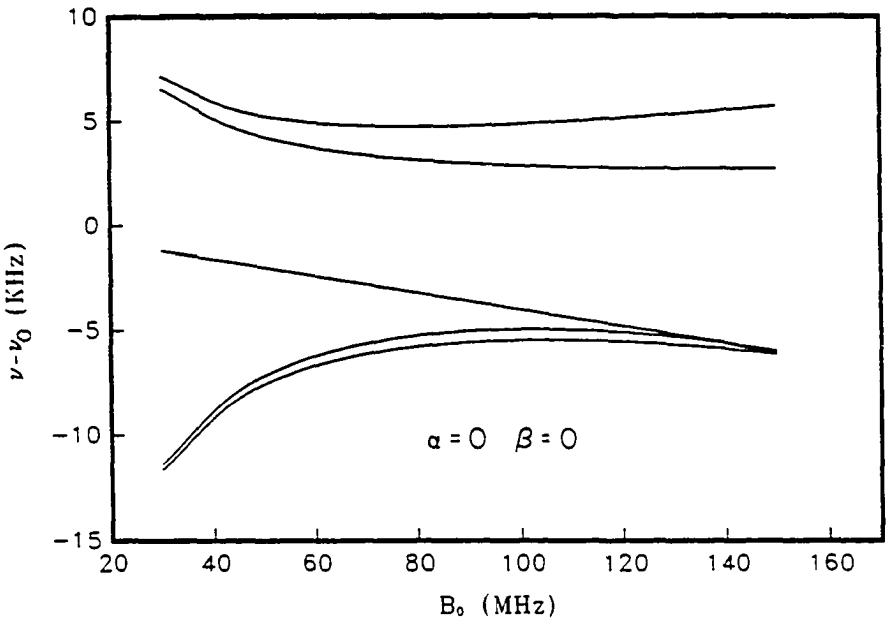
10
5
0
-5
-10
-15
20
40
60
80
100
120
140
160
ν-ν0 (KHz)
B0 (MHz)
α = 0 β = 0

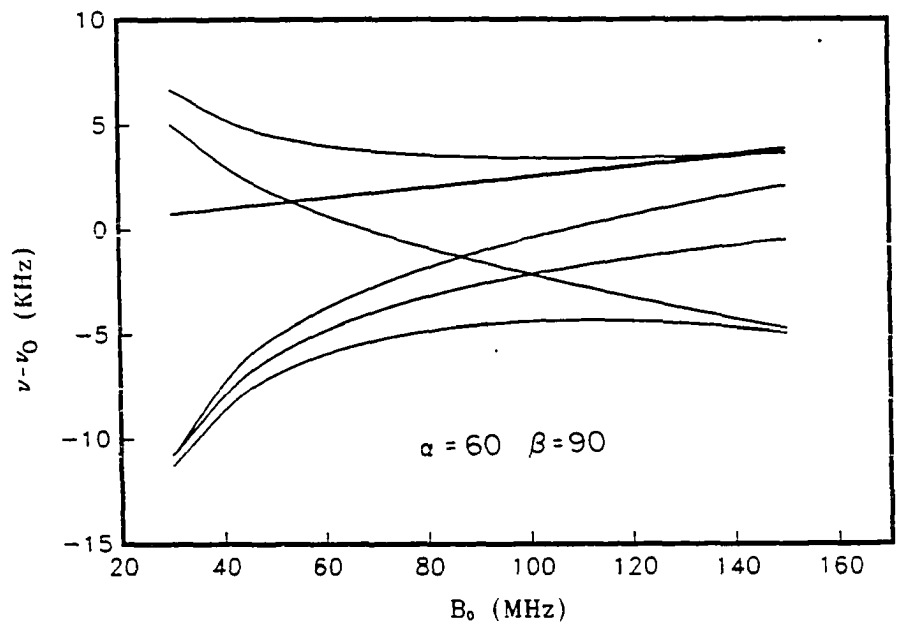
10
5
0
-5
-10
-15
20
40
60
80
100
120
140
160
ν-ν0 (KHz)
B0 (MHz)
α = 60 β = 90

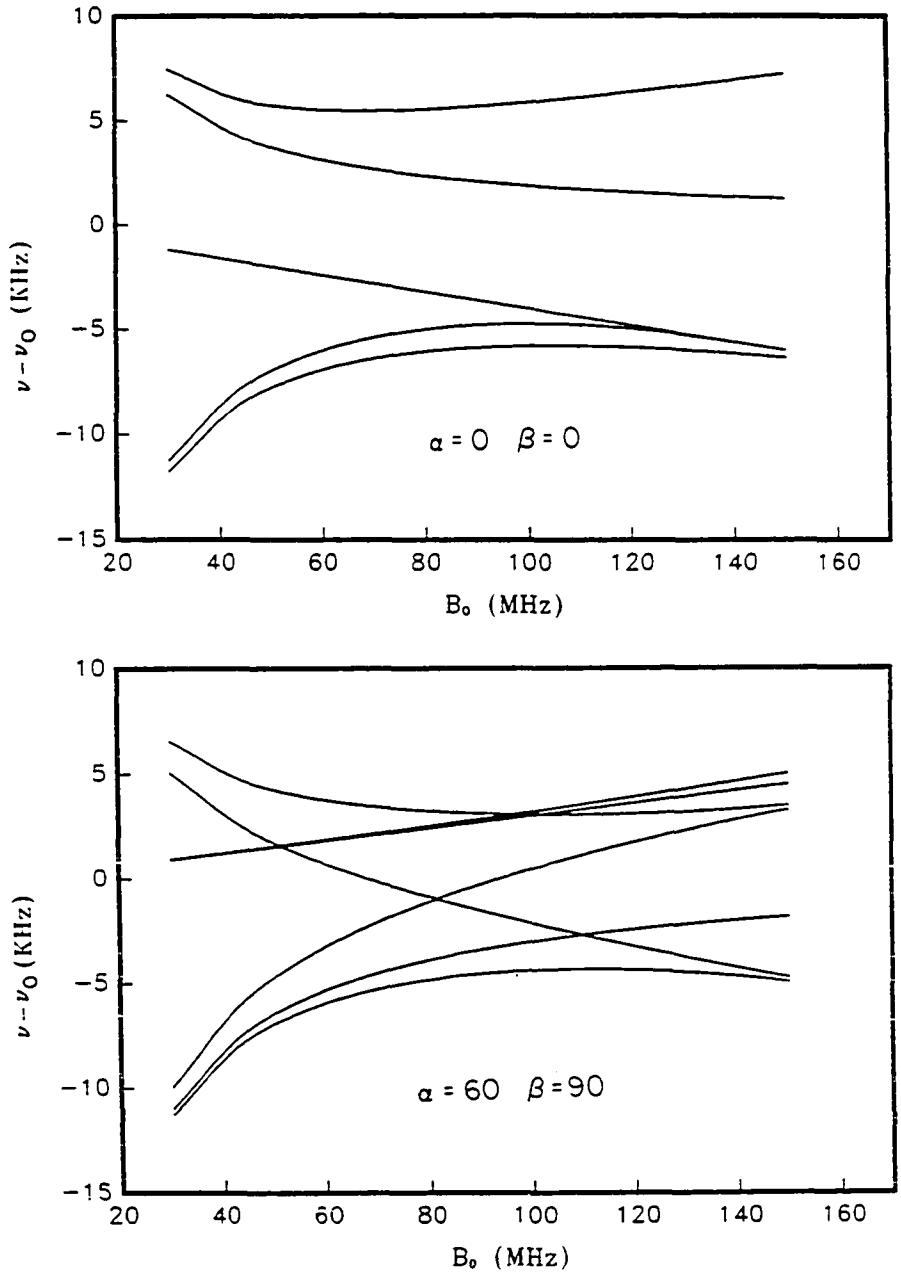

Figure 4 (continued)

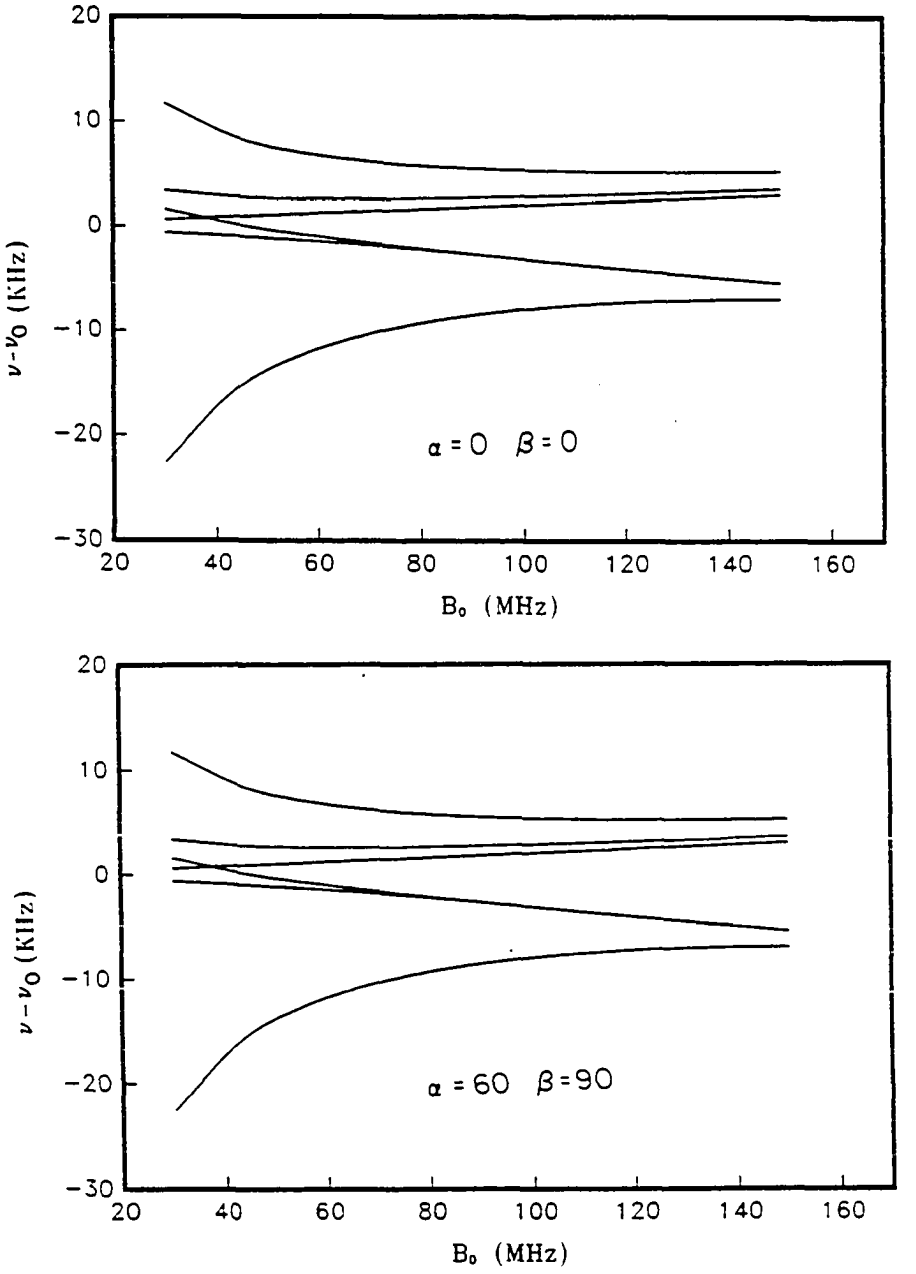

Figure 4 (continued)

Figure 5. The experimental spectra taken at 56, 100, and 220 Mhz respectively. The peak at the center of the 56 MHz spectrum is due to the small amount of water present in the sample. This has been removed by further drying the sample before measuring at 100 and 220 MHz. Upfield is to the right. The major intensity (and the center of mass) is shifted downfield as the Larmor frequency increases.

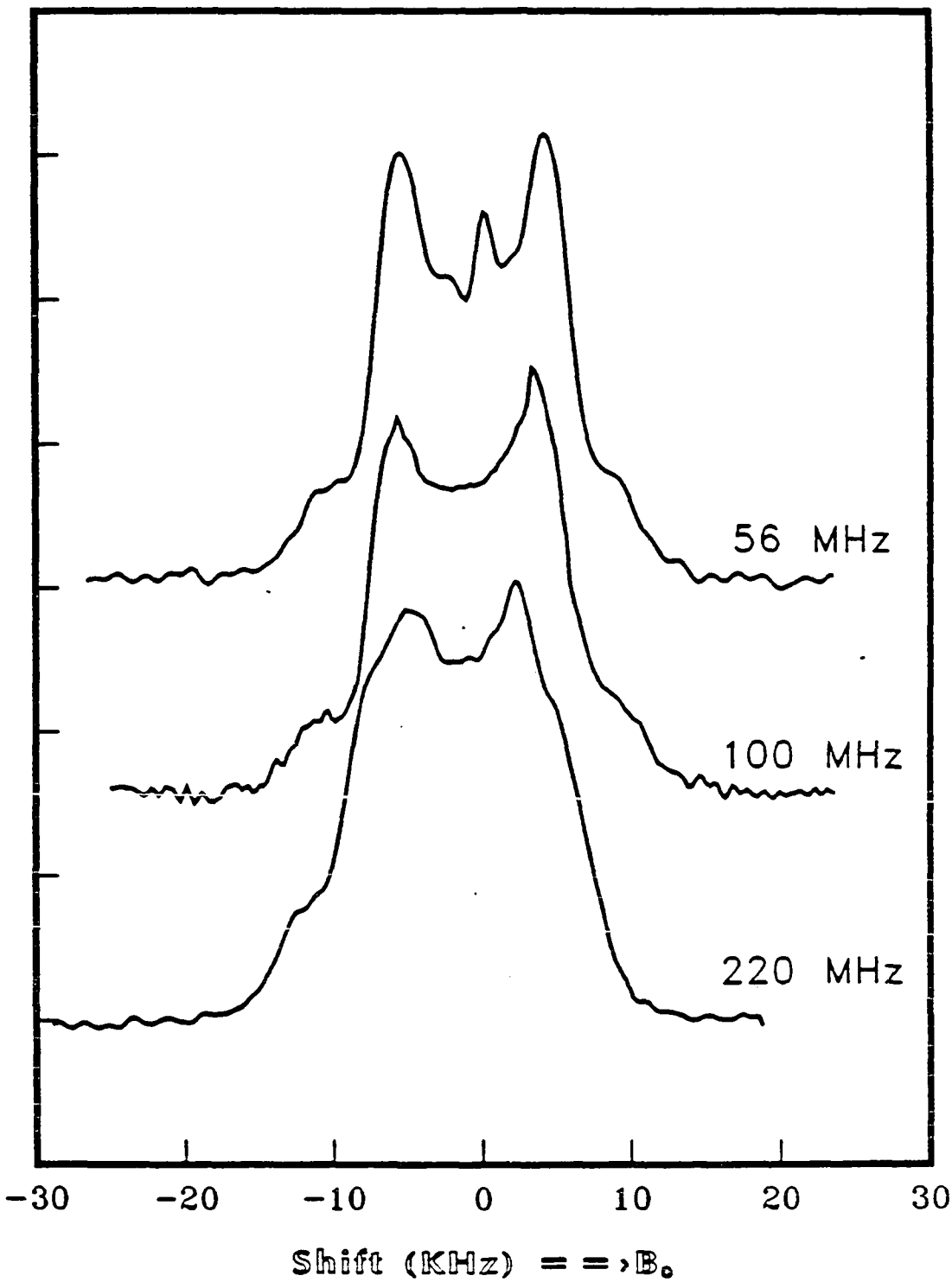
56 MHz
100 MHz
220 MHz
−30
−20
−10
0
10
20
30
Shift (KHz) ==›B₀

Figure 6. The critical frequencies of the above spectra as listed in the second half of Table I are correlated with the magnetic field. The linear least squares fits are represented by the solid or the broken lines connecting those points. The solid line corresponds to the singularities or the steps in the spectra, while the broken line with larger error represents the mapping of the shoulder. The interaction parameters as well as the mutual orientation of the two tensors can be determined by analyzing these curves.

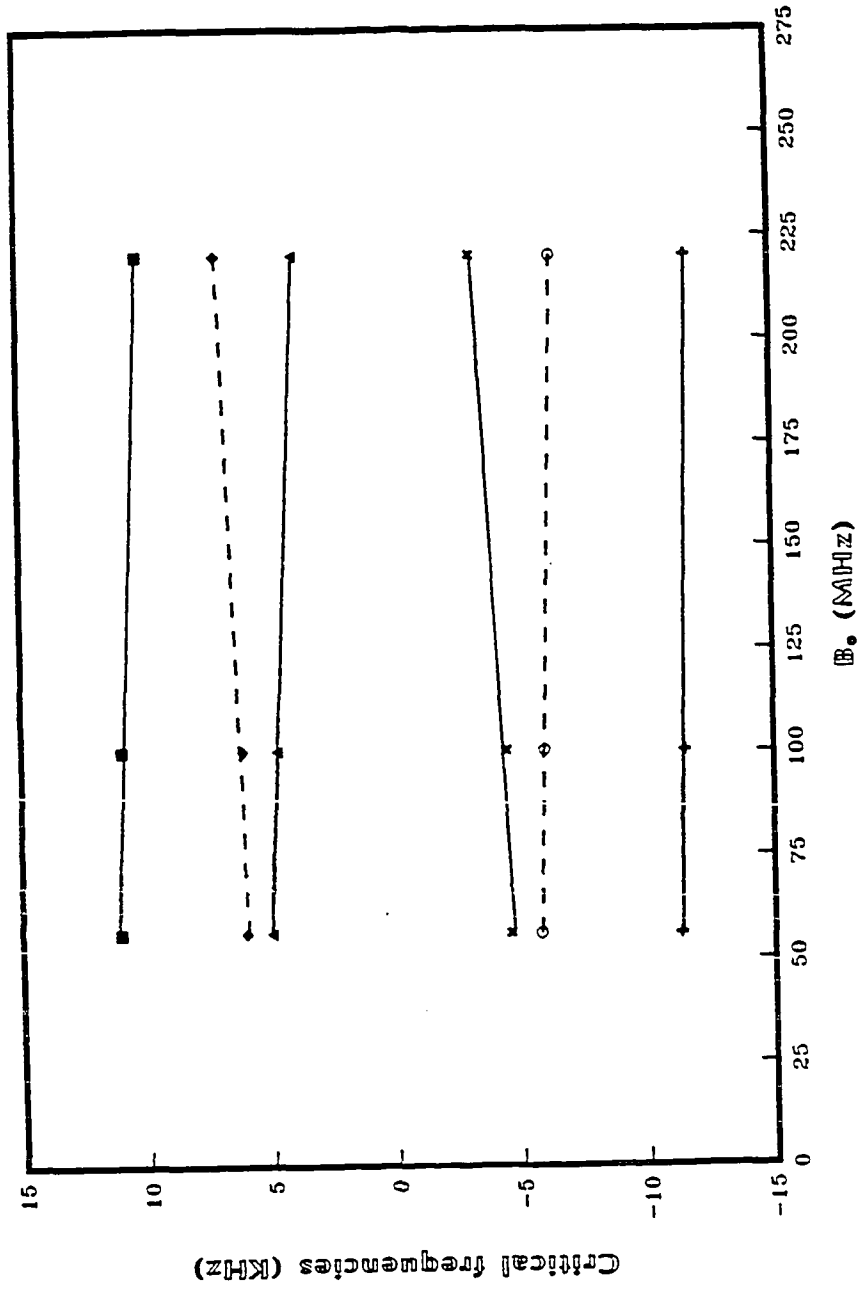
Critical frequencies (kHz)
15
10
5
0
-5
-10
-15
0
25
50
75
100
125
150
175
200
225
250
275
B₀ (MHz)

Figure 7. Complete powder line shape calculated for the three magnetic fields measured. The calculation uses the result listed in the first row of Table III. A Lorentzian broadening function with half width of 3.5 KHz has been applied. The powder average uses 2. x 2. degree mash in both θ, and ϕ. The results are to be compared with the experimental in Fig. 5.

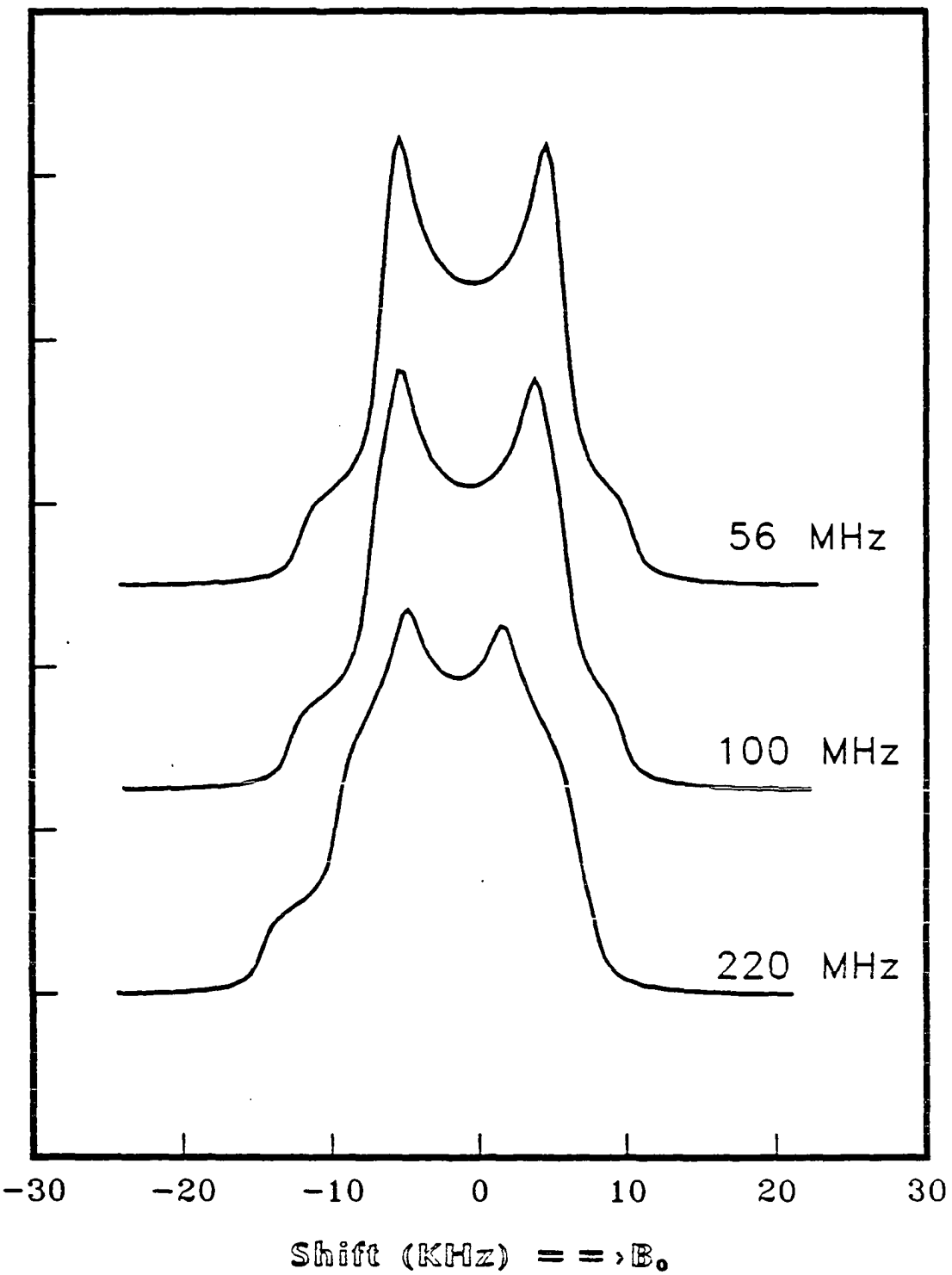
56 MHz
100 MHz
220 MHz
−30
−20
−10
0
10
20
30
Shift (KHz) ==› B_o

PART II. A STUDY BY SOLID STATE NMR OF ^{133}Cs AND ^{1}H OF A HYDRATED AND DEHYDRATED CESIUM MORDENITE

A study by solid state NMR of ^{133}Cs and ^{1}H of a hydrated and dehydrated cesium Mordenite

P. J. Chu and B. C. Gerstein
Department of Chemistry and Energy and Mineral Resources
Research Institute*, Iowa State University
Ames, Iowa 50011

* Operated for the US Department of Energy by Iowa State University under contract number No.W-7405-Eng-82. This research was supported by the Assistant Secretary for Energy Research, Office of Energy Sciences, WPAS-KC-03-02-01.

ABSTRACT

The solid state NMR of ^{133}Cs and ^{1}H in cesium exchanged mordenite has been monitored as a function of dehydration of the zeolite. In the fully hydrated mordenite, ^{133}Cs (I=7/2) exhibits a single line 64 ppm upfield of aqueous saturated CsCl. The anhydrous sample exhibits two major lines of intensities 3:1 with center of mass at -57 and -190 ppm respectively for Cs under magic-angle spinning. The major intensity is upfield of the line observed in the hydrated sample. The electric field gradient parameters for Cs of the anhydrous sample are e^2qQ=3.1 MHz, η=0.65 which reduced to e^2qQ=210 KHz, and η=0 for the hydrated sample. Assignment for the three sites occupied by Cs in the anhydrous sample and the corresponding chemical shifts are: site II, -157 ppm, site IV, -186 ppm, and site VI, -24 ppm after correction for the second order quadrupolar shift. The static proton spectra decrease in intensity by a factor of 35 between the fully hydrated and anhydrous sample. While maintaining a roughly constant width of 6.6 KHz, the shape of the proton line changes with dehydration, and exhibits an anisotropy in the anhydrous sample.

INTRODUCTION

Solid state NMR has been shown to be a useful tool for studying both the static chemical environments and the dynamic behavior of nuclei in zeolite.[1] The nuclei studied in these systems have been predominantly ^{29}Si, ^{27}Al, and ^{1}H. ^{29}Si and ^{1}H are both spin 1/2 and amenable to quantitative and qualitative detection by standard pulse techniques. ^{27}Al is a quadrupolar nucleus with spin 5/2, and thus exhibits residual broadening under rapid sample spinning, and a difficulty with quantitative detection associated with the magnitude of the quadrupolar splitting of the outer transitions relative to the bandwidth of the rf pulse. Nevertheless, its relatively small quadrupole moment allows NMR to be a useful technique for studying aluminum in, and the dealumination of zeolites. Cesium is an important promoter in catalysts used among other reactions for the fixation of CO and the production of higher alcohols. ^{133}Cs is therefore a nucleus that would be useful as a monitor of the chemistry of these systems. The nucleus has a natural abundance or 100%, a nuclear spin I = 7/2, and a relatively weak quadrupole moment of $-3.0 \times 10^{-3}/10^{-28} m^2$. However, its relatively low gyromagnetic ratio, and the relatively low mole ratios of Cs to zeolite in standard exchanged catalysts raise questions about the applicability of NMR of ^{133}Cs for monitoring processes taking place in zeolitic catalysts. The present work was undertaken to determine the utility of ^{133}Cs as a nucleus to monitor local chemistry in zeolites and more generally the local structures around this ion in surface sites. Specifically the dehydration of Cs doped mordenite has been followed by tracking the high resolution solid state NMR of ^{133}Cs. The broad line

NMR of ^{1}H has been used as ancillary information to verify the model used in explaining the changes in Cs doped mordenite with dehydration.

The crystallographic sites of Cs in mordenite have been characterized by Schlenker, Pluth, and Smith.[2] The sites for large univalent cations are labeled II, IV, and VI, and have relative occupancies for Cs of 3.78: 1.86: 1.75. Sites II and IV place Cs near the center of an eight-ring of oxygen, and site VI places the Cs off center of a six-ring. Although the 8-ring sites II and IV could accommodate all the cations, occupation is also found for the one sided coordination site VI. This site indication for II, IV and VI are equivalent to A,D and E respectively used by Mortier.[3]

EXPERIMENTAL

NMR experiments on ^{133}Cs (I=7/2) and hydrogen were performed at 28.877 MHz and 220 MHz respectively in a home-built pulsed NMR spectrometer which has been previously described.[4]

The Cs exchanged mordenite was prepared by repeated contact of 20% of Na mordenite with 250 mls of 1M $CsNO_3$ at 90°C, until essentially complete removal of Na was effected. The Na content of the zeolite was monitored by atomic absorption analysis for Na after zeolite dissolution using HF. X-ray diffraction analysis before and after ion exchange confirmed that no loss in crystallinity occurred during sample preparation. Samples with varying degrees of hydration were prepared as indicated in Table I.

The frequency of the sample spinning during NMR experiments on ^{133}Cs was varied from 3.6 KHz to 5.2 KHz to distinguish sideband structure from the central transitions. NMR measurements on Cs were taken with the sample static, and spinning. All spectra of protons were taken under static conditions.

NMR spectra of static and spinning samples were all taken at room temperature. Spin temperature inversion of the preparation pulses was used to minimize baseline artifacts in the Fourier transformed spectra. All data were taken with fixed gain of the receiver-A/D chain. The spectra were normalized to constant intensity for graphical presentation. The normalization constant was then divided by the ratio of the weight of the sample compared to the fully hydrated sample in order to obtain relative amplification factors for each spectrum. For example, the relative amplification factors of the proton spectra shown

in Fig. 1 (vide infra) indicate that the proton signal intensity in the anhydrous sample was 35 times less than that of the fully hydrated sample.

Longitudinal relaxation times for Cs in all samples were determined to be approximately 10 msec, so that a re-cycle rate of 0.1 seconds was used for accumulating NMR of Cs. Total scans of 65,536 were accumulated for signal averaging on all samples.

The longitudinal relaxation of hydrogen in the samples varies with the degree of hydration, the fully hydrated sample having a T_1 of less than 0.05 sec, and the anhydrous sample having a T_1 of less than 1 second. The trend of decreasing of T_1 at room temperature as degree of hydration increases is consistent with other measurements reported for univalent cation exchanged zeolite A.[5] Re-cycle rates of greater than five T_1 were used in accumulation of proton NMR. 10,000 scans were taken in each set of accumulations in the proton measurements.

All values of chemical shifts of ^{133}Cs are referenced to a saturated aqueous solution of CsCl. The chemical shift of ^{1}H is referenced to water. The shift scales are expressed with increasing negative values being upfield.

RESULTS

The ^{1}H spectra with increasing degree of hydration are shown in Fig. 1. The NMR spectra of ^{133}Cs with increasing hydration are shown in Figs. 2 and 3 for samples under static and magic-angle sample spinning (MAS) conditions respectively.

The relative intensities of the ^{1}H spectra give an approximate ratio of the water content in the dehydrated to that in the fully hydrated samples. The proton line width decreases with dehydration and gives indication of inhomogeneous dipolar broadening as in sample B. Upon further dehydration, the line width gradually increases and develops an asymmetry at full dehydration. This trend in the change of the ^{1}H spectra with dehydration is consistent with that observed for different degrees of hydration for the cation exchanged zeolite A.[6]

The quadrupole coupling constant e^2qQ can be measured from the singularities of the first satellite transitions (3/2,1/2) and (-1/2,-3/2) by the following equation:[7,8]

$$B_q = \frac{3e^2qQ}{4I(2I-1)} \cdot (m-\frac{1}{2}) \cdot (1 \pm \eta) \qquad [1]$$

where B_q equals the splitting of the singularity of the first satellite m=3/2, or m = -1/2 from the center of mass. These singularities correspond to the orientation with the principal axis of the e.f.g. tensor being perpendicular to the external magnetic field.[7] Equation [1] implies that splitting B_q depends also on the asymmetry parameter η of the electric field gradient (e.f.g.) tensor. For each of the m=3/2 and m=-1/2 transitions there will be two critical frequencies if $\eta \neq 0$.

These will coincide when $\eta=0$. The term $(1 + \eta)$ corresponds to a shoulder of the satellite, which is not visible in the powder spectrum. The term $(1 - \eta)$ corresponds to an infinity in the unbroadened powder spectrum; it is this singularity which is measured in the experimental spectrum which we listed in the first row in Table II. The negative sign is therefore chosen when utilizing the first satellite transition, and a nonzero of η to calculate e^2qQ.

Both the static and MAS spectra show a consistent trend of increase in quadrupole coupling constant with extent of dehydration. This is to be expected, as the electric field gradient would be expected to become more intense as the spherically symmetrical first coordination sphere of waters is removed. As the dehydration proceeds and the coupling constant becomes larger, the satellite transitions become more removed from the central transition, and less intense. Thus, the accuracy of determining the coupling constant from the position of the satellite transition decreases with increasing extent of dehydration.

Since calculating quadrupole coupling constant, e^2qQ, from the first satellite singularity depends also upon the asymmetry parameter, η, a value be determined from the satellite splitting alone. In general, a line shape fitting is required to determine both e^2qQ and η value. In principal, this can be performed for either the satellite or the central transition under MAS.

For the highly hydrated samples, i.e., those with well defined satellite splittings, the central transition is narrower than the dipolar broadening and furthermore the transitions from Cs in sites II, IV, and VI are too closely superimposed. To perform a line shape

fitting to a superposition of central transition powder patterns under MAS is not practical in this case. Recalling the fact that η was found to decrease with increased water content due to the spherically symmetrical first coordination sphere of water, the values of e^2qQ for samples A, B,and C were determined from the first satellite transition alone, assuming a value of zero for η.

As the dehydration proceeds, the splitting from these three sites separate, and it is possible to perform a meaningful fit of the central transition MAS spectra to a superposition of theoretical powder patterns. The fitting of the central transition in samples D,E, and F (discussed further in the Discussion section) yielded values of both e^2qQ and η. As a comparison, the η value was again used to determine e^2qQ using the observed first satellite transitions from [1] for these samples as well. The larger deviation observed for sample F is due to the larger uncertainty present in estimating the first satellite splitting as mentioned previously.

The values of the quadrupole coupling constant, e^2qQ, determined both from fit of the central transition and from the splitting of the first satellite, are listed in Table II. Also listed are the experimentally observed values of the first satellite splitting, B_q, and of η inferred from the fit to the central transition of samples D,E, and F.

The second satellite transition (5/2,3/2) and (-3/2,-5/2) cannot be observed for Cs in the anhydrous sample, and is just observable in the fully hydrated sample where the quadrupolar coupling is the weakest.

The central transition line width (600Hz) for the fully hydrated sample A in the MAS spectrum turns out to be three to four times larger than that calculated by using the quadrupole coupling constant estimated from the position of the satellites. This residual experimental broadening for sample A may be accounted for in three ways: (a) The homogeneous broadening of the Cs nucleus due to heteronuclear dipolar coupling to ^{27}Al, (b) an inhomogeneous distribution of the e.f.g. or the isotropic chemical shift throughout the sample,[9] (c) a nonzero value of the asymmetry parameter η, yielding a magnitude of e^2qQ larger then 210 KHz.

The center of mass of a quadrupolar nuclei obtained by zeroing the first moment is a combined effect of the shift interaction and the second order quadrupolar interaction.[10,11] Hence the true isotropic chemical shift, σ_{cs}, does not coincide with the center of gravity of the spectrum. A correction for the second order quadrupolar shift, σ_{qs}, should be made once the quadrupole coupling constant e^2qQ is determined by the relation:[11]

$$\sigma_{cm} = \sigma_{cs} + \sigma_{qs}$$

$$\sigma_{qs}(m) = \frac{-3}{40}\left(\frac{e^2qQ}{\nu_0}\right)^2 \cdot \left[\frac{I(I+1)-9m(m-1)-3}{I^2(2I-1)^2}\right]\left(1+\frac{\eta^2}{3}\right)$$

$$= \frac{-3}{40}\left(\frac{e^2qQ}{\nu_0}\right)^2 \cdot \left(1+\frac{\eta^2}{3}\right) \cdot f \qquad [2]$$

Where σ_{cm} is the center of mass of the central transition. The multiplification factors f of the quadrupolar shifts are summarized in Table III for different transitions of half integer spin up to I=9/2.

The centers of mass of each peak in the ^{133}Cs MAS spectra are obtained through zeroing the first moment of the center band of the half-half central transition. These values with different degrees of hydration are listed in the first two rows in Table IV. The second order quadrupolar shift σ_{qs} for the central transition of ^{133}Cs (I=7/2) is calculated from [2] using ν_0=28.87 Mhz and the best measured value of e^2qQ (Table II). The values of σ_{cs} are then obtained from $\sigma_{cs}=\sigma_{cm}-\sigma_{qs}$. These values characterizing the NMR spectra of ^{133}Cs in the samples of the present work are listed in Table IV. All shift values are tabulated with increasing negative values being upfield.

DISCUSSION

In the fully hydrated Cs mordenite the Cs^+ ions can be considered as floating in the zeolite water, the coordination sphere of Cs^+ thus being occupied by water molecules. This has the effect of placing all the Cs^+ ions in the same symmetrical nearest neighbor environment and thus of all Cs^+ ions having the same isotropic chemical shifts. Dehydration results in the loss of the hydration water and the subsequent migration of Cs^+ ions to sites II, IV, and VI of the zeolite lattice where coordination is now provided by the framework oxygen. Because of the differences in geometry, coordination number, and because of the replacement of water oxygens by lattice oxygens, different chemical shifts are expected for ^{133}Cs in the different cation positions. In the present study, a detailed analysis of the ^{133}Cs NMR spectra for the anhydrous sample is greatly facilitated by the X-ray diffraction work of Schlenker, Pluth and Smith[2] who have described in detail the geometry of the Cs^+ ions located at the eight-ring sites II, IV, and the six-ring site VI with the site occupancy in fully exchanged Cs mordenite. This picture fits with the observed single sharp peak in the fully hydrated sample while the anhydrous sample exhibits individual chemical shifts at different sites.

As the degree of hydration increases the quadrupole constant e^2Qq gradually decreases from 3.1 MHz to 210 KHz for the fully hydrated sample. This trend is seen in Fig. 2, where the first satellites for samples A, B can be observed, and the satellite splitting gradually increases with dehydration. The spectrum under MAS further confirms that the residual broadening is mainly due to the second order

quadrupolar interactions. The broadening changes the observed chemical shift from 1.2 KHz for the anhydrous sample to 600 Hz for the fully hydrated sample.

In the fully anhydrous sample, there appear two main peaks from the Cs spectrum under MAS. The peaks have ratio of 3:1, indicating that there are at least two different Cs populations in the structure. The higher field peak (-157 ppm) under MAS appearing in the anhydrous compound has been fitted by a superposition of two central transitions with an intensity ratio of 2:1. The fit is shown in under the upfield peak in Fig. 4. The parameters obtained in this fit are: the asymmetry parameter, $\eta = 0.6$; the quadrupole coupling constant, $e^2qQ = 3.1$ MHz; and the isotropic values of the two shifts in the upfield peak, σ_{cs} = -157, and -186 ppm.[12] The choice of single quadrupole coupling constant and asymmetry parameters for Cs at the two sites is based upon the fact that the two Cs species resides in similar environment. This choice reduced the parameters and greatly simplifies the calculation.

The downfield peak was fitted to a single central transition powder pattern under MAS. The parameters are: $\eta = 0.7$, $e^2qQ = 3.2$ MHz, and $\sigma_{cs} = -32$ ppm. The asymmetry parameter of the e.f.g. tensor is only a rough estimate. This cannot be determined unambiguously through line shape analysis of the MAS spectra due to the signal-to-noise ratio limitations and the possible inhomogeneous distribution of these parameters.[7,12] Although the quadrupole coupling constant is expected to be much different from the -157 ppm species, this is not observed, however. This results may also explains that only one first satellite singularity is found for sample F.

To exclude the possibility that the upfield peak of the fully anhydrous sample might include the overlap of the rotational side bands from the low field peak (-24ppm), the spectrum was recorded for several different rotational frequencies. Invariance of the line shape with the varying rotation speed supported the idea that the upfield peak is a inhomogeneous superposition of two peaks but not overlapping of rotational side bands.

Considering the information from x-ray data that a Cs ion at site VI is coordinated only on one side of the six ring, while Cs in sites II and IV are only slightly off center of an eight-ring, assignments for the three Cs nuclei are made as shown in Table V.

The proton spectra and the T_1 relaxation time for samples A-F also show interesting changes which are consistent with the above proposed mechanism of hydration. The trend of decreasing line width with decreasing water contents can be attributed to the chemical exchange motion of hydroxyl and water protons. As the water content decreases the hydroxyl group and water molecules tend to be less mobile and T_1 increases.[13,14] The further broadening of the ^1H spectra for the anhydrous sample can be due to shielding anisotropy plus an inhomogeneous distribution of the chemical shifts.

CONCLUSION

^{133}Cs is shown to be a useful nucleus for monitoring the local environments in mordenite by NMR. The NMR spectrum of ^{133}Cs in cesium exchanged mordenite indicates that the e.f.g. tensor increases with decreasing water content. The quadrupole coupling constant increases from 210 KHz for the fully hydrated sample to 3.1 MHz for the anhydrous sample. The static spectra increase in line width from 1.2 KHz for the fully hydrated sample to 6 kHz for the anhydrous sample. Under MAS, the anhydrous sample shows two peaks, with relative intensities of roughly 1:3. Two different sites are clearly observed in the anhydrous sample with center of mass of the peaks at -191.0 ppm and -57 ppm. The assignment of the peaks to Cs locations is made on the basis of the structural difference of the six-ring coordination site VI from the eight-ring sites II, and IV. After correcting for the second order quadrupolar shift the down field peak, -24ppm; may be attributed to site VI while sites II and IV with similar structures yield similar chemical shifts at -157 ppm and -186 ppm (see Table V). In the fully hydrated sample all three sites possess an identical isotropic value of -64 ppm.

Table I

Conditions of sample preparation

Sample	Calcination Temperature, ^{o}C/Time
A	Fully hydrated
B	100/8 hours
C	320/2 hours (deep bed in NMR tube)
D	320/4 hours "
E	450/4 hours "
F	450/10 hours (shallow bed in 10 mm bulbs)

Table II

The quadrupole coupling constant and the asymmetry

Sample	F	E	D	C	B	A
B_q(KHz)[a]	58.	46.	39.	32.	12.8	7.5
e^2qQ(MHz)[b]	4.6	2.6	1.8	0.9	0.36	0.21
e^2qQ(MHz)[c]	3.1	2.1	1.7			
η[c]	0.65	0.5	0.4	0.0	0.0	0.0

[a] The first satellite splitting from the center of mass of the static sample.

[b] Calculated from [1] and B_q assuming η value obtained from lineshape simulation for samples D, E, F and $\eta = 0.0$ for samples A, B, C.

[c] Obtained from the line shape simulation of the MAS center band of the central transition.

Table III

Multiplication factor, f, of Quadrupolar shift in eq. [2][a]

I \ m	1/2	3/2	5/2	7/2	9/2
3/2	1/3	-2/3			
5/2	8/100	-1/100	-28/100		
7/2	$15/21^2$	$6/21^2$	$-21/21^2$	$-66/21^2$	
9/2	$24/94^2$	$15/94^2$	$-12/94^2$	$-57/94^2$	$-120/94^2$

[a] (m,m-1) and (-m+1,-m) yield identical σ_{qs}.

Table IV

NMR parameters of ^{133}Cs of Cs exchanged Mordenite

Sample	F	E	D	C	B	A
σ_{cm}(ppm)[a]	-57	-61.	-63.	-65.	-65.	-64
	-190.0	-195.0	-198.	x	x	x
σ_{qs}(ppm)[b]	-33.	-15.	-10.	-2.5	0.	0
σ_{cs}(ppm)[c]	-24.	-46.	-53.	-62.5	-65.	-64.
	-157.	-179.	-188.	x	x	x

[a] The center of mass of the central transition.

[b] The second order quadrupole shift calculated from [2].

[c] The isotropic chemical shift value.

Table V

Assignment of ^{133}Cs shift value of Cs exchanged Mordenite

site[a]	II	IV	VI
σ_{CS} (ppm)	-157.0	-186.0	-24.0
area (NMR)	2	1	1
population(X-ray)	3.78	1.86	1.75

[a] Site indications are the same as those in reference 2.

REFERENCES

1. C. A. Fyfe, Solid State NMR for Chemists (CFC Press, Guleph, Ontario, 1983).

2. J. L. Schlenker, J. J. Pluth and J. V. Smith, Mat. Res. Bull. 14, 751, (1979); and J. L. Schlenker, J. J. Pluth and J. V. Smith, Mat. Res. Bull. 13, 901 (1978).

3. W. J. Mortier, Compilation of extra framework sites in Zeolites (Butterworth & Co. Ltd., London, 1982).

4. T. T. P. Cheung, L. E. Worthington, P. D. Murphy, and B. C. Gerstein, J. Magn. Reson. 41, 158 (1980).

5. R. M. Barrer, Zeolites and Clay Minerals as Sorbents and Molecular Sieves (Academic Press, New York, 1978).

6. W. Maiwald, and W. D. Basler in Magnetic resonance in colloid and interface science, J. P. Fraissard, and H. A. Reesing eds. (D. Reider Publishing Company, Dordrecht, 1979), p 629.

7. D. R. Torgeson, and R. G. Barnes, J. Chem. Phys. 62, 3968 (1974).

8. B. C. Gerstein, and C. Dybowski, Transient Techniques in NMR of Solids (Academic Press, New York, 1985).

9. P. C. Taylor, and P. J. Bray, J. Magn. Reson. 2, 305 (1970).

10. E. Kundla, A. Samoson, and E. Lippmaa, Chem. Phys. Lett. 83, 229 (1981).

11. A. Samoson, Chem. Phys. Lett. 119, 29 (1985). Equation [2] has been written in a different expression from eq. [3] of this reference.

12. P. J. Chu, Manual for calculating quadrupole NMR powder line shape, Ames Laboratory report, April (1986). The program for simulating the center transition of the MAS spectra for arbitrary transition of half integer quadrupolar nuclei are written according to the spatial dependent eigen-energy expression from reference 10. The transient decay governed by the above eigen energy is first calculated then Fourier transform to obtain the spectrum.

13. K. Klier, J. Chem. Phys. 58, 737 (1973).

14. J. H. Shen, A. C. Zettlemoyer, and K. Klier, J. Phys. Chem. 84, 1453 (1980).

Figure 1. NMR spectra of ^{1}H in Cs exchanged mordenite as a function of degree of hydration. Bottom, spectrum A, is the fully hydrated sample. Top, spectrum F is the anhydrous sample.

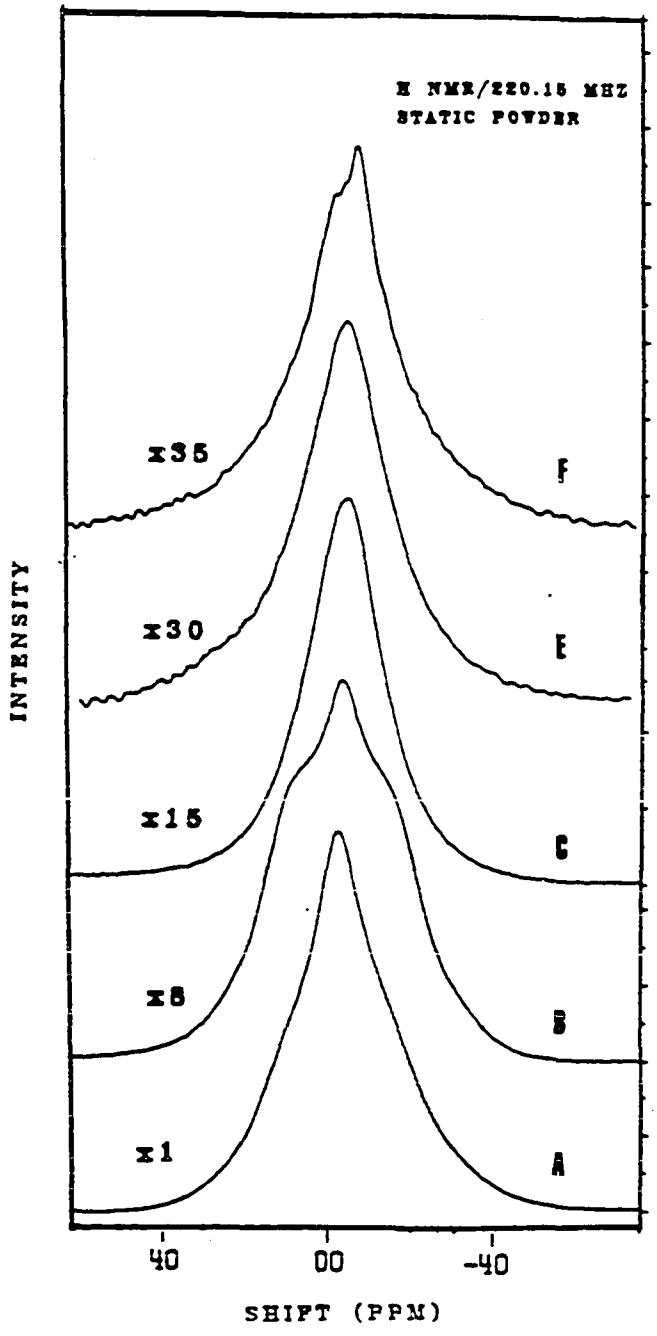
H NMR/220.15 MHZ
STATIC POWDER
x35
F
x30
E
x15
C
x8
B
x1
A
INTENSITY
40
00
-40
SHIFT (PPM)

Figure 2. Static NMR spectrum of ^{133}Cs in Cs exchanged mordenite, as a function of degree of hydration. Bottom, spectrum A, fully hydrated sample. Top, spectrum F, anhydrous sample. Note the satellite transitions visible in spectra A and B.

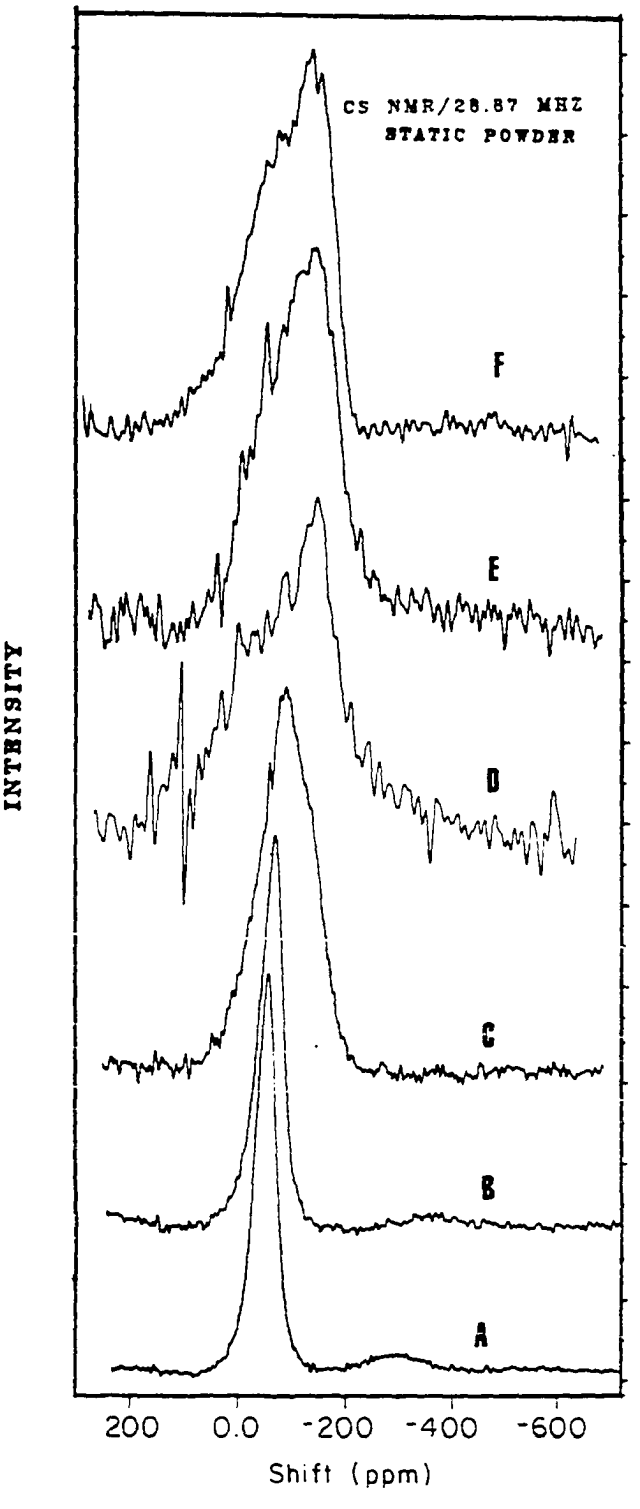
CS NMR/28.87 MHZ
STATIC POWDER
F
E
D
C
B
A
INTENSITY
200
0.0
-200
-400
-600
Shift (ppm)

Figure 3. MAS spectra of ^{133}Cs in Cs exchanged mordenite as a function of degree of hydration. Bottom, spectrum A, fully hydrated sample. Top, spectrum F, anhydrous sample. Sample rotation speed in KHz is indicated at the right of each spectrum. Starred (*) peaks are spinning sidebands.

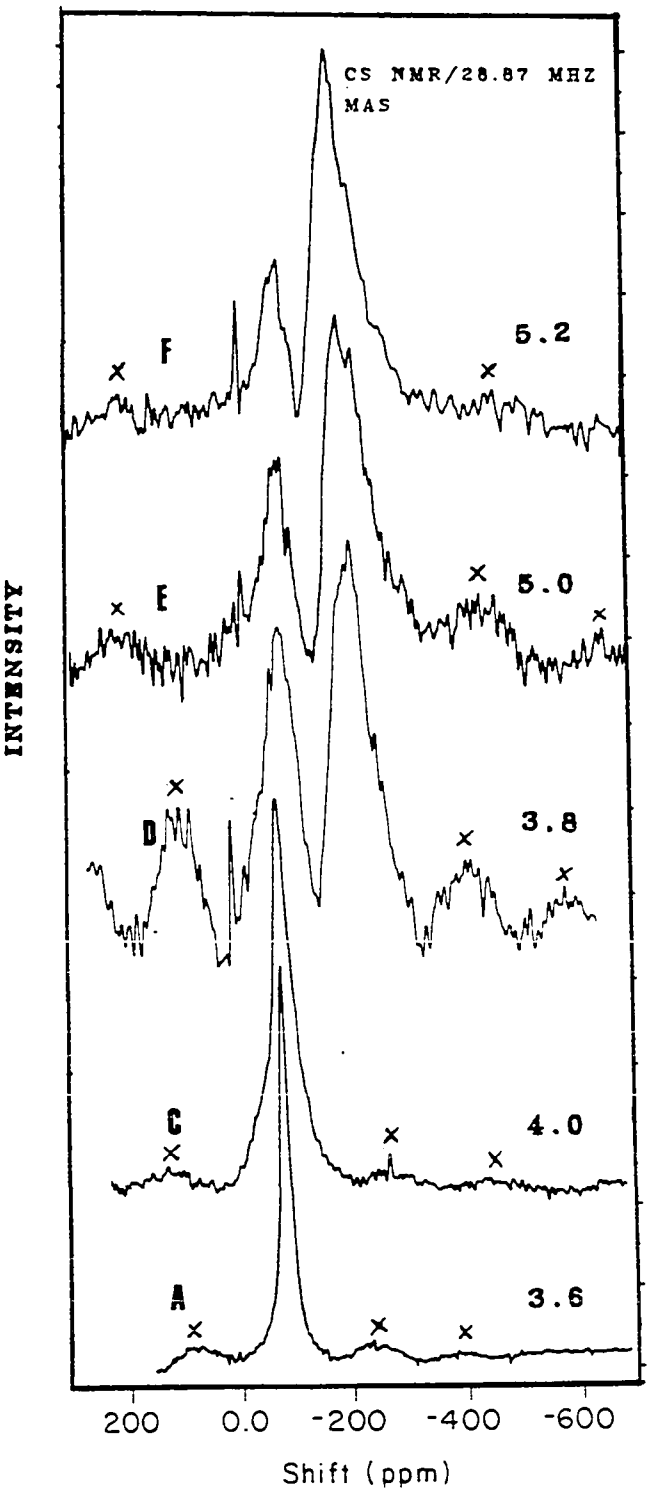
CS NMR/28.87 MHZ
MAS
F
5.2
E
5.0
D
3.8
C
4.0
A
3.6
INTENSITY
200
0.0
-200
-400
-600
Shift (ppm)

Figure 4. Fit of the MAS peaks of ^{133}Cs in anhydrous Cs exchanged mordenite to a superposition of three peaks. See discussion for the fitting parameters.

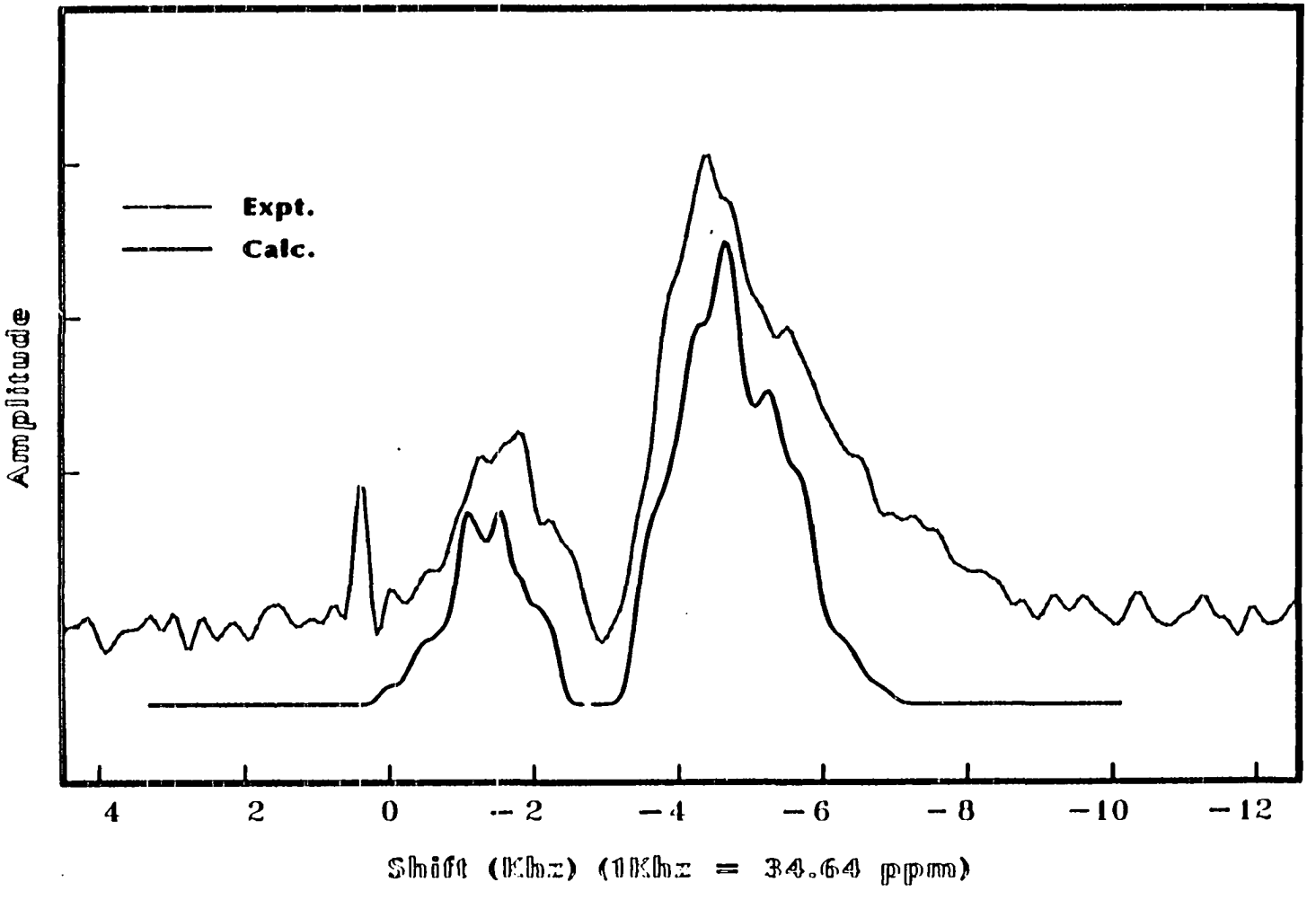
Expt.
Calc.
Amplitude
4
2
0
−2
−4
−6
−8
−10
−12
Shift (Khz) (1Khz = 34.64 ppm)

PART III: EXCHANGE DYNAMICS OF ^{23}Na AND THE STRUCTURAL INCOMMENSURATION IN $NaMo_4O_6$: NMR DYNAMIC LINE SHAPE FOR SECOND ORDER QUADRUPOLAR CENTRAL TRANSITION

Exchange dynamics of ^{23}Na and the structural incommensuration in $NaMo_4O_6$: NMR dynamic line shape for second order quadrupolar central transition

P. J. Chu, and B. C. Gerstein
Ames Laboratory and Department of Chemistry
Iowa State University

ABSTRACT

Sodium nuclei in $NaMo_4O_6$ show dynamic motion as evidenced by the change of the asymmetry parameter of the ^{23}Na central transition in the variable temperature NMR. The nonaxially symmetric electric field gradient observed in the slow motion limit implies that the preferred occupation of the sodium nucleus is not at the center of the tetragonal oxygen cage. This fact explains the unrealistic thermal ellipsoid for sodium observed in the room temperature X-ray diffraction. Dynamic NMR line shape simulations for the second order central transition were performed based upon models of four site exchange, and all site random exchange models. Both models yield indistinguishable results with an activation energy E_a of 1.95 Kcal/mole.

The anomalous upfield shoulder in the central transition is found to be related to an unusual structural incommensuration. The transition temperature at T_c = 140 K is evidenced by jump-discontinuities in both the temperature dependence of T_1 and the quadrupole coupling constant, e^2qQ. Using the "plane-wave" approximation to describe the structural incommensuration, the appearance and the gradual downfield shift of the anomalous shoulder can be satisfactorily fit to the data. From the temperature dependence of the quasi-continuous frequency distribution associated with the incommensurate structure, the anti-ferroelectric to para-electric transition temperature, T_i is estimated to be 520 K.

INTRODUCTION

NMR studies of quadrupolar nuclei have been of recent interest. Most of these studies concentrated upon half integer quadrupolar nuclei in the Zeeman region (nuclei with relatively weak quadrupole coupling constants), where the central transition, dominated by the second order perturbation of the electric field gradient upon the Zeeman levels, produces a characteristic line width in the range of few kHz.[1-8] Valuable information such as the isotropic shift, the electric field gradient (e.f.g.), and the asymmetry of the e.f.g. tensor can be obtained from studying the line shape. Combined with the magic-angle and variable-angle sample spinning techniques,[9-13] the studies can be extended to more complicated systems where quadrupolar nuclei possess different e.f.g. principal values. These studies and calculations are however limited only to rigid structures.

In this article is studied for the first time the second order quadrupolar powder line shape under the influence of multisite dynamic motion. Of particular interest in the current studies is the effect of coherent, discrete site jump motion upon the central transition line shape to second order in perturbation theory. The fundamental formalism in calculating the dynamic NMR line shape associated with the second order quadrupolar interaction and the spatial dependence of the characteristic frequencies required in the dynamic motion are also discussed. From these line shape studies, the following can be revealed: (a) the type of motion; (b) the activation energy of the dynamic process; and (c) the equilibrium location of sodium in $NaMo_4O_6$.

The sample used in the current study is the ternary molybdenum oxide $NAMo_4O_6$.[14,15] This compound consists of infinite chains derived from octahedral metal cluster units jointed at opposite edges. A three dimensional view of the $NaMo_4O_6$ structure along the C axis is given in Fig. 1, where oxygen atoms bridge the outwardly exposed edge of the octahedral molybdenum metal units and bind one chain to another through Mo-O-Mo bridges. From this figure, it is seen that the sodium ions are stacked along the c axis in tunnels created by four metal-oxide cluster chains cross-linked by metal-oxygen bonds. Each Na^+ ion occupies a site of tetragonal coordination symmetry surrounded by eight oxygen atoms at a distance 2.74 Å. At room temperature the resistivity of the single crystal along the needle axis is ca 10^{-4} ohm·cm, indicating that the system is a moderately good one dimensional electrical conductor.

The principal values of the thermal ellipsoid[15] for sodium are B11=B22=9.0, B33=2.9, where 11 and 22 axis are coincident with the a-b plane and the 33 axis is along the c crystal axis. On the other hand ^{113}In in $InMo_4O_6$, isostructural with $NaMo_4O_6$, exhibits a thermal ellipsoid with principal values of: B11=B22=1.1, B33=3.1. Both nuclei possess comparable 33 principal values, but sodium exhibits an unrealistically large anisotropy in the 11 − 22 plane. The origins of this large thermal anisotropy, with prolate shape distribution in the a-b plane of the unit lattice are possibly related to the following behavior: (a) a large amplitude of sodium motion in the a-b plane. The thermodynamic stable occupation of the sodium nucleus may either be in the center, or off-center of the tetragonal oxygen; and (b) a structural incommensuration or some periodic lattice distortion of this quasi-one

dimensional channel compound.

The presence of a long range displacement or a superlattice structure is usually reflected by the appearance of satellites in X-ray diffraction studies of the solids. Since an X-ray diffraction pattern is an ensemble average of the lattice over time long compared to lattice motion, a local displacement and a long range incommensuration of superlattice structure are hard to distinguish, if the anisotropic motion of the sodium nucleus has not been completely frozen. NMR spectroscopy, on the other hand, is sensitive to both the local dynamic behavior, and at the same time the line shape is subject to the quasi-continuous distribution of the interaction constant due to long range structural incommensuration. NMR offers the promise of discerning local structure and long range displacements. In the latter part of the study, a possible structural incommensuration in this channel compound is examined. A simple calculation is performed for the powder spectrum based upon the plane wave approximation of the incommensurate structure and the resulting quasi-continuous e.f.g. distribution to account for the observed NMR spectra.

THEORY

NMR spectra line shapes subject to nuclear motion have been widely studied for systems governed by interactions described by first order perturbation theory. Examples include shift anisotropy, inhomogeneous dipolar broadening, and the effect of an electric field gradient upon the I=1 quadrupolar nucleus, deuterium in particular. Since second order terms also contain nonsecular components, describing the time dependence in stochastic processes becomes more complicated. The applicability of the formalism used for the first order interaction in the dynamic studies for systems governed by second order quadrupolar perturbation will be examined. Another major concern will be in the determination of the spatially dependent transition frequencies of each well defined "site" associated with a second order perturbation in the dynamic system.

In this work is considered a half integer quadrupole spin experiencing dynamic exchange motion. In the following, the matrix formalism describing the discrete multisite dynamic motion governed by both the second order quadrupolar interaction and the shift anisotropy are discussed.

The operator Π_Ω is introduced as the generator of the Markov process, which describes the rate of the mass transfer within the n-site dynamic ensemble. The orientation, Ω representing the different sites available in the discrete site exchange can be defined by the Euler angles as will be explained later. The n by n matrix has elements $\Pi_{ij} = 1/\tau_{ij}$. The Stochastic Liouville-Von Newman (SLE) equation written in

term of superoperator notation becomes:[9,16]

$$\dot{\rho}(\Omega_t) = (-i\hat{\bar{H}}_e(\Omega,t)+\Pi_\Omega)\,|\rho(\Omega_t)) \qquad [1]$$

The first term is the ordinary Liouville-Von Newman equation for the stationary system. This equation implies that the evolution of the density matrix is governed by an energy conserved oscillation term represented by the effective Hamiltonian, $\bar{H}_e$, and an energy dissipation (damping) term originating from nuclear motion.

The effective Hamiltonian for each distinctive site, $\bar{H}(\Omega_i)$, is obtained by average Hamiltonian theory over the fundamental cycle time of one Larmor period $2\pi/\omega_0$. In the current studies, only the averaged term for the shift anisotropy, C, and the quadrupolar coupling, Q, is considered. To first order, the Magnus expansion[17,18] of the effective Hamiltonian for site i becomes:

$$\bar{H}_e(\Omega_i)= V_C^{(0)}(\Omega_i)+V_Q^{(0)}(\Omega_i)+ V_Q^{(1)}(\Omega_i) \qquad [2]$$

From the SLE equation, the master equation for discrete n-site dynamics can be derived assuming a Markov dynamic process and the slow motion limit.[9,19] The spin magnetization in this limit can be shown to follow the nuclear motion adiabatically. The magnetization, following the derivation of Abragam, is therefore equal to:[19]

$$\frac{d}{dt}\vec{M}(t)= (i\tilde{\omega}+\tilde{\Pi}-\tilde{R})\cdot\vec{M}(t) \qquad [3]$$

This expression under the Markov approximation is independent of the

order of pertubation in [2].

The transient signal G(t) under dynamic motion can therefore be calculated from [3] after summing the magnetization over all distinctive sites.

$$G(t)=\vec{\underleftarrow{I}}\cdot\vec{M}(t) = \underleftarrow{I} \exp\,[(i(\tilde{\omega}+\tilde{\Pi}-\tilde{R})t]\cdot\vec{W} \qquad [4]$$

Here $\underleftarrow{I}$ is an unit row vector multiplied with $\vec{M}(t)$ to obtain the sum. The row vector, $\vec{W}$ corresponds to the population weight function. The dynamic matrix, $\tilde{\Pi}$ characterizing the type of motion, gives the off diagonal elements in the argument of the complex exponential that will finally produce the dynamic "averaging" of the static NMR spectra. The elements in the diagonal matrices $\tilde{\omega}$ and $\tilde{R}$ correspond to the characteristic frequencies, $\omega(\Omega_i)$; and the spin spin relaxation time, T_{2i} respectively, for each distinctive site, i. All matrices and vectors in [4] are dimensioned by the total number of sites, n.

In the following are determined, the spatial dependence of the characteristic transition frequencies $\omega(\Omega_i)$ for each site.

The Magnus expansion in [2] is written specifically for the shift and the quadrupole interactions. This average Hamiltonian becomes:

$$V_C^{(0)} + V_Q^{(0)} = \omega_0 R_0^2 \sqrt{\frac{2}{3}}\, I_0 + \frac{1}{3}\,\omega_q R_0^2 \sqrt{\frac{2}{3}}\,(3I_0^2 - I^2) \qquad [5]$$

$$\text{with} \quad \omega_0=\gamma B_0 \quad \text{and} \quad \omega_q = \frac{3eQ}{4I(2I-1)\hbar}$$

The next term in the Magnus expansion is obtained after evaluating

the commutators and the double time integral. For the quadrupolar interaction this becomes:

$$V_Q^{(1)} = \frac{\omega_q^2}{9\omega_0} 2\cdot\{|R_1^2|^2(4I^2-8I_0^2-1)I_0 - |R_2^2|^2(2I^2-2I_0^2-1)I_0$$
$$+ \frac{\sqrt{6}}{2} R_0^2 [R_{-1}^2(4I_0^2-4I_0+1)I_+ - R_1^2(4I_0^2+4I_0+1)I_-]$$
$$+ \sqrt{6}\, R_0^2[R_2^2(I_0+1)I_-^2 + R_{-2}^2(I_0-1)I_+^2]\} \qquad [6]$$

The above results are obtained by assuming an oscillation of the spatial dependent terms, R_m^2 slow compared with the Larmor frequency. Evaluated in the Zeeman frame, the resonance frequency of any single quantum transition associated with the i-th site can be calculated straightforwardly from the effective Hamiltonians:

$$\omega(\Omega_i) = \frac{2\pi}{h}\{\langle m|\bar{H}_e(\Omega_i)|m\rangle - \langle m-1|\bar{H}_e(\Omega_i)|m-1\rangle\} \qquad [7]$$

the explicit expression can be obtained when the spatial dependence of the irreducible components R_m^2, and eigenvalue of the spin operators are determined. The resulting characteristic frequencies for the first two orders according to [5] and [6] becomes:

$$\omega_m^{(0)}(\alpha_i,\beta_i,\gamma_i,\Theta,\phi) = \sqrt{\frac{2}{3}}[\omega_0 R_0^2(\mathrm{CSA}) + \frac{1}{3}\omega_q^2 R_0^2(\mathrm{QDP})(2m-1)] \qquad [8]$$

$$\omega_m^{(1)}(\alpha_i,\beta_i,\gamma_i,\Theta,\phi) = \frac{\omega_q^2}{9\omega_0}[2M_1|R_1^2(\mathrm{QDP})|^2 - M_2|R_2^2(\mathrm{QDP})|^2] \qquad [9]$$

with $M_1 = 4I(I+1)-24m(m-1)-9$

and $M_2 = 4I(I+1)-12m(m-1)-6$

To simplify the calculation, the off diagonal elements in [6] have been completely neglected in deriving [9]. This assumption allows us to use the Zeeman states as basis functions in evaluating the spin eigenvalues, and dramatically reduces the complexity of the line shape calculation. The validity of this truncation will be discussed later.

In [8] and [9], the spatially dependent terms, R_m^2 have not been determined. To obtain this quantity, two transformations in the dynamic system need be performed (see Fig. 2). First, a rigid, time independent cartesian frame, (X_R, Y_R, Z_R) in the molecule or lattice frame has been conveniently chosen. The transformation from the principal axes (PAS) (X', Y', Z') of the interaction tensor at site i to the reference frame R is characterized by the Euler angles $(\alpha_i, \beta_i, \gamma_i)$. For an axially symmetric tensor, either $(\alpha, \beta, 0)$ or $(0, \beta, \gamma)$ are sufficient to characterize the orientation of the interaction. For in-plane motion, the simplest choice of the reference frame is the one that containing the jumping axis, Z_R, in which the nuclei jump in the X_R-Y_R plane of this frame.

The second transformation is identical to that performed for a static sample and accounts for the relative orientation of the R frame in the crystal with respect to the Zeeman quantization axis system. Due to the axial symmetry of the laboratory frame (there are no difference in the X and Y direction of a well shimmed magnetic field), two Euler angles (θ, ϕ) are sufficient to characterize the transformation.

The irreducible components at each nuclear site, i after the double frame transformation are expressed through the Wigner rotation matrices[20] as follows:

$$R^2_m(\alpha_i,\beta_i,\gamma_i,\Theta,\ \phi)= \sum_{m'} D^{(2)}_{m',m}(0,\Theta,\phi)\sum_{m''} D^{(2)}_{m'',m'}(\alpha_i,\beta_i,\gamma_i)\rho^{\lambda}_{2m''} \qquad [10]$$

λ represents either the shift or the quadrupolar interaction in the current study. The definition of the rotation of the Euler angles are identical to that given by Edmonds[21] where the reduced rotation matrices $d_{m',m}(\beta)$ are related to Jacobian polynomials. The related irreducible spherical components ρ^{λ}_{2m} in the principal axis system are known to be:

$$\rho^{\lambda}_{2\pm2} = \frac{1}{2}\,\eta^{\lambda}\delta^{\lambda} \qquad \rho^{\lambda}_{20} = \sqrt{\frac{3}{2}}\,\delta^{\lambda} \qquad [11]$$

where the anisotropy $\delta=\sigma_{zz}-\sigma_0$, asymmetry $\eta=(\sigma_{yy}-\sigma_{xx})/\sigma_{zz}-\sigma_0$, and the isotropic value $\sigma_0= (\sigma_{xx}+\sigma_{yy}+\sigma_{zz})/3$ are defined and σ_{xx}, σ_{yy}, σ_{zz} are the three principal values of the interaction tensor. For the e.f.g tensor, the elements $\sigma_{ii} = eq_{ii}$, and therefore the trace σ_0 is zero. The convention $|q_{zz}|>|q_{yy}|>|q_{xx}|$ as defined by Haeberlen[20] is used in the follwing treatment. Antisymmetric elements that yield off diagonal terms in the Hamiltonians are neglected. In the appendix, the explicit expressions of the irreducible tensor components, R^2_m after a double frame transformation, which will be used in the line shape calculation, are tabulated.

In the presence of two or more interactions, the principal axes are in general oriented independently of each other. This fact might imply that a triple frame transformation is required in order to describe the mutual orientation between interactions and the molecular frame. This can be avoided by utilizing the common rigid reference frame, R, defined

previously. To simplify the discussion, consider the two interactions being A and B, with relative orientations as shown in Fig. 2. For the first interaction, the transformation characterized by the Euler angle $(\alpha_i, \beta_i, \gamma_i)_A$, orients A into the reference coordinate, R. A second transformation to the laboratory frame is characterized by angles (0, θ, ϕ). The second interaction, B, will orient at different angles $(\alpha_i, \beta_i, \gamma_i)_B$ with respect to the common and fixed cartesian coordinate system, R. These angles are chosen to maintain the mutual orientation between tensors A and B. The second transformation for B, characterized by (0, θ, ϕ) is performed identically as for A. The characteristic frequency $\omega(\Omega_i)$ is finally obtained by summing over all the transition frequencies in [8] and [9] after the above double frame transformation.

EXPERIMENTAL

The NMR spectra were taken at three different magnetic fields with ^{23}Na resonance frequencies of 14.8, 58.23 and 92.3 MHz. The spectra were taken on a home-built spectrometer similar to that described previously.[22] Variable temperature experiments performed at 58.23 MHz used a home-built cryogenic system and a Scientific Instrument temperature controller. Variable temperature experiments performed at 92.3 MHz used an Oxford Instruments cryogenic temperature control system.

The sample chamber temperature was controlled by a flow of liquid helium or liquid nitrogen. A Constantan vs Alumel thermocouple monitored the sample temperature to an accuracy of $\pm$1.0 K. The lowest stable attainable temperature was 49K. Below this temperature, the rf coil began to arc-discharge in the helium gas.

The T_1 measurement was obtained through progressive saturation of the transient signal after a string of $\pi/2$ pulses separated by variable spacing τ. These values of T_1 ranged from $\approx$6 msec at 77K to $\approx$20 msec at room temperature for sodium. A recycle time of 160 msec was therefore used at all temperatures.

An Andrew-Beams type rotor was used in the variable-angle spinning and MAS experiments at 58.23 MHz. Spinning speeds varied from 4.2 kHz to 5.4 kHz to differentiate the rotational side bands.

Tuning of the spectrometer was achieved using 7M aqueous NaCl. $\pi/4$ nominal pulse widths were used at all fields, following the (I+1/2) scaling relation[23] for weak quadrupole nuclei. Experimentally, this pulse also yielded the maximum signal.

A 4.0 mm o.d. teflon tube was used to contain the sample instead of the pyrex glass tubing which contains sodium. To avoid interference of the ^{63}Cu resonance from a copper coil, silver wire was used in constructing the rf coil in the static, the spinning and the variable temperature NMR probes. Although no consistent background signal was observed, background scans were still taken for each variable temperature measurement.

The receiver dead time and giant pulse breakthrough was reduced to 5.5 μ sec, after series L-C circuits were inserted between each stage of the video-amplifier. The linear phase error produced by the truncation of the initial time decay is numerically corrected by a linear phase correction after each Fourier transform of the spectra.

The $NaMo_4O_6$ samples were supplied by C. Torardi and R. E. McCarley. Detailed descriptions of the synthesis and the structural parameters of the compound are given in references 14 and 15.

RESULTS and DISCUSSION

Determination of the interaction parameters

The parameters of each individual spin interaction governing the sodium nucleus are determined first in this section. Details of the variable temperature NMR line shape studies will be discussed in the latter section.

From the crystallographic structure, $\bar{d}$(Na-Na) is estimated to be 8 Å and $\bar{d}$(Na-Mo) is ≈ 6. The Mo nucleus has a relatively weak quadrupole moment and small gyromagnetic ratio, while the nucleus, ^{16}O, the closest nucleus to sodium is spin zero and the natural aboundance of the I= 3/2 isotope ^{17}O is only 0.372 %. Under these circumstances, sodium can be considered as an isolated spin. The two major interactions governing sodium are the chemical shift anisotropy and the electric field gradient interaction. Homonuclear and heteronuclear dipolar interactions can be neglected.

The parameters of the quadrupolar interaction of ^{23}Na in $NaMo_4O_6$ are first determined by variable- and magic-angle sample spinning (MAS) At 58.23 MHz and 298 K. The MAS line shape of the center band of the central transition shows the split that is characteristic of an axially symmetric e.f.g. tensor (Fig. 3). A simulation of the central transition line shape under MAS[10,11,12] is superimposed on the experimental spectrum in the inset of Fig. 3. In the calculation, the quadrupole coupling constant (QCC), e^2qQ = 1.58 MHz, the asymmetry parameter η=0.2 and the isotropic shift σ_{cs}= -36.3 ppm as listed in Table I. The discrepancies between the calculation and the experimental

data are due to the nuclear motion and the interference of the satellite transition side bands.[11]

Room temperature NMR spectra taken at three magnetic fields are shown in Fig. 4. Approximate parameters of the shift interaction have been determined by mapping the singularities of the spectra taken at three different magnetic fields. The singularities in the downfield portion follow an inverse field scaling relation. This implies that the shift interaction, linearly proportional to the field, is much smaller than the second order quadrupolar interaction. Notice that the inverse relation does not apply to the upfield shoulder and is completely absent for spectra taken at 14.82 MHz.

The center of mass σ_{cm} has been shifted from the true chemical shift value due to the second order quadrupole interaction.[24,25] The second order quadrupolar shift, σ_{qs} can be calculated from the coupling constants and the asymmetry. Written specifically for spin I=3/2, the constant F equals:[24]

$$F= \frac{-3}{40} \left(\frac{e^2qQ}{\nu_0}\right)^2 \cdot \left(1+ \frac{\eta^2}{3}\right) \qquad [12]$$

The second order quadrupolar shift σ_{qs} equals -F/3 for the central transition and 2F/3 for the satellite transition. The values of the measured center of mass, the calculated quadrupolar shift and the corrected chemical shift are listed in Table I. Also shown are the same parameters obtained from the MAS experiment. The isotropic chemical shift is less accurate at low fields due to the fact that higher order perturbations become important and larger errors occur in evaluating the first moment of the broader spectra. The averaged value of σ_{cs}=-22±5

ppm referred to the saturated NaCl aqueous solution is obtained.

Variable temperature NMR

Variable temperature measurements at 58.23 MHz are shown in Fig. 5. The spectrum is a single peak at 78 K and gradually splits into two peaks which continue to sharpen as the temperature increases. A third peak appearing at the high field side of the major resonance also becomes observable at ≈ 140 K. The exact temperature for this upfield shoulder to emerge can not be determined. This peak seems to remain at ≈ 150 ppm to room temperature and then gradually coalesces with the downfield major component of the resonance as the temperature further increases. To better study the "anomalous" upfield peak, the experimental temperature was further raised to 403 K in the VT measurement performed at 92.3 MHz. The spectrum is shown in Fig. 6 for several selected temperatures. The major features of the spectrum are quite similar to that observed at 58.23 MHz, with resonance of the downfield portion scaled approximately 1.6 times in kHz unit and ≈2.5 times in ppm units. The tendency of the upfield shoulder to shift toward the major resonance as the temperature increases is well illustrated.

The central transition line shape of ^{23}Na changes with variable temperature from a nonaxial symmetry-like spectrum at 78 K to an axially symmetric appearing spectrum at room temperature. This behavior may be due to: (a) the gradual shifting of the equilibrium position from nonaxial e.f.g. symmetry to an axially symmetric environment as temperature increases; and (b) the exchange average of the sodium nuclei

between sites possessing a nonaxially symmetric e.f.g tensor is averaged under rapid motion and yields an effective axially symmetric e.f.g. tensor at high temperatures. The first possibility is inconsistent with the anomalous thermal ellipsoid observed in the room temperature x-ray diffraction data. The second possibility is examined using an analysis of the central transition line shape under dynamic motion taken to second order.

Calculation of the central transition line shape under motion

According to the symmetry of the structure, dynamic motion may take place between four equivalent but off center of the sodium sites shown in Fig. 7. Due to the chemical equivalence of these sites, identical ground state energies can be inferred, hence unit vector for $\vec{W}$ in [4] can be assumed. From this model, two different types of discrete site jump motions are considered. The first is that the jumps take place only between the nearest neighbors. The other is that the jumps occur between all four sites. These two motion models are shown in Fig. 7. In this dynamic system, the reference frame, (X_R, Y_R, Z_R), is chosen for convenience with Z_R being the motional axis which is parallel to the c axis of the crystal, and with X_R, and Y_R axes in the motional (a-b) plane.

A brief description of the calculation is given. The transient signal, G(t), related to a specific spatial orientation, (θ, ϕ) is first calculated according to [4]. In this calculation, the argument of the exponential is a nondiagonal matrix. The quantity G(t) is calculated following the so-called QR transformation[26] by diagonalizing the non-

Hermitian exponential argument. Simplification of the treatment can be achieved using the analytical expression, [4], associated with either a simple two site jump,[27] or an all site exchange.[28,29] For calculating the powder line shape governed by a specific type of dynamic motion, the above procedures are repeated for each random orientation (θ, ϕ). The final averaged transient decay is obtained by summing all individual transient signals associated with one specific orientation after multiplying by the probability, $\sin\theta\, d\theta\, d\phi$. The powder averaged spectra is then directly calculated by Fourier transforming the averaged transient decay. Reference 16 gives further details of different computational approach.

The dynamic spectra of a quadrupolar nucleus are dependent upon: (a) the geometry of the distinct sites involved; (b) the orientation of the e.f.g. tensor at each distinctive site with respective to the reference frame as characterized by $(\alpha_i, \beta_i, \gamma_i)_Q$; (c) the interaction parameters; the quadrupole coupling constant e^2qQ, the e.f.g. asymmetry η and the isotropic shift σ_0, and (d) the dynamic exchange frequency. In the presence of a nonnegligible shift anisotropy, the results will also be dependent upon the orientation of the shielding tensor to the reference frame, $(\alpha_i, \beta_i, \gamma_i)_{CS}$, the shift interaction parameters, δ, and shielding asymmetry η_{CS}.

In the following, the second order central transition under the model of a four site exchange with nearest neighbors is considered first. Calculations for four different e.f.g. tensor orientations under various exchange frequencies are shown. The parameters e^2qQ= 1.58 MHz, ν_0= 58.23 MHz and I=3/2 are chosen to be the common parameters.

In the first calculation, the dynamic NMR spectra calculated to second order in perturbation theory for an axially symmetric e.f.g. with orientation $(\alpha_1, \beta_1, \gamma_1)_Q$ = (-90., 90., 90.) is considered. This e.f.g. orientation in the four sites jump model is shown in case (a) of Fig. 8. The calculated spectra are shown in Fig. 9(a) for six jump frequencies. It is seen that in the slow jump regime, the spectra exhibit an axially symmetric central transition. As the jump frequency increases, the asymmetry remains as seen from the two peak feature that is characteristic of the axially symmetric e.f.g., but the effective quadrupole coupling constant as reflected by the splitting between the singularities has been scaled by 1/2. The same calculation repeated for the case, η=1.0 shows no change with jump frequency and exhibits a nonaxially symmetric transition. This behavior can be seen from Fig. 8(a) that under all motional frequencies in the X_R-Y_R plane, the effective e.f.g. component q_{xx} and q_{zz} remain unchanged for η=1.0 at this specific tensor orientation but is scaled by 1/2 for the case η=0.0 in the rapid motion regime. In both cases the asymmetry, η, still remains constant.

To demonstrate that this behavior is dependent upon the orientation of the e.f.g. tensor with respect the the molecular frame, the case of a nonaxially symmetric e.f.g. tensor with orientation $(\alpha_1, \beta_1, \gamma_1)_Q$ = (0., -45., -90.) is considered, and is shown as case (b) of Fig. 8. The calculated spectra of the second order perturbed central transition are shown in Fig. 9(b). In the low jump rate regime, the spectra show a typical static central transition spectrum, η=1.0. In the high jump regime, the resulting spectra do not resemble the static spectra with

any e.f.g. asymmetry.

In the third case, we consider again a nonaxially symmetric e.f.g. tensor, η=1, with the e.f.g. orientation coincident with the reference frame, R, in Fig. 8(c). The calculated powder spectra of the second order central transition under a four site jump model are shown in Fig. 9 (c). The change from a nonaxial symmetric-like spectrum to an axially symmetric-like spectrum in the high jump rate regime is again due to the fact that the components q_{xx} and q_{yy} components are averaged to the value of $(q_{xx}+q_{yy})/2$ in the rapid jump regime. In contrast to the first calculation performed, the effective quadrupole coupling constants, e^2qQ is not changed due to the motion. This is expected since the q_{zz} axis is parallel to the jump axis and will not be altered with varying jump frequency. Any change of the quadrupole coupling constant observed experimentally, therefore, must be due to the interaction between the lattice and is independent of the dynamic motion of the sodium nucleus.

Finally the effects of shift anisotropy are demonstrated in Fig. 9 (d). The parameters for the quadrupole interaction are the same as those in the previous case. The shift parameters are chosen to be δ = -16 ppm, and η_{cs}= 0.4. The orientation of the shielding tensor is $(\alpha_1, \beta_1, \gamma_1)_{cs}$ = (0., 0., 0.), coincident with the e.f.g. tensor. These spectrum (vide infra) most resemble the experimental variable temperature spectra. Due to the the relatively small contribution of 1.2 kHz shift anisotropy as compared with the ≃ 8 kHz second order quadrupole residual line width the spectra will be very little dependent upon the shift orientation, $(\alpha_1, \beta_1, \gamma_1)_{cs}$ in this calculation.

In the calculation, we use a 3.0 kHz wide Gaussian broadening function which is multiplied with the powder averaged transient decay before the 256 point Fourier transform. The powder average uses a 4.0 degree mesh in (θ, ϕ) angles with time increments equal $1/\Delta$ where Δ is the total spectral width (= 20 kHz) desired in the calculation.

From these calculations it is observed that: (a) the experimental spectra resemble most the fourth case, i.e., q_{zz} of the e.f.g. tensor being parallel to the jump axis; and (b) the upfield shoulder appearing in the high temperature region is not predicted by sodium nuclear motion.

With these results as hints to what might be happening with the sodium in $NaMo_4O_6$, an iterative calculation is performed using only the the downfield portion of the variable temperature spectrum, neglecting the upfield features for purposes of the zero order fit. To reduce the variables involved in the iteration, the parameters for the shift interaction are held constant. The orientations of the e.f.g. tensor and shielding tensor are identical to that shown in Fig. 8 (d) where the principal Z axis of the tensors are coincident with the motional Z axis. The three fitting parameters are η, the e.f.g. asymmetry; e^2qQ, the quadrupole coupling constant; and σ_0, the isotropic shift.

The results of the line shape simulation are now discussed. The fit for the dynamic motion of sodium at room temperature for two fields are shown in Fig. 10. Other then the upfield peak, the calculated downfield portions of the spectra are compare quite well with experiment. The major differences for the two dynamic models, i.e., a nearest neighbor and an all site exchange, appear in the low jump rate region and give

indistinguishable spectra when the jump rate becomes higher. To differentiate the type of motion, detailed studies should be performed in the low jump rate regime. This is not possible in the current case, due to the smoothing of the experimental spectra.

A plot of the log of the jump rate obtained from the dynamic NMR line shape analysis against inverse temperature is linear, as shown in Fig. 11. Assuming that the activation energy, E_a, is independent of temperature, $E_a$is determined to be 1.95 Kcal/mole from the slope.[30]

In the line shape analysis, the quadrupole coupling constant e^2qQ shows gradually increased from 1.12 MHz at 78 K to 1.6 MHz at 300 K while the asymmetry parameters maintains constant at $\eta = 0.95 \pm 0.1$ throughout the calculation. The experimentally observed change of the spectra from a nonaxially symmetric at low temperature to an axially symmetric-like spectra in the high temperature region is well accounted for by the calculation.

The strong temperature dependence of the QCC is typical of quadrupolar nuclei. In Fig. 12 the quadrupole coupling constant obtained through the fitting is plotted vs. temperature. Although the temperature dependence of the quadrupole coupling constants need not be linear, the data seem to be well divided into two linear regimes where straight lines are drawn through the points to show the differences. The temperature coefficients, $(\partial e^2qQ/\partial T)_p$, are found to be 1.5 kHz/K and 3.9kHz/K respectively above and below ≈140 K. As mentioned previously, this change is not related to dynamic motion, but rather to either the change of the equilibrium position of the sodium nucleus or to interaction with the lattice. The increase in QCC with increasing

temperature implies that as the temperature increases, the amplitude of the sodium motion becomes larger and larger, i.e.; the stationary sodium position moves further and further off center of the tetragonal channel, therefore experiencing a stronger e.f.g. with motion, even though the motion results in an averaging of the q_{xx} and q_{yy} components and produces a symmetric-like e.f.g.

The study of the temperature dependence of the QCC constants makes it possible to derive interesting information concerning properties (in particular, microscopic ones) of the crystals. Qualitatively, from the different temperature coefficients, $(\partial e^2qQ/\partial T)_p$, in the two temperature regions it can be readily inferred that the internal pressure at the sodium site differs above and below temperature 140 K. Although the actual value of the internal pressure is to be determined by combining with variable pressure studies, this conclusion already suggests that a phase transition may take place. A first order phase transition can be excluded since the change in crystal cohesive energy will be reflected in the sudden jump of the activation energy, E_a, and hence will show the jump discontinuity in the Eyring plot (Fig. 11). This behavior is not observed. The suggested phase transition also accounts for the appearance of the anomalous peak as discussed in next section.

STRUCTURAL INCOMMENSURATION

The simulation of the dynamic NMR line shape for systems exhibiting multisite jump exchange motion correlates well with the downfield features of the variable temperature NMR spectra taken at 92.32 and 58.23 MHz. The appearance of the upfield peak, however, can not be explained by the exchange motion models under any combination of interaction parameters and was neglected in the theoretical calculation of the dynamic NMR spectra. Several possible sources of this high field peak are now discussed.

The mutual orientation between CSA and e.f.g. tensors dictates the shape of the static central transition spectrum, particularly when the two interactions are of comparable "size".[2,3] Hence it seems reasonable to attribute the occurrence of the upfield peak to some unique orientation of the two interaction tensors. After examining the singularities at the highest field for two oriented interaction tensors as a function of the magnetic field, it is found that the upfield singularity is much too large to be accounted for by differing orientations of the shielding and e.f.g. tensors under any combination of the interaction parameters. The approximate inverse magnetic field dependence of the singularities and the measurements from the MAS experiments also indicate that the effect of the chemical shifts upon the spectra are relatively small. Therefore relating the high field peak to the unique orientation between the shift and the e.f.g. tensor is not plausible.

The satellite transitions, (3/2, 1/2) and (-1/2, -3/2), should be symmetric about the center of mass according to the first order

perturbation theory. When the motional frequency becomes large compared to the splitting between the two satellite singularities, a third peak emerging around the center of mass of the satellite transitions is predicted.[17] This dynamic phenomenon is similar to that observed for a shielding tensor and a Pake doublet spectrum where only the first order effect is observed.[16,31] The increasing sharpness of the upfield peaks as the temperature increases seems to support this behavior. However, it may be shown that this peak will appear at the downfield side of the central transition instead of at the upfield side. From data listed in Table I, for a spin I=3/2 nucleus at ν_0 =58.23 MHz, the second order quadrupolar interaction shifts the central transition =19 ppm upfield from the true isotropic value. Hence the center of mass of the satellite transition should be shifted =38 ppm downfield from the true isotropic chemical shift. This is to say that the center of mass for the satellite transition should appear = 57 ppm downfield from the center of mass of the central transition. This conclusion is opposite to the observed behavior of the upfield peak in so far as the position and the sign are concerned. For a quadrupolar nucleus with $e^2qQ \simeq 1.58$ MHz and $\eta \simeq 0$, the satellite splitting will be = 400 kHz. From the dynamic line shape simulation, the motional frequency at room temperature is about 70 kHz. This value is too small to yield extra peaks associated with the satellite transitions.

The off-diagonal elements in [6] have been neglected in calculating the characteristic frequencies as shown in [9]. A similar truncation has also been performed in evaluating the MAS powder spectra.[10] Incorporating the nonsecular terms shows somewhat different results[9] but

does not predict any features of the line shape. To attribute the upfield feature to the nonsecular term in [6] is, therefore, not plausible. Considering particularly the gradual coalescence of the upfield peak with the major portion of the spectra as the quadrupole coupling constant increases with increasing temperature, this possibility can be excluded.

To attribute the upfield resonance to the presence of an impurity sodium phase is not in accord with the X-ray powder diffraction of the sample used in the NMR experiments. Identical spectra are obtained when repeating the variable temperature measurements using a newly prepared samples. The inverse field dependence of this peak in frequency units also excludes the possibility that this peak is due to either extra sodium phase or the copper background from the probe body.

From the above discussion, it is concluded that:

(1). The upfield singularity does not originate from noncoincident orientations of the shielding and e.f.g. interaction tensors.

(2). The upfield singularity is not part of the first satellite transition of sodium nucleus under dynamic motion.

(3). The off-diagonal elements neglected in the magnus expansion, [6], do not produce the upfield features.

(4). The upfield peak is not due to the impurity sodium phase, or from copper resonance of the probe background.

There is considerable evidence that the line shape of the wide-line NMR spectra of quadrupolar nuclei are subject to a random variation of the local environment of a particular nuclear site due to crystal defects and internal strains within the crystal.[4,32,33] This local

variation results in a continuous distribution of the Hamiltonians. The absorption spectrum is now not only an ensemble average of the random orientation of the crystallites with respect to the Zeeman axis, but also an average of the ensemble of the translation parameters where the interaction parameters are characterized by some distribution function. Hence the powder spectra are strongly influenced by the random distribution of QCC, the asymmetry parameter of the e.f.g. tensor, and the CSA tensor. The calculation accounting for these effects relies upon: (a) a proper and reasonable choice of the distribution function, (b) the assumption that the random orientation of microcrystallites and the parameters distribution through lattice site are independent. Following this discussion, a calculation is performed using the formulae proposed by France.[33] We consider only the e.f.g. distribution which is represented by a Gaussian function, i.e., a completely random distribution. Results show that this distribution only broadens and smooths the spectrum but does not, under any circumstances, produce "anomalous" features at the upfield side of the central transition.

This result gives rise to another possibility that the distribution of interaction parameters may have several local maxima, or represented by a quasi-continuous function. This type of frequency distribution has been recently found in the incommensurate insulator such as $NaNO_2$[34] Rb_2ZnCl_4,[35-37] and Rb_2ZnBr_4[38,39] as well as in the incommensurate charge density wave (ICDW) system associated with low dimensional conductivity such as VSe_2,[40] $NbSe_3$,[41,42] 2H-$NbSe_2$[43], and $Rb_{.3}MoO_3$.[44] For both metals and insulators, the formation of structural incommensuration is characterized by a lattice distortion with a periodicity not necessarily

being a rational multiple of the fundamental lattice periodicity. The absence of anomalies in the resistivity measurement[45] at the temperature where the anomalous NMR peak emerges suggests that the phase transition is not electronic in nature. The transition is therefore attributed to the mass density incommensuration. To verify this idea, the NMR spectra governed by structural incommensuration are calculated and compared with the experiment.

An incommensurate system in either metals or insulators manifests itself in magnetic resonance by the fact that the resonance frequency of a given nucleus depends upon the nuclear displacement of the nuclei relative to each other and the details of the electronic charge density. The real displacement of the nuclei can be described as:

$$u = A\cos\phi(x) \qquad [13]$$

Using Landau theory,[46] the resonance frequency can be expanded in the Taylor series of the displacement (the order parameter) as

$$\begin{aligned}\nu &= \nu_0 + a_1 A\cos\phi(x) + \frac{1}{2} a_2 A^2\cos^2\phi(x) + \ldots \\ &= \nu_0 + \nu_1\cos\phi(x) + \nu_2\cos\phi(x) + \ldots \end{aligned} \qquad [14]$$

A is the amplitude of the displacement and depends upon temperature as $A = (1-T/T_i)^{\beta}$. β is the critical exponent. The coefficients a_1, a_2,... depend upon the crystal orientation with respect to the magnetic field.

To calculate the spectrum, the lattice dependent phase factor, $\phi(x)$, need be determined. In the commensurate structure, the phase $\phi(x)$ is a constant for all unit cells. In the incommensurate structure, the phase of the incommensurate wave can be approximated at two limit: (a) the

"plane wave" limit where the phase $\phi(x)$ is linearly dependent upon the displacement; and (b) the "soliton" limit where phase is governed by the sine-Gorden equation describing the formation of a multi-soliton lattice which shows commensurate domains separated by "soliton-like" domain walls. In the current study, only polycrystalline samples are available, and the "soliton" effect can not be observed. Therefore, it is reasonable to use the plane wave approximation and simplifies the calculation.

Blinc[35,37] et al. have shown that when only ν_1 is present, the two edge singularities appear at $\nu-\nu_0= \pm\nu_1$, and when only the ν_2 term is present, the edge singularities appear at $\nu-\nu_0 = 0$ and ν_2. Since value of $\cos\phi(x)$ ranges between -1 and 1, the frequency distribution will be symmetric for odd order terms (ν_1, ν_3 etc.) and will be distributed only on one side of the frequency ν_0 when even order terms (ν_2, ν_4 etc.) are considered. In general, a combination of these terms are required. The calculation associated with a single crystal orientation are shown in Fig. 13, for various values of ν_1 and ν_2, ν_3, and ν_4.

To simplify the calculation of the polycrystalline spectrum associated with an incommensurate structure, we assume that ν_i are independent of crystal orientation. This implies that the resulting spectrum is a "convolution" of the frequency distribution associated with single crystal orientations with the commensurate polycrystalline NMR spectra of the corresponding temperature. The NMR spectrum in the commensurate phase has been discussed previously. As observed from the two "edge singularity" features of the calculation shown in Fig. 13, the extra upfield peak appearing in the experimental spectrum can also

be predicted as reflected by the presence of the singularity associated with the incommensurate structure.

As observed from the experimental spectra, the position of the downfield components remains almost constant with temperature, while the spacing between the two singularities becomes smaller at high temperature. This implies that the even terms (ν_2 and ν_4) in [14] are responsible for the observed behavior of the spectrum. From the unequal intensities of the upfield and downfield components in the experimental spectra, it is further inferred that the frequency distribution is mainly composed of the fourth order term ν_4.

Based upon these, the NMR line shapes are calculated for various temperatures. The room temperature spectra taken at 58.23 and 93.32 MHz as shown in Fig. 14. The parameters used in this calculation are ν_4= 7.5 kHz, and 5.0 kHz at the two fields respectively. As the temperature increases, the coefficient ν_4 decreases, and the spacing between the two edge singularities has been reduced. This, therefore, also reduces the splitting of the upfield peak from the central portion of the spectrum. Knowing that the upfield peak position is mainly determined by the ν_4 term which follows the relation, $(1-T/T_i)^{4\beta}$, a fit is performed for $\nu_4(T)$ obtained as shown in the inset of Fig 14. From this fit, another transition temperature T_i is found to close to 520 K and the exponent, β= 0.15.

The incommensurate-commensurate transition temperature T_c is harder to estimate from the line shape analysis due to the difficulties in observing the commensurate line in the polycrystalline sample. However, from the previous dynamic line shape measurements, where the apparent value of QCC shows a jump discontinuity at 140 K, the transition

temperature is estimated to be $T_c \simeq 140$ K.

Although the above calculation and discussion shows that the appearance of the upfield peak is related to an incommensurate structure, the exact incommensurate structure and the reason why the fourth order or even higher even order term dominates the frequency distribution still remains unclear. Two possible models are proposed, however, to describe the incommensurate structure and the mass density wave of this compound.

Due to the off center occupation of the sodium nucleus, the electric dipole moment of each unit lattice is not zero with a net electric field perpendicular to the channel. In the temperature regime above 520 K, the sodium nucleus exhibits rapid anisotropic motion and gives an averaged position at the center of the cage where the sample becomes paraelectric and the effect of incommensuration is absent. In the low temperature regime (< 140 K) the sodium nucleus, off center in the channel, forms a mass density wave of integer (with four being most probable) multiple periodicity of that of the fundamental lattice and the compound becomes ferroelectric, therefore, also commensurate with the lattice. Between these two temperatures, the crystal symmetry gradually changes from a space group symmetry with possible four fold or two fold skew axis 4_1, or 4_2 at low temperature to a space group symmetry of P4/mbm at high temperature. The electric dipole forms a modulation wave that becomes incommensurate with the fundamental lattice periodicity. As a result the quadrupole interaction, strongly dependent upon the electric field gradient, exhibits a quasi-continuous distribution due to this incommensuration. The decreasing amplitude of

the incommensurate modulation wave (equation [14]) with increasing temperature is reflected in the gradual coalescence of the upfield shoulder with the major component of the spectrum. When the transition temperature, 520 K is reached, the structure becomes commensurate and the upfield shoulder disappears. This phenomenon is similar to that observed in $NaNo_2$ and is explained by Heine.[47]

Another possible source of the incommensuration may be associated with the twisting of the channel where the "phase" of the channel compound changes gradually or exhibit a sudden jump and twist. This forms a soliton-like mass density which again is incommensurate with the fundamental lattice periodicity. Due to this structure, each and every sodium nuclei along the channel experiences a different e.f.g. This quasi-continuous distribution therefore gives rise to the upfield peak observed in the incommensurate regime.

CONCLUSION

From the dynamic NMR line shape studies, it is found that the anomalous X-ray thermal ellipsoid observed for sodium in $NaMo_4O_6$ is not due to isotropic thermal motion but due to anisotropic exchange motion between four equivalent sites, where the sodium resides off center of the tetragonal oxygen cluster. This result has the implication that the sodium atom binds more strongly with four oxygen atoms with a shorter bond distance than being equally shared with eight oxygens of a longer internuclear distance. From the dynamic line shape studies of the second order central transition, an activation energy of discrete site jump motion is calculated to be 1.95 Kcal/mole with a temperature independent E_a. The temperature dependent QCC determined from the calculation shows two linear dependent regions separated by 140 K with the coefficients equal 1.5 kHz/K and 3.9 kHz/K respectively. The difference in the temperature coefficients of the quadrupole coupling constant implies that a phase transition may take place.

The anomalous upfield peak that cannot be accounted for by the dynamic motion model is found to closely related to the structural incommensuration of this channel compound. The quasicontinuous e.f.g. distribution associated with this phase transition predicts both the appearance of the upfield shoulder and the gradual shift of the anomalous peak toward the major portion of the spectra. The jump discontinuity appearing in the quadrupole coupling constant and in T_1 further supports the incommensuration structure with the I-C transition temperature estimated to be around 140 K. Several incommensuration structure models have been proposed.

ACKNOWLEDGEMENTS

D. R. Torgesen is acknowledged for extensive help in obtaining the variable temperature spectra at 92.32 MHz. Also thanks to J. Ross, and V. Rutar for helpful discussions of the soliton behavior in both the incommensurate mass density and charge density wave. Discussions with Dr. Richard Barnes concerning the quadrupolar interaction are gratefully acknowledged. Dr. Russ Walker provides numerous discussions and help in the variable temperature experiment.

This research was supported by the U.S. Department of Energy, Office of Basic Energy Sciences, Chemical Science Division, under contract W-7405-Eng. 82.

APPENDIX

The irreducible components expressed by the Wigner rotation is

$$R^2_m(\alpha_i,\beta_i,\gamma_i,\Theta,\phi)=\sum_{m'} D^{(2)}_{m',m}(0,\Theta,\phi)\sum_{m''} D^{(2)}_{m'',m'}(\alpha_i,\beta_i,\gamma_i)\rho^{\lambda}_{2m''} \qquad [A\text{-}1]$$

Inserting the appropriate rotational matrix and the principal elements shown in [11], the components of the second rank tensor are found:

(1). $R^2_0(\alpha,\beta,\gamma,\Theta,\phi)$

$$\begin{aligned}
&= \rho^2_2 \sqrt{\tfrac{3}{2}} \{ P_2(\cos\Theta)\sin^2\beta\cos2\alpha && m'=0\\
&\quad +2\cos\Theta\sin\Theta(\cos\beta\sin\beta\cos2\alpha\cos\Omega-\sin\beta\sin2\alpha\sin\Omega) && m'=\pm1\\
&\quad +\sin^2\Theta\left(\frac{1+\cos^2\beta}{2}\cos2\alpha\cos2\Omega-\sin\beta\sin2\alpha\sin2\Omega\right)\} && m'=\pm2\\
&+ \rho^2_0\{ P_2(\cos\Theta)\cdot P_2(\cos\beta) - 3\cos\Theta\sin\Theta\cos\beta\sin\beta\cos\Omega && m'=0,\pm1\\
&\quad + \tfrac{3}{4}\cos^2\Theta\sin^2\beta\cos2\Omega \} && m'=\pm2
\end{aligned}$$

(2). $R^2_1(\alpha,\beta,\gamma,\Theta,\phi)$

$$\begin{aligned}
&= \rho^2_2 \{ \tfrac{3}{2}\cos\Theta\sin\Theta\sin^2\beta\cos2\alpha && m'=0\\
&\quad +2\left(\cos^2\Theta-\tfrac{1}{2}\right)(\cos\beta\sin\beta\cos2\alpha\cos\Omega-\sin\beta\sin2\alpha\sin\Omega)\\
&\quad -i\cos\Theta(\cos\beta\sin\beta\cos2\alpha\sin\Omega+\sin\beta\sin2\alpha\cos\Omega) && m'=\pm1\\
&\quad +\cos\Theta\sin\Theta\left(\frac{1+\cos^2\beta}{2}\cos2\alpha\cos2\Omega-\sin\beta\sin2\alpha\sin2\Omega\right)\}\\
&\quad -i\sin\Theta\left(\frac{1+\cos^2\beta}{2}\cos2\alpha\cos2\Omega-\sin\beta\sin2\alpha\sin2\Omega\right)\} && m'=\pm2
\end{aligned}$$

$$+\rho_0^2\{\sqrt{\frac{3}{2}}\cos\theta\sin\theta\cdot P_2(\cos\beta) \qquad m'=0$$

$$+\sqrt{\frac{3}{2}}\cos\beta\sin\beta\,[\cos 2\theta\cos\Omega+i\cos\theta\sin\Omega] \qquad m'=\pm 1$$

$$+\sqrt{\frac{3}{8}}\sin^2\beta\,[\cos\theta\sin\theta\cos 2\Omega-i\sin\theta\sin 2\Omega]\ \} \qquad m'=\pm 2$$

(3). $R_2^2(\alpha,\beta,\gamma,\theta,\phi)$

$$=\rho_2^2\ \{\ \frac{3}{4}\sin^2\theta\sin^2\beta\cos 2\alpha \qquad m'=0$$

$$-\cos\theta\sin\theta(\cos\beta\sin\beta\cos 2\alpha\cos\Omega-\sin\beta\sin 2\alpha\sin\Omega)$$

$$i\sin\theta(\cos\beta\sin\beta\cos 2\alpha\sin\Omega-\sin\beta\sin 2\alpha\cos\Omega) \qquad m'=\pm 1$$

$$\frac{1+\cos^2\theta}{4}\left(\frac{1+\cos^2\beta}{2}\cos 2\alpha\cos 2\Omega-\sin\beta\sin 2\alpha\sin 2\Omega\right)$$

$$-\frac{i}{2}\cos\theta\left(\frac{1+\cos^2\beta}{2}\cos 2\alpha\sin 2\Omega+\sin\beta\sin 2\alpha\cos 2\Omega\right)\} \qquad m'=\pm 2$$

$$+\rho_0^2\ \{\ \sqrt{\frac{3}{8}}\sin^2\theta\cdot P_2(\cos\beta) \qquad m'=0$$

$$+\sqrt{\frac{3}{2}}\cos\beta\sin\beta(\cos\theta\sin\theta\cos\Omega-i\sin\theta\sin\Omega) \qquad m'=\pm 1$$

$$+\sqrt{\frac{3}{8}}\sin^2\beta\left(\frac{1+\cos^2\theta}{2}\cos 2\Omega-i\cos\theta\sin 2\Omega\right)\ \} \qquad m'=\pm 2$$

Relations $R_{-2}^2 = R_2^{2*}$ and $R_{-1}^2 = -R_1^{2*}$ give expressions of the other two components. The sign, * represents the complex conjugate of the quantity. In the above, $\Omega = \phi + \gamma$. Note that m" equals 0, 2 only. The components of the individual terms of the first summation in [A-1] is denoted at the right side of each terms. The Euler angles have been defined in Fig. 2.

Table I

List of center of mass σ_{cm}, second order quadrupole shift σ_{qs} and the chemical shift σ_{cs}

ν(MHz)	σ_{cm}(ppm)[a]	σ_{qs}(ppm)	σ_{cs}(ppm)
14.82	220.0	284.9[b]	-64.9
58.23	-13.5	18.9[b]	-32.4
92.30	-25.5	7.5[b]	-33.0
58.23(MAS)	-20.0	16.3	-36.3[c]

[a] Center of mass was obtained by zeroing the first moment.

[b] Calculated from equation [12] using e^2qQ =1.58 MHz, η=0.

[c] Calculated from the average of the rotation side band.[24]

REFERENCES

1. M. H. Cohen, and F. Reif, in Solid State Physics, Vol. V, F. Seitz and D. Turnbull, eds. (Academic Press, New York, 1957).

2. J. F. Bauger, P. C. Taylor, T. Oja, and P. J. Bray, J. Chem. Phys. 50, 4914 (1969), and references therein.

3. D. R. Torgeson, R. G. Barnes, and R. B. Creel, J. Chem. Phys. 56, (1972).

4. P. C. Taylor, and P. J. Bray, J. Magn. Reson. 2, 305 (1970).

5. P. C. Taylor, J. F. Baugher, and H. M. Kriz, Chem. Rev. 75, 202 (1975).

6. D. R. Torgeson, and R. G. Barnes, J. Chem. Phys. 62, 3968 (1975).

7. G. E. Jellison, Jr., S. A. Feller, and P. J. Bray, J. Magn. Reson. 27, 121 (1977).

8. E. D. Meerwall, Comp. Phys. Commun. 13, 107 (1977).

9. M. M. Maricq, and J. S. Waugh, J. Chem. Phys. 70, 3300 (1978).

10. E. Kundla, A. Samoson, and E. Lippmaa, Chem. Phys. Lett. 15, 229 (1981).

11. A. Samoson, E. Kundla, and E. Lippmaa, J. Magn. Reson. 49, 350 (1982).

12. S. Ganapathy, S. Schramm, and E. Oldfield, J. Chem. Phys. 77, 4360 (1982).

13. S. Schramm, and E. Oldfield, J. Am. Chem. Soc. 106, 2502 (1982).

14. C. C. Torardi, R. E. McCarley, J. Am. Chem. Soc. 101, 3963 (1979).

15. R. E. McCarley, T. R. Ryan, and C. C. Torardi, ACS Symposium Series, 15, 43 (1981).

16. M. Mehring, Principles of High Resolution NMR in Solids, second Ed. (Springer-Verlag, Heidelberg, 1983).

17. C. M. Gall, J. A. Diverdi, and S. J. Opella, J. Am. Chem. Soc. 103, 5039 (1981).

18. B. C. Gerstein, and C. R. Dybowski, Chapter 4, in Transient Techniques in NMR of Solids; an Introduction to the Theory and Practice (Academic Press, New York, 1985).

19. A. Abragam, Chapter 4, in The Principles of Nuclear Magnetism (Oxford University Press, London, 1961).

20. U. Haeberlen, Chapter 2, in High Resolution NMR in Solids, Selective Averaging, J. S. Waugh eds. (Academic Press, New York, 1976).

21. A. R. Edmonds, Angular Momentum in Quantum Mechanics (Princeton University Press, Princeton, 1974).

22. T. T. P. Cheung, L. E. Worthington, P. D. Murphy, and B. C. Gerstein, J. Magn. Reson. 41, 158 (1980).

23. D. Fenzke, D. Freude, T. Frohlich, and J. Haase, Chem. Phys. Lett. 111, 171 (1984).

24. A. Samoson, Chem. Phys. Lett. 119, 29 (1985).

25. D. Freude, J. Hass, J. Kleinowski, T. A. Carpenter, and G. Ronikier, Chem. Phys. Lett. 119, 365 (1985).

26. R. G. Gorden, and R. P. McGinnis, J. Chem. Phys. 49, 2455 (1968).

27. P. W. Anderson, J. Phys. Soc. Japan, 9, 316 (1954).

28. D. E. Wemmer, D. J. Ruben, and A. Pines, J. Am. Chem. Soc. 103, 28 (1981).

29. D. E. Wemmer, Ph.D. thesis, University of California, Berkeley (1979).

30. L. M. Jackman, and F. A. Cotton, eds. Dynamic Nuclear Magnetic Resonance Spectroscopy (John Wiley & Sons, New York, 1978).

31. T. T. P. Cheung, and B. C. Gerstein, IS-4814, UC-13 (1982).

32. B. R. McCart, and R. G. Barnes, J. Chem. Phys. 48, 127 (1968).

33. P. W. France, J. Magn. Reson. 40, 311 (1980).

34. I. P. Aleksandrova, R. Blinc, B. Topic, S. Zumer, and A. Rigamonti, Phys. Status Solidi 61, 95 (1980).

35. R. Blinc, V. Rutar, B. Topič, F. Milia, and Th. Raising, Phys. Rev. B. 33, 1721 (1986).

36. R. Blinc, V. Rutar, B. Topič, S. Zumer, J. Seliger, I. P. Aleksandrova, and F. Milia, J. Phys. C. Solid State Phys. 19, 3421 (1986).

37. R. Blinc, V. Rutar, and F. Milia, Phys. Rev. 23, 4577 (1981).

38. R. Blinc, p 23 in Proc. XXIInd Ampre Congress, K. A. Muller, R. Kind, and J. Roos eds. (ETH, Zurich, 1984).

39. R. Blinc, V. Rutar, B. Topič, F. Milia, and P. Aleksandrova, Phys. Rev. Lett. 46, 1406 (1981).

40. A. V. Skripov, A. P. Stepanov, A. D. Shevchenko, and Z. D. Kovalyuk, Phys. Status Solidi 119, 401 (1983).

41. N. P. Ong, Phys. Rev. B, 17, 3243 (1978).

42. H. J. Ross, Z. Wang, and C. P. Slichter, Phys. Rev. Lett. 56, 663 (1986).

43. C. Berthier, D, Jerome, and, P. Molinie, J. Phys. C: Solid State Phys. 11, 797 (1978).

44. P. Butaud, P. Segransan, C. Berthier, J. Dumas, and C. Schlenker, Phys. Rev. Lett, 55, 253 (1985).

45. C. C. Torardi, Ph.D. thesis, Iowa State University, Ames Iowa (1981).

46. R. Blinc, and A. P. Levanyuk eds. Modern Problems in Condensed Matter Sciences, Vol. 14.1 Incommensurate Phases in Dielectrics, Fundamentals (North Holland, Amsterdam, 1986).

47. V. Heine, and J. C. McConnell, Phys. Rev. Lett. 1092, 46 (1981).

Figure 1. Three dimensional view of the $NaMo_4O_6$ crystallographic structure as seen along the c-axis. The thermal ellipsoid in the a-b basal plane is abnormally large.

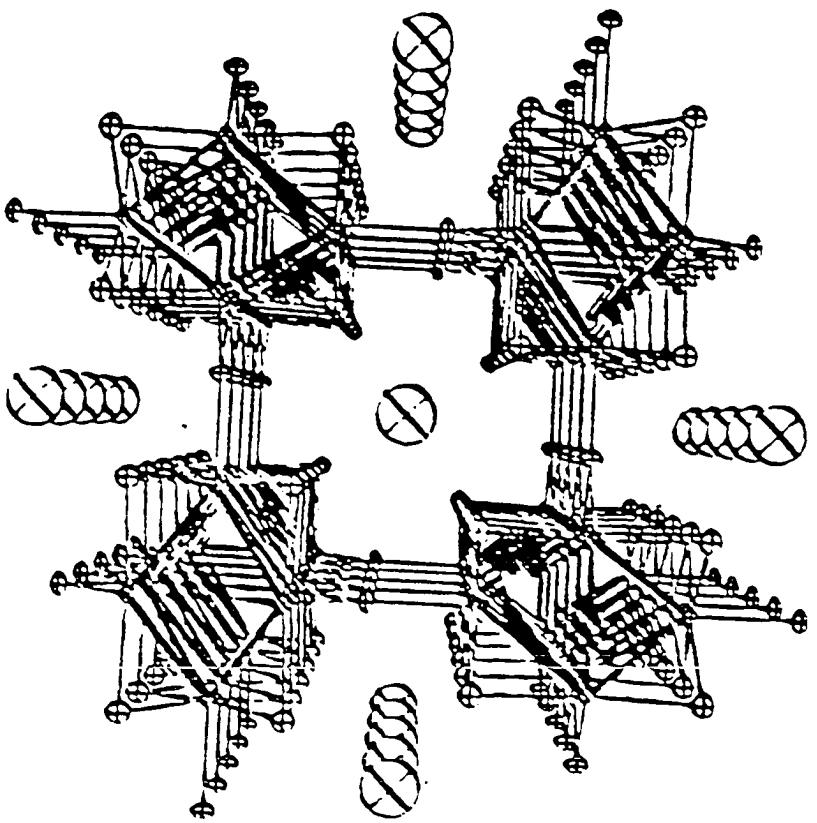

Figure 2. Relative orientation and the transformation in the presence of two interactions for one of the discrete sites in the dynamic system. Interactions A and B are oriented with fixed angles $(\alpha, \beta, \gamma)_A$ and $(\alpha, \beta, \gamma)_B$ with respect to the reference frame. This maintains the mutual orientations between the interactions.

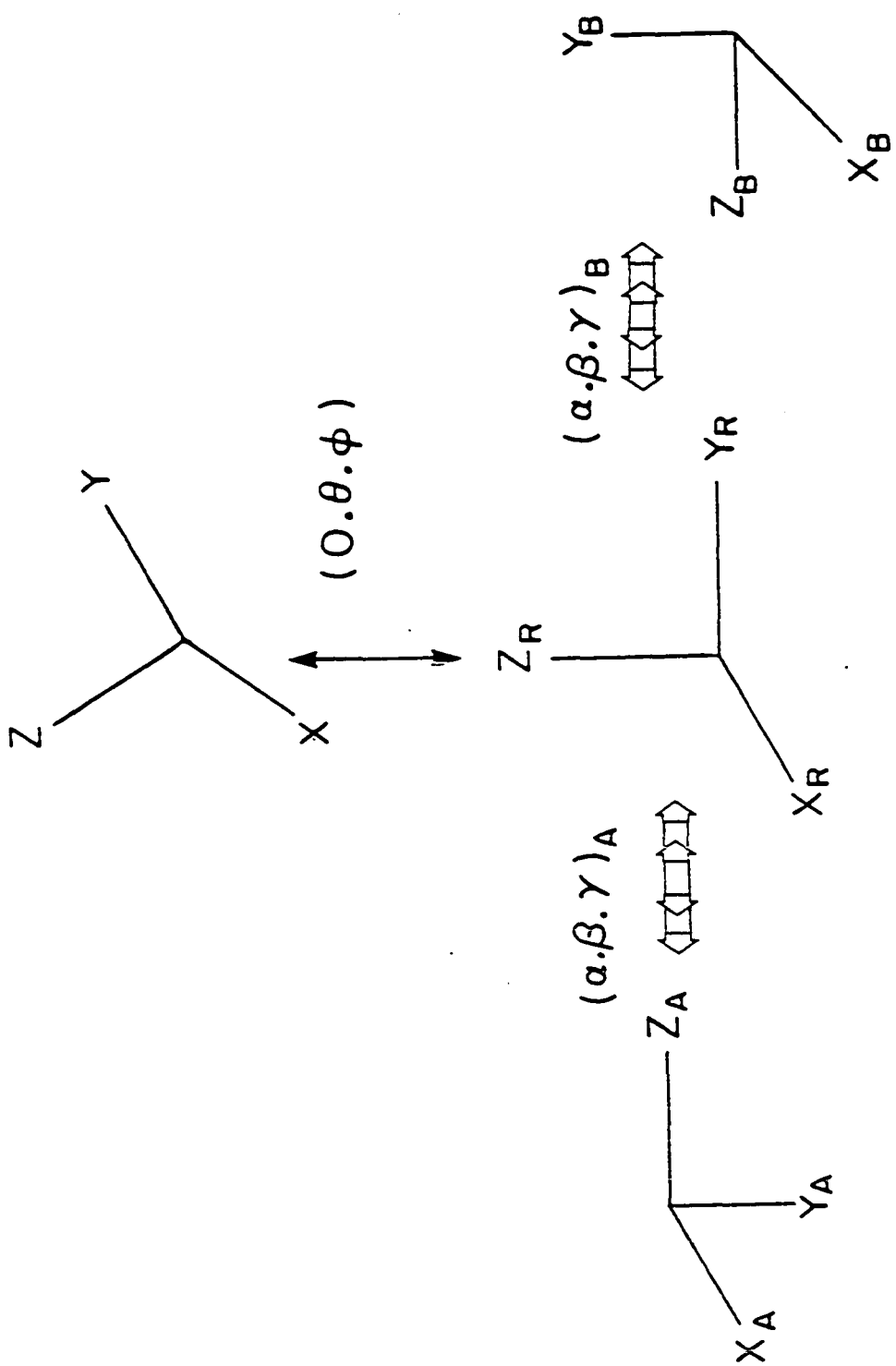
Y
Z
X
(O.θ.φ)
Z_R
Y_R
X_R
(α.β.γ)_B
Y_B
Z_B
X_B
(α.β.γ)_A
Z_A
Y_A
X_A

Figure 3. ^{23}Na magic-angle spinning spectrum at ν_0 = 58.23 MHz is shown together with the static powder spectrum. The spinning rate varies from ν_r = 4.2 kHz to 5.4 kHz to differentiate the side bands. In the inset, fitting of the center-band of the quadrupolar MAS spectra is superimposed with experiment. Parameters in the calculation are: η=0.2, e^2qQ/h= 1.58 MHz and σ_{CS}= -36.3 ppm.

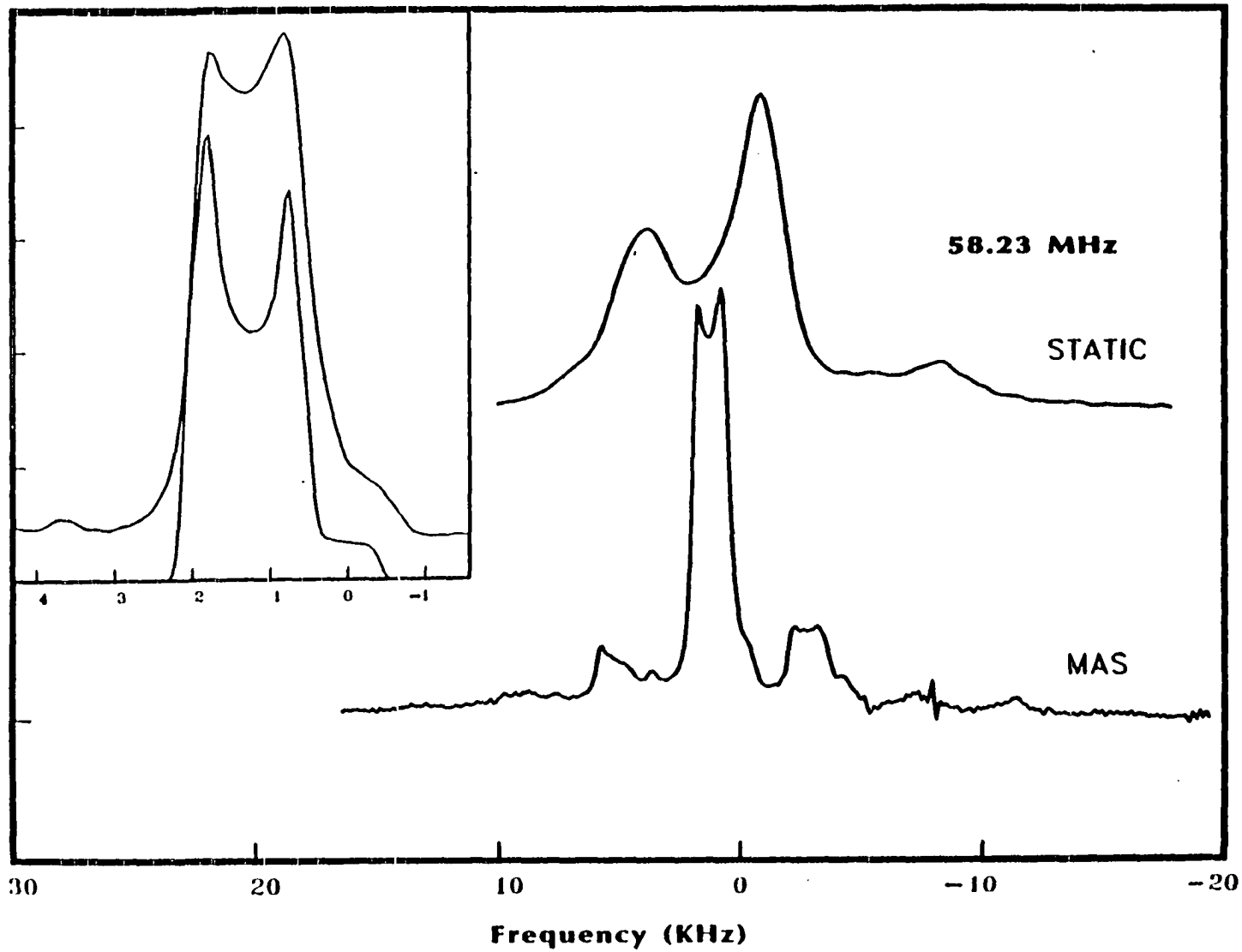
58.23 MHz
STATIC
MAS
4
3
2
1
0
−1
30
20
10
0
−10
−20
Frequency (KHz)

Figure 4. Room temperature ^{23}Na NMR spectra taken at 92.32, 58,23, and 14.82 MHz respectively. The central transition spectra is governed by both the second order quadrupolar interaction and the shift interaction. The inverse field dependence shown in the line width and the critical frequencies in frequency units are characteristic of those transitions governed by second order perturbation, implying the contribution from shift anisotropy is relatively small.

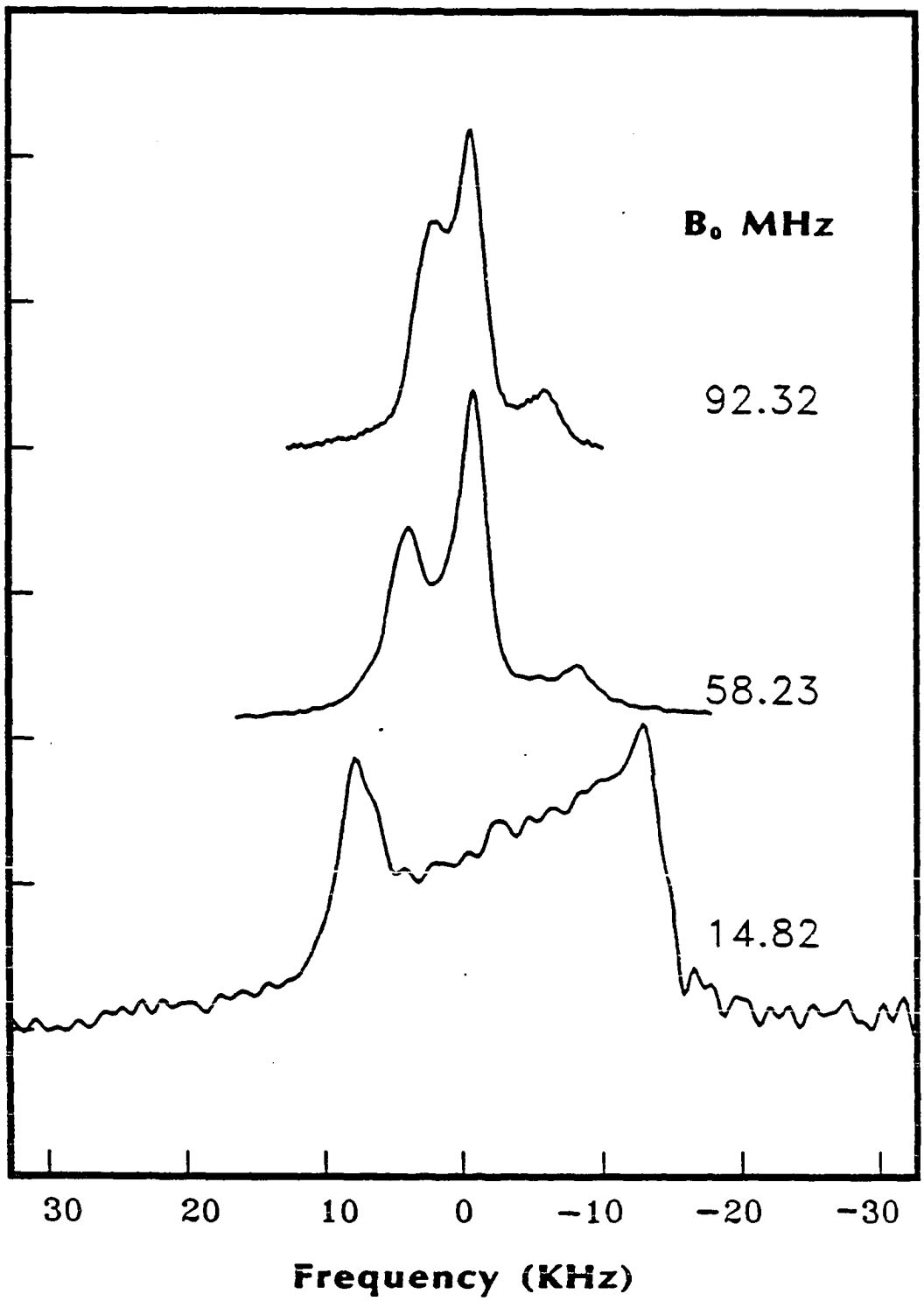
B_0 MHz
92.32
58.23
14.82
30
20
10
0
−10
−20
−30
Frequency (KHz)

Figure 5. The variable temperature ^{23}Na NMR spectra from 80K to 298K at ν_0= 58.23 MHz. Notice the gradual change of the asymmetry of the central transition from η = 1.0 at low temperature to η = 0.0 at room temperature. The upfield shoulder gradually coalesces with the major component of the spectra. The upfield shoulder is associated with the appearance of structural incommensuration.

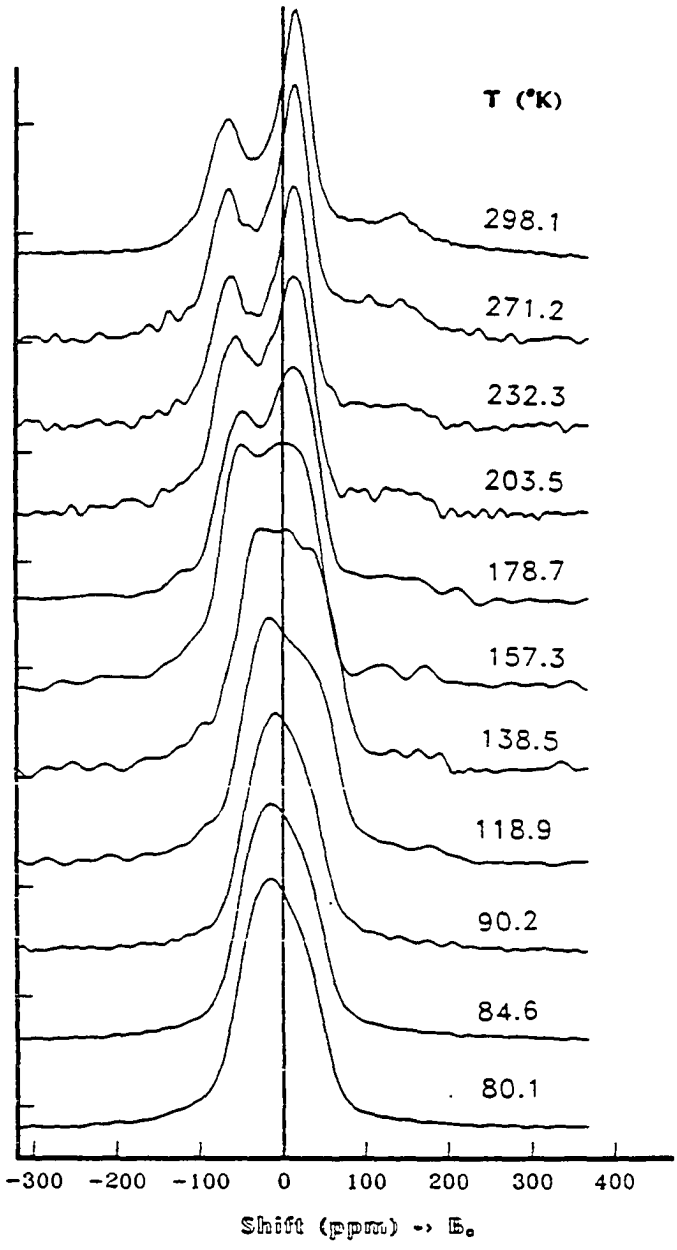
T (°K)
298.1
271.2
232.3
203.5
178.7
157.3
138.5
118.9
90.2
84.6
80.1
-300 -200 -100 0 100 200 300 400
Shift (ppm) ↔ B_o

Figure 6. Variable temperature ^{23}Na NMR spectra at ν_0= 92.32 MHz are shown. Note the gradual downfield shift of the upfield shoulder as the temperature increases to 403 K. The major features of the variable temperature spectra are similar to that of 58.23 MHz but scaled by a factor of roughly 1.58.

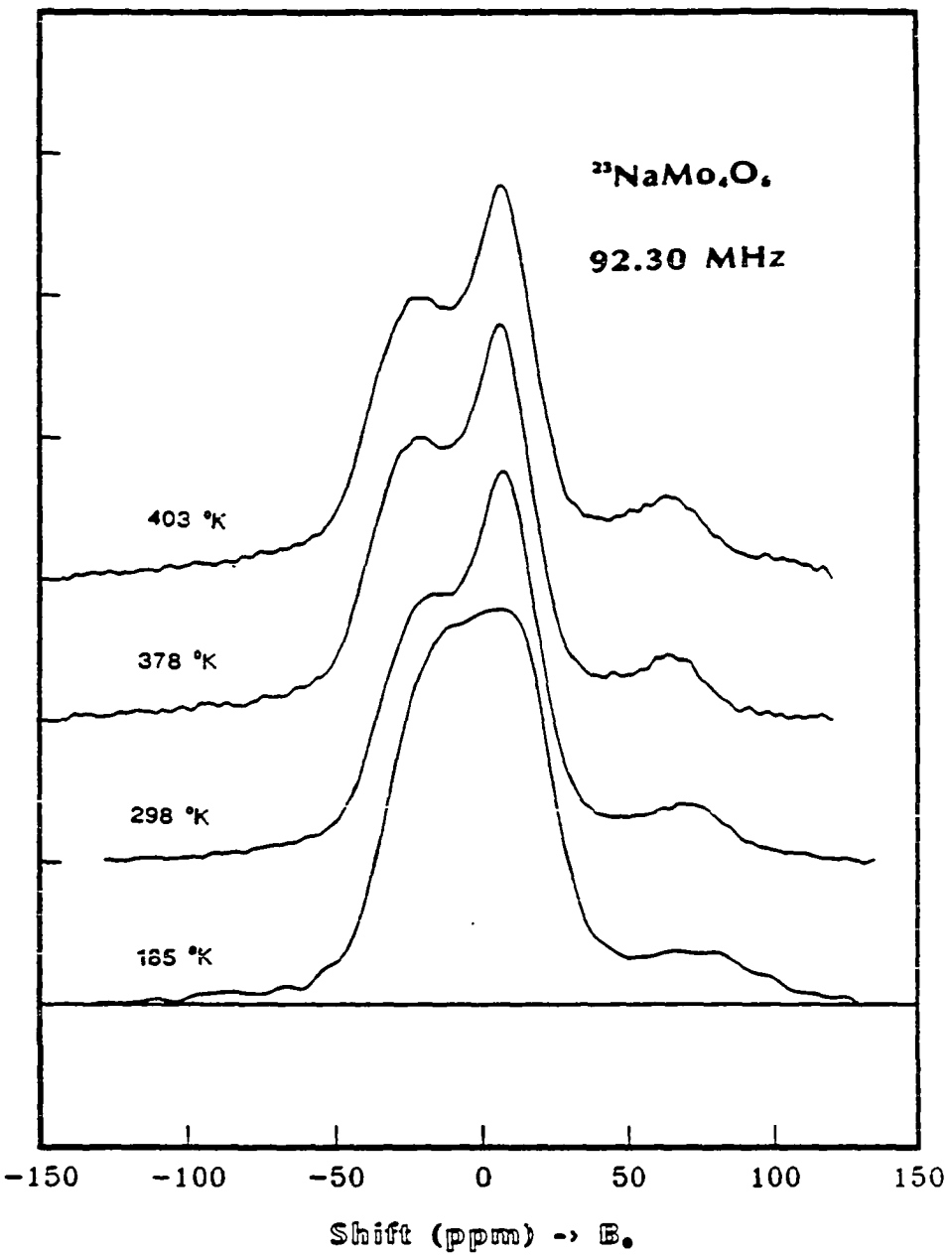
$^{23}NaMo_4O_6$
92.30 MHz
403 °K
378 °K
298 °K
185 °K
−150
−100
−50
0
50
100
150
Shift (ppm) → B_o

Figure 7. The possible fourfold jump model and the relative orientations of the e.f.g. tensor at each distinct site, viewed in the c axis direction of the tetragonal structure, i.e., along the channel direction.

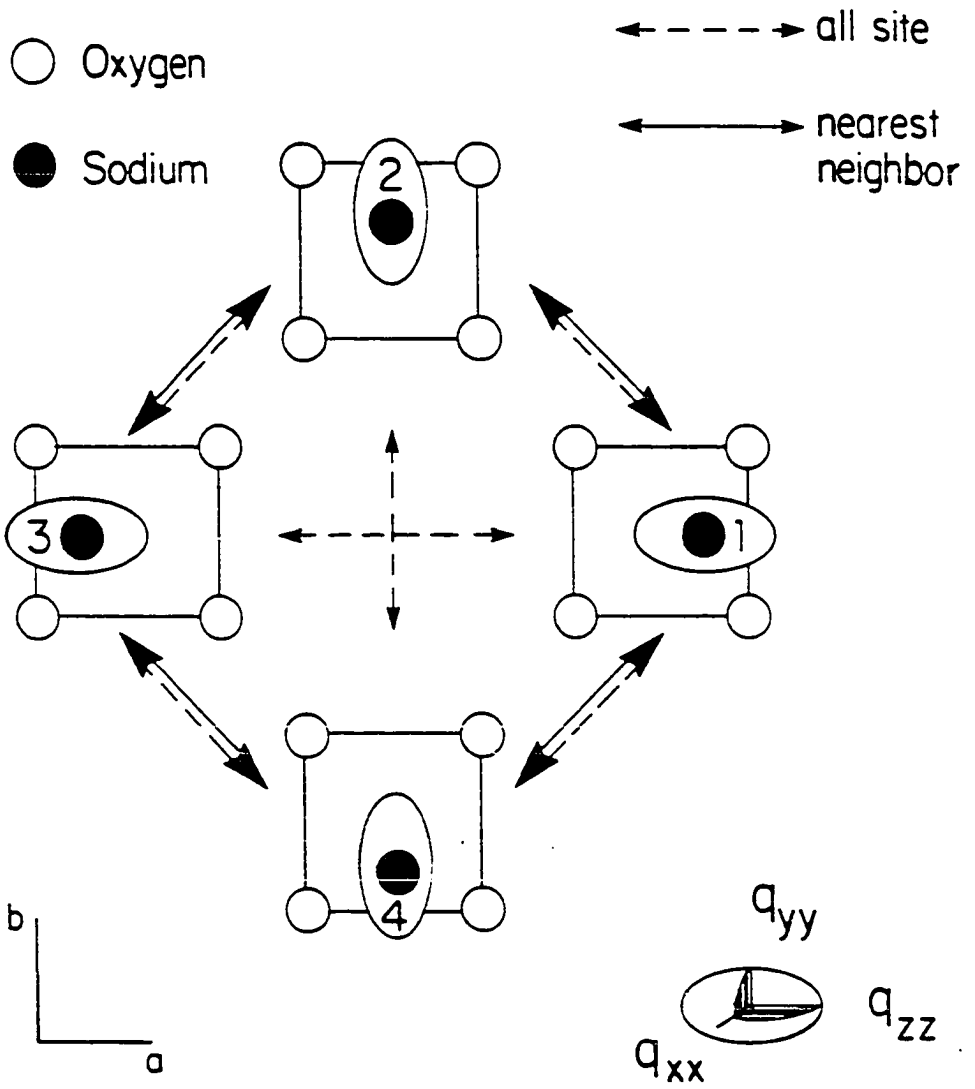
Oxygen
Sodium
all site
nearest neighbor
2
3
1
4
b
a
q_{yy}
q_{zz}
q_{xx}

Figure 8. The four relative e.f.g. tensor orientations in the above calculation are shown. The Euler angles are written for the first site with respect to the reference frame (X_R,Y_R,Z_R). The shielding tensor should in principle be oriented independently from that of the e.f.g. tensor.

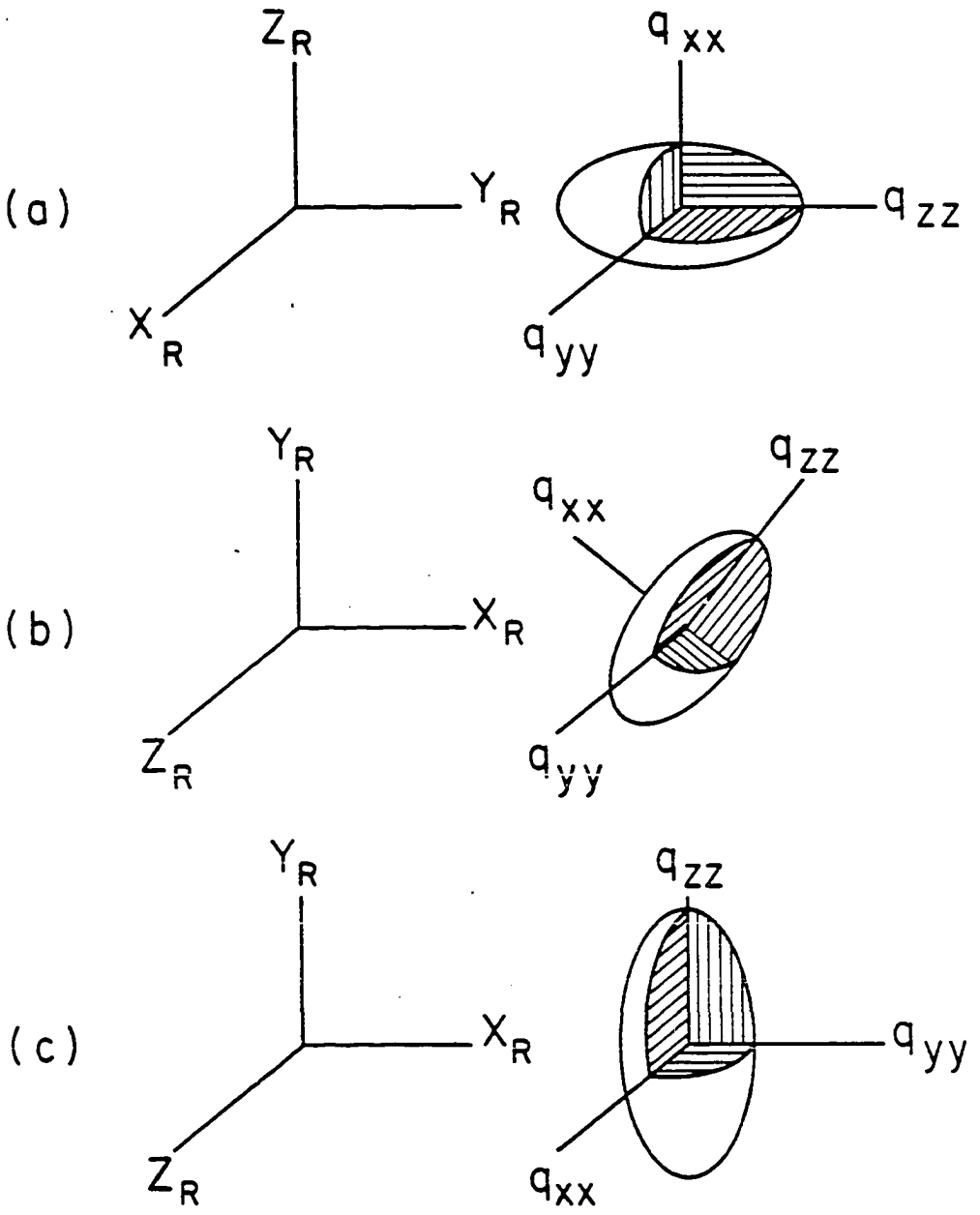
(a)
Z_R
Y_R
X_R
q_{xx}
q_{zz}
q_{yy}
(b)
Y_R
X_R
Z_R
q_{zz}
q_{xx}
q_{yy}
(c)
Y_R
X_R
Z_R
q_{zz}
q_{yy}
q_{xx}

Figure 9. Theoretical NMR spectra for four site exchange motion for the four different e.f.g. orientations. The parameters used in the calculations are: e^2qQ= 1.58 MHz, B_0= 58.23 MHz, I=3/2. The individual parameters are: (a) η=0, (α, β, γ)= (-90., 90., 90), (b) η=1.0, (α, β, γ)= (0., -45., -90.0) (c) η=1.0 (α, β, γ)= (0., 0., 0.), and (d) same as (c) but incorporate CSA with δ = -16 ppm, η_{cs}= 0.4. See text for the detail of this calculation.

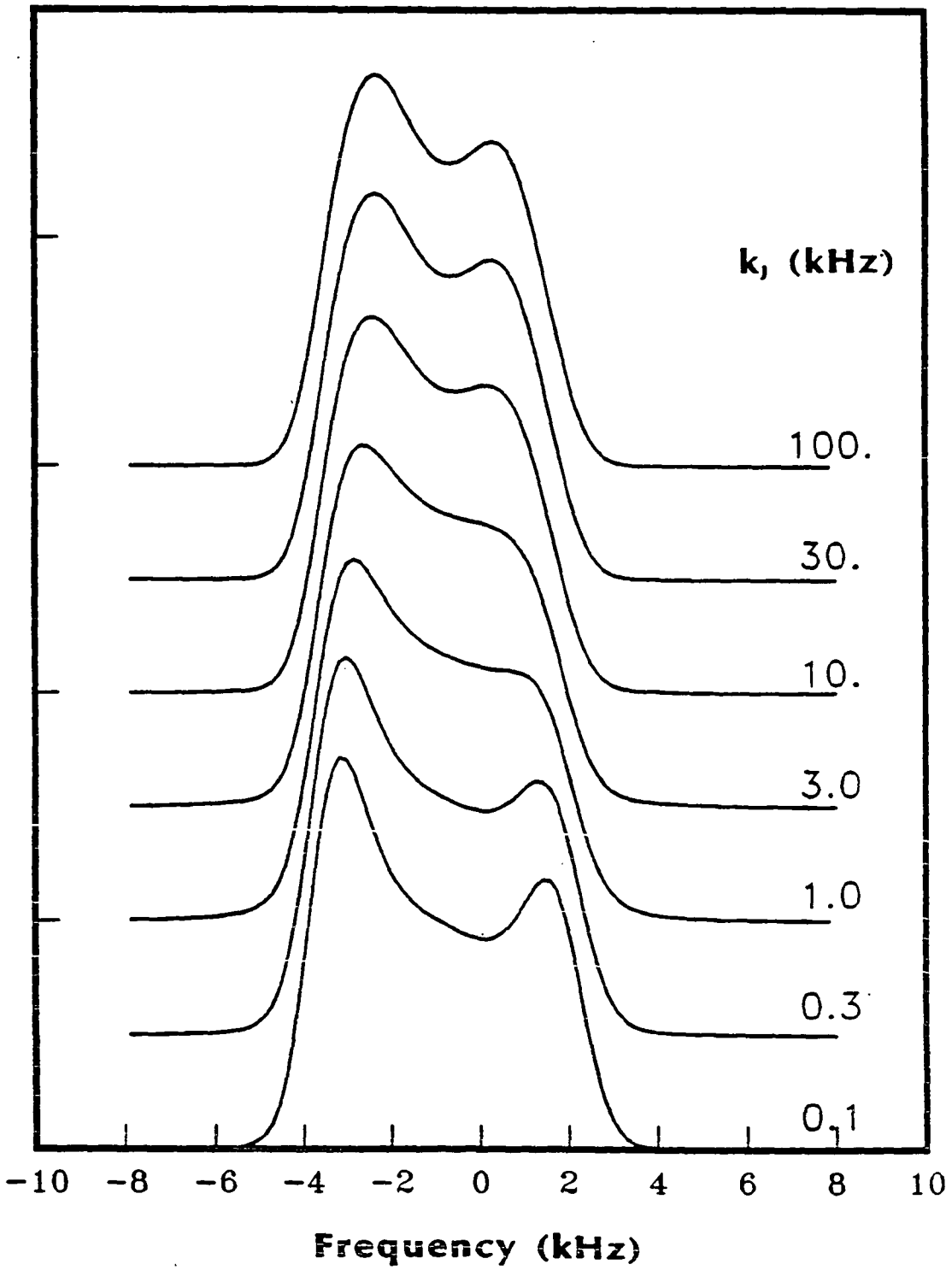
k, (kHz)
100.
30.
10.
3.0
1.0
0.3
0.1
−10 −8 −6 −4 −2 0 2 4 6 8 10
Frequency (kHz)

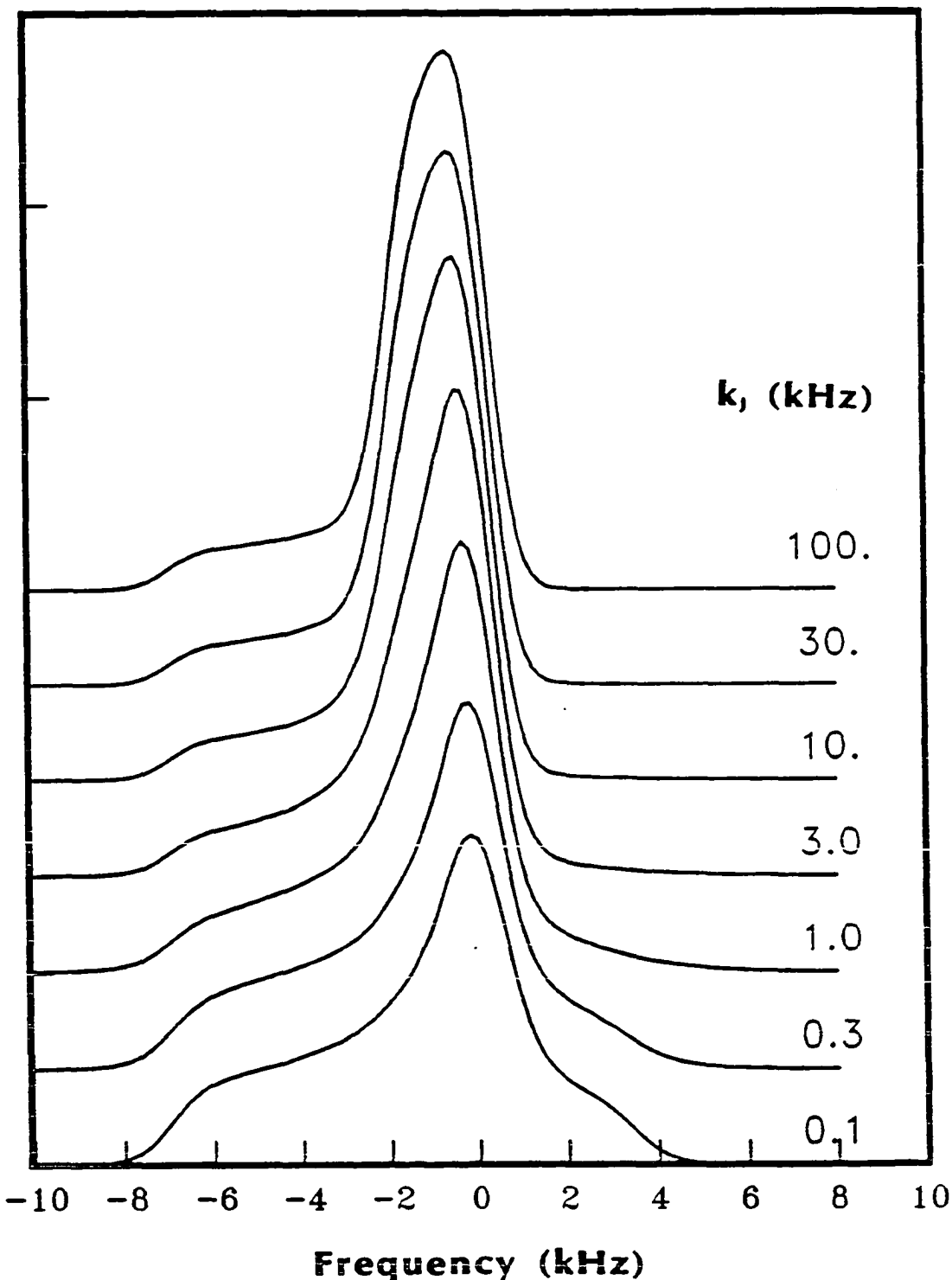

Figure 9 (continued)

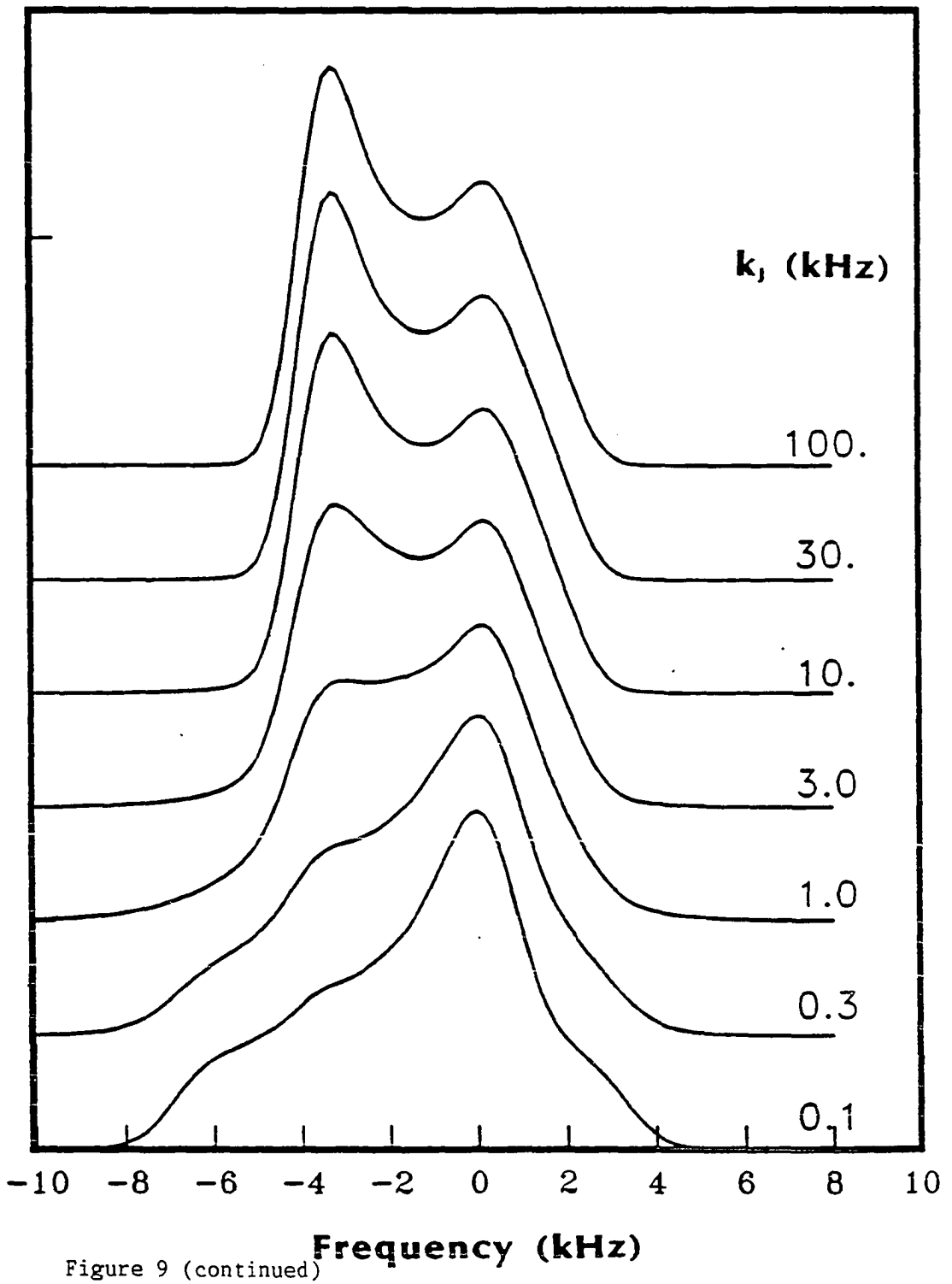

Figure 9 (continued)

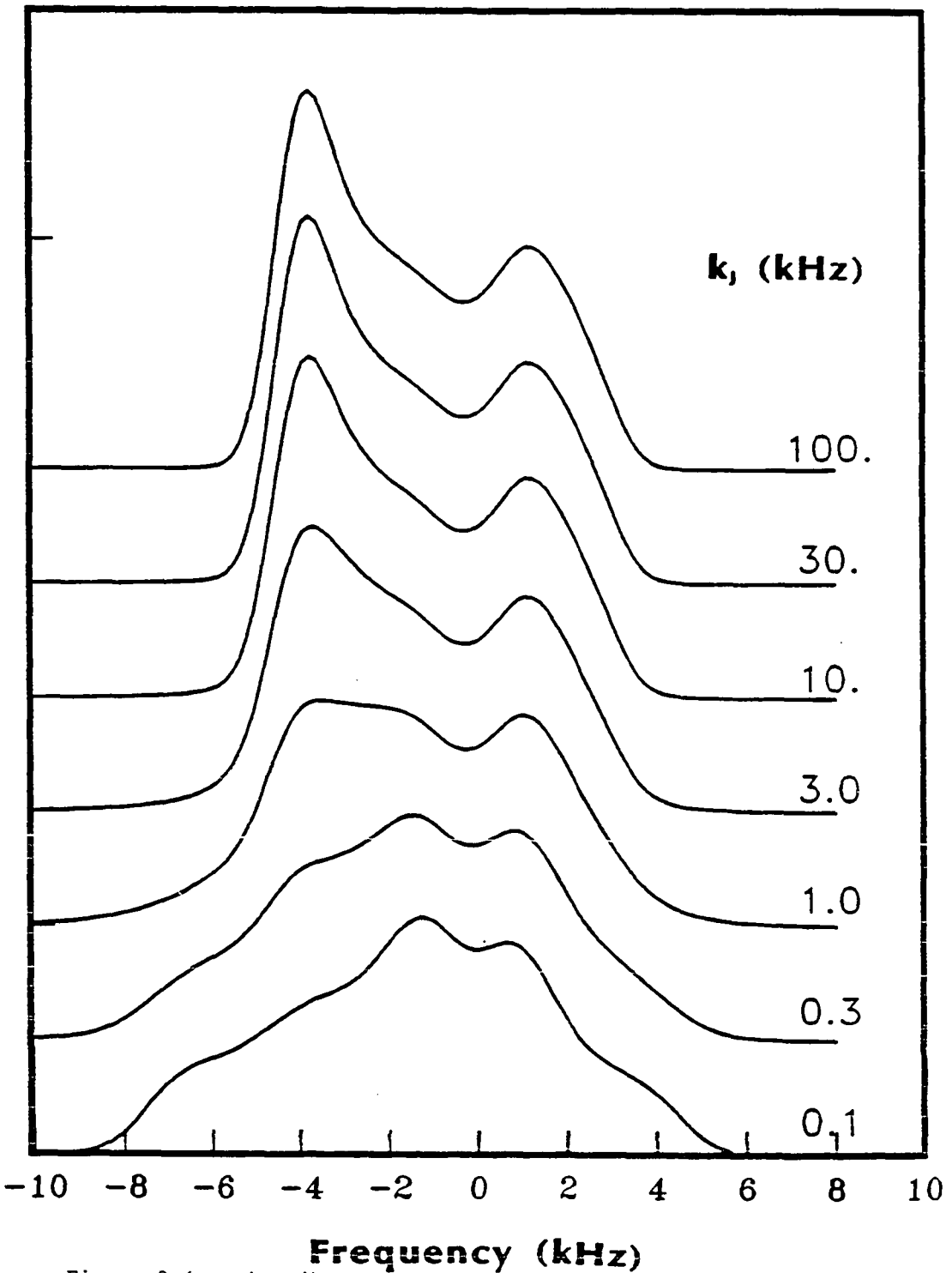

Figure 9 (continued)

Figure 10. Typical iterative fitting results shown for the two room temperature spectra taken at ν_0= 58.23 and 92.32 MHz. Parameters used in the calculation are e^2qQ = 1.58 MHz, η=0.95, k= 70 kHz, δ= -16 ppm., η_{cs}=0.4, σ_0= -36 ppm.

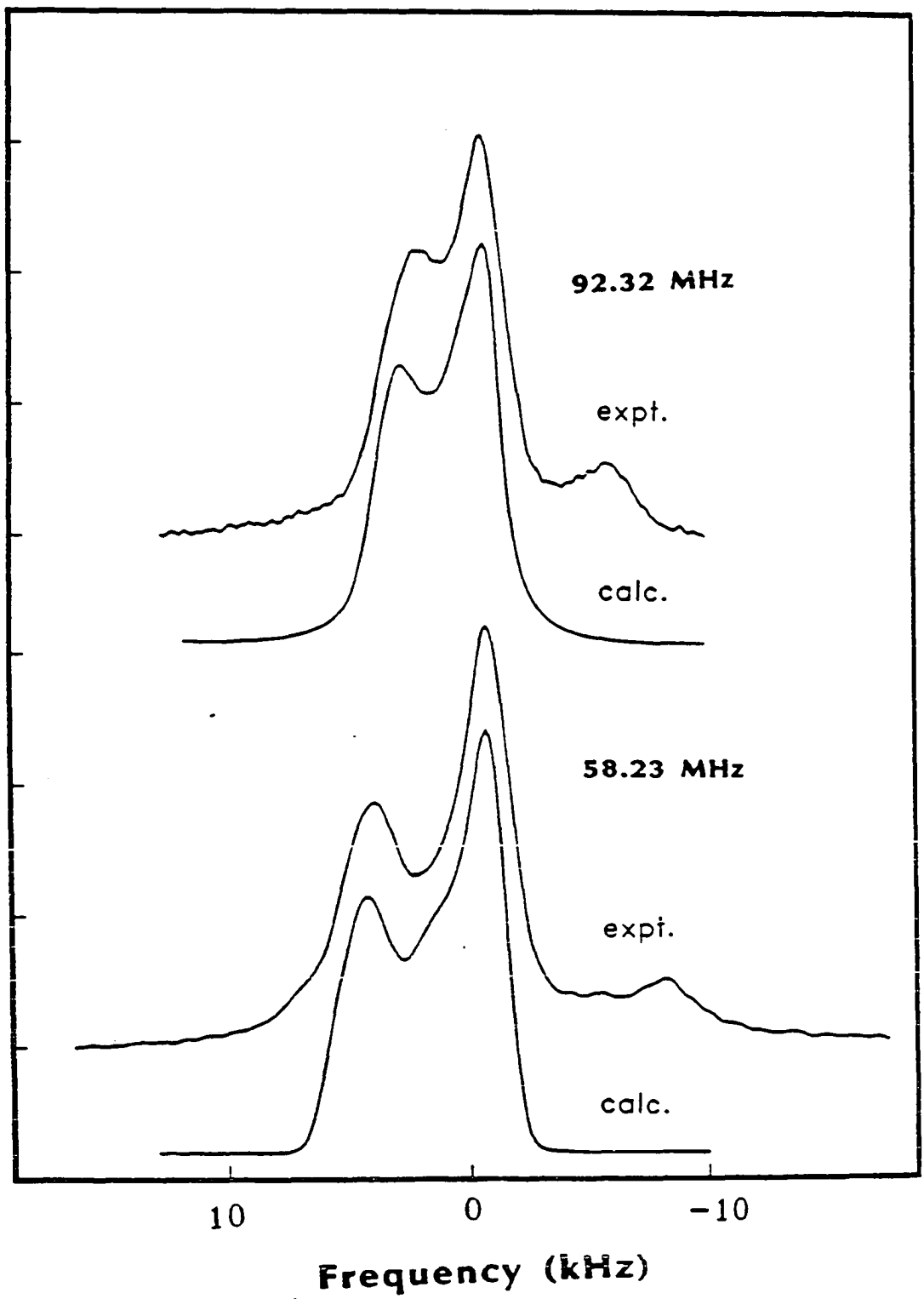
92.32 MHz
expt.
calc.
58.23 MHz
expt.
calc.
10
0
−10
Frequency (kHz)

Figure 11. A plot of the exchange rate against the inverse temperature. From the linear relation, the activation energy E_a is calculated to be 1.95 Kcal/mole.

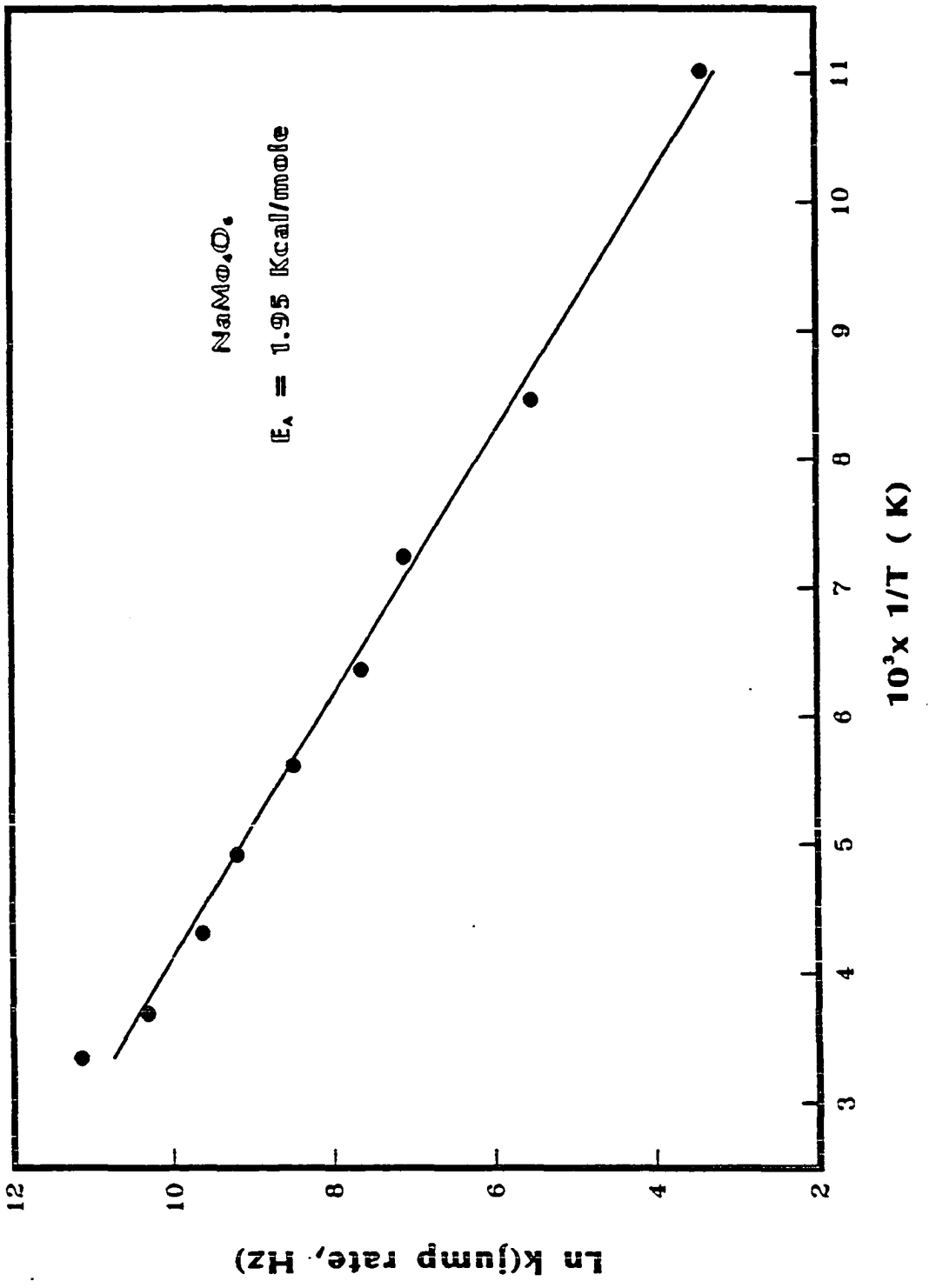
NaMΦ₄O₄
E_A = 1.95 Kcal/mole
ln k(jump rate, Hz)
10^3x 1/T (K)
12
10
8
6
4
2
3
4
5
6
7
8
9
10
11

Figure 12. A plot of the temperature dependence of the QCC. Two linear regimes can be resolved. The coefficient, $\partial e^2qQ/\partial T$, equals 1.5 kHz/deg and 3.9kHz/deg respectively above and below 140 K.

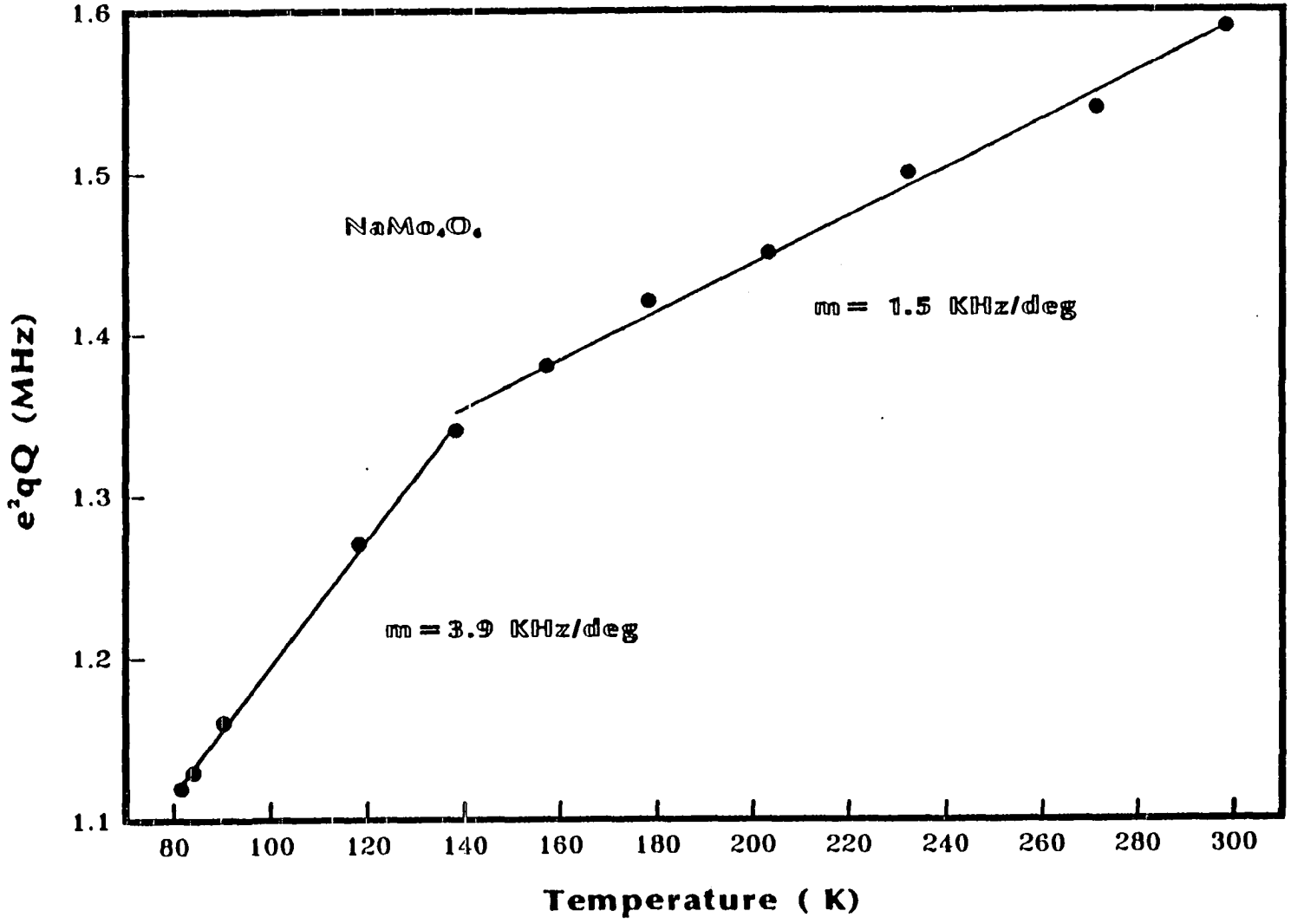
1.6
1.5
1.4
1.3
1.2
1.1
e^2qQ (MHz)
$NaMo_4O_6$
m = 1.5 KHz/deg
m = 3.9 KHz/deg
80
100
120
140
160
180
200
220
240
260
280
300
Temperature (K)

Figure 13. Calculation of the frequency distribution from [14] in the incommensurate regime for various values of coefficients ν_i. The phase, $\phi(x)$, in the calculation is evaluated from the "plane wave" model, i.e., $\phi(x) = cx$.

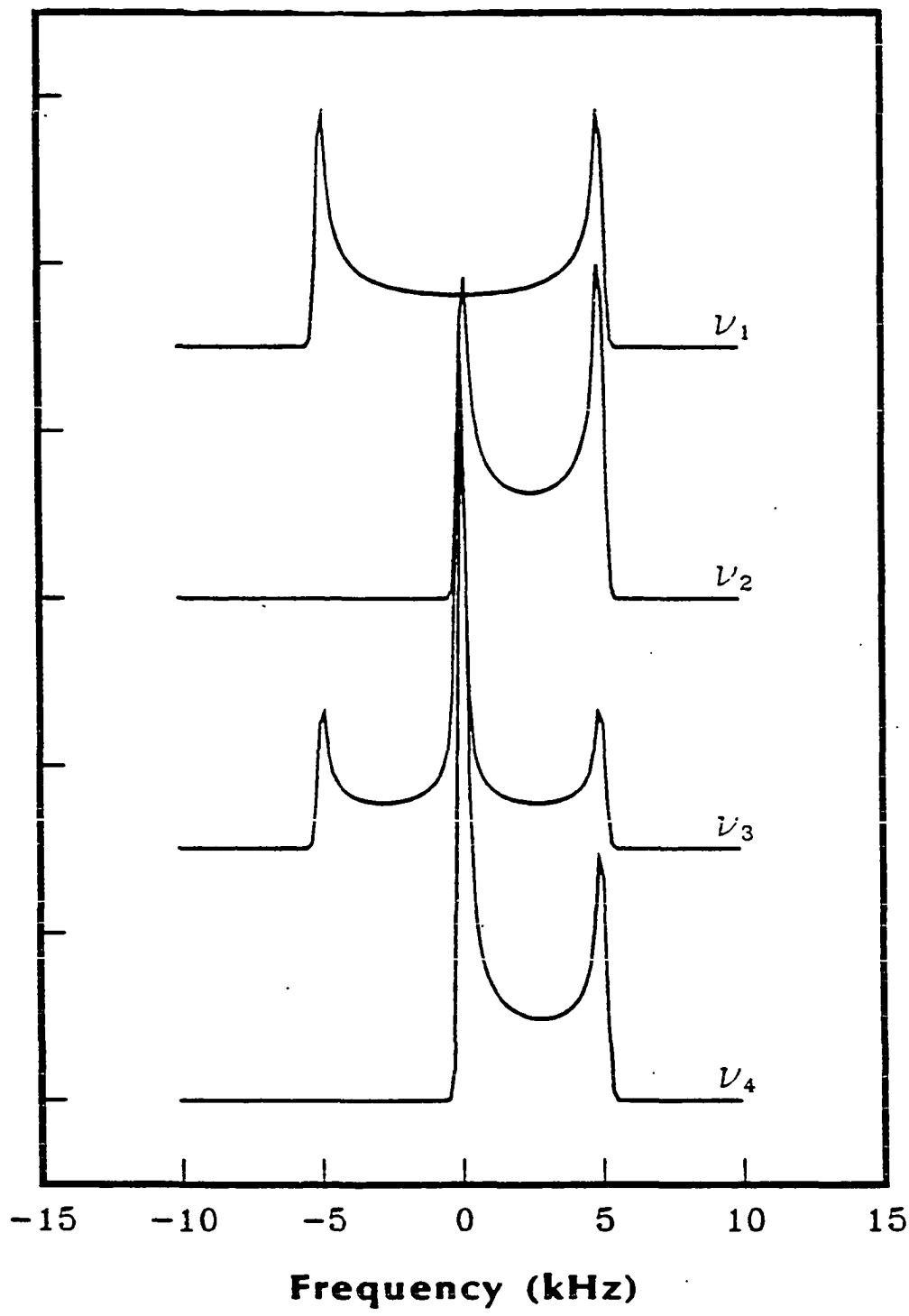
ν_1
ν_2
ν_3
ν_4
−15
−10
−5
0
5
10
15
Frequency (kHz)

Figure 14. Simulation of the room temperature NMR spectra taken at two different fields incorporating the frequency distribution governed by the structural incommensuration. The distribution is dominated by the ν_4 term. In the inset, the amplitude ν_4 is plotted with the temperature, from which the transition temperature $T_1 \simeq 520$ K and the critical exponents $\beta = 0.15$ can be found.

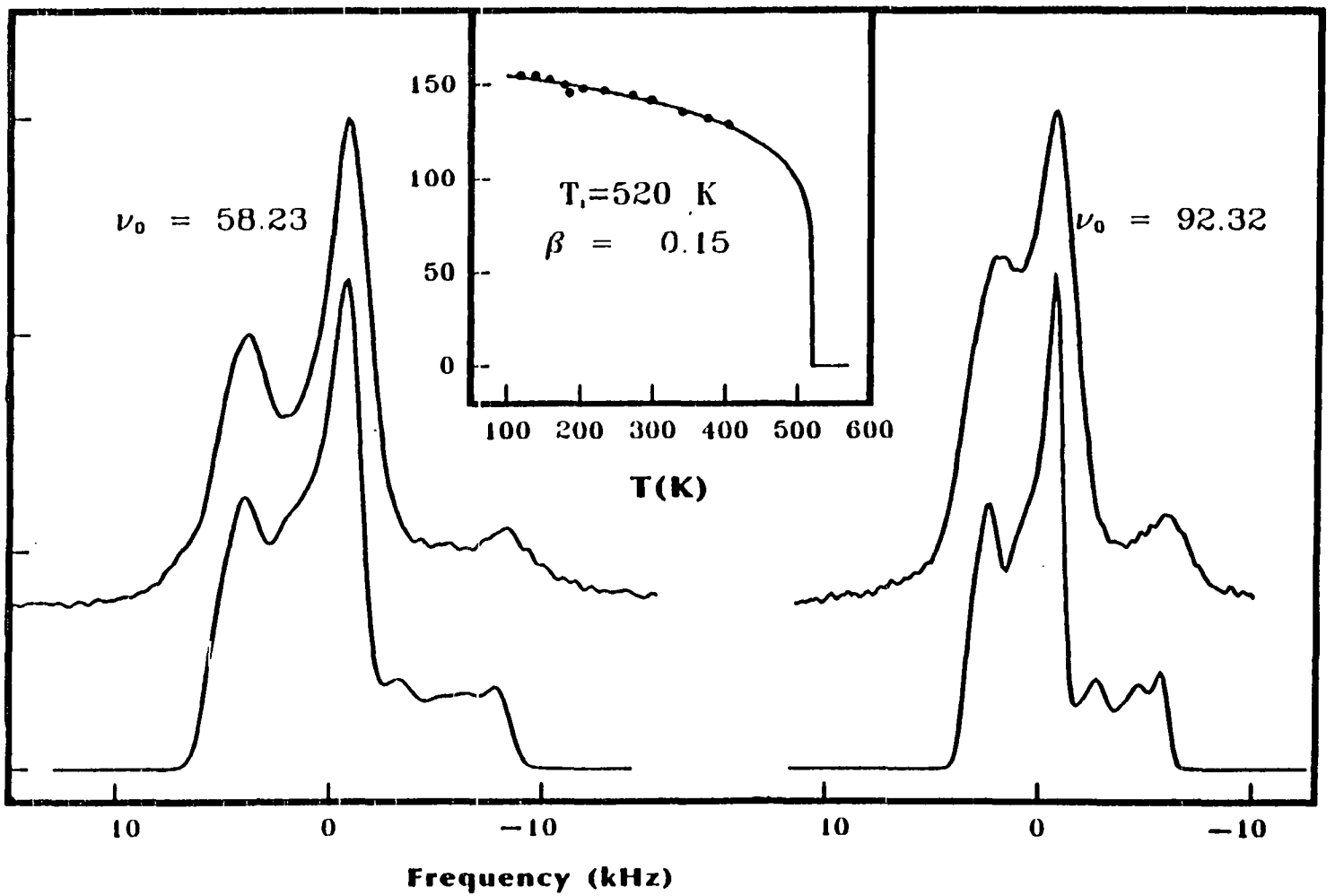
ν_0 = 58.23
ν_0 = 92.32
T_1=520 K
β = 0.15
150
100
50
0
100 200 300 400 500 600
T(K)
10
0
−10
10
0
−10
Frequency (kHz)

PART IV. CHARACTERIZATION OF HYDROGEN IN $Zr_6Cl_{12}H$ AND $ZrClO_xH_y$: STUDIES OF INTERSTITIAL HYDROGEN WITHIN METAL CLUSTERS BY SOLID STATE NUCLEAR MAGNETIC RESONANCE

Characterization of hydrogen in $Zr_6Cl_{12}H$ and $ZrClO_xH_y$: studies of interstitial hydrogen within metal clusters by solid state nuclear magnetic resonance

P. J. Chu, and B. C. Gerstein

Ames Laboratory, and
Department of Chemistry, Iowa State University
Ames, Iowa 50011

ABSTRACT

Solid state NMR studies of hydrogen have been performed on samples of the cluster compound $Zr_6Cl_{12}H$ that contained discernible amounts of the layered $ZrClO_xH_y$ ($x + y \leq 1$) impurity phase. The hydrogen in $Zr_6Cl_{12}H$ resonates at 500 ppm upfield from $H_2O(l)$ at 298 K and shows a strong Curie-Weiss paramagnetic shift relation but no change in line width; $\sigma(ppm) = 2.234 \cdot 10^5 T^{-1}(K) - 241.04$. This temperature dependence indicates the presence of unpaired electron density in the proton environment, consistent with the odd electron count in and paramagnetism expected for $Zr_6Cl_{12}H$. Total suppression of this resonance under multiple pulse homonuclear decoupling indicates that the hydridic species therein experiences rapid random motion with a correlation time shorter than 18 μsec (> 50 kHz), consistent with the oversized Zr_6 metal cluster cavity available. These results are consistent with many observations on other interstitial atoms in Zr_6 octahedral clusters and with the strong correlation of yield with the presence of H_2 in earlier synthesis of several "Zr_6Cl_{12}" phases.

The second hydrogen species exhibits a broad temperature-independent resonance with center of mass at -5.0 ppm. Experiments involving a variety of nuclear spin dynamics indicate that the primary contributions to this signal come from pairs of hydride with $\bar{d}(H\text{—}H) = 2.5 \pm 0.2$ Å and each of these protons interacts to a lesser degree with one or more chlorine atoms at a $\bar{d}(H\text{—}Cl) \geq 2.7$ Å and with shift parameters $\delta = -22.7$ ppm, $\eta = 0.6$. A third, minor species with center of mass at -5.5 ppm, is postulated to originate from isolated hydride units in the same phase. These parameters and the observed orientation of the principal axis of

the H-H dipole interaction with respect to the shift tensor are completely consistent with the structure of the $ZrClO_xH_y$ ($x + y \leq 1.0$) phase observed in the samples by Guinier diffraction.

INTRODUCTION

Although the metal cluster phase Zr_6Cl_{12} has been known for some time,[1,2] questions concerning its actual composition and stability as an empty cluster remain. The compound was initially discovered in small amounts following $ZrCl/ZrCl_4$ equilibrations near the composition $ZrCl_2$.[1] The structure deduced by X-ray powder diffraction was identical to that of 'Zr_6I_{12}', which is now known to actually be $Zr_6I_{12}C$ [3] with carbon centered in the metal cluster.[3,4] However, consistent preparation of Zr_6Cl_{12} was never achieved, and sufficient quantities for physical property measurements were not obtained.

More recently, Imoto and Corbett[5] serendipitously obtained Zr_6Cl_{12}, Zr_6Br_{12} and the related $M_2ZrCl_6 \cdot Zr_6Cl_{12}$ (=$M_2Zr_7Cl_{18}$, M=Na, K, Cs) double salts by the thermal decomposition of ZrX (X=Cl, Br) in the presence of H_2 and, when appropriate, MCl near 750°C. Good yields of the clusters were obtained, but these were contaminated by sizable amounts of inseparable ZrH_{2-x}, the other product. Reactions with Zr:Cl ratios more appropriate to the composition of the cluster phase were not attempted. The greatly improved yields of Zr_6Cl_{12} achieved in the presence of hydrogen and its 0.3% larger lattice parameters compared with those from the earlier $ZrCl/ZrCl_4$ equilibrations[2] led to speculation that Zr_6Cl_{12} might exist both as an empty cluster and as a hydride, similar to Nb_6I_{11} and $Nb_6I_{11}H$.[6]

Solid state ^1H NMR spectra of small samples of the Zr_6Cl_{12} and $Na_2ZrCl_6 \cdot Zr_6Cl_{12}$ prepared earlier under hydrogen showed only broad Lorentzian-shaped resonances (56-41 kHz at ν_0=56 MHz) which were attributed to the ZrH_{2-x} contaminant in the samples. The NMR spectrum

of ^1H in binary compound $ZrH_{1.9}$ was featureless, and showed 55 kHz wide resonance under similar conditions. The homogeneously dipolar broadened spectrum can be compared with the relatively sharper line observed for noninteractive and immobile protons in hydrogen-centered metal clusters. For example, the proton NMR spectrum of $CsNb_6I_{11}H$,[7] a diamagnetic, hydrogen-centered niobium cluster, contains a single peak 0.6 kHz wide (ν_0=35 MHz).[8] Thus it was concluded on the basis of the NMR evidence that neither Zr_6Cl_{12} nor the $M_2Zr_7Cl_{18}$ compounds contained interstitial hydrogen. The greatly improved yields in the presence of hydrogen were attributed to the kinetic factors and to the fact that disproportionation of ZrCl appeared driven by the formation of ZrH_{2-x}. Potential causes for a broad ^1H resonance in other than ZrH_{2-x}, such as from a possibly paramagnetic cluster, were dismissed as was the very broad ESR spectrum observed for only one of two 'Zr_6Cl_{12}' samples at room temperature.[5]

Our recent studies of NMR of ^{13}C nuclei within a zirconium iodide cluster[4] phase suggests that the breadth of a hydrogen NMR signal from $Zr_6Cl_{12}H$ could be associated with the unique structure type. Thus the NMR spectrum of ^{13}C in the diamagnetic $Zr_6I_{12}C$, isostructural with Zr_6Cl_{12}, contains only a very broad resonance that extends from about 28 to 480 ppm. The breadth of the resonance is in distinct contrast to the well resolved resonance ≈38 ppm wide seen for ^{13}C in the paramagnetic $CsZr_6I_{14}C$.[3] The factors responsible for the broadening of the ^{13}C resonance in the former have not been elucidated.

The present lack of conclusive physical evidence for the presence of hydrogen in Zr_6Cl_{12} appears to stem from the poor quality of the earlier

sample as well as the difficulties in detecting small amounts of hydrogen. Circumstantial evidence,[5] however, indicates the presence of interstitial hydrogen. The idea that hydrogen could be present is augmented by a great deal of recent experience which indicates that a large number of other zirconium and scandium chloride cluster phases can be obtained only when an interstitial element Be, B, C,.... is bound in each cluster, raising the cluster-based electron count into the range of 13-16, with 14 electrons being most favored.[3,9-11] Three of the four signs associated with the discovery of these other interstitially-stabilized clusters also point to interstitial hydrogen in the Zr_6Cl_{12} phases: low and irregular yields, an otherwise electron deficient M_6X_{12} cluster (12 e), and improved yields upon the addition of the appropriate interstitial element. The fourth sign, a residual electron density in the cluster center from X-ray studies, would not be expected for hydrogen, of course. Preparation of good quality samples appeared to be the key to unraveling the role of hydrogen in the preparation and stability of Zr_6Cl_{12}.

As an abundant spin I=1/2 species, ^1H is easily detectable by NMR, the lower limit of detectability being roughly 10^{17} spins for a line 10 Hz wide. ^1H has been the dominant NMR-active tag in chemistry of liquids for almost 40 years, the primary interactions used being the isotropic chemical shift and the isotropic scalar coupling.[12] There are a broad range of transient techniques to perturb and control nuclear spin dynamics in order to probe the possible identities of the local surroundings in a solid.[13] The presence of nearby hydrogen atoms is reflected in the homonuclear dipolar coupling interaction. The possible

location of the proton in the structure and the symmetry of the surroundings is probed by the anisotropic shielding. Motion of the protons is probed by the response of the proton magnetization to multiple pulse sequences with cycle times of order of the motional correlation time.[14] Particularly noteworthy with respect to the last point is the structural observation that the cavity in Zr_6Cl_{12} (as measured in $K_2Zr_7Cl_{18}$) is considerably oversized for a hydrogen, viz., $\bar{d}$(Zr-H)= 2.26 Å here vs. 2.08 Å in ZrH_2 and 2.10 Å in Zr_2Br_2H, both with four-coordinate hydrogen.[15]

Possible identities of nearest neighbors may also be probed using homo- and heteronuclear scalar and dipolar couplings, utilizing differences in the dependencies of the forms of these couplings on spatial and spin variables and on whether or not one of the partners in the coupling is a spin 1/2 nucleus. For example, dipolar couplings between pairs of spin 1/2 nuclei will result in inhomogeneous broadening which will split into sharp lines under magic-angle sample spinning (MAS) at a speed lower than the anisotropy of the inhomogeneous broadening. On the other hand, dipolar coupling between a spin 1/2 and a nonspin 1/2 nucleus will not be completely sharpened under MAS, and the resultant structure can be used as a diagnostic tool for identities of one of the pair of coupled atoms. Specifically as applied to the present samples, the presence of ^1H, ^{35}Cl (75.53% abundance) and ^{37}Cl (24.47% abundance) offers the possibility of using the heteronuclear coupling to discern hydrogen in the neighborhood of chlorines. A parameter immediately extractable from the spectra under MAS is the internuclear distance between hydrogen and chlorine.

EXPERIMENTAL

Materials

Because of their air- and moisture-sensitive nature, all products and reactants were handled under an inert atmosphere or in vacuum. Zirconium powder was prepared from reactor-grade crystal bar zirconium (<500 ppm Hf) via the thermal decomposition of ZrH_{2-x} in high vacuum as previously described.[3] The $ZrCl_4$ was prepared by the direct reaction of the elements at 300-350°C and purified by several successive high-vacuum sublimations over Zr metal and through a coarse-grade Pyrex frit. Hydrogen was introduced into the reactions in the form of ZrH_{2-x} which had been obtained from the reactions of the reactor-grade zirconium with hydrogen at 650°C followed by cooling under hydrogen to room temperature over a 6 hr period. The final hydride composition, $ZrH_{1.8}$, was calculated from the initial zirconium weight and the change in pressure of the known volume of hydrogen used in the reaction.

Synthesis

The reactivity of reduced zirconium halides with fused silica at the elevated temperatures sufficient for clusters formation (>600°C) necessitated the use of welded Ta tubing encapsulated in evacuated and sealed fused silica jackets. Samples of $Zr_6Cl_{12}H$ were prepared by the reaction of Zr powder (>100 mesh), $ZrCl_4$ and $ZrH_{1.8}$ at 700°C over a two—three week period.

Two different samples were initially prepared. Sample A, used for all the spectra shown, was prepared from a reaction stoichiometry with a Zr:Cl:H ratio of 6:12:4. An excess of $ZrCl_4$ sufficient to give

approximately 5 atm at 700°C (assuming ideal gas behavior) was also included to reduce disproportionation of the desired cluster compound at this temperature. The yield of $Zr_6Cl_{12}H$ was estimated from relative intensities in the Guinier powder diffraction pattern to be on the order of 90%, although a microscopic examination of the product suggested it might be 5–10% lower. (This assessment excludes the excess $ZrCl_4$ which was first sublimed off under dynamic vacuum at 250°C.) The other phase present was tentatively identified as $ZrClO_xH_y$ ($0 < x < .43$, $x + y < 1$) in a ZrCl-type structure.[16,17] The identification was based on line positions, intensities, and lattice constants determined from X-ray (Guinier) powder diffraction ($a = 3.4854(5)$ Å, $c = 27.04(2)$ Å). The excess hydrogen used in the $Zr_6Cl_{12}H$ synthesis is presumably partially taken up by both the Ta tube and this second oxide phase.

Sample B was prepared under similar conditions with a Zr:Cl:H ratio of 6:12:1.8 and an approximately equivalent amount of excess $ZrCl_4$. The yield of $Zr_6Cl_{12}H$ was marginally lower than reaction A (≈5%) with a slightly hydrogen-poorer $ZrClO_xH_y$ (ZrCl-type structure) making up the difference. The identification of this oxygen-containing species correlates with the line shape analyses and the proton spin counting in the NMR experiments.

The assignment of $ZrClO_xH_y$ as the second phase is consistent with the evidence obtained from a third reaction. A sample C prepared similarly from a mixture with a Zr:Cl:H ratio of 6:12:1.8 and ≈10 atm equivalent excess of $ZrCl_4$ was further hydrogenated at 200°C in a Mo boat with 1 atm H_2. The small sample size and large hydrogen volume prevented an accurate measure of the hydrogen uptake. However, the

observed conversion of the $ZrClO_xH_y$ impurity from the ZrCl- to ZrBr-type structure was consistent with the previous experimental experience which showed that the ZrBr structure type is adopted by $ZrClO_xH_y$ when x+y approaches unity.[17] Unfortunately, insufficient data are available to estimate the amount of hydrogen in the $ZrClO_xH_y$ in either sample A or B.

The presence of an oxygen-containing phase in both samples of $Zr_6Cl_{12}H$ is inconvenient but not particularly surprising considering the air- and moisture-sensitive nature of the reactants and their small particle size. Contamination by oxygen in any or all of the reactants may be at fault. Separation of the two phases is considered nearly impossible at the present time.

We have also observed that $Zr_6Cl_{12}H$ can be prepared in good yield by heating the layered $ZrCl_{2-z}$ (3R-MoS_2 structure type[2]) under hydrogen at 710°C. The product is contaminated with ZrH_{2-x} both from the degree that z>0 and from disproportionation owing to the high equilibrium pressure of $ZrCl_4$ at this temperature.

NMR measurements

NMR experiments were performed at 5.2 T in a superconducting magnet and at 1.3 T in an iron core solenoid magnet using a home-built pulsed NMR spectrometer similar to that described earlier.[18] Hydrogen resonates at 220 MHz and 56 MHz respectively in these two fields. A total of 32766 scans were required to obtain a satisfactory signal-to-noise ratio of the transient decay signal. A simple $\pi/2$ pulse was applied with inverse phase cycling (alternate pulses 180° out of phase)

in order to minimize baseline artifacts from pulse breakthrough and ringing. A longitudinal relaxation time measured by progressive saturation yielded a value of roughly 0.1 second at 220 MHz and slightly less at 56 MHz. A repetition rate of 0.5 second was therefore used for most of the experiments. An aqueous $FeCl_3$ solution was used for tuning the spectrometer and as a resonance frequency reference for experiments performed at both fields. Pure water was used as a reference in the spin counting experiments.

Variable temperature experiments were performed on a home built cryogenic system with a Varian temperature controller to regulate the N_2 flow rate and the temperature.

Variable-angle sample spinning experiments were performed at a home built CRAMPS probe[19] using a Gay type[20] rotor for the sealed samples. The magic angle was adjusted by utilizing the Pake doublet feature of the spectrum of gypsum powder. The angle Θ between the rotation axis and the external magnetic field was measured from the scaled Pake doublet of the rotational side bands according to the equation:

$$\Delta B = \frac{(3\cos^2\Theta-1)}{2} \cdot \omega_D = P_2(\cos\Theta)\ \omega_D \qquad [1]$$

ΔB is the splitting of the scaled pake doublet within a single rotational side band, and ω_D is the splitting of the static Pake doublet spectrum. A single sharp center peak will appear if the condition $3\cos^2\Theta-1 = 0$ is satisfied. The larger the value of ω_D and the smaller the homogeneous dipolar broadening, the more accurate the angle Θ can be calibrated.

Multiple pulse experiments were performed as described previously.[13] After maximizing the power, a 1.2 μsec π/2 pulse width was obtained. The MREV-8 pulse cycle time was 36 μsec. The scaling factor under the multiple pulse experiment was determined by the response of H_2O at several off-resonance frequencies.[14]

NMR data are presented on either the σ scale, with increasing σ value corresponds to higher field, or in kHz units where more negative values are at higher field. All spectra are plotted with field increasing to the right.

NMR spin counting

Proton spin counting measurement was accomplished by comparing the zero-time free induction decay (FID) between the samples and a distilled water reference. The initial decay amplitude was measured by extrapolating the transient to the center of the preparation pulse.

The relative ratios of the two hydrogen species observed (with shift) that were inferred from the integrated area of the two absorptions are 2.0 (-5ppm) to 1.0 (500 ppm) for sample A, about 2.2 (-5.ppm) to 1 (500ppm) for sample B, and 4.2±0.4 (-5.0ppm) to 1 (500ppm) for sample C, indicating that an increasing amount of the $ZrClO_xH_y$ phase was produced as the preparation proceeded from A to C.

Description of structures

The structure of $Zr_6Cl_{12}H$ has previously been shown by Guinier powder diffraction to be isostructural with $Zr_6I_{12}C$.[3,5] As shown in Fig. 1, the principal building block is the Zr_6Cl_{12} cluster, a trigonal

antiprismatic Zr_6 core surrounded by 12 chlorine atoms that bridge each of the 12 edges. The structure is a cubic-close-packed array of these Zr_6Cl_{12} clusters with the $\bar{3}$ axis of each cluster normal to the layer direction. An extensive sharing of the chlorine atoms between clusters is necessitated by the stoichiometry and the bonding requirements of the cluster. Specifically, the six chlorine atoms around the waist, i.e., those bridging edges with a component parallel to the $\bar{3}$ axis, serve as more distant terminal chlorine atoms to metal vertices on six adjacent clusters, three above and three below. The connectivity is conveniently formulated as $[Zr_6Cl_6{}^{i}Cl^{i-a}{}_{6/2}]Cl^{a-i}{}_{6/2}$, where Cl^{i-a} and Cl^{a-i} reflect the connectivity just described while Cl^{i} is not shared. A hydrogen atom presumably is bound within each Zr_6Cl_{12} cluster, similar to that for the carbon atom in $Zr_6Cl_{12}C$. PES, dimensional and theoretical evidence indicate the hydrogen in such electron-rich environments should be considered hydridic in character.[21]

A $ZrClO_x$ phase is known to form via continuous random insertion of oxygen into tetrahedral metal interstities in the 3R-ZrCl, a structure in which tightly bound slabs are formed from cubic-closed-packed homoatomic layers sequenced Cl-Zr-Zr-Cl.[16] The oxide derivative has subsequently been found to take up hydrogen as $ZrClO_xH_y$, evidently utilizing the remaining tetrahedral sites, to an experimentally determined limit of $x + y \simeq 1.0$.[17] (Different hydride structures are formed in the absence of oxygen.[15]) The stacking of the four-layered slabs is found to change from ZrCl- to ZrBr-type as x + y approaches 1.0, a change that is not reflected in the proton NMR.

RESULTS AND DISCUSSION

The Fourier transform of the FID, obtained by applying a simple $\pi/2$ pulse to sample A at two different magnetic fields, is shown in Fig. 2. Two peaks were resolved at both fields. The first moment of the downfield peak is at -5.0 ppm as referenced to $Fe^{+3}(aq)$. The center of mass of the upfield peak is at approximately 500 ppm. The integrated areas of the two peaks give a ratio of about two (-5 ppm) to one (500 ppm). The spectrum of sample B is similar to that of sample A except that this area ratio is slightly higher. In sample C, this ratio is even higher, about four to one. Of particular importance is the recognition that the measurements were performed on a two-phase mixture, with rather different properties of hydrogen in the two phases. In the following, the NMR spectra of the upfield and the downfield peaks are discussed individually and identified with $Zr_6Cl_{12}H$ and $ZrClO_xH_y$, respectively.

Upfield component

The effective transverse relaxation time T_2^* of the upfield peak was determined by nonlinear least squares fitting of the spectrum to Gaussian, Lorentzian, and multiplication of Lorentzian and Gaussian line shape functions.[22] Although the relaxation times are roughly equal for different kinds of line shape functions, the Gaussian function seems to yield the best fit for the spectra taken at both magnetic fields. The implication is that this peak is homogeneously broadened (vide infra). The relaxation times and the isotropic values obtained in the fitting of the peaks are listed in Table I. For comparison of the line shape and

the line width, the spectra are re-drawn in Fig. 3 with the x-axis in units of kHz.

MAS experiments with a rotor frequency of ≈2 kHz at the NMR frequency of 220 MHz were performed in order to confirm that the upfield peak is homogeneously broadened. The line width of the upfield peak (7.5 kHz) changes only slightly and exhibits no rotational side bands in the MAS spectra, indicating that the limiting line width of the homogeneous broadening is approximately 5.5 kHz (T_2=80 μsec). This result correlates with the fact that the line width of this peak at 56 MHz (4.7 kHz) is not one-fourth of that taken at 220 MHz, as would be expected for an inhomogeneously broadened shift interaction.

Upon homonuclear decoupling using the MREV-8 multiple pulse sequence,[19] the upfield peak is reduced to the noise level. This phenomenon has been found in several other systems undergoing rapid nuclear motion where the effective magnetization changes owing to the motion of the nuclei on a time scale shorter than the sampling time of the multiple pulse sequence.[14,19] As a result, the transient signal is not coherently averaged in the stroboscopic observation windows. The failure to observe the upfield peak under homonuclear decoupling supports the idea that the proton in this environment is undergoing isotropic and incoherent motion with correlation time τ shorter than the sampling time of the multiple pulse homonuclear decoupling experiment (18 μsec).

We now consider the origins of the large upfield shift. Consider first clusters with no unpaired electrons. The theoretical basis for the screening effect of paired electrons was initially formulated by

Ramsey[23] by evaluating the induced current from the environmental electron density as follows:

$$\sigma_\lambda = \sigma_{\lambda d} + \sigma_{\lambda p} \qquad (\lambda = x,y,z) \qquad [2]$$

where

$$\sigma_{\lambda d} = \frac{e^2}{2mc^2} \langle 0\lambda | \frac{x^2 + y^2}{r^3} | 0\lambda \rangle \qquad [3]$$

$$\sigma_{\lambda p} = -4\mathrm{Re} \sum_{n',\lambda'} \frac{\langle 0\lambda | \sum_{k=1}^{N} m_{zk} | n'\lambda' \rangle \langle n'\lambda' | \sum_{k=1}^{N} m_{zk} r^{-3} | 0\lambda \rangle}{E_{n'} - E_n}$$

$$m_{zk} = (ie\hbar/2mc) \left(x_k \frac{\partial}{\partial y_k} - y_k \frac{\partial}{\partial x_k} \right)$$

Ramsey's formulation separates the shielding tensor into two components, a diamagnetic term, σ_d, which is calculated from the ground state wavefunction, and a paramagnetic term, σ_p, which involves a summation over all the excited states arising from the lack of spherical symmetry of the electric potential at the nucleus site. The magnitude of the σ_p term can be comparable with that of σ_d and can serve to cancel the contribution from the diamagnetic term.

For the high upfield shift observed to occur within this model, the diamagnetic term σ_d must significantly override the paramagnetic term σ_p. The disappearance of the signal under multiple pulse excitation implies that the proton is hopping within the cluster with a correlation time of less than 18 μsec. This motion would considerably reduce the shielding anisotropy observed in a static system. Considering only the isotropic value in equation [2] and [3], the diamagnetic component σ_d

becomes:[24]

$$\sigma_d = \frac{e^2}{3mc^2} \langle 0 | \sum_{k=1}^{N} \frac{1}{r_k} | 0 \rangle \qquad [4]$$

If the upfield shift is caused by the hydridic character of the proton, this shift should be independent of temperature because of the temperature independence of the electronic wavefunctions as implied by equation [4].

Another possibility to account for the observed upfield shift is that produced by an unpaired electron spin. Addition of a hydrogen atom to the empty, 12-electron Zr_6Cl_{12} cluster would result in an unpaired electron configuration, probably deriving from a hole in the t_{2g} or t_{1u} orbital set.[3] The unpaired electron density in the ground state of the cluster produces a strong local magnetic field which result in a chemical shift to the hydrogen nucleus that is orders of magnitude larger than the shift usually observed in diamagnetic molecules.

By relating the mean value of the electron magnetic moment, $\langle S_z \rangle$ to the bulk Curie Law magnetic susceptibility,[25,26] the magnitude of the shift associated with the unpaired electronic spin density in the ground state of the $Zr_6Cl_{12}H_x$ cluster can be found to equal to

$$\frac{\Delta H}{H} = \frac{g\beta}{\gamma\hbar} \frac{a(S+1)S}{3KT}$$

Substituting the constants and changing unit yields

$$\frac{\Delta H}{H} = 0.01053 \frac{a(S+1)S}{T} \qquad [5]$$

where "a" is the hyperfine coupling constant in units of MHz. Variable temperature experiments were performed in the range from 218 to 298 K to verify the postulate that the unusual isotropic shift of the upfield peak is associated with the presence of unpaired electron spin density in the ground state of the cluster. The upfield peak shifts further upfield as the temperature decreases. In Fig. 4 the shift is plotted as a function of the inverse of temperature with the linear least squares fit passing through the points with a slope of 2.234×10^5 ppm-K and the intercept, -241.04 ppm. The linear behavior indicates that the upfield peak is associated with a Curie Law type magnetic susceptibility, and the presence of unpaired electrons in the ground state.

The difference of ≈16 ppm in the center of mass of the upfield peak in the spectra taken at two different fields, Fig. 2, is clearly related to this highly temperature dependent shift relation. A correction of 15.4 ppm to the isotropic shift value is found from the above inverse temperature relation when consideration is given to the fact that the experiments were performed in different laboratories where the ambient temperatures were 19°C (ν_0 = 56 MHz) and 25°C (ν_0 = 220 MHz) respectively.

From the slope of the ($\Delta H/H$) vs. T^{-1} curve (Fig. 4) the hyperfine coupling constant a is determined to be 28.29 MHz or 6.64 kGauss, a value quite typical of organic radicals.[25] This shift can be related to the unpaired electron density at the nuclear, $\rho(N)$. According to Fermi's formula:

$$a = \frac{8\pi}{3} \gamma_{\bar{n}} g \beta \rho(N) \qquad [6]$$

$\rho(N)$ is determined to be $4.27 \cdot 10^{22}$ electron/cm^3 which is about 0.02 times of the unpaired electron density found at the nucleus of an isolated hydrogen atom.[25,26] This value is also comparable with a variety of organic radicals.

The above results indicate that the upfield hydrogen species resides in the environment of unpaired and localized electron and is highly mobile at room temperature. It is therefore reasonable to locate the hydrogen inside the octahedral zirconium cluster. Both the rapid proton motion and the temperature dependence of the shift described above are supportive of the hypothesis regarding the formation and stability of Zr_6Cl_{12} (cf. Introduction), namely, that hydrogen is needed for its synthesis, and, as with all other examples of $Zr_6Cl_{12}Z$ clusters, the interstitial nonmetal atom contributes both electrons and bonding to the cluster.[9] In the particular case of $Zr_6Cl_{12}H$, the cavity size is determined largely by the Zr-Zr bonding with 11 electrons in metal-metal bonding t_{2g} and t_{1u} sets (in the octahedral limit[3]). This leaves $\bar{d}$(Zr-H) $\simeq$ 2.26 Å, at least 0.15 Å too large for optimal bonding.[5,15] The rapid motion thus allowed prevents the observation of the resonance under conditions of homonuclear multiple pulse decoupling.

NMR line shape of the downfield component

The line shape of the downfield peak changes with applied field (Fig. 3). However, the line width does not scale proportionally, which is strongly indicative of the presence of a field-independent homonuclear dipolar interaction. At high fields the shift anisotropy seem to dominate while at lower fields, a structure that is inferred to

originate from inhomogeneous dipolar broadening begins to appear. The resulting spectra depend not only on the individual interaction parameters characterizing shielding and dipolar tensors, but also strongly on the mutual orientation between these two interactions (vide infra).

In the MAS spectrum, (Fig. 5), several interesting features are observed from which the major Hamiltonians affecting the investigated protons can be determined. The bulk shape of the spectrum resembles that of a Pake doublet, as expected if the spectrum were inhomogeneously broadened by two-body homonuclear dipolar interactions. The skewed intensity of the rotational side band under MAS indicates that an asymmetric interaction of the same order of strength as the dipolar interaction also contributes to the spectrum. This interaction is attributed to the chemical shift interaction.

Under rapid sample spinning each rotational side band splits into four peaks. There are three possible reasons for this splitting: (a) the presence of more than one hydrogen species, each possessing a different isotropic shift; (b) an incorrect setting of the magic angle such that the scaling factor $P_2(\cos\theta)$ is not zero; and (c) the presence of another interaction that is not scaled by $P_2(\cos\theta)$.

The relative intensities and locations of the split peaks are reproduced in all rotational side bands. This suggests that the splitting does not originate from different hydridic species possessing different isotropic shifts, since this would produce different relative intensities and progressive shifts of the split peaks from one rotational side band to another. Therefore, the first possibility is

excluded. When the sample was spun at an angle of ±2 degrees from the magic angle, the splitting of the individual center band (as shown in the inset of Fig. 5) did not scale as expected for homonuclear dipolar interactions; therefore the residual fine structure does not come from an error in setting the magic angle. The rotational angle was found to match the magic angle to within 0.1 degree as estimated from the rotational side bands of the Pake doublet in gypsum.

The variable-angle sample spinning (inset of Fig. 5) shows a systematic change in the relative intensities of the split peaks, with almost constant spacing as θ deviates from the magic angle by $\pm 2^{\circ}$. This behavior is characteristic of heteronuclear dipolar coupling between a quadrupolar nucleus and a spin 1/2 nucleus[27] where the scaling upon rotation does not follow $P_2(\cos\theta)$.

Therefore, we conclude that the major contributions to the peak at -5 ppm are homonuclear dipolar interactions and chemical shift interactions with a single isotropic value. The contribution of the next-nearest neighbors of the proton pair to the dipolar structure appear to be negligible (vide infra). Although the heteronuclear dipolar interaction between hydrogen and the quadrupolar spin nuclei Cl were observed from the splitting of the rotational side band, this interaction is an order of magnitude smaller than the two major interactions.

A line-shape simulation based upon the model of a proton pair experiencing dipolar plus chemical shift interactions has been performed and is detailed elsewhere.[28] The calculation involves both first order dipolar and chemical shift interactions with noncoincident tensor

orientations. The interaction parameters obtained from the simulation of the spectra at both fields are listed in Table II.

In Fig. 6, the calculated best-fit spectra are compared with the experimentally observed spectra. Good agreement is obtained not only in the fit for a single field, but the results are also consistent for the fit performed at a second field. This supports the assumption that the majority of hydrogen atoms contributing to the downfield peak are isolated dipolar pairs of hydride with identical chemical shifts. From the dipolar coupling constants, the internuclear distance of the dipolar pair is calculated to be 2.5 ± 0.2 Å. The fitting results are sensitive to a change in the angle β as small as two degrees, but a change in α by 20 degrees does not produce a visible change in the spectrum. This explains the difference in α between two fields given in Table II.

Another simulation assuming that the two interaction tensors are coincident has been carried out as a comparison to the previous calculation. The fitting parameters obtained under this constraint for the spectrum taken at two different fields are quite different. This indicates that allowing interaction tensors to have nonparallel orientations is in general necessary to obtain a satisfactory fit.

In fitting the downfield peak, the small component of proton species appearing at the center of the spectrum has been ignored. The appearance of this peak can be related to either the coupling of a relatively distant third proton to the above mentioned proton pair or a small percentage of the protons experiencing equi-distant three-proton dipolar coupling. Another possibility is that the species associated with this signal are isolated protons in $ZrClO_xH_y$. Notice that the r^{-3}

dependence of the dipolar coupling constant implies that a proton twice the distance from the "isolated" pair of hydrogens that lead to the major portion of the downfield signal produces only one-eighth of the dipolar coupling strength and hence can be considered as a remote or isolated hydrogen.

Finally, to confirm the above conclusion and the fitting results, we applied the MREV-8 multiple pulse sequence to suppress the homonuclear dipolar coupling. This yielded a tensor-like shielding spectrum for the downfield peak. A simple calculation for the chemical shift tensor gave an anisotropy parameter δ of -22.7 ppm and an asymmetry parameter η of 0.6. This further confirms the above line shape fitting. Fig. 7 shows the superimposed experimental and fitted shift anisotropy for the multiple pulse spectrum. The absence of more than a single shielding anisotropy contributing to the downfield proton species, as inferred from the MAS spectrum, is supported by the fitting of a single shielding tensor to the multiple pulse spectrum.

The relative orientations of the shielding and dipolar tensors obtained above are shown within the layered Cl-Zr-Zr-Cl structure in Fig. 8 to demonstrate the presence of pairs of close hydrogen atoms in tetrahedral interstices. The line shape fitting predicts that the principal axis of the shielding tensor oriented $(\alpha, \beta) = (25.^{\rho}, 60.^{\rho})$ with the inter-protonic vector (Table II), suggests that the major electron density is distributed perpendicular to the layer as seen from Fig. 8. This orientation should in principle be consistent with that obtained through theoretical calculation using [2] or [3].

Heteronuclear dipolar coupling of the downfield species

The fine features observed in Fig. 5 are attributed to the heteronuclear coupling between a quadrupolar nucleus and a spin 1/2 nucleus. In the system investigated they correspond to Cl and H, respectively. As mentioned previously, this relatively small heteronuclear coupling does not affect the spectrum simulation of the oriented dipole and chemical shift interactions for a static spectrum. However, upon further investigation of the fine features of the rotational side bands, more specific details concerning the identity of the downfield component can be found.

The NMR spectra of a spin 1/2 nucleus affected by heteronuclear dipolar coupling to quadrupolar nuclei have been investigated.[27,29-32] In this circumstance the quantization axis of the quadrupolar nucleus deviates from that of the Zeeman field in the presence of the external magnetic field.[29] This results in the product basis eigenstates for the two-body dipolar problem not being pure Zeeman states but a linear combination governed by the quadrupolar coupling Hamiltonian. The heteronuclear dipolar coupling is therefore strongly dependent upon the quadrupole coupling strength and the mixing of Zeeman states of the quadrupolar nucleus.

The heteronuclear dipolar coupling is usually small compared with other interactions and can be resolved only in experiments with single crystals or under sample spinning. For a single crystal experiment Natio, Ganapathy and McDowell[30] found that the heteronuclear dipolar coupling causes nonsymmetric splitting of the spin 1/2 spectrum into 2I+1 peaks. Hexem, Frey, and Opella[29] have shown that heteronuclear

dipolar coupling is not averaged to zero under the magic-angle sample spinning i.e; it does not follow the $P_2(\cos\theta)$ scaling relation. The residual line shapes of the MAS spectrum of the spin 1/2 nucleus are influenced by: (a) the ratio e^2qQ/ω, (b) the sign and the asymmetry parameter of the electric field gradient (e.f.g.) tensor of the quadrupolar nucleus, (c) the internuclear distance, and (d) the mutual orientation of the e.f.g tensor and the dipole internuclear vector. In the sample spinning the splitting can appear as a doublet for a small value of the ratio of the quadrupole coupling constant and Larmor frequency, e^2qQ/ω_0 and as up to 2I+1 splittings when this ratio is very large.

All the above calculations were performed for the two body problem. The influence of a third, either quadrupolar or spin 1/2 nucleus has not been investigated. In principle, a detailed line shape calculation for the variable angle sample spinning results can be performed to obtain the Cl-H internuclear distance, the chlorine electric field gradient, and the mutual orientation between the e.f.g. tensor and the dipole interaction tensor. The possibility of heteronuclear dipolar coupling of hydrogen to more than one Cl nucleus in the system studied and the presence of two Cl isotopes adds additional features to the spectrum. Furthermore, the scalar J coupling between Cl and H is only slightly smaller than the dipolar coupling. These factors increase the complexity of an exact line shape calculation of the heteronuclear coupling MAS spectrum for the proton. Hence only a rough estimation is obtained from the previous calculations.

Although coupling to more than one chlorine nucleus produces a different spectrum, the "size" of the splitting is basically governed by the strongest coupling in the closest Cl-H pair, and if all chlorines coupled to the proton are chemically equivalent, the "size" of the splitting, while not additive, can be approximated by a single Cl-H pair. Therefore, the simplest case is assumed that allows us to apply the calculation performed by Zumbulyadis, Henrichs, and Young[27] and by Menger and Veeman.[32] Comparing the three peak structure observed experimentally (inset of Fig. 5) with their calculations, we find that the ratio e^2qQ/ω_o equals ≈2.5. Since the Larmor frequency for ^{35}Cl is 21.06 MHz and for ^{37}Cl is 17.95 MHz at this magnetic field, this yields a quadrupole coupling constant e^2Qq of ≈ 40 MHz from ratio e^2qQ/ω_o. This value is comparable to that of chlorine nuclei in most organic molecules, where typical quadrupole coupling constants are in the range of 25 to 35 MHz.[33] The heteronuclear dipolar structure caused by the different chlorine isotopes could not be resolved because of the closeness of their Larmor frequencies. The sign of the quadrupole coupling constant is found to be negative ($e^2qQ < 0$). Experimentally, the spacing of 950 Hz between the most upfield and most downfield splittings for a spin 3/2(I) coupled to a spin 1/2(S) equals ≈ 1.6 times that of the dipolar coupling constant, Δ_{Cl-H} where

$$\Delta_{Cl-H} = \gamma_{Cl}\gamma_H \hbar / r^3_{Cl-H} = 11.77\ (kHz \cdot Å^3)\ r^{-3}_{Cl-H} \qquad [7]$$

From this result, we determine that the internuclear Cl-H distance is roughly 2.7 Å. This value is a lower limit since we have assumed the

strongest coupling case, as mentioned previously.

The identity of the species associated with the downfield peak

Attribution of the -5.0 ppm resonance to ZrClH is immediately excluded by comparison with the results of a previous study of these phases.[34,35] ZrClH shows a positive shift anisotropy of approximately 100 ppm which at 220 MHz should give a spectrum with at least a 20 kHz half width; a line width of 12 kHz is observed in the present case.

This downfield signal insteaded evidently arises from a small amount of the hydrogen-richer second phase that was identified in the sample, $ZrClO_xH_y$ ($x < 0.4$, $x + y \leq 1$). This phase has a close packed, layered structure sequenced Cl-Zr-Zr-Cl with O and H distributed randomly over the tetrahedral sites between the zirconium layers.[16,17] This assignment is supported by the following NMR results: (a) The upper limit for the closest hydrogen-hydrogen distance in this compound is equal to the 2.6 to 2.7 Å oxygen separation found in the refined structure of $ZrClO_x$. A value that is quite consistent with the value of 2.5 ±0.2 Å determined from the powder line shape simulation; (b) The hydrogen-chlorine distance in this structure is found ≃ 2.85 Å on the same basis, which is consistent with the lower limit of 2.7 Å estimated from the MAS fine structures; (c) The variation of the ratio of the two peak areas with increasing hydrogen pressure used in the synthesis is consistent with the known nonstoichiometry of hydrogen in $ZrClO_xH_y$. In addition, the change in structure of this phase from the ZrCl to the ZrBr type as x + y approaches unity observed with these samples is consistent with the previous studies of the $ZrClO_xH_y$ sample.[17]

CONCLUSION

Proton NMR studies on nominal Zr_6Cl_{12} preparation containing minor $ZrClO_xH_y$ impurity levels revealed the presence of two completely different hydrogen species. The shift of the upfield peak at ≈ 500 ppm relative to $H_2O(l)$ at ambient temperature shows a linear dependence on inverse temperature indicating that the shift originates mainly because of the presence of an unpaired electron in the vicinity of the corresponding hydrogen nucleus. The local hyperfine splitting is determined from this shift-T^{-1} dependence to be 28.29 MHz (6.64 Kgauss). From the unpaired electron density, this hydrogen is located inside the octahedral zirconium cage where a single localized unpaired electron is predicted from the stoichiometry $Zr_6Cl_{12}H$. The high electronic density within the Zr_6 octahedron and the probable hydridic character of the proton investigated may also contribute to the observed temperature dependence of the shift. Total suppression of this resonance in MREV-8 multiple pulse experiments and the invariance of the line width to temperature indicate that the proton within the Zr_6 metal cluster must exhibit a rapid random motion on a time scale short compared with the 18 μsec sampling time of the experiment,

A second hydrogen species is observed 5.0 ppm downfield from $H_2O(l)$ with an isotropic value that is independent of temperature. Variable-angle sample spinning spectra show that the peak is composed of three major inhomogeneous interactions, namely the shielding anisotropy, the homonuclear dipolar interaction between a pair of hydrogens, and the heteronuclear dipolar interaction between the protons and one or more ^{35}Cl (or ^{37}Cl) nuclei. This heteronuclear dipolar interaction is about

an order of magnitude less than the dominant shielding and homonuclear dipolar interactions. This fact allows a comparison of the line shape associated with noncoincident dipolar and chemical shift tensors with that of the static powder spectrum. The fitting shows that the dipolar splitting between the proton pair is 8.6 ±0.5 kHz, corresponding to an internuclear proton distance of 2.5±0.2 Å. The shift anisotropy δ is -22.7 ppm and the asymmetry parameter, η=0.55. Principal axis of the dipolar interaction (coincide with the internuclear vector) is found to be oriented with Euler angles (α, β) = (25.0°, 60.0°) with respect to the shift tensor. Since the shift tensor is related to the electron density, the noncoincident orientation is found to be consistent with the $ZrClO_xH_y$ structure. The proton shielding parameters were confirmed by the homonuclear decoupling experiments using the MREV-8 pulse sequence.

A simple line shape analysis of the hetronuclear dipolar interaction from the MAS rotation side shows that the the proton pairs in the phase $ZrClO_xH_y$ are coupled to one or more equivalent chlorine nuclei with a $\bar{d}$(H-Cl) approximately 2.7 Å. This and the proton separation are both consistent with the structure of $ZrClO_xH_y$.

ACKNOWLEDGEMENTS

The NMR part of this research was supported by the U.S. Department of Energy, Office of Basic Energy Sciences, Chemical Science Division, under contract W-7405-Eng.82. The synthetic and structural portion (R.P.Z) was supported by the National Science Foundation, Solid State Chemistry, Grant DMR-8318616, and was also performed in the Ames Laboratory, DOE.

Table I

Locations and the transverse relaxation times of the upfield peak of $Zr_6Cl_{12}H$ at two fields

Field	Location		T_2^* relaxation time (μ sec)		
ν_0(MHz)	(ppm)	(kHz)	Gaussian	Lorentzian	Lrnz*Gaus
56.03	500.3	28.03	80.8±9.3	74.4±18.	83.7±11.
220.15	484.2	106.6	52.5±2.1	42.5±4.2	53.4±3.1

Table II

Fitting parameters for the two interactions of the downfield peak for $ZrClO_xH_y$ at 220 MHz and 56 MHz

Field(MHz)	DCP(kHz)	δ(kHz)[a]	η	α(deg)[b]	β(deg)
220.15	8.8	5.2	0.55	25.0	60.0
56.03	9.3	1.25	0.6	45.	55.0

[a] δ average value = -22.9 ppm.

[b] This fit is relatively insensitive to the angle α.

REFERENCES

1. A. Cisar, Ph.D. thesis, Iowa State University, Ames, IA 1978.

2. A. Cisar, J. D. Corbett, and R. L. Daake, Inorg. Chem. 18, 836 (1979).

3. J. D. Smith, and J. D. Corbett, J. Am. Chem. Soc. 107, 5704 (1985).

4. C. G. Fry, J. D. Smith, B. C. Gerstein, and J. D. Corbett, Inorg. Chem. 25, 117 (1986).

5. H. Imoto, J. D. Corbett, and A. Cisar, Inorg. Chem. 20, 145 (1981).

6. A. Simon, Z. Anorg. Allg. Chem. 355, 311 (1967).

7. H. Imoto, and J. D. Corbett, Inorg. Chem. 19, 1241 (1980).

8. R. G. Barnes, Department of Physics, Iowa State University, private communication, (1980).

9. R. P. Ziebarth, and J. D. Corbett, J. Am. Chem. Soc. 107, 4571 (1985).

10. S. J. Hwu, and J. D. Corbett, J. Solid State Chem. 64, 331 (1986).

11. R. P. Ziebarth, and J. D. Corbett, J. Am. Chem. Soc. 109, accepted (1987).

12. E. D. Becker, High Resolution NMR (Academic Press, New York, 1980).

13. B. C. Gerstein, and C. R. Dybowski, Chapter 3 in Transient Techniques in NMR of Solids (Academic Press, New York, 1985).

14. U. Haeberlen, Chapter 2, in High Resolution NMR in Solids, Selective Averaging, J. S. Waugh eds. (Academic Press, New York, 1976).

15. S. D. Wijeyesekera, and J. D. Corbett, Inorg. Chem. 25, 4709 (1986).

16. L. M. Seaverson, and J. D. Corbett, Inorg. Chem. 22, 3203 (1983).

17. S. D. Wijeyesekera, and J. D. Corbett, Ames Laboratory unpublished research, Ames, IA (1985).

18. T. T. P. Cheung, L. E. Worthington, P. D. Murphy, and B. C. Gerstein, J. Magn. Reson. 41, 158 (1980).

19. B. C. Gerstein, Phil. Trans. Roy. Soc. Lond. A 299, 521 (1981).

20. I. D. Gay, J. Magn. Reson. 58, 413 (1984).

21. J. D. Corbett, and H. S. Marèk, Inorg. Chem. 22, 3194 (1983).

22. P. J. Chu, Manual for interactive eight-peak fitting. Ames Laboratory Report, Jan. (1986).

23. N. Ramsey, Phys. Rev. 78, 699 (1950).

24. K. F. Lau, and R. W. Vaughn, Chem. Phys. Lett. 33, 550 (1975).

25. J. Jesson, Chapter 1 in NMR of Paramagnetic Moleculaes, G. La Mar, W. Horrocks, and R. Holm, eds. (Academic Press, New York, 1973).

26. A. Carrington, and A. McLachlan, Chapter 13 in Introduction to Magnetic Resonance (Harper & Row, New York, 1967).

27. N. Zumbulyadis, P. M. Henrichs, and R. H. Young, J. Chem. Phys. 46, 257 (1981).

28. P. J. Chu, and B. C. Gerstein, J. Chem. Phys. submitted (1987).

29. J. G. Hexem, M. H. Frey, and S. J. Opella, J. Chem. Phys. 77, 3847 (1982).

30. A. Natio, S. Ganapathy, and C. A. McDowell, J. Magn. Reson. 48, 367 (1982).

31. R. A. Haeberkorn, R. E. Stark, H. van Willigen, and R. G. Griffin, J. Am. Chem. Soc. 103, 2534 (1981).

32. E. M. Menger, and W. S. Veeman, J. Magn. Reson. 46, 257 (1981).

33. E. A. C. Lucken, Chapter 13 in Nuclear Quadrupole Coupling Constants (Academic Press, New York, 1969).

34. P. D. Murphy, and B. C. Gerstein, J. Magn. Reson. 34, 333 (1979).

35. P. D. Murphy, and B. C. Gerstein, J. Chem. Phys. 70, 4552 (1979).

Figure 1. A [110] projection of the structure of the $Zr_6Cl_{12}H$. The proton is believed to occupy the center of the Zr_6 clusters.

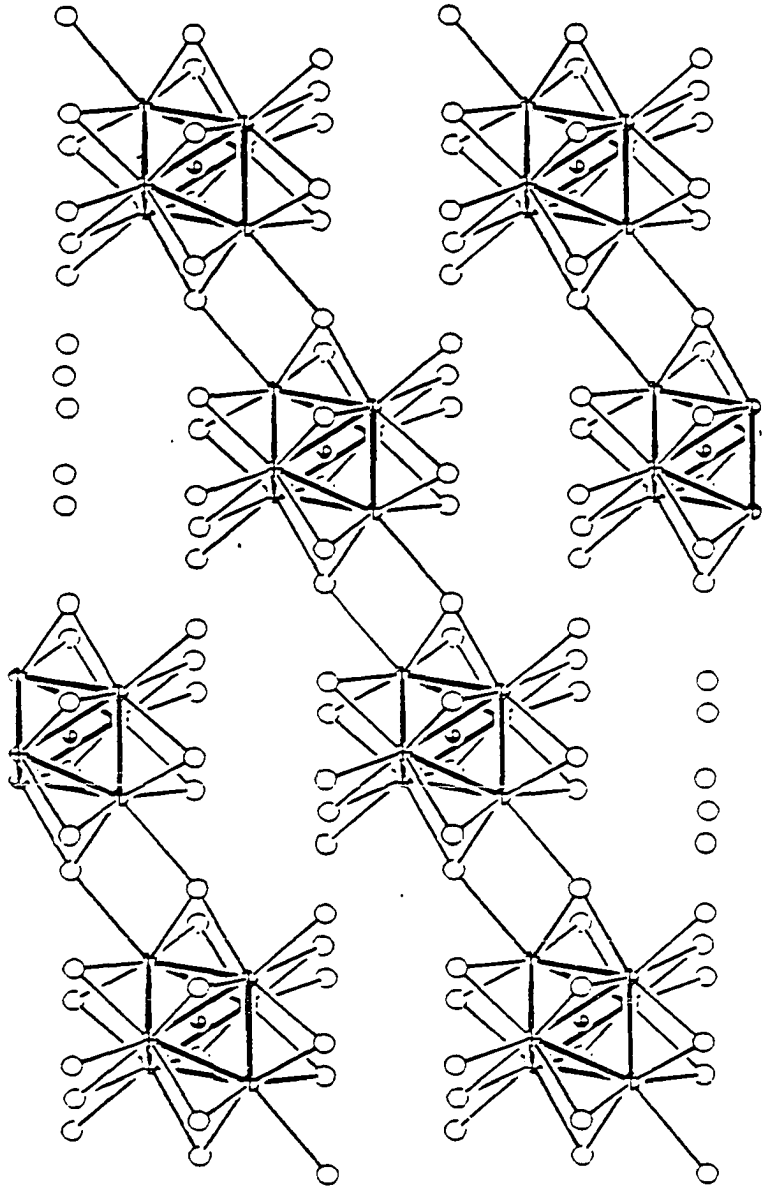

Figure 2. ^{1}H NMR spectrum for the $Zr_6Cl_{12}H$ + $ZrClO_xH_y$ samples at 220 and 56 MHz. Notice the large upfield shift at approximately 500 ppm.

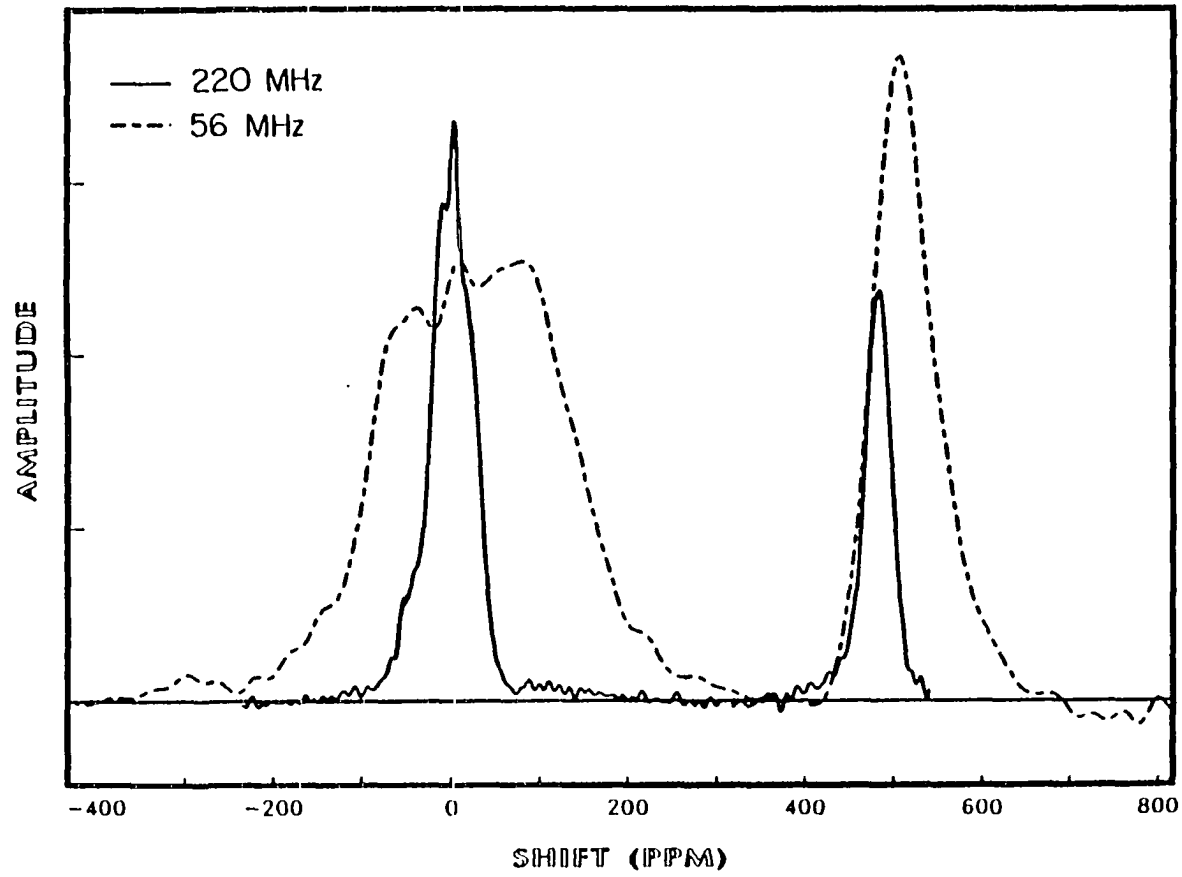
220 MHz
56 MHz
AMPLITUDE
-400
-200
0
200
400
600
800
SHIFT (PPM)

Figure 3. ^{1}H NMR spectrum of Fig. 1 re-drawn in kHz units to demonstrate the relative line widths. The upfield peak shows a good fit to a Gaussian line shape. The downfield spectra show the features of mutually oriented dipolar and chemical shift interactions.

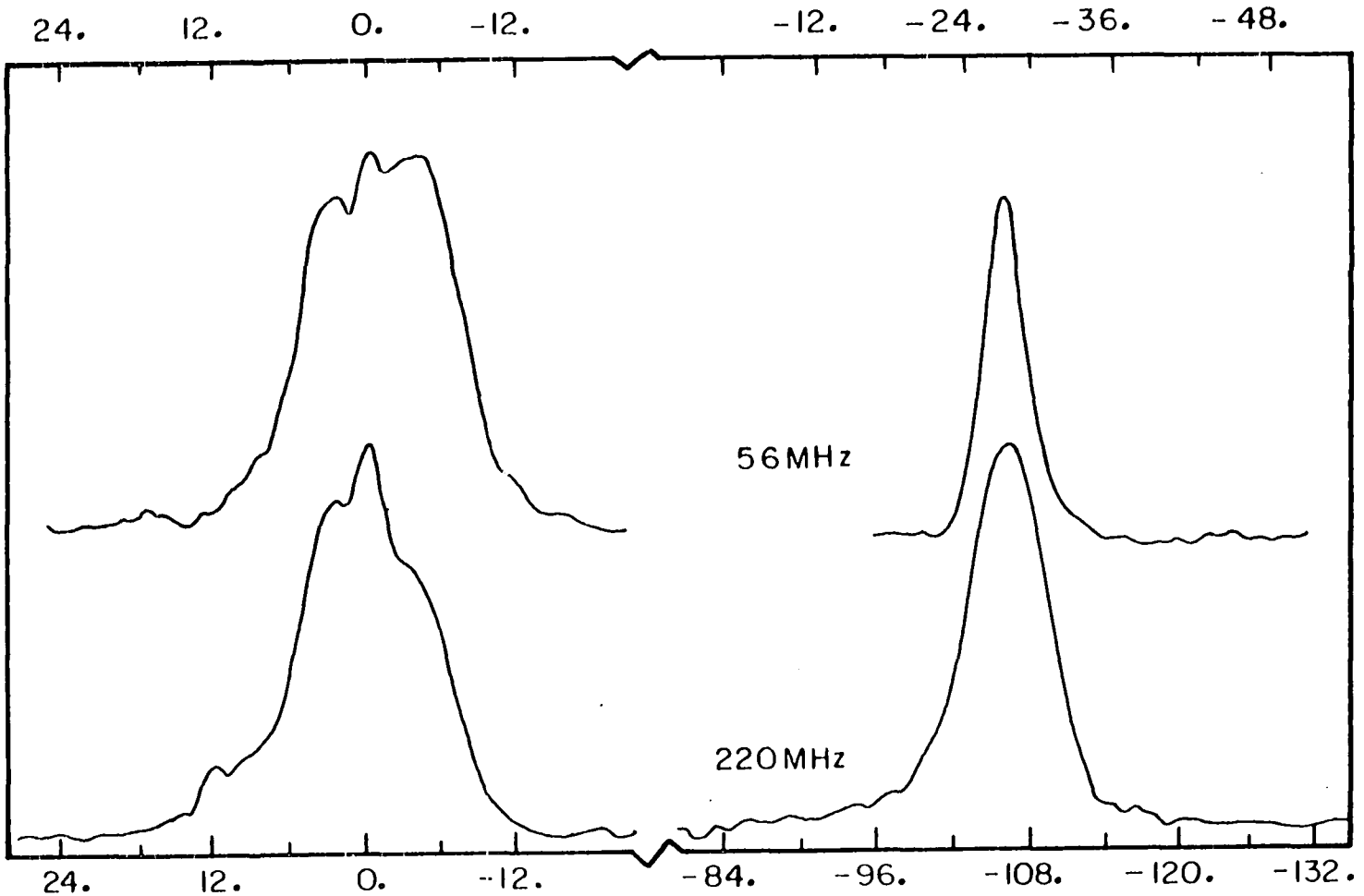
24.
12.
0.
-12.
-12.
-24.
-36.
-48.
56MHz
220MHz
24.
12.
0.
-12.
-84.
-96.
-108.
-120.
-132.
Shift (k Hz) → Up Field

Figure 4. Temperature variation of the shift of the upfield peak between 218 K and 298 K. The linear relation with T^{-1} is characteristic of a Curie-Weiss paramagnetic shift from a proton coupled to an unpaired electron.

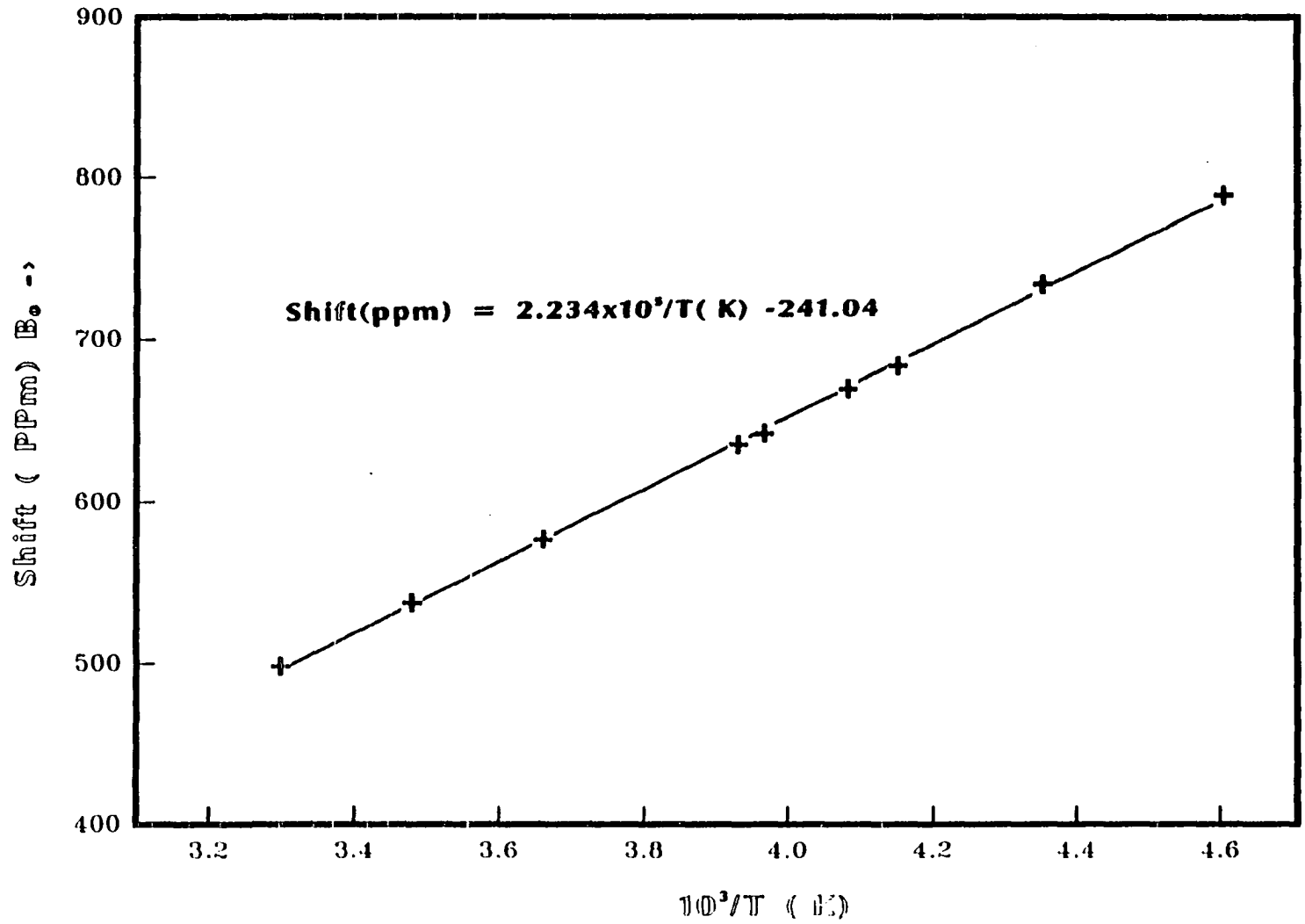
900
800
700
600
500
400
Shift (PPm) B. -
Shift(ppm) = 2.234x10³/T(K) -241.04
3.2
3.4
3.6
3.8
4.0
4.2
4.4
4.6
10³/T (K)

Figure 5. The magic-angle sample spinning (MAS) spectra at 220 MHz. The inset shows the change of the center band with sample spinning at 52.7, 54.7 and 56.7 degrees with respect to the magnetic field. The spinning frequency for the sealed samples is 2 kHz which allows the profile of the inhomogeneous interaction to be maintained.

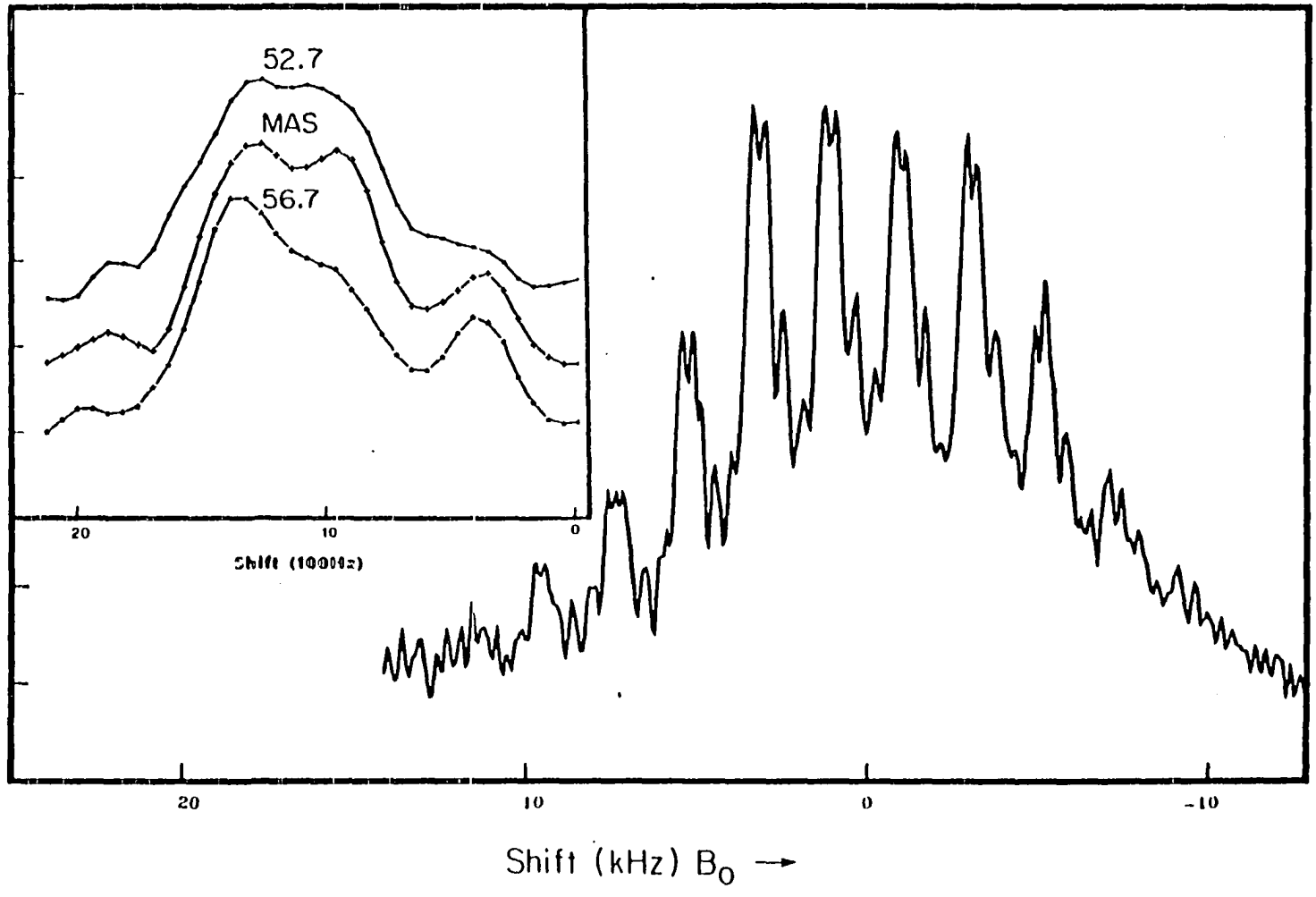
52.7
MAS
56.7
20
10
0
20
10
0
-10
Shift (kHz) B_0 →

Figure 6. The fitted (bottom) vs. experimental (top) spectra of the down field component at 220 and 56 MHz. The parameters are those listed in Table II.

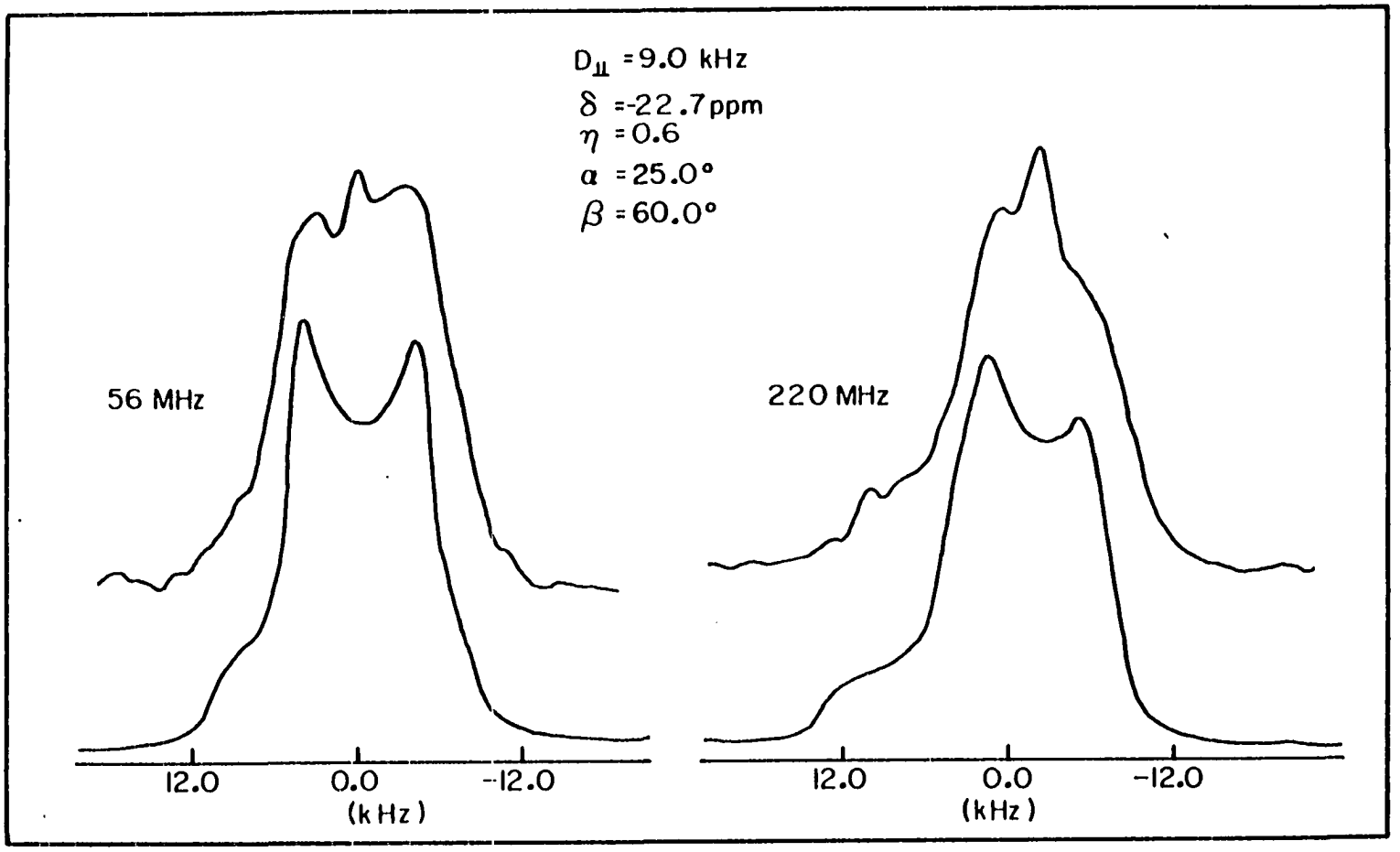
$D_{\perp\!\!\!\perp}$ = 9.0 kHz
δ = -22.7 ppm
η = 0.6
α = 25.0°
β = 60.0°
56 MHz
220 MHz
12.0
0.0
-12.0
(kHz)
12.0
0.0
-12.0
(kHz)

Figure 7. Superposition of a single shielding tensor with the MREV-8 multiple pulse spectrum (36 μsec cycle time). The calculated parameters are $\delta = -22.7$ ppm, $\eta = 0.6$ ppm. This spectrum has been corrected by the scaling factor 1.95.

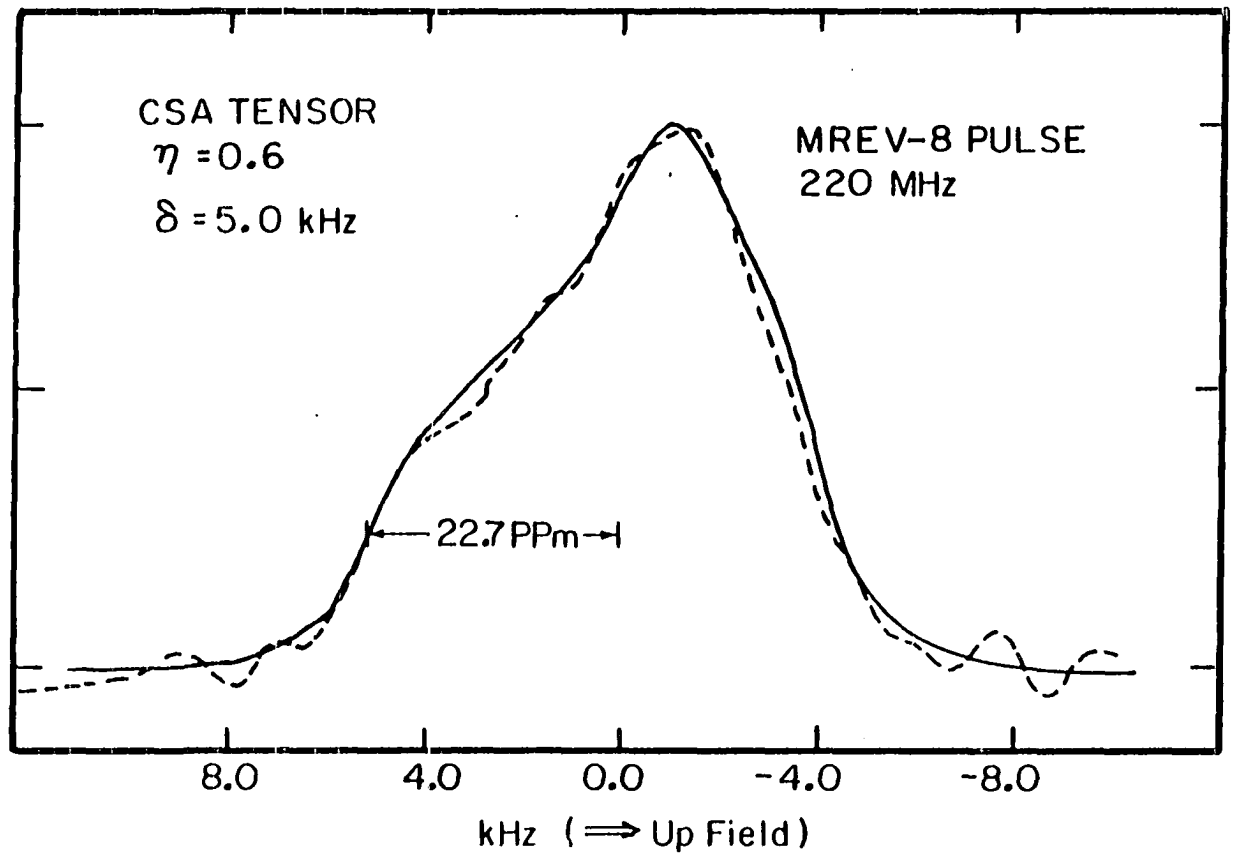
CSA TENSOR
η = 0.6
δ = 5.0 kHz
MREV-8 PULSE
220 MHz
22.7 PPm
8.0
4.0
0.0
-4.0
-8.0
kHz (⟹ Up Field)

Figure 8. The orientation of the dipolar and the chemical shift interactions of the downfield proton species, $ZrClO_xH_y$. The inter-proton vector determines the Z axis of the axially symmetric dipolar tensor. The orientation of these two interactions is seen to be consistent with the structure. Parameters are those listed in table II from fitting of the static powder spectrum at 220 MHz.

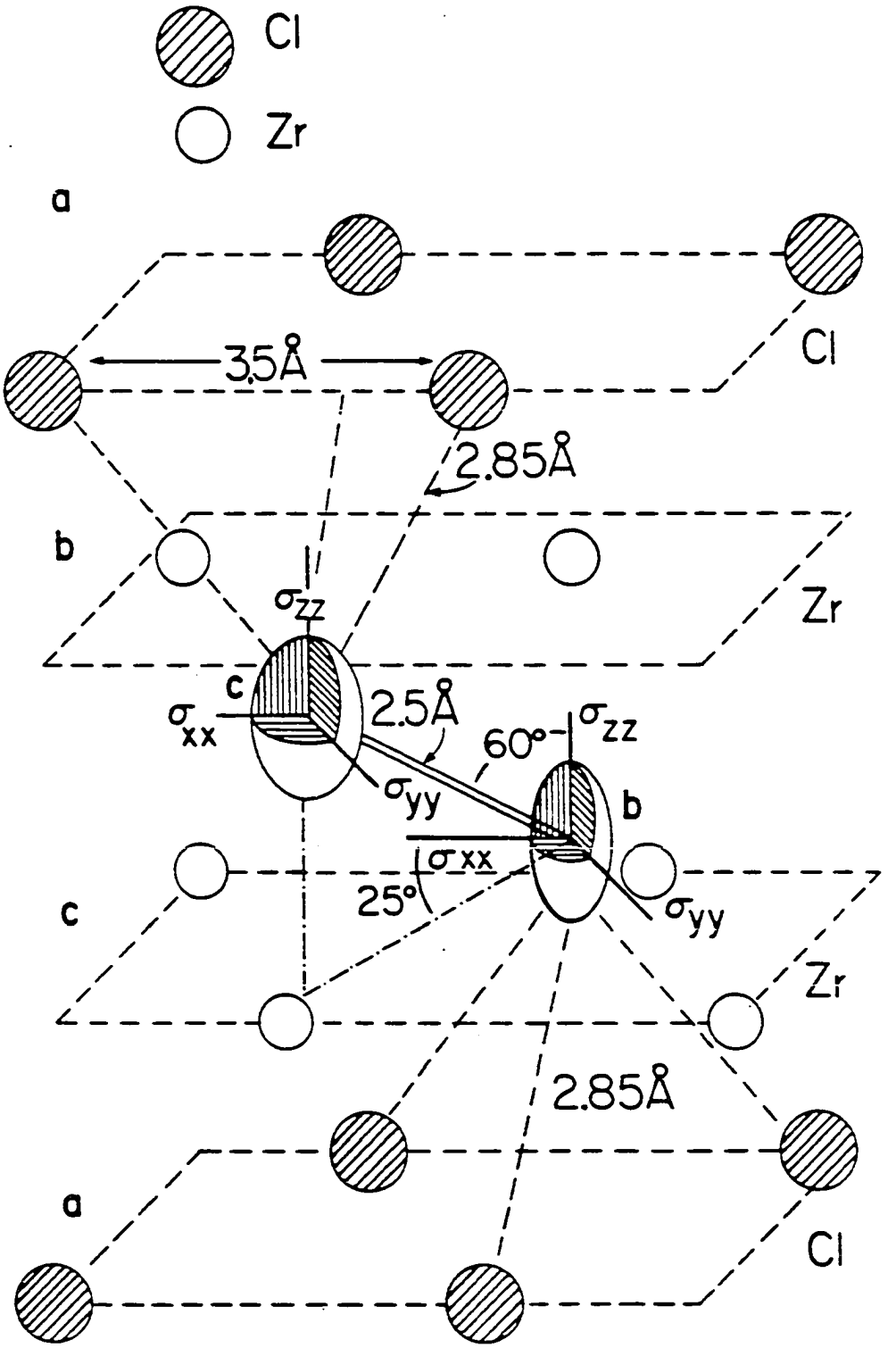
Cl
Zr
a
3.5Å
Cl
2.85Å
b
Zr
σ_{zz}
c
σ_{xx}
2.5Å
60°
σ_{zz}
σ_{yy}
b
σ_{xx}
25°
c
σ_{yy}
Zr
2.85Å
a
Cl

GENERAL CONCLUSIONS AND APPLICATIONS

The NMR line shape study of both static and dynamic system are demonstrated in four parts under different conditions. The conclusions and the application to an appropriate system in individual part are summarized.

Part I. In a nuclear system governed by two interactions where neither interactions dominates, the combined effects are an inhomogeneously broadened spectrum which depends not only upon the individual interaction parameters but also strongly upon the mutual orientations between these tensors. The current studies shows that: (a) the effects of the mutual orientation between interaction tensors are reflected in both the static powder line shape and the distinctive features of the field dependent critical frequencies; and (b) the tensorial orientation between interactions and the individual interaction parameters can be determined by analyzing the critical frequencies (singularities, shoulders, and steps) of a powder spectrum vs. the magnetic field strength.

Although the method is developed for both satellite transitions and the central transition of spectra of quadrupolar nuclei under the influence of a shift interaction, modification can be made easily to incorporate three interactions, e.g., quadrupolar, dipole and shift interactions, or to involve higher order perturbations.

Part II. The NMR spectrum of ^{133}Cs in Cs exchanged mordenite indicates that the e.f.g. tensor increases with decreasing water content. The coupling constant increases from 210 kHz for the fully hydrated sample to 3.1 MHz for the anhydrous sample. Under MAS, the

anhydrous sample shows two peaks, with relative intensities of roughly 1:3. Two different sites are clearly observed in the anhydrous sample with center of mass of the peaks at -191.0 ppm and -57 ppm. The assignment of the peaks to Cs locations is made on the basis of the structural difference of the six-ring coordination site VI from the eight-ring sites II, and IV. After correcting for the second order quadrupolar shift the down field peak, -24 ppm; may be attributed to site VI while sites II and IV with similar structures yield similar chemical shifts at -157 ppm and -186 ppm. In the fully hydrated sample all three sites possess an identical isotropic value of -64 ppm.

Part III. From the dynamic NMR line shape studies, it is found that the anomalous X-ray thermal ellipsoid observed for sodium in $NaMo_4O_6$ is not due to isotropic thermal motion but due to anisotropic exchange motion between four equivalent sites, where the sodium resides off center of the tetragonal oxygen cluster. This result has the implication that the sodium atom binds more strongly with four oxygen atoms with a shorter bond distance than being equally shared with eight oxygens with longer internuclear distance. From the dynamic line shape studies of the second order central transition, an activation energy of discreet site jump motion is calculated to be 1.95 Kcal/mole with a temperature independent E_a. The temperature dependent QCC, determined from the calculation shows two linear dependent regions separated by 140 K with the coefficients equal 1.5 kHz/K and 3.9 kHz/K respectively. The difference in the temperature coefficients of the quadrupolar coupling constant implies a phase transition may take place.

The anomalous up field peak that can not be accounted for by the

dynamic motion model is found to closely related to the structural incommensuration of this channel compound. The quasicontinuous e.f.g. distribution associated with this phase transition predicts both the appearance of the upfield shoulder and the gradual shift of the anomalous peak toward the major portion of the spectra. The jump discontinuity appeared in the quadrupole coupling constant further supports the incommensuration structure with the I-C transition temperature estimated to be around 140 K. Several incommensuration structure models have been proposed.

Part IV. Proton NMR studies on nominal Zr_6Cl_{12} preparation containing minor $ZrClO_xH_y$ impurity levels revealed the presence of two completely different hydrogen species. The shift of the upfield peak at $\simeq$ 500 ppm relative to $H_2O(l)$ at ambient temperature shows a linear dependence on inverse temperature indicating that the shift originates mainly because of the presence of an unpaired electron in the vicinity of the corresponding hydrogen nucleus. The local hyperfine splitting is determined from this shift-T^{-1} dependence to be 28.29 MHz (6.64 Kgauss). From the unpaired electron density, this hydrogen is located inside the octahedral zirconium cage where a single localized unpaired electron is predicted from the stoichiometry $Zr_6Cl_{12}H$. The high electronic density within the Zr_6 octahedron and the probable hydridic character of the proton investigated may also contribute to the observed temperature dependence of the shift. Total suppression of this resonance in MREV-8 multiple pulse experiments and the invariance of the line width to temperature indicate that the proton within the Zr_6 metal cluster must exhibit a rapid random motion on a time scale shorter than 18 μsec.

ACKNOWLEDGEMENTS

To my wife, Meiling whose assistance
and encouragement made this work possible.
Any achievement belongs to her.

I would like to thank a few people who have assisted this work.

I have benefited extensively from conversations with Dr. Richard Barnes regarding the quadrupole and the Knight shift interactions.

Thanks to Dr. Robert McCarley who showed continuous support during the studies of the dynamic behaviour and the incommensurate structures of the $NaMo_4O_6$ samples.

Also thanks to Dr. Hugo Franzen for his various inspiring discussions concerning the second order phase transition, which substantiated the work of the structural incommensuration in $NaMo_4O_6$.

Dr. David Torgeson is gratefully acknowledged for the assistance in obtaining the variable temperature and high field ^{23}Na spectra in Dr. R. Barnes's laboratory. Critical discussions of the schemes of constructing the quadruture phase detector and the r.f. units are also acknowledged.

Thanks to Robin Ziebarth of Dr. John Corbett's group who supplied the samples of $Zr_6Cl_{12}H$ and $ZrClO_xH_y$ in the zirconium studies and H-D Yang of Dr. Robert Shelton's group who supplied the $Lu_5T_4Si_{10}$ (T=Ir, Rh) and $Sc_5Ir_4Si_{10}$ samples in the studies of the ICDW phase transitions.

Thanks to Dennis Jensen and Harold Skank of the instrumentation service for helpful discussions and assistance in the NMR experiments.

There are many good friends who have made my stay in the U.S. a pleasurable, memorable and inspiring experience. Lance Miller, Dr. Russ Walker, Dr. Chuck Fry, Dr. Serge Lacelle, and Joe Iwamiya to name just a few.

I would finally like to sincerely thank Dr. Bernard C. Gerstein for his enthusiastic guidance, encouragement and support during the past years. His friendship, scientific insights and particularly the ability to bring out the best of each student's potential are gratefully appreciated.

APPENDIX A: COMPARISON OF DIRECT AND INDIRECT SPECTRUM CALCULATIONS

This appendix illustrates the mathematic identity between the method proposed in equation [20] of Part I and other techniques developed earlier in calculating the spectrum. The advantages of the computational technique by first evaluating the FID developed here over other methods will be discussed in terms of the simplicity, speed and the easiness of formulation.

Identity relation is illustrated by deriving the core calculation formulae of other direct methods from the theory proposed in the previous section.

First we insert the variable $\Omega=(\theta, \phi)$ into [20] in part I and let the FID for that unique orientation Ω be $f(\Omega, t)$ incorporating the effect of spin-spin relaxation, the transient signal for a single quantum transition with transition probability P_k between levels k-1 and k becomes:

$$f(\Omega,t)=g(t)\cdot e^{-i\omega_k(\Omega)t}\cdot P_k \qquad [20]$$

Where $\hbar\cdot\omega_k(\Omega)=\Delta\varepsilon_{k,k-1}$

$\langle f(t)\rangle$ is used to denote the powder averaged FID, and $\langle F(\omega)\rangle$ for the averaged spectrum. The averaged transient signal from [20] can be written as:

$$\langle f(t)\rangle=\frac{N}{4\pi}\int_\Omega d\Omega\ f\ (\Omega,t)=\frac{N}{4\pi}\int_0^\pi d\theta\sin\theta\int_0^{2\pi}d\phi\ f\ (\Omega,t) \qquad [A\text{-}1]$$

The expression $\int_\Omega d\Omega$ will be used in the following for the average of spatial variable $\int\sin\theta d\theta\int d\phi$. N is the normalization constant proportional to the density of the nuclei and the transition

probability.

Numerically the average can be approximated by summation over discreet increments of angles Θ and ϕ. Calculating the powder averaged frequency spectrum on the other hand can be formulated similarly.

Now let $F(\Omega, \omega)$ be the corresponding complex Fourier transform of $f(\Omega, t)$, the averaged spectrum will be:

$$\langle F(\omega)\rangle = \frac{N}{4\pi} \int_{\Omega} d\Omega\, F(\Omega,\omega) = \frac{N}{4\pi} \int_{\Omega} d\Omega \int_0^{\infty} dt\, e^{-i\omega t} f(\Omega,t) \qquad [A\text{-}2a]$$

$$= \frac{N}{4\pi} \int_0^{\infty} dt\, e^{-i\omega t} \int_{\Omega} d\Omega\, f(\Omega,t) \qquad [A\text{-}2b]$$

Combining [A-1] and [A-2b], we obtain the well known results.

$$\langle F(\omega)\rangle = \int_0^{\infty} dt\, e^{-i\omega t} \langle f(t)\rangle \qquad [A\text{-}3]$$

The real and the imaginary parts yields the in phase absorption and the out of phase dispersion respectively. Notice that [A-2a] and [A-2b] differ in the order of integration which implies that the order of powder average and the Fourier transform can be interchanged without affecting the results. Henceforth we have reached an important conclusion that the final powder spectrum, $\langle F(\omega)\rangle$ can be reached by the following two mathematically equivalent approaches:

(1). By powder averaging the Fourier transform of the individual FID of each orientation; $F(\Omega,t)$ according to [A-2a] and

(2). By the Fourier transform of its powder averaged FID $\langle f(t)\rangle$ according to [A-2b], or equivalently by applying [A-1] first and then applying [A-3].

It is the second approach that is taken in the present work and all

other line shape calculation performed in the thesis. Several advantages using this approaches as compared with other direct approaches derived from [A-2a] are pointed out later.

Before this comparison of these two approaches, we wish to develop several important fundamental relations from [A-2a] which becomes the bases of several well known variations of the first approaches in direct calculating the spectrum. And since [A-2a] and [A-2b] are equivalent, the following derivation implies the identity between the method proposed here and the other well known direct methods previously prescribed.

As mentioned before, g(t) in [20] is spatially independent, it can be separated from the averaging over $\Omega=(\Theta, \phi)$ which broadens the delta response of $F(\Omega, \omega)$. Hence the Fourier transform of [20] yields a delta function $\delta(\omega-\omega_k(\Omega))$ convoluted with $G(\omega)$. δ is the Dirac delta function that will be zero everywhere but equal to unity when $\omega=\omega_{km}(\Omega)$. and $G(\omega)$ is the corresponding Fourier transform of g(t). From the above discussion the powder average for the frequency spectrum according to eq [A-2a] is equivalent to the following:

$$I(\omega)=\mathrm{Re}\langle F(\omega)\rangle = G(\omega) * \{ \frac{N}{4\pi} \int_{\Omega} \delta(\omega-\omega_k(\Omega))d\Omega\}$$
$$= G(\omega) * H(\omega) \qquad [A-4]$$

Where * represents convolution, $I(\omega)$ is the line shape of the final absorption powder spectrum, and $H(\omega)$ represents the corresponding function as understood. This equation states that the powder spectra are calculated by superimposing all the stick spectra corresponding to each unique spatial orientation Ω of the K-th transition which resonates

at $\omega=\omega_k(\Omega)$ as represented by function $H(\omega)$, which is finally convoluted with the broadening function $G(\omega)$ to yield the powder spectrum.

Although [A-4] already provides a direct approach in simulating the spectrum, there are two widely used variations originated from this equation will be derived in the follows.

(1). Convolution method:

The first variation of this method is performed when function $G(\omega)$ can be expressd by an analytical expression which is physically meaningful.

By utilizing the property of Dirac delta function that

$$\int_{-\infty}^{\infty} g(x')\cdot\delta(x-x')dx' = g(x) \qquad [A-5]$$

and by directly applying the convolution relation to [A-4], equation [A-4] can be further simplified as:

$$\begin{aligned} I(\omega)= G(\omega)* H(\omega)&= \int G(\omega')\cdot H(\omega-\omega')\, d\omega' \\ &= \frac{N}{4\pi}\int G(\omega')\cdot\{\int_{\Omega}\delta(\omega-\omega'-\omega_k)d\Omega\}\, d\omega' \\ &= \frac{N}{4\pi}\int_{\Omega}\{\int G(\omega')\cdot\delta(\omega-\omega'-\omega_k)d\omega'\}\, d\Omega \\ &= \frac{N}{4\pi}\int_{\Omega} G(\omega-\omega_k(\Omega))\, d\Omega \end{aligned} \qquad [A-6]$$

Changing the order of integration in the third step in the derivation is valid since $G(\omega)$ is spatially independent. Equation [A-6] states that the spectrum line shape $I(\omega)$ of the k-th transition can be readily calculated by replacing the variable ω in $G(\omega)$ by $\omega-\omega_k(\Omega)$ and perform the powder average to obtain the final spectrum.

(2). Gradient method:

A second variation of this direct approach is much simpler in form. This expression relates more directly to the orientation dependent transition energies which we shall derive also from [A-4] by changing the parameters. In order to simplify the following discussion we shall assume $G(\omega)$ being a delta function. General expression for $G(\omega)$ can be easily incorporated after the $H(\omega)$ has been derived.

The identity relation, [A-7] shall be derived first. First integrating over the variable ω on both side of [A-4] and applying the relation of Dirac delta to [A-4] yields

$$\int_{-\infty}^{\infty} H(\omega)d\omega = \frac{N}{4\pi} \int_0^{\pi} d\theta \sin\theta \int_{-\infty}^{\infty} \delta\{(\omega-\omega_k(\theta,\phi)\}d\omega$$

$$= \frac{N}{4\pi} \int_{\Omega} d\Omega \qquad [A-7]$$

This equation states that the first moment of the spectrum is conserved, which is independent of principal axis frame transformation since the spatially dependent resonance frequency is absent on the left hand side. Next by changing the variable of ω_k to its implicit variable θ, ϕ as follows:

$$d\omega_k(\theta,\phi) = \frac{d\omega_k}{d\theta} d\theta + \frac{d\omega_k}{d\phi} d\phi = \text{grad}\{\omega(\theta,\phi)\}\cdot(d\theta, d\phi)$$

$$= |\text{grad}\{\omega_k(\theta,\phi)\}||dr|\cos\xi \qquad [A-8]$$

Where ξ is the angle between the vector $\text{grad}(\omega_k)$ and the displacement vector $dr = (d\theta, d\phi)$. When the gradient is not zero, we can divide $\text{grad}(\omega_k)$ on both side of the above equation and integrating over

ω_k, this gives:

$$\int d\omega_k \left|\text{grad}\{\omega_k(\Theta,\phi)\}\right|^{-1} = \int \left|(d\Theta, d\phi)\right| \cos\xi$$

The left hand side of the above equation is a constant. This relation is finally inserted in to [A-7] which gives:

$$\begin{aligned}
\int H(\omega)d\omega &= N' \oint_{\Omega} \{\int[\int \delta\{\omega-\omega_k(\Omega)d\omega]\cdot \left|\text{grad}\{\omega_k(\Omega)\}\right|^{-1} d\omega_k(\Omega)\}d\Omega \\
&= N' \oint_{\Omega} \{\int[\int \delta\{\omega-\omega_k(\Omega)\cdot \left|\text{grad}\{\omega_k(\Omega)\}\right|^{-1} d\omega_k(\Omega)]d\omega\}d\Omega \\
&= N' \oint_{\Omega} \{\int \left|\text{grad}\{\omega_k(\Omega)\}\right|^{-1}_{\omega=\omega_k} d\omega\}d\Omega \\
&= N' \int\{\int_{\Omega} \left|\text{grad}\{\omega_k(\Omega)\}\right|^{-1}_{\omega=\omega_k} d\Omega\}d\omega
\end{aligned}$$

By equating the integrands on both sides we have

$$H(\omega) = N' \int d\Theta \text{isn}\Theta \int d\phi \left|\text{grad}\{\omega_k(\Theta,\phi)\}\right|_{\omega=\omega_k} \qquad [A\text{-}9]$$

An equivalent expression of [A-9] frequently used is obtained after replacing $\sin\Theta d\Theta = -\cos\Theta = d\mu$ which gives:

$$H(\omega) = N' \int d\mu \int d\phi \left|\text{grad}\{\omega_k(\mu,\phi)\}\right|^{-1}_{\omega_k=\omega} \qquad [A\text{-}10]$$

Important physically meaning of [A-9] and [A-10] is that: the inverse of the amplitude of the gradient represents the contributions to the intensity for the individual orientation $\Omega=(\Theta,\phi)$ or (μ,ϕ) at the frequency $\omega=\omega_k(\Omega)$.

The conditions when the gradient approaches zero corresponds to a flattening region in the $\omega_k(\Theta, \phi)$ surface as can be seem from [A-7] that $d\omega_k$ also approaches zero. Hence these points may corresponds to a

saddle points or a local optimum in the ω_k surfaces. The character of these points can be determined by Wronskian determinant which we will not discuss further. The significance of equation [A-9] or [A-10] is that the singularities of the spectrum can be obtained from the condition when grad($\omega_k(\theta, \phi)$=0 where intensity $I(\omega)$ is infinity at $\omega=\omega_k(\Omega)$. Hence combining with the character of these critical points the prominent feature of the spectrum can be determined even before a complete line shape calculation is performed.

In deriving [A-7], [A-8], [A-9] and [A-10] we have neglected the broadening function $G(\omega)$ by assuming that it is a delta function. For any other type of functions used for $G(\omega)$ the final powder line shape will be a results of convolution of $G(\omega)$ and $H(\omega)$ as was indicated in [A-4]. A result in applying this function is a smoothing of the spectrum calculated by the above equations. And in some cases the prominent features of the spectrum may be smeared out it is smoothed by a relative large homogeneous interaction or a inhomogeneous lattice distribution.

Notice that the assumption that each and every inhomogeneous delta function is influenced by the same homogeneous broadening effect represented by $g(t)$ has been made. Therefore the orientationally independent $G(\omega)$ has also been assumed. The assumption is valid when it accounts for the homogeneous broadening due to the nonsecular terms of the dipolar Hamiltonians. It is not true when the interaction parameters such as the electric field gradient possess inhomogeneous distribution, specifically depending on the translational lattice variable x hence the broadening function becomes $g(x,t)$. The powder

spectrum will require further average over x, in this case the separation of $G(\omega)$ from the average over the variable $\Omega=(\theta,\phi,x)$ will not be allowed.

In the following, we shall proceed comparing the two approaches as indicated in equation [A-2a] and [A-2b] from the point of numerical stabilities, calculation speed (cpu time) and the efforts in programing.

In practical calculation, it was point out earlier by several authors that the first method is the most straightforward scheme especially when the relation between orientation and frequency distribution can be expressed analytically. Usually the integration or summation can be replaced by evaluating an simpler function such as elliptical integral of the first kind for shift interaction. Unfortunately the analytical form does not generally available when the spatial dependent energy becomes more complicated such as that of the second order quadrupolar interaction. When function g represents inhomogeneous lattice distribution which is nonrandom as can be represented by a Gaussian function but rather a quasicontinuous distribution which does not posses any analytical form, the above direct method will be extremely hard to evaluate. Other disadvantages in using this approach are noted:

First calculating the spectra according the [A-2a] or the related relations [A-4], [A-6], [A-9], or [A-10] the frequency ω_k as well as the gradient will need to be evaluated. The frequencies will then be truncated to give the corresponding discreet integer channel which causes some error. Secondly the gradient is evaluated to obtain the

points where infinity intensity is encountered before convoluting with a broadening function as pointed out before

On the other hand, the second approach according to [A-2b] or the related relations, [A-1] and [A-3], requires only the spatial expression of resonance frequencies in calculating both the absorption and the dispersion of the spectrum. Because multiplying a decay function g(t) is performed at the same time when the transient signal is calculated, this smooth the spectrum, and resulting the following advantages:

(1). It does not require as large sampling points (or small dot matrix) as those needed in the previous approach. Usually a 4 by 4 degree mesh is sufficient to give a smooth spectrum with negligible digital noise.

(2). Since the transient is calculated first, this approach will not encounter an singularity problem.

(3). In addition to generating an artificial transient decay, this scheme follows the same experimental data manipulation procedure, hence the calculation can be easily understandable and easily formulated by following the existing experimental routines.

(4). Since this straight forward integration method needs to calculated only a complete cycle of the transient signal. This implies that in the bottle neck of the calculation, only relatively small number of the powder averaged points in the time domain should be evaluated. Since the resolution is determined mainly by the number of the Fast fourier transform, and the cpu for the FFT is essentially negligible in the calculation this approach can yield better resolved spectrum with much less calculation cpu.

APPENDIX B: LIOUVILE SPACE OPERATOR

We first define the Liouville space (L-space) operators as parallel to that of the Hilbert space (H-space). Ordinary Hilbert operators (Hamiltonians) in Quantum Mechanics that used to be expressed as matrices of dimensions of the complete bases are now considered as "state vectors" in the L-space that linear functions f(Q) in the L-space (which are matrices) can be expressed as linear combination of its basis state "vectors". In applying these operators to NMR studies, several definitions for the L-space basis sets have been found; for example multipole tensors, fictitious spin -1/2 operators, or simply multiplication of the angular momentum I_x, I_y, I_z. In the following section we use only the irreducible tensor operators as the complete basis set.

The linear properties are parallel to that of H-space where all state vectors can be represented by linear combinations of the complete basis set. Using the notation $|Q)$ for ket and $(Q|$ for bra as L-space basis, the linear combination relations in L-space states:

$$|f(Q))=\sum_n a_n \ |Q_n) \qquad \text{L-space}$$

$$|f(\psi)\rangle=\sum_n a_n \ |\psi_n\rangle \qquad \text{H-space}$$

The scalar product between two Liouville vectors is defined as:

$$(A|B)=(B^+|A^+)=Tr\{AB\} \qquad [B\text{-}1]$$

Where A^+ is the adjoin of A. Liouville operators are then defined as superoperators denoted by a hat $\hat{Q}$. The operation is defined as:

$$\hat{Q}|A) = |[Q,A]) \qquad [B\text{-}2a]$$

$$(A|\hat{Q} = |[Q^{+},A]) \qquad [B\text{-}2b]$$

Notice that a L-operator (a superoperator) operating on L-space "vectors" implies the commutation relation need to be evaluated. Due to the linear relation of the commutator, the superoperators are also linear operators.

When the superoperator is the argument of an exponential, this occurs frequently in the evolution and the preparation stage of NMR transient experiments, the function of this operator can be evaluated by Taylor expansion. Invoking the definition in [B-2], we have

$$e^{\lambda\hat{A}}|B) = [1 + \lambda\hat{A} + \frac{1}{2!}(\lambda\hat{A})^2 + \frac{1}{3!}(\lambda\hat{A})^3 + \ldots]\,|B)$$

$$= B + \lambda[A,B] + \frac{\lambda^2}{2}[A,[A,B]] + \frac{\lambda^3}{6}[A,[A,[A,B]]]\ldots \qquad [B\text{-}3]$$

$$= e^{\lambda A} B\, e^{-\lambda A} \qquad [B\text{-}4]$$

Relation [B-3] and [B-4] can be proved directly by the following:

Let $f(\lambda) = e^{\lambda A} B\, e^{-\lambda A}$

$$\frac{\partial f}{\partial \lambda} = A\, f(\lambda) - f(\lambda)\, A = [A, f(\lambda)]$$

$$\frac{\partial^2 f}{\partial \lambda^2} = [A, \frac{\partial}{\partial \lambda} f(\lambda)] = [A,[A, f(\lambda)]]$$

Higher order derivative can also be found iteratively from this procedure. We now inserting the differential terms as the coefficient in the expansion of $f(\lambda)$, it gives

$$f(\lambda)= B+ \lambda[A,B]+\frac{\lambda^2}{2}[A,[A,B]]+\frac{\lambda^3}{6}[A,[A,[A,B]]]+... \qquad [B-5]$$

When express the above L-space "vector" using Ket and Bra notation, we arrive at [B-3]. This prove also indicate that notation [B-2] equals the commutation for L-space operators is consistent with the quantum mechanic relations.

Notice the different expression given in [B-3] and [B-4] for the exponential operator. The compact expression in [B-4] means the infinite expansion of [B-3] should be calculated. The importance of the exponential L-operators cannot be overemphasized, in studying the spin dynamics it is always the type of exponential operators that should be solved, which implies an infinite series of commutators must be evaluated in general. However there are several simplifications which can reduce the calculation or yield approximation of the solutions.

Several important and useful relations originated from [B-3] and [B-4] are discussed below.

(1). It is immediately realized from [B-4] together with the prove that, the following relations should also exists:

$$(B|e^{\lambda\hat{A}}= e^{-\lambda A}B\, e^{\lambda A} \qquad [B-6]$$

(2). When a commutator $[A,B]= \gamma B$ exists, where γ being a complex constant. (e.g., for $A=I_0$ and B arbitraty). Inserting the value of the commutator into [B-3], we found

$$e^{\lambda\hat{A}}|B) = |e^{\lambda\gamma}B) = e^{\lambda\gamma}|B) \qquad [B-7]$$

Infinite commutation now becomes a simple exponential multiplied by a complex constant.

(3). When A,B commute [A,B]=0, from [B-5] or [B-7] we have

$$e^{\lambda\hat{A}}|B) = e^{\lambda\gamma}|B) = |B) \qquad [B-8]$$

$$e^{\lambda\hat{A}}|A) = |A) \qquad [B-9]$$

(4). By using [B-1] the scalar product of [B-4] with another L-space "vector" $|C)$ becomes:

$$(C|e^{\lambda\hat{A}}|B) = Tr\{C^{+}e^{\lambda A}B\ e^{-\lambda A}\} = Tr\{e^{-\lambda A}C^{+}e^{\lambda A}B\} \qquad [B-10]$$

Similar trace expression as [B-10] can be obtained by using the even permutation relations.

$$Tr\{XYZW\} = Tr\{WXYZ\} = Tr\{YZWX\} = Tr\{ZWXY\}$$

(5). The special commutation relations from (1) to (3) implies that [B-10] can be further simplified if $[A,B]=\lambda B$ or $[A,C]=\lambda C$.

$$(C|e^{\lambda\hat{A}}|B) = e^{\lambda\gamma}\ Tr\{CB\} \qquad [B-11]$$

(6). Using definition [B-1] we may generate the following relation:

$$\hat{A}\hat{B}\hat{C}\ldots\hat{D}|\Xi) = A[B[C\ldots[D,\Xi]_{\cdot_{n}}]] \qquad [B-12]$$

if n=even

$$(A|\hat{B}^{n}|A) = ([A,B]|\hat{B}^{n-2}|[B,A]) = \mathrm{Tr}\{[B_{\frac{n}{2}},[B,A]\}^{2} \qquad [B\text{-}13]$$

(7). When operator B of [B-4] is also an exponential operator, the following equation can be used to facilitates the calculation.

$$e^{\hat{\lambda A}}|e^{B}) = \exp\, e^{\hat{\lambda A}}|B) \qquad [B\text{-}14]$$

The argument at the right of the equation is the same as [B-3], which allows the evaluation of [B-14] by using the inverse of [B-3]. The prove of this relation is straightforward.

Let $X = e^{\hat{\lambda A}}|B)$

$$e^{X} = 1+e^{\hat{\lambda A}}|B) + \frac{1}{2} e^{\lambda A}B\, e^{-\lambda A}\, e^{\lambda A}B\, e^{-\lambda A} + \frac{1}{6}[e^{\hat{\lambda A}}|B)]^{3} \ldots$$

$$= 1+e^{\hat{\lambda A}}|B)+\frac{1}{2} e^{\hat{\lambda A}}|B^{2})+\frac{1}{6} e^{\hat{\lambda A}}|B^{3})+ \ldots$$

$$= e^{\hat{\lambda A}}|1+B+\frac{1}{2} B^{2}+\frac{1}{6} B^{3}+ \ldots\ )$$

$$= e^{\hat{\lambda A}}|e^{B})$$

This results is found to be particularly useful when the general rotation of a tensor is related to the Wigner rotation matrix as shown in Appendix D.

APPENDIX C: DEFINITIONS OF THE EULER ANGLES

Several conventions exist in choosing the so called Euler angles.

The general displacement of a rigid body due to a rotation about a fixed point may be obtained by performing three rotations about two of the three mutually perpendicular axis field of the body. We shall assume a right handed frame of axes. A definition of a positive rotation about a given axis is the one that carries a right hand screws in the positive direction along that axis. For example a positive 90 degree rotation about the Z-axis carries the X-axis into the origional position of the Y-axis.

A Wigner rotation as described are to be performed in the following successive order.

(1). A rotation α $(0,2\pi)$ about the Z-axis. This brings the axes frame form initial frame S to the intermediate frame S',

(2). A rotation β $(0,\pi)$ about the Y-axis in the S' frame. A resulting frame of axes is symbolized by S''. Notice the Y-axis in this rotation is usually different from the original Y-axis.

(3). A rotation γ $(0,2\pi)$ about the Z-axis in the S'' frame. The position of this axis depends on the previous rotations α, and β. The resulting final axes frame is denoted as S'''.

Notice that a unique transformation can be carried out by several possible values of α, β, and γ. There is no 1 to 1 correspondence between the rotations and the parameters.

For simplifying the discussion we represent a rotation of angle δ about axis ζ being $D_\zeta(\delta)$ and for successive rotation operations they are arranged from right to left.

The above Wigner rotation is then written as

$$D(\alpha,\beta,\gamma) = D_{z''}(\gamma)D_{y'}(\beta)D_z(\alpha) \qquad [C\text{-}1]$$

In the above description of the general Wigner rotation, the angels γ,β have been defined relative to the axes frame of the moving body in frame S'' and S' respectively. In many applications it is convenient to refer these rotation angles to the original rigid frame of axes S.

Since rotation $D_y'(\beta)$ is equivalent to $D_z(\alpha)D_y(\beta)D_z(-\alpha)$, also the rotation $D_{z''}(\gamma)$ is equivalent to $D_{y'}(\beta)D_{z'}(\gamma)D_{y'}(-\beta)$, and hence to $D_z(\alpha)D_y(\beta)D_z(\gamma)D_y(-\beta)D_z(-\alpha)$ we may therefore express the above rotation with another equivalent form, e.g.,

$$D(\alpha,\beta,\gamma) = D_{z''}(\gamma)D_{y'}(\beta)D_z(\alpha) = D_z(\alpha)D_y(\beta)D_z(\gamma) \qquad [C\text{-}2]$$

This relation states that the Wigner rotation defined above is equivalent to the following rotation carried out in successive order: (a) a rotation γ about the Z axis; (b) a rotation β about the Y axis; and (c) a rotation α about the Z axis. Notice that the angels α,β,γ are now relative to the original fixed axes frame S.

Both notations are used frequently in studying the spin dynamics as well as the interaction frame transformation in the line shape calculations.

APPENDIX D: WIGNER ROTATION MATRIX ELEMENTS FOR k=1, 3/2 AND 2

The Wigner rotation matrix can be easily constructed using the following relation:

$$D^{(k)}_{m'm}\ (\alpha\beta\gamma) = \exp(im'\gamma)d^{(k)}_{m'm}\ (\beta)\ \exp(im\alpha)$$

where the Euler angles (α, β, γ) have been defined in Appendix C. In the following tables, the matrix elements for $d_{m',m}^{(k)}\ (\beta)$ are tabulated in Table I; k= 1, Table II; k=3/2, and Table III; k=2. Notations X=cosβ, Y=sinβ are used.

Table I

Table of elements of $d_{m',m}^{(2)}(\beta)$

m' \ m	2	1	0	-1	-2
2	$(\frac{1+X}{2})^2$	$\frac{1}{2}Y(1+X)$	$\sqrt{\frac{3}{8}}Y^2$	$\frac{-1}{2}Y(X-1)$	$(\frac{1-X}{2})^2$
1	$\frac{-1}{2}Y(X+1)$	$\frac{1}{2}(2X-1)(X+1)$	$\sqrt{\frac{3}{2}}XY$	$\frac{1}{2}(2X+1)(1-X)$	$\frac{-1}{2}Y(X-1)$
0	$\sqrt{\frac{3}{8}}Y^2$	$-\sqrt{\frac{3}{2}}XY$	$\frac{1}{2}(3X^2-1)$	$\sqrt{\frac{3}{2}}XY$	$\sqrt{\frac{3}{8}}Y^2$
-1	$\frac{1}{2}Y(X-1)$	$\frac{1}{2}(2X+1)(1-X)$	$-\sqrt{\frac{3}{2}}XY$	$\frac{1}{2}(2X-1)(X+1)$	$\frac{1}{2}Y(X+1)$
-2	$(\frac{1-X}{2})^2$	$\frac{1}{2}Y(X-1)$	$\sqrt{\frac{3}{8}}Y^2$	$\frac{-1}{2}Y(X+1)$	$(\frac{X+1}{2})^2$

Table II

Table of elements $d_{m',m}^{(3/2)}(\beta)$

m' \ m	3/2	1/2	-1/2	-3/2
3/2	X^3	$\sqrt{3}X^2Y$	$\sqrt{3}XY^2$	Y^3
1/2	$-\sqrt{3}X^2Y$	$X(3X^2-2)$	$-Y(3Y^2-2)$	$\sqrt{3}XY^2$
-1/2	$\sqrt{3}X^2Y$	$Y(3Y^2-2)$	$X(3X^2-2)$	$\sqrt{3}X^2Y$
-3/2	$-Y^3$	$\sqrt{3}XY^2$	$-\sqrt{3}X^2Y$	X^3

Table III

Table of elements $d_{m',m}^{(1)}(\beta)$

m' \ m	1	0	-1
1	$\frac{1}{2}(1+X)$	$\frac{1}{\sqrt{2}}Y$	$\frac{1}{2}(1-X)$
0	$\frac{1}{\sqrt{2}}Y$	X	$\frac{1}{\sqrt{2}}Y$
-1	$\frac{1}{2}(1-X)$	$\frac{1}{\sqrt{2}}Y$	$\frac{1}{2}(1+X)$

APPENDIX E: SPHERICAL TENSOR REPRESENTATION OF SPIN OPERATORS

H^{λ}	T_{00}	T_{10}	$T_{1\pm1}$
shift	$\frac{-1}{\sqrt{3}} I_0 B_0$	0	$\frac{-1}{2} I_{\pm} B_0$
J-coupling	$\frac{-1}{\sqrt{3}} \mathbf{I}\cdot\mathbf{S}$	$\frac{-1}{2\sqrt{2}}(I_+S_- - I_-S_+)$	$\frac{1}{2}(I_0S_{\pm} - I_{\pm}S_0)$
Spin-J	$\frac{-1}{\sqrt{3}} \mathbf{I}\cdot\mathbf{J}$	$\frac{-1}{2\sqrt{2}}(I_+J_- - I_-J_+)$	$\frac{1}{2}(I_0I_{\pm} - I_{\pm}I_0)$

H^{λ}	T_{20}	$T_{2\pm1}$	$T_{2\pm2}$
Shift	$\sqrt{\frac{2}{3}} I_0 B_0$	$\mp \frac{1}{2} I_{\pm} B_0$	0
Dipoler	$\frac{1}{\sqrt{6}} (3I_0S_0 - \mathbf{I}\cdot\mathbf{S})$	$\mp \frac{1}{2} (I_0S_{\pm} + I_{\pm}S_0)$	$\frac{1}{2} I_{\pm}S_{\pm}$
J-Coupling	$\frac{1}{\sqrt{6}} (3I_0S_0 - \mathbf{I}\cdot\mathbf{S})$	$\mp \frac{1}{2} (I_0S_{\pm} + I_{\pm}S_0)$	$\frac{1}{2} I_{\pm}S_{\pm}$
Spin-Rotatio	$\frac{1}{\sqrt{6}} (3I_0J_0 - \mathbf{I}\cdot\mathbf{J})$	$\mp \frac{1}{2} (I_0J_{\pm} + I_{\pm}J_0)$	$\frac{1}{2} I_{\pm}J_{\pm}$
Quadrupole	$\frac{1}{\sqrt{6}} (3I_0^2 - I^2)$	$\mp \frac{1}{2} (I_0I_{\pm} + I_{\pm}I_0)$	$\frac{1}{2} I_{\pm}I_{\pm}$

APPENDIX F: LIST OF IRREDUCIBLE COMPONENTS R_n^2 UNDER SINGLE AND DOUBLE INTERACTION FRAME TRANSFORMATION

Interaction frame transformation for the second rank irreducible components R_n^2 are calculated under single and double transformation. The irreducible components expressed in its principal axis system are defined as:

$$\rho_{2\pm2}^{\lambda} = \rho_{22}^{\lambda} = \frac{1}{2}(\sigma_{xx}^{\lambda}-\sigma_{yy}^{\lambda}) \pm i\sigma_{xy}^{\lambda} = \frac{1}{2}\eta^{\lambda}\delta^{\lambda}$$

$$\rho_{2\pm1}^{\lambda} = (\sigma_{xz}^{\lambda} \pm i\ \sigma_{yz}^{\lambda}) = 0$$

$$\rho_{20}^{\lambda} = \sqrt{3}/2\ (\sigma_{zz}^{\lambda}-\sigma_{0}^{\lambda}) = \sqrt{3}/2\ \delta^{\lambda}$$

Where anisotropy $\delta=\sigma_{zz}-\sigma_0$, asymmetry $\eta=(\sigma_{yy}-\sigma_{xx})/\sigma_{zz}-\sigma_0$, and isotropic value $\sigma_0=(\sigma_{xx}+\sigma_{yy}+\sigma_{zz})/3$. The three principal values of the interaction λ are $\sigma_{xx},\sigma_{yy},\sigma_{zz}$. Notice we have completely neglected the antisymmetric elements and hence $\rho_{2\pm1}=0$ is assumed for all interactions.

(A) Single interaction frame transformation is as follows:

$$R_n^2(\psi,\theta,\phi) = \rho_2^2\ e^{in\psi}[e^{i2\phi}d_{2n}(\theta) + e^{-2i\phi}d_{-2n}(\theta)] + \rho_0^2\ e^{in\psi}d_{0n}(\theta) \qquad [F\text{-}1]$$

(1). $R_0^2(\psi,\theta,\phi) = \rho_2^2\ \sqrt{\frac{3}{2}}\sin^2\theta\cos2\phi + \rho_0^2\ P_2(\cos\theta)$

(2). $R_1^2(\psi,\theta,\phi) = e^{i\psi}[\rho_2^2\ (\cos\theta\sin\theta\cos2\phi+i\sin\theta\sin\phi) - \rho_0^2(\sqrt{\frac{3}{2}}\cos\theta\sin\theta)]$

(3). $R_1^2(\psi,\theta,\phi) = e^{2i\psi}[\rho_2^2(\frac{1+\cos^2\theta}{2}\cos2\phi+i\cos\theta\sin2\phi) + \rho_0^2\ \sqrt{\frac{3}{8}}\sin^2\theta\ ]$

(B) Double interaction frame transformation is defined as:

$$R_n^2(\alpha,\beta,\gamma,\theta,\phi) = \rho_2^2 \sum_m e^{im\Omega} d_{mn}(\theta)[e^{2i\alpha} d_{2m}(\beta)+e^{-2i\alpha} d_{-2m}(\beta)] + \rho_0^2 \sum_m e^{im\Omega} d_{mn}(\theta)\, d_{0m}(\beta) \qquad [F-2]$$

(1). $R_0^2(\alpha,\beta,\gamma,\theta,\phi) =$

$$\rho_2^2 \sqrt{\tfrac{3}{2}} \{ P_2(\cos\theta)\sin^2\beta\cos 2\alpha \qquad m=0$$

$$+2\cos\theta\sin\theta(\cos\beta\sin\beta\cos 2\alpha\cos\Omega-\sin\beta\sin 2\alpha\sin\Omega) \qquad m=\pm 1$$

$$+\sin^2\theta(\frac{1+\cos^2\beta}{2}\cos 2\alpha\cos 2\Omega-\sin\beta\sin 2\alpha\sin 2\Omega)\} \qquad m=\pm 2$$

$$+ \rho_0^2\{ p_2(\cos\theta)\cdot P_2(\cos\beta) - 3\cos\theta\sin\theta\cos\beta\sin\beta\cos\Omega \qquad m=0,\pm 1$$

$$+ \tfrac{3}{4}\cos^2\theta\sin^2\beta\cos 2\Omega \} \qquad m=\pm 2$$

(2). $R_1^2(\alpha,\beta,\gamma,\theta,\phi) =$

$$\rho_2^2 \{ \tfrac{3}{2}\cos\theta\sin\theta\sin^2\beta\cos 2\alpha \qquad m=0$$

$$+2(\cos^2\theta-\tfrac{1}{2})(\cos\beta\sin\beta\cos 2\alpha\cos\Omega-\sin\beta\sin 2\alpha\sin\Omega)$$

$$-i\cos\theta(\cos\beta\sin\beta\cos 2\alpha\sin\Omega+\sin\beta\sin 2\alpha\cos\Omega) \qquad m=\pm 1$$

$$+\cos\theta\sin\theta(\frac{1+\cos^2\beta}{2}\cos 2\alpha\cos 2\Omega-\sin\beta\sin 2\alpha\sin 2\Omega)\}$$

$$-i\sin\theta(\frac{1+\cos^2\beta}{2}\cos 2\alpha\cos 2\Omega-\sin\beta\sin 2\alpha\sin 2\Omega)\} \qquad m=\pm 2$$

$$+\ \rho_0^2\{\ \sqrt{\tfrac{3}{2}}\cos\theta\sin\theta\cdot P_2(\cos\beta) \qquad m=0$$

$$+\sqrt{\tfrac{3}{2}}\cos\beta\sin\beta\ [\cos 2\theta\cos\Omega+i\cos\theta\sin\Omega] \qquad m=\pm 1$$

$$+\sqrt{\tfrac{3}{8}}\sin^2\beta\ [\cos\theta\sin\theta\cos 2\Omega-i\sin\theta\sin 2\Omega]\ \} \qquad m=\pm 2$$

(3). $R_2^2(\alpha,\beta,\gamma,\theta,\phi) =$

$$\rho_2^2\ \{\ \tfrac{3}{4}\sin^2\theta\sin^2\beta\cos 2\alpha \qquad m=0$$

$$-\cos\theta\sin\theta(\cos\beta\sin\beta\cos 2\alpha\cos\Omega-\sin\beta\sin 2\alpha\sin\Omega)$$

$$i\sin\theta(\cos\beta\sin\beta\cos 2\alpha\sin\Omega-\sin\beta\sin 2\alpha\cos\Omega) \qquad m=\pm 1$$

$$\tfrac{1+\cos^2\theta}{4}\ (\tfrac{1+\cos^2\beta}{2}\cos 2\alpha\cos 2\Omega-\sin\beta\sin 2\alpha\sin 2\Omega)$$

$$-\tfrac{i}{2}\cos\theta(\tfrac{1+\cos^2\beta}{2}\cos 2\alpha\sin 2\Omega+\sin\beta\sin 2\alpha\cos 2\Omega)\} \qquad m=\pm 2$$

$$+\ \rho_0^2\ \{\ \sqrt{\tfrac{3}{8}}\sin^2\theta\cdot P_2(\cos\beta) \qquad m=0$$

$$+\sqrt{\tfrac{3}{2}}\cos\beta\sin\beta(\cos\theta\sin\theta\cos\Omega-i\sin\theta\sin\Omega) \qquad m=\pm 1$$

$$+\sqrt{\tfrac{3}{8}}\sin^2\beta(\ \tfrac{1+\cos^2\theta}{2}\cos 2\Omega-i\cos\theta\sin 2\Omega)\ \} \qquad m=\pm 2$$